

Understanding the systemic immune response in COVID-19 – one cell at a time

Dissertation

zur Erlangung des Doktorgrades (Dr. rer. nat.)
der Mathematisch-Naturwissenschaftlichen Fakultät
der Rheinischen Friedrich-Wilhelms-Universität Bonn

vorgelegt von

Jonas Schulte-Schrepping

aus

Dorsten, Deutschland

Bonn, 2023

Angefertigt mit Genehmigung und nach den Richtlinien der Mathematisch-Naturwissenschaftlichen Fakultät der Rheinischen Friedrich-Wilhelms-Universität Bonn.

1. Gutachter: Prof. Dr. Joachim L. Schultze

2. Gutachter: Prof. Dr. Andreas Schlitzer

Tag der Promotion: 06.03.2023

Erscheinungsjahr: 2023

Index

Index.....	I
Index of Figures.....	II
Index of Tables.....	II
Abbreviations.....	III
Relevant publications.....	IV
Acknowledgements.....	VII
Summary.....	VIII
1. Preface.....	1
2. Introduction.....	2
2.1. Systems approaches for modern medicine.....	2
2.2. Challenges in clinical application of single-cell transcriptomics.....	4
2.3. The immune system – a prime target for single-cell omics.....	7
2.3.1. The myeloid cell compartment in health and disease.....	8
2.4. The COVID-19 pandemic and pathology of SARS-CoV-2.....	10
2.4.1. Understanding the myeloid cell response in COVID-19 pathogenesis.....	12
3. Aim of the thesis.....	14
4. Publications.....	15
4.1. Optimized workflow for single-cell transcriptomics on infectious diseases including COVID-19.....	15
4.2. Severe COVID-19 is marked by a dysregulated myeloid cell compartment.....	17
4.3. Effective CD8 ⁺ T cell immunity against SARS-CoV-2 depends on the integration of type 1 IFN signals and CD4 ⁺ T cell help by antigen-presenting cells.....	19
5. Conclusion.....	25
5.1. Dissecting the innate immune system in COVID-19 – cell by cell.....	25
5.2. Future perspectives of single-cell omics in medicine.....	27
6. References.....	29
7. Appendix A-C.....	45

Index of Figures

Figure 1: Schematic depiction of the development of omics technologies	3
Figure 2: Development of single-cell studies over space and time	4
Figure 3: Complexity of single-cell transcriptomics workflows	5
Figure 4: Reporting statistics for blood-based single-cell RNA-seq studies	6
Figure 5: Combinatorial transcriptome responses to type 1 IFN and CD40 stimulation by monocytes and DCs correlate with milder outcomes of COVID-19	20
Figure 6: Open chromatin profiles in monocytes and DCs support the combinatorial transcriptome responses to type 1 IFN and CD40 stimulation in milder cases of COVID-19..	21
Figure 7: Severe outcomes of COVID-19 are associated with ‘unhelped’ CD8 ⁺ T cells	22

Index of Tables

Table 1: Reporting overview for blood-based single-cell RNA-seq studies.....	6
--	---

Abbreviations

PBMC	Peripheral blood mononuclear cells
RNA-seq	RNA sequencing
scRNA-seq	Single-cell RNA sequencing
SOP	Standardized operation procedures
IBD	Inflammatory Bowel Disease
MS	Multiple sclerosis
HCA	Human Cell Atlas
NGS	Next generation sequencing
BCR	B cell receptor
TCR	T cell receptor
CAR-T	Chimeric antigen receptor T cells
ATAC-seq	Assay for Transposase-Accessible Chromatin using sequencing
WHO	World Health Organization
LDN	Low density neutrophils
APC	Antigen presenting cell
DC	Dendritic cell
IFN	Interferon
ARDS	Acute respiratory distress syndrome
HSPC	Hematopoietic stem and progenitor cell

Relevant publications

2023

Gressier E*, **Schulte-Schrepping J***, Petrov L, Brumhard S, Stubbemann P, Hiller A, Obermayer B, Spitzer J, Kostevc T, Whitney PG, Bachem PG, Odainic A, van de Sandt C, Nguyen THO, Ashhurst T, Wilson K, Oates CVL, Gearing LJ, Meischel T, Hochheiser K, Greyer M, Clarke M, Kreutzenbeck M, Gabriel SS, Kastenmüller W, Kurts C, Londrigan SL, Kallies A, Kedzierska K, Hertzog PJ, Latz E, Chen YCE, Radford KJ, Chopin M, Schroeder J, Kurth F, Gebhardt R, Sander LE, Sawitzki B, Schultze JL, Schmidt SV, Bedoui S, „**CD4+ T cell calibration of antigen-presenting cells optimizes antiviral CD8+ T cell immunity**”, Nat Immunol (2023). doi: 10.1038/s41590-023-01517-x

2022

Bonaguro L*, **Schulte-Schrepping J***, Ulas T*, Aschenbrenner AC, Beyer M, Schultze JL, “**A guide to systems-level immunomics.**”, Nat Immunol, 2022 Sept 22, doi: 10.1038/s41590-022-01309-9

2021

Krämer B, Knoll R, Bonaguro L, ToVinh M, Raabe J, Astaburuaga-García R, **Schulte-Schrepping J**, Kaiser KM, Rieke GJ, Bischoff J, Monin MB, Hoffmeister C, Schlabe S, De Domenico E, Reusch N, Händler K, Reynolds G, Blüthgen N, Hack G, Finnemann C, Nischalke HD, Strassburg CP, Stephenson E, Su Y, Gardner L, Yuan D, Chen D, Goldman J, Rosenstiel P, Schmidt SV, Latz E, Hrusovsky K, Ball AJ, Johnson JM, Koenig1 P-A, Schmidt FI, Haniffa M, Heath JR, Kümmerer BM, Keitel V, Jensen B, Stubbemann P, Kurth F, Sander FE, Sawitzki B, Deutsche COVID-19 Omics Initiative (DeCOI), Aschenbrenner AC, Schultze JL, Nattermann J, “**Early IFN- α signatures and persistent dysfunction are distinguishing features of NK cells in severe COVID-19**”, Immunity. 2021 Sep 4, doi: 10.1016/j.immuni.2021.09.002

Knoll R, Schultze JL, **Schulte-Schrepping J**, “**Monocytes and Macrophages in COVID-19.**”, Front Immunol. 2021 Jul 21;12:720109. doi: 10.3389/fimmu.2021.720109.

Warnat-Herresthal S, Schultze H, Shastry KL, Manamohan S, Mukherjee S, Garg V, Sarveswara R, Händler K, Pickkers P, Aziz NA, Ktena S, Tran F, Bitzer M, Ossowski S, Casadei N, Herr C, Petersheim D, Behrends U, Kern F, Fehlmann T, Schommers P, Lehmann C, Augustin M, Rybniker J, Altmüller J, Mishra N, Bernardes JP, Krämer B, Bonaguro L, **Schulte-Schrepping J**, De Domenico E, Siever C, Kraut M, Desai M, Monnet B, Saridaki M, Siegel CM, Drews A, Nuesch-Germano M, Theis H, Heyckendorf J, Schreiber S, Kim-Hellmuth S; COVID-19 Aachen Study (COVAS), Nattermann J, Skowasch D, Kurth I, Keller A, Bals R, Nürnberg P, Rieß O, Rosenstiel P, Netea MG, Theis F, Mukherjee S, Backes M, Aschenbrenner AC, Ulas T; Deutsche COVID-19 Omics Initiative (DeCOI), Breteler MMB, Giamarellos-Bourboulis EJ, Kox M, Becker M, Cheran S, Woodacre MS, Goh EL, Schultze JL, “**Swarm Learning for decentralized and confidential clinical machine learning.**”, Nature. 2021 Jun;594(7862):265-270. doi: 10.1038/s41586-021-03583-3.

Reusch N, De Domenico E, Bonaguro L, **Schulte-Schrepping J**, Baßler K, Schultze JL, Aschenbrenner AC, „**Neutrophils in COVID-19.**”, Front Immunol. 2021 Mar 25;12:652470. doi: 10.3389/fimmu.2021.652470.

Aschenbrenner AC, Mouktaroudi M, Krämer B, Oestreich M, Antonakos N, Nuesch-Germano M, Gkizeli K, Bonaguro L, Reusch N, Baßler K, Saridaki M, Knoll R, Pecht T, Kapellos TS, Doulou S, Kröger C, Herbert M, Holsten L, Horne A, Gemünd ID, Rovina N, Agrawal S, Dahm K, van Uelft M, Drews A, Lenkeit L, Bruse N, Gerretsen J, Gierlich J, Becker M, Händler K, Kraut M, Theis H, Mengiste S, De Domenico E, **Schulte-Schrepping J**, Seep L, Raabe J, Hoffmeister C, ToVinh M, Keitel V, Rieke G, Talevi V, Skowasch

D, Aziz NA, Pickkers P, van de Veerdonk FL, Netea MG, Schultze JL, Kox M, Breteler MMB, Nattermann J, Koutsoukou A, Giamarellos-Bourboulis EJ, Ulas T; German COVID-19 Omics Initiative (DeCOI)., **“Disease severity-specific neutrophil signatures in blood transcriptomes stratify COVID-19 patients.”**, *Genome Med.* 2021 Jan 13;13(1):7. doi: 10.1186/s13073-020-00823-5.

2020

De Domenico E*, Bonaguro L*, **Schulte-Schrepping J***, Becker M, Händler K, Schultze JL., **„Optimized workflow for single-cell transcriptomics on infectious diseases including COVID-19.”**, *STAR Protoc.* 2020 Dec 16;1(3):100233. doi: 10.1016/j.xpro.2020.100233. eCollection 2020 Dec 18.

Bernardes JP, Mishra N, Tran F, Bahmer T, Best L, Blase JI, Bordoni D, Franzenburg J, Geisen U, Josephs-Spaulding J, Köhler P, Künstner A, Rosati E, Aschenbrenner AC, Bacher P, Baran N, Boysen T, Brandt B, Bruse N, Dörr J, Dräger A, Elke G, Ellinghaus D, Fischer J, Forster M, Franke A, Franzenburg S, Frey N, Friedrichs A, Fuß J, Glück A, Hamm J, Hinrichsen F, Hoepfner MP, Imm S, Junker R, Kaiser S, Kan YH, Knoll R, Lange C, Laue G, Lier C, Lindner M, Marinos G, Markewitz R, Nattermann J, Noth R, Pickkers P, Rabe KF, Renz A, Röcken C, Rupp J, Schaffarzyk A, Scheffold A, **Schulte-Schrepping J**, Schunk D, Skowasch D, Ulas T, Wandinger KP, Wittig M, Zimmermann J, Busch H, Hoyer BF, Kaleta C, Heyckendorf J, Kox M, Rybniker J, Schreiber S, Schultze JL, Rosenstiel P; HCA Lung Biological Network; Deutsche COVID-19 Omics Initiative (DeCOI)., **“Longitudinal Multi-omics Analyses Identify Responses of Megakaryocytes, Erythroid Cells, and Plasmablasts as Hallmarks of Severe COVID-19.”**, *Immunity.* 2020 Dec 15;53(6):1296-1314.e9. doi: 10.1016/j.immuni.2020.11.017.

Kalafati L, Kourtzelis I, **Schulte-Schrepping J**, Li X, Hatzioannou A, Grinenko T, Hagag E, Sinha A, Has C, Dietz S, de Jesus Domingues AM, Nati M, Sormendi S, Neuwirth A, Chatzigeorgiou A, Ziogas A, Lesche M, Dahl A, Henry I, Subramanian P, Wielockx B, Murray P, Mirtschink P, Chung K-J, Schultze JL, Netea MG, Hajishengallis G, Verginis P, Mitroulis I, Chavakis T, **“Innate immune training of granulopoiesis promotes anti-tumor activity”**, *Cell.* 2020 Oct 29;183(3):771-785.e12. doi: 10.1016/j.cell.2020.09.058.

Schulte-Schrepping J*, Reusch N*, Paclik D*, Baßler K*, Schlickeiser S*, Zhang B*, Krämer B*, Krammer T*, Brumhard S*, Bonaguro L*, De Domenico E*, Wendisch D*, Grasshoff M, Kapellos TS, Beckstette M, Pecht T, Saglam A, Dietrich O, Mei HE, Schulz AR, Conrad C, Kunkel D, Vafadarnejad E, Xu C-J, Horne A, Herbert M, Drews A, Thibeault C, Pfeiffer M, Hippenstiel S, Hocke A, Müller-Redetzky H, Heim K-M, Machleidt F, Uhrig A, Bosquillon de Jarcy L, Jürgens L, Stegemann M, Glösenkamp CR, Volk H-D, Goffinet C, Landthaler M, Wyler E, Georg P, Schneider M, Dang-Heine C, Neuwinger N, Kappert K, Tauber R, Corman V, Raabe R, Kaiser KM, To Vinh M, Rieke G, Meisel C, Ulas T, Becker M, Geffers R, Witzernath M, Drosten C, Suttorp N, von Kalle C, Kurth F, Händler K, Schultze JL, Aschenbrenner AC, Li Y, Nattermann J, Sawitzki B, Saliba A-E, Sander LE, Deutsche COVID-19 OMICS Initiative (DeCOI), **“Severe COVID-19 Is Marked by a Dysregulated Myeloid Cell Compartment”**, *Cell.* 2020 Aug 5; S0092-8674(20)30992-2. doi: 10.1016/j.cell.2020.08.001.

Cirovic B, de Bree LCJ, Groh L, Blok BA, Chan J, van der Velden WJFM, Bremmers MEJ, van Crevel R, Händler K, Picelli S, **Schulte-Schrepping J**, Klee K, Oosting M, Koeken VACM, van Ingen J, Li Y, Benn CS, Schultze JL, Joosten LAB, Curtis N, Netea MG, Schlitzer A, **“BCG Vaccination in Humans Elicits Trained Immunity via the Hematopoietic Progenitor Compartment”**, *Cell Host Microbe.* 2020 Aug 12;28(2):322-334.e5. doi: 10.1016/j.chom.2020.05.014.

Schulte-Schrepping J, Ferreira HF, Saglam A, Hinkley E, Schultze JL. **“Advances in Single-Cell Epigenomics of the Immune System”**, *“Epigenetics of the Immune System”*, Volume 18 in *Translational Epigenetics*, 2020, Pages 185-216, doi: 10.1016/B978-0-12-817964-2.00008-3.

2019

Warnat-Herresthal S, Perrakis K, Taschler B, Becker M, Baßler K, Beyer M, Günther P, **Schulte-Schrepping J**, Seep L, Klee K, Ulas T, Haferlach T, Mukherjee S, Schultze JL. “**Scalable Prediction of Acute Myeloid Leukemia Using High-Dimensional Machine Learning and Blood Transcriptomics**” *iScience*. 2019 Dec 18;23(1):100780. doi: 10.1016/j.isci.2019.100780.

Baßler K, **Schulte-Schrepping J**, Warnat-Herresthal S, Aschenbrenner AC, Schultze JL. „**The Myeloid Cell Compartment – Cell by Cell**“. *Annu Rev Immunol*. 2019 Apr 26;37:269-293. doi: 10.1146/annurev-immunol-042718-041728.

Baßler K, Günther P, **Schulte-Schrepping J**, Becker M, Biernat P. „**A Bioinformatic Toolkit for Single-Cell mRNA Analysis**.“ *Methods Mol Biol*. 2019;1979:433-455. doi: 10.1007/978-1-4939-9240-9_26.

2018

Christ A, Günther P, Lauterbach MAR, DUEWELL P, Biswas D, Pelka K, Scholz CJ, Oosting M, Haendler K, Baßler K, Klee K, **Schulte-Schrepping J**, Ulas T, Moorlag SJCFM, Kumar V, Park MH, Joosten LAB, Groh LA, Riksen NP, Espevik T, Schlitzer A, Li Y, Fitzgerald ML, Netea MG, Schultze JL, Latz E. “**Western Diet Triggers NLRP3-Dependent Innate Immune Reprogramming**.“ *Cell*. 2018 Jan 11;172(1-2):162-175.e14. doi: 10.1016/j.cell.2017.12.013.

Thion MS, Low D, Silvin A, Chen J, Grisel P, **Schulte-Schrepping J**, Blecher R, Ulas T, Squarzoni P, Hoeffel G, Culpier F, Siopi E, David FS, Scholz C, Shihui F, Lum J, Amoyo AA, Larbi A, Poidinger M, Buttgerit A, Lledo PM, Greter M, Chan JKY, Amit I, Beyer M, Schultze JL, Schlitzer A, Pettersson S, Ginhoux F, Garel S. “**Microbiome Influences Prenatal and Adult Microglia in a Sex-Specific Manner**.“ *Cell*. 2018 Jan 25;172(3):500-516.e16. doi: 10.1016/j.cell.2017.11.042.

Acknowledgements

This work would not have been possible without the help and support of many people which should not remain unmentioned. I would like to thank all the people who contributed in some way to the work described in this thesis.

First and foremost, I would like to express my special appreciation to my mentor Prof. Dr. Joachim L. Schultze for the opportunity to work on such fascinating projects, his most helpful support and motivation throughout the highs and lows of my doctorate, the provision of all necessary means, and for examining this thesis.

I would also like to thank Prof. Dr. Andreas Schlitzer for his guidance and support during my doctorate and for taking the time to examine this thesis.

In addition, I would like to express my special appreciation to PD Dr. Marc Beyer for the many joyful and thought-provoking discussions.

Furthermore, I would like to acknowledge all past and present members of the Schultze group for an instructive, stimulating and very enjoyable time. In particular, I would like to thank Lorenzo Bonaguro, Kevin Baßler, Stefanie Warnat-Herresthal, Tal Pecht, Caterina Carraro, Charlotte Kröger, Rainer Knoll, Nico Reusch, Lisa Holsten, Ioanna Gemünd, Arik Horne, Collins Osei-Sarpong, Theo Kapellos, Patrick Günther, Heidi Theis, Michael Kraut, Elke Schubert, Elena De Domenico, Pawel Biernat, Kristian Händler, Thomas Ulas and Matthias Becker for their helpfulness, honesty, friendship and team spirit.

My sincere appreciation also goes to the many collaborators I had the pleasure to work with over the time of my doctorate.

Finally, I am forever grateful to my family and friends for providing a supportive environment that allowed me to focus on my research.

Thank you!

Summary

The introduction of severe acute respiratory syndrome coronavirus 2 (SARS-CoV-2) into the human population presented an enormous medical and economic crisis that required an immediate response from the scientific community. In this unprecedented effort, recent developments in the field of single-cell omics have proved particularly helpful in deciphering the complex immune response to this new pathogen and have contributed significantly to a detailed understanding of the immunopathology of COVID-19.

In this cumulative thesis, I review the major developments in the field of single-cell omics for systems immunology, describe ongoing challenges and improvements in their clinical implementation, and present my contributions to understanding the systemic immune response in COVID-19 using single-cell omics approaches through three publications.

Initially, we developed an optimized and safe workflow for the application of single-cell transcriptomics and proteomics to infectious diseases. Using this workflow, we studied changes in the systemic composition and activation of immune cells across COVID-19 disease severities and reported profound dysregulation of the myeloid cell compartment in severe disease with dysfunctional monocytes and neutrophils and signs of emergency myelopoiesis. In addition, we examined the potential consequences of the derailment of the innate immune system for the induction of the adaptive immune response against SARS-CoV-2 and identified critical alterations in the signal integration processes by antigen-presenting cells and their interaction with T cells in severe diseases.

Finally, I discuss our findings in the context of long-term sequelae of COVID-19 and persistent adaptations of the innate immune system after infection and present my perspective on the future of the clinical application of high-dimensional omics techniques with single-cell resolution.

Zusammenfassung

Die Einschleppung von SARS-CoV-2 (Schweres Akutes Respiratorisches Syndrom Coronavirus 2) in die menschliche Bevölkerung stellte eine enorme medizinische und wirtschaftliche Krise dar, die eine sofortige Reaktion der wissenschaftlichen Gemeinschaft erforderte. Bei dieser beispiellosen Anstrengung erwiesen sich die jüngsten Entwicklungen auf dem Gebiet der Einzelzellgenomik zur Entschlüsselung der komplexen Immunantwort auf diesen neuen Erreger als besonders hilfreich und trugen wesentlich zu einem detaillierten Verständnis der Immunpathologie von COVID-19 bei.

In dieser kumulativen Dissertation gebe ich einen Überblick über die wichtigsten Entwicklungen auf dem Gebiet der Einzelzellgenomik für die Systemimmunologie, beschreibe bestehende Herausforderungen und notwendige Verbesserungen für ihre klinische Anwendung und stelle meine Beiträge zum Verständnis der systemischen Immunantwort bei COVID-19 vor, welche ich mithilfe der Einzelzellgenomik gewonnen habe.

Zunächst haben wir einen optimierten und sicheren Arbeitsablauf für die Anwendung der Einzelzell-Transkriptomik und Proteomik auf Infektionskrankheiten entwickelt. Mithilfe dieses Arbeitsablaufs haben wir Veränderungen in der systemischen Zusammensetzung und Aktivierung von Immunzellen über diverse Verläufe von COVID-19 untersucht und eine tiefgreifende Dysregulation des myeloiden Zellkompartiments bei schweren Erkrankungen mit dysfunktionalen Monozyten und Neutrophilen, sowie Anzeichen von Notfall-Myelopoese beschrieben. Darüber hinaus haben wir die Relevanz dieser Störungen des angeborenen Immunsystems für die Induktion der adaptiven Immunantwort gegen SARS-CoV-2 untersucht und kritische Veränderungen in der Signalintegration antigenpräsentierender Zellen und deren Interaktion mit T-Zellen bei schweren Erkrankungen identifiziert.

Abschließend diskutiere ich unsere Erkenntnisse im Kontext von Langzeitfolgen von COVID-19 und der Adaption des angeborenen Immunsystems nach einer Infektion und präsentiere meine Zukunftsperspektiven der klinischen Anwendung hochdimensionaler Omik-Techniken mit Einzelzellauflösung.

1. Preface

The blue tit, a small passerine bird in the tit family, has for a long time been classified as sexually monochromatic based on human color perception. Unlike humans, however, most birds are visually sensitive to wavelengths in the near-ultraviolet (300-400 nm) and, for the female bird's eye, the male blue tit shines in a special guise invisible to us. Only using UV photography, we discovered its unexpected beauty (Hunt et al., 1998; Tedore and Nilsson, 2019).

Human perception is naturally limited in many ways. We are unable to fully appreciate the beauty and complexity of nature on our own. Only through the development and use of technological aids we can uncover what was previously hidden. In addition to the discoveries, methodological advances spark new questions and therefore have a determining influence on the path of discovery.

While modern technologies allow us to investigate biological phenomena at molecular resolution in reductionist systems for decades, linking the individual observations to a larger context presents a remaining challenge. Recent technological developments in modern biology tackle this challenge to capture the underlying mechanisms at system-wide scale.

The present work aims to summarize the recent developments in the field of single-cell omics for systems immunology, map out persisting challenges and solutions for their clinical application and demonstrate their power at the example of COVID-19.



2. Introduction

2.1. Systems approaches for modern medicine

A cell is the smallest structural and functional unit of an organism. Therefore, every attempt at a holistic understanding of a biological phenomenon in health and disease ultimately requires the study of its underlying phenotypic features and molecular mechanisms at single-cell resolution. Assessing cellular identity, heterogeneity and function is crucial to map the complex networks of biological processes.

Since the genetic material, i.e. the genome, of every cell in an organism is largely identical, cellular identity is defined – at least in parts – by the precise and dynamic use of its functional elements, the genes. Technological advances over the last decades, particularly in the field of DNA sequencing, enable researchers today to measure gene expression and regulation at unprecedented resolution and scale. So-called ‘omics’ technologies are characterized by the aim of universal detection of their target molecules and molecular structures. ‘Genomics’ focuses on the structure, function, evolution, and editing of an organism's complete set of DNA, its genome. ‘Epigenomics’ comprises a broad range of technologies measuring various epigenetic features reflecting the wide variety of regulatory mechanisms controlling gene expression. ‘Transcriptomics’ describes a group of technologies targeting the products of transcription, that is the whole of the RNA present in a cell at a given time. Recent technological advances go beyond sequencing-based assessment of the genome, its output, and its regulation. Proteomics, metabolomics, microbiomics, and lipidomics have been introduced and will contribute to a condensed understanding of complex biological relationships.

Unlike reductionist experimental approaches to elucidate individual parts of the puzzle, systems approaches aim at putting the pieces together, which requires specialized methodologies (Aderem, 2005). DNA microarray analysis was first described in 1995 (Schena et al., 1995). This technology for the first time allowed to probe the expression of thousands of genes simultaneously – a new capability with revolutionary potential at the time (Figure 1). The highly parallelized technique presented the starting point for the use of high-dimensional transcriptomics in medicine and allowed for fundamental observations, such as the identification of specific genes for tumor classification (Quackenbush, 2006) and those involved in cancer progression (DeRisi et al., 1996), the development of asthma (Erle and Yang, 2003) or the role of immature granulocytes in Systemic Lupus Erythematosus (Bennett et al., 2003). While microarrays use pre-defined probes to quantify the expression of selected genes, the development of massive scale RNA sequencing (RNA-seq) based on next generation sequencing (NGS) allowed for unbiased, near-complete transcriptome analysis (Cloonan et al., 2008; Shendure et al., 2005; Wang et al., 2009) and thus expanded the means to identify new disease biology and to profile biomarkers and therapeutic targets for clinical indications (Figure 1). This facilitated the examination of diverse RNA species, including non-coding RNAs, as well as alternative splicing in medical contexts and has generated novel concepts regarding their diagnostic, prognostic and therapeutic applicability (Byron et al., 2016). For example, genome-wide profiling of the cardiac transcriptome has revealed heart-specific long non-coding RNA expression relevant to cardiac function and regeneration after myocardial infarction (Ounzain et al., 2015).

Large consortia, such as GTEx (GTEx Consortium, 2013), FANTOM (Kawai et al., 2001) or ImmGen (Heng et al., 2008), formed to establish extensive resources of standardized omics data across organisms, tissues and cell types with the aim to increase our understanding of how changes in our genes contribute to human health and disease.

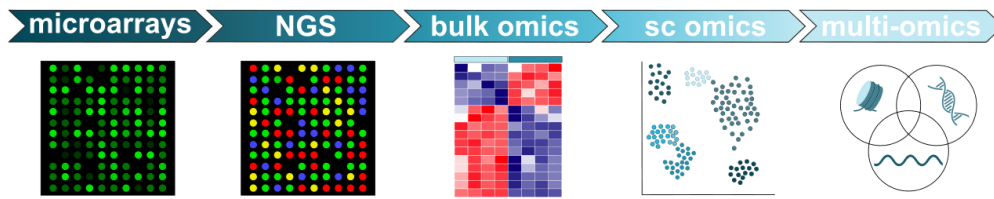


Figure 1: Schematic depiction of the development of omics technologies

Since the introduction of microarray analysis in 1995, omics technologies have continued to evolve. In particular, thanks to the development of highly parallelized next generation sequencing (NGS) in 2005, throughput and resolution of genome-wide measurements were continuously improved and now enable the measurement of multiple layers of information in thousands of cells.

In this early phase of the omics era, technological limitations restricted genome-wide measurements to collections of cells yielding averaged signals. While these bulk readouts have proven to be highly informative, they mask signals from rare cellular sub-populations or transcriptionally distinct cellular states.

Consequently, it did not take more than 4 years from the introduction of RNA-seq to the first whole-transcriptome analysis of a single cell (Figure 1) (Islam et al., 2011; Tang et al., 2009). Critical advances in cell isolation and library production for DNA sequencing have helped overcome these limitations and now allow for high-throughput and high-resolution transcriptomic profiling at single-cell level (Svensson et al., 2018). While the physical isolation of cells by fluorescence-activated cell sorting (FACS) enables the analysis of rare and selected cells (Jaitin et al., 2014), it limits the investigation to pre-defined populations and restricts the throughput. In contrast, non-selective isolation of single cells using, for example, microfluidics or micro-liter well arrays allows for nearly unbiased profiling of the cellular composition of a given sample (Gierahn et al., 2017; Macosko et al., 2015). In addition, split-pool approaches use combinatorial indexing to identify single cells without physical isolation of individual cells (Cao et al., 2017; Rosenberg et al., 2018).

In the last decade, omics studies with single-cell resolution have become widespread. While pioneering academic protocols for single-cell RNA-seq (scRNA-seq) were applied by highly specialized labs, commercial products helped to spread the technology across the globe (Figure 2A). In addition to the escalating spread and frequency of studies applying single-cell methods, technological advances are also enabling a continuous increase in sensitivity and throughput now reaching millions of cells in a single experiment (Figure 2B).

This new resolution and throughput naturally come with novel opportunities and challenges in data analysis. Apart from the computing resources needed to process and handle the ever-growing amounts of data, analysis and biological interpretation require new computational solutions and algorithms (Lähnemann et al., 2020). Appropriate statistical approaches to model the sparsity of the information derived from a single cell, either due to limited sensitivity of the method or the stochastic nature of gene expression, and to tackle the uncertainty of the measurements in thousands of cells need to be developed, tested, and continuously optimized. Accordingly, new methods for data analysis are published at very high pace. This wave of new developments has spawned creative solutions that incorporate state-of-the-art statistical and machine learning approaches to open unprecedented possibilities to analyze cellular composition, probe the dynamics and regulation of gene expression at the single-cell level, infer cellular plasticity and developmental hierarchies and integrate data sets of different studies (Zappia and Theis, 2021).

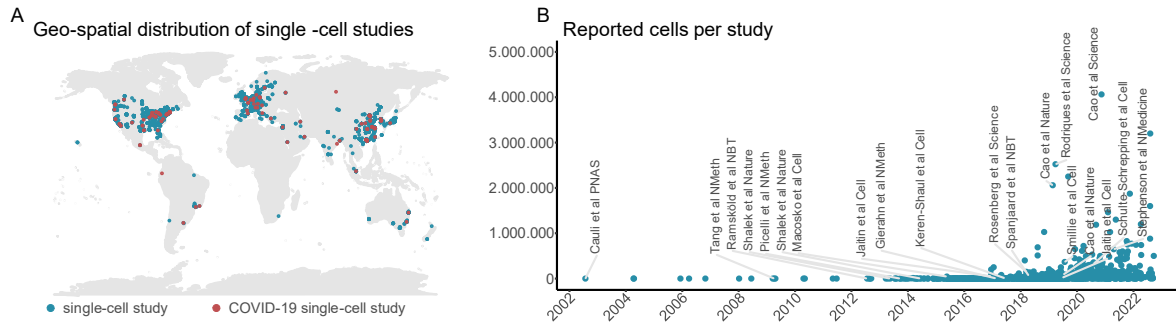


Figure 2: Development of single-cell studies over space and time

A) Geo-spatial distribution of original research publications including single-cell methods in 2022 (https://github.com/jsschrepping/Geospatial_PubMed_Visualization). B) Visualization of single-cell transcriptomics studies over time and their respective number of profiled cells reported (data source: <https://www.nxn.se/single-cell-studies/> date: 220926).

Transcriptomics is the most advanced field for the application of single-cell methods. However, methods for genomics and epigenomics at single-cell level are following up rapidly (Evrony et al., 2021; Schulte-Schrepping et al., 2020a). In contrast to transcriptomics, which quantifies the frequency of copies of the transcribed genes, genomics and epigenomics directly target the DNA molecules of a cell. Hence, the respective data suffers from even higher sparsity and noise as the genomic material assessed in a single cell of diploid organisms is limited to two copies. Despite these challenges, sophisticated approaches have been developed that enable analysis of mutational processes and genetic mosaicism in health and disease (Dong et al., 2017; Guo et al., 2022), lineage tracing in humans (Ludwig et al., 2019), and inference of genetic and epigenetic mechanisms of transcriptional regulation (Morabito et al., 2021; Perez et al., 2022). Measuring individual modalities in isolation is informative, but to understand how the different levels of regulation interact to control the state and behavior of a cell through transcription multiple measurements need to be combined in one experiment. Obtaining information about the state of the genome and its output from the same cell using multi-omics approaches is therefore a major goal of current developments (Figure 1) (Chappell et al., 2018; Meers et al., 2022; Wang et al., 2021).

2.2. Challenges in clinical application of single-cell transcriptomics

Omics technologies with single-cell resolution open entirely new possibilities to explore multiple disease-relevant parameters, including cell-type distributions in diseased tissues, cell type-specific changes in gene expression as well as identification of potential biomarkers and therapeutic targets in an unbiased fashion in one experiment. A pioneering study by Tirosh et al. used the technology to dissect the multicellular ecosystem of metastatic melanoma and identified distinct transcriptional states of malignant cells (Tirosh et al., 2016) – a work that preceded a whole series of research exploring the role of rare cells in tumor invasion, metastasis and progression (Jia et al., 2022). Beyond cancer, also complex chronic inflammatory diseases, such as inflammatory bowel disease (IBD) or multiple sclerosis (MS), have quickly become the subject of investigations using the new analytical possibilities of single-cell resolution (Martin et al., 2019; Schafflick et al., 2020; Smillie et al., 2019). In addition, understanding the dynamics and heterogeneity of cellular immune responses to infection, such as HIV, presented another utilization of single-cell transcriptomics (Kazer et al., 2020), that should be repeated frequently in subsequent years.

As a concerted effort to organize this new wave of research and join forces, many institutions and researchers formed the Human Cell Atlas (HCA) consortium with the overarching aim to create comprehensive reference maps of all cells in the human body as a basis for understanding health and disease (Rozenblatt-Rosen et al., 2017).

While falling sequencing prices and the competitive market for single-cell kits and instruments are gradually removing the financial barriers to taking omics-based solutions from the bench to the bedside, there are still numerous technical hurdles to overcome.

Single-cell protocols are highly complex and involve many steps to go from a tissue sample to the high-dimensional readings. The workflows allow for high technical mutability at each step to optimize the whole protocol for a specific sample (Figure 3). While this modularity is beneficial for obtaining the best possible data, it creates the risk of missing standards and lack of comparability. Furthermore, the multitude of necessary decisions requires extensive knowledge and experience in diverse fields ranging from clinical practice to molecular biology and biochemistry to bioinformatics data analysis, resulting in an imperative need for transdisciplinary teams with a broad expertise, which consequently hampers its use. Pursuing the goal to transform single-cell omics technologies from research to routine application in the clinical setting thus demands both the informed optimization, but also standardization of many aspects of the experimental and analytical workflows.

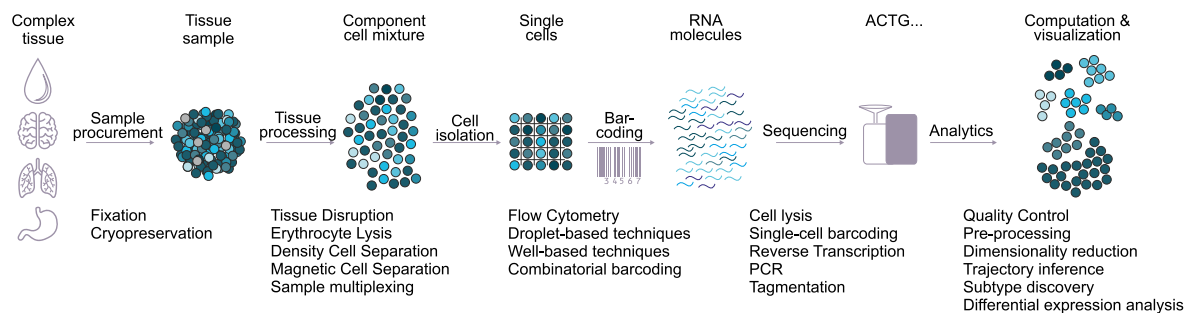


Figure 3: Complexity of single-cell transcriptomics workflows

Single-cell transcriptomics methods require a complex sequence of experimental and analytical steps to get from the tissue sample of interest to the high-dimensional readout. After sample procurement and optional preservation, the tissue needs to be dissociated to get to a cell suspension. After cell purification, individual cells need to be isolated for lysis, RNA extraction and cDNA synthesis. Barcoded cDNA products are then pooled for library production and sequencing.

Due to its sensitivity and resolution, scRNA-seq techniques are highly susceptible to technical factors affecting data quality and content. The resulting technical artefacts, also known as batch effects, can significantly impair the compatibility and comparability of data sets and, in the worst case, distort the information in such a way that misinterpretation occurs. Among the most relevant confounding factors are methods of sample procurement, processing, and storage, the technology for cell isolation and chemistry for library preparation, as well as other variables, such as daytime or season of sampling. Hence, rigorous optimization and highest standardization are essential for the reliable use of omics technologies in the clinic and, ultimately, for diagnostic purposes – a scenario that is unfortunately still far from the current practice.

The peripheral blood presents the primary source of information to investigate the systemic immune state of a patient. Beyond the advantage of simple sampling by venous or capillary blood draw, the blood contains many of the major immune cell types and can provide insights into a large variety of

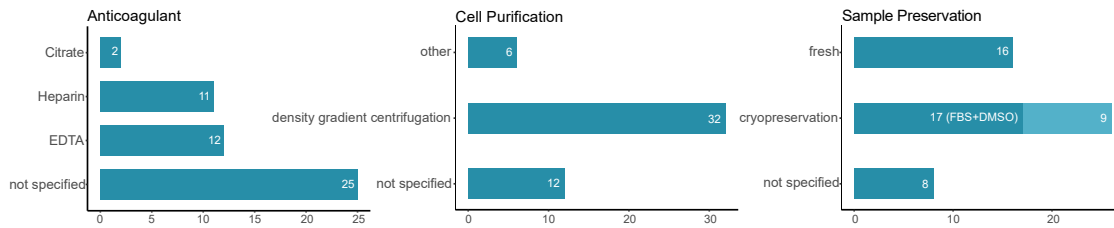


Figure 4: Reporting statistics for blood-based scRNA-seq studies

Reporting summary of the used anti-coagulant, the cell purification procedure, and the sample preservation protocol of 50 scRNA-seq studies on human circulating immune cells published between May 2019 and January 2022.

Shorthand	DOI	Anticoagulant	Purification	Storage
Moreno-Villanueva et al	10.3390/ijms20092316	NA	density gradient centrifugation	fresh
Kallionpää et al	10.2337/db19-0287	Heparin	density gradient centrifugation	cryopreservation
Wohnhaas et al	10.1038/s41598-019-46932-z	NA	NA	DMSO vs Methanol vs Cellcover
Martin et al	10.1016/j.cell.2019.08.008	EDTA	density gradient centrifugation	fresh
Yang et al	10.1038/s41467-019-11947-7	NA	density gradient centrifugation	fresh
Ramachandran et al	10.1038/s41586-019-1631-3	EDTA	red blood cell lysis	fresh
Szabo et al	10.1038/s41467-019-12464-3	NA	density gradient centrifugation	fresh
Liu et al	10.1159/000503737	Heparin	density gradient centrifugation	fresh
Hashimoto et al	10.1073/pnas.1907883116	EDTA	density gradient centrifugation	fresh
Kim et al	10.1038/s41591-019-0733-7	Heparin	density gradient centrifugation	fresh
Rendeiro et al	10.1038/s41467-019-14081-6	NA	NA	cryopreservation
Reyes et al	10.1038/s41591-020-0752-4	EDTA	density gradient centrifugation	cryopreservation (CS10)
Goel et al	10.1073/pnas.1916897117	NA	density gradient centrifugation	NA
Hu et al	10.1038/s41598-020-59827-1	NA	NA	NA
Cai et al	10.1016/j.ebiom.2020.102686	EDTA	density gradient centrifugation	NA
Ha et al	10.1002/sml.201907674	EDTA	density gradient centrifugation	NA
Pereira et al	10.1038/s41590-020-0643-3	Heparin	density gradient centrifugation	cryopreservation
Smith et al	10.1038/s41467-020-15361-2	Citrate	centrifugation	cryopreservation
Mereu et al	10.1038/s41587-020-0469-4	Heparin	density gradient centrifugation	cryopreservation (DMSO)
de Vries et al	10.1371/journal.ppat.1008408	EDTA	CPT	cryopreservation (DMSO)
Mair et al	10.1016/j.celrep.2020.03.063	NA	NA	cryopreservation
Smith et al	10.1182/bloodadvances.2019000699	EDTA	density gradient centrifugation	fresh
Cano-Gamez et al	10.1038/s41467-020-15543-y	NA	density gradient centrifugation	fresh
Zhao et al	10.1038/s41421-020-0157-z	Heparin	density gradient centrifugation	fresh
Psaila et al	10.1016/j.molcel.2020.04.008	NA	NA	cryopreservation
Zhou et al	10.3389/fcell.2020.00384	NA	density gradient centrifugation	fresh
Karagiannis et al	10.1038/s41467-020-16159-y	NA	NA	cryopreservation
Witkowski et al	10.1016/j.ccell.2020.04.015	NA	NA	cryopreservation
Lee et al	10.1126/sciimmunol.abd1554	NA	density gradient centrifugation	cryopreservation
Nehar-Belaid	10.1038/s41590-020-0743-0	NA	NA	cryopreservation (DMSO)
Schulte-Schrepping et al	10.1016/j.cell.2020.08.001	Heparin	density gradient centrifugation	cryopreserved
Boland et al	10.1126/sciimmunol.abb4432	NA	CPT	cryopreservation (DMSO)
Wang et al	10.1080/22221751.2020.1826361	NA	density gradient centrifugation	cryopreserved
Hughes et al	10.1016/j.immuni.2020.09.015	NA	NA	cryopreservation (DMSO)
Rasouli et al	10.1126/sciimmunol.aba9953	NA	density gradient centrifugation	NA
Steele et al	10.1038/s43018-020-00121-4	NA	NA	NA
Travaglini et al	10.1038/s41586-020-2922-4	EDTA	density gradient centrifugation	NA
Bernardes et al	10.1016/j.immuni.2020.11.017	Citrate	CPT	cryopreservation (DMSO)
He et al	10.1186/s13059-020-02210-0	EDTA	red blood cell lysis	fresh
Borcherding et al	10.1038/s42003-020-01625-6	NA	density gradient centrifugation	cryopreservation (DMSO)
Ren et al	10.1016/j.cell.2021.01.053	NA	density gradient centrifugation	cryopreservation (Cytodelics)
Pauken et al	10.1084/jem.20200920	Heparin	density gradient centrifugation	fresh
Stephenson et al	10.1038/s41591-021-01329-2	EDTA	density gradient centrifugation	cryopreservation (DMSO)
Causi et al	10.1038/s41586-021-03752-4	NA	NA	cryopreservation
Fischer et al	10.1038/s41467-021-24730-4	EDTA	density gradient centrifugation	cryopreservation (DMSO)
Yamagishi et al	10.1038/s41467-021-25101-9	NA	density gradient centrifugation	cryopreservation (CELLBANKER 1)
Huang et al	10.1073/pnas.2023216118	Heparin	density gradient centrifugation	fresh
Qiu et al	10.1002/jlb.5ma0721-825r	Heparin	density gradient centrifugation	cryopreservation
Sinha et al	10.1038/s41591-021-01576-3	Heparin	NA	fresh
Liu et al	10.3389/fneur.2021.807646	NA	density gradient centrifugation	NA

Table 1: Reporting overview for blood-based scRNA-seq studies

Table listing the anti-coagulant, the cell purification procedure, and the sample preservation protocol of 50 scRNA-seq studies on human circulating immune cells using the 10x chromium platform published between May 2019 and January 2022.

relevant immune processes, which explains why most clinical single-cell transcriptomics studies to date investigate this tissue. A meta-analysis of 50 scRNA-seq studies on human circulating immune cells using the 10x genomics Chromium platform published between May 2019 and January 2022 (Table 1) reveals striking variation in sample isolation and processing procedures. Most importantly, however, this analysis demonstrates a dramatic lack in reporting of relevant methodological information (Figure 4). While the method of cell purification and the protocol for cell preservation are missing from roughly 20 % of the studies, the choice of anti-coagulant to prevent blood clotting is only stated in half of the publications.

Since the experimental workflows of published data are too multifaceted to pinpoint the effect of single technical variables and there are no rigorous systematic evaluations of these technical factors published to date, we can only speculate on the influence of certain factors. Nevertheless, this observation illustrates the high variability in the protocols of published studies and further demonstrates the variability in the quality of reporting of methodological details.

To improve the compatibility and comparability of the vast amounts of data being produced using advanced single-cell methods, the research community must agree on standard procedures and reporting criteria. Within the HCA, benchmarking studies are performed to identify and distribute best-possible experimental protocols for cell atlas projects (Mereu et al., 2020). Furthermore, extensive efforts are made to compare computational tools and evaluate their advantages and suitable applications for the analysis of single-cell data (Luecken et al., 2022; Saelens et al., 2019). Nevertheless, it is important to note that there is still a lack of community-supported guidelines for the application of single-cell omics technologies to medical questions in clinical trials. In (Bonaguro et al., 2022), we present a guide to the application of systems-level approaches in immunology with a particular focus on the application of single-cell omics technologies to clinical samples. The purpose of the publication is to introduce immunologists with no particular experience in the field of omics to system-level approaches, providing a solid basis for improved data production and documentation to counteract the progressive lack of standards.

In addition to such review articles summarizing best practices and introducing standards, online platforms, such as protocols.io, and journals, e.g. STAR Protocols and Nature Protocols, dedicated to publishing high-quality, peer-reviewed protocols are highly valuable to optimize and harmonize experiments and facilitate the dissemination of validated protocols. In (De Domenico et al., 2020), we have developed and published a comprehensive workflow for flow cytometry and scRNA-seq on potentially infectious samples to ensure reproducible and safe data acquisition for combating COVID-19.

2.3. The immune system – a prime target for single-cell omics

The human immune system is a complex organ system distributed throughout the organism with many cell types and states that monitor developmental and homeostatic processes and dynamically react to endogenous and exogenous stimuli. The concerted action of the innate and adaptive branch of the immune system protects the organism against pathogens and establishes long-lasting immune memory to respond rapidly and effectively to pathogens that have been encountered before. Understanding the cellular heterogeneity and plasticity of the immune system and the complex interplay of its parts is critical for the progress of medicine. Therefore, the immune system presents a prime target for the application of high-resolution single-cell methods.

In 2014, Jaitin et al. have introduced an approach that allows a bottom-up characterization of *in vivo* cell type compositions (Jaitin et al., 2014). With just over 1000 single-cell transcriptome profiles, this

study presented a breakthrough in mapping of uncharted immune cell landscapes and served as a blueprint for many subsequent studies to understand cellular heterogeneity in health and disease (Papalexi and Satija, 2018). The application of this approach in an Alzheimer's model has identified a disease-associated microglia type conserved in mice and human underlining its clinical relevance (Keren-Shaul et al., 2017). Extending the analysis to multimodal single-cell data by combining transcriptome and proteome readouts presents a remarkable refinement of this approach and improves our ability to resolve cell states, allowing us to identify previously unreported lymphoid subpopulations even in the most deeply studied organ of the human body, the peripheral blood (Hao et al., 2021). Shalek, Satija and Shuga et al. took single-cell transcriptomics beyond cell type classification in steady-state by challenging murine dendritic cells (DC) with different stimuli *in vitro* and profiling their transcriptional response over time. Using this approach, they created a window into the cellular dynamics of immune responses and found substantial variation between identically stimulated cells, indicating carefully orchestrated paracrine control of immune responses by a few precocious cells (Shalek et al., 2014). Antigen-specific immune responses and immune memory mediated by antigen-specific lymphocytes are critical features of adaptive immunity against invading pathogens. Understanding the diversity of recombined B cell receptors (BCRs) and T cell receptors (TCRs) using specialized sequencing approaches and combining this information with single-cell transcriptomic and epigenomic measurements allows the study of the composition, functional state, and specificity of the adaptive immune repertoire (Pai and Satpathy, 2021; Satpathy et al., 2018). Mathew et al. highlighted the medical relevance of such approaches by using scRNA-seq in combination with BCR-seq to profile B cell subpopulations and their clonality in lymph nodes, spleen and lungs after influenza infection in mice and described spatiotemporal dynamics of antigen-specific B cells (Mathew et al., 2021). In addition, the immune receptor specificity has great therapeutic potential. Treatment of hematopoietic malignancies using chimeric antigen receptor T cells (CAR-T) has shown remarkable success but suffers from high relapse rates and poor *in vivo* persistence. Epigenomic profiling of CAR-T cells using the Assay for Transposase-Accessible Chromatin with high-throughput sequencing at single-cell resolution (scATAC-seq) has revealed mechanisms of CAR-T exhaustion and provided new insights into CAR-T engineering to improve treatment benefits (Jiang et al., 2022). These selected examples demonstrate the power of omics technologies with single-cell resolution to advance our understanding of the immune system and emphasize the clinical relevance of such research.

2.3.1. The myeloid cell compartment in health and disease

The myeloid cell compartment encompasses monocytes, dendritic cells (DCs), macrophages, and granulocytes, including neutrophils, eosinophils, and basophils, and presents a major part of the innate immune system performing a wide variety of functions. In addition to tissue surveillance ensuring immediate response to invading pathogens, diverse defense functions, and mediation of leukocyte recruitment, cells of the myeloid cell compartment have critical functions in immune regulation, tissue homeostasis and development as well as wound healing. Furthermore, as professional antigen-presenting cells (APCs), they serve as the orchestrators of adaptive immune responses (Roche and Furuta, 2015).

Neutrophils are the most abundant population of circulating white blood cells and mediate the earliest phase of the immune response (Nauseef and Borregaard, 2014). In response to invading microorganisms, they are recruited to the site of infection and perform their effector functions, including phagocytosis of pathogens, degranulation of antimicrobials and reactive oxygen species (Winterbourn et al., 2016) and the release of neutrophil extracellular traps (NETs), web-like structures

composed of cytosolic and granule proteins assembled on a scaffold of decondensed chromatin (Papayannopoulos, 2018).

According to the classical view of the neutrophil life cycle, mature neutrophils that have developed from granulocyte-macrophage precursors are released from the bone marrow under homeostatic conditions and patrol the blood vessels for signs of microbial infection or inflammation; when found, they respond rapidly and extravasate to exert their defense mechanisms followed by resolution of inflammation, neutrophil apoptosis, and clearing of dead or dying neutrophils by macrophages. Otherwise, if there is no immunological threat to the organism, they home to the bone marrow, liver, or spleen to be eliminated from the circulation. The advent of single-cell genomics has challenged this model and, despite technical difficulties due to cell fragility and high RNase content, has contributed significantly to our understanding of neutrophil biology (Evrard et al., 2018; Kwok et al., 2020; Montaldo et al., 2022). While traditionally thought of as poorly plastic and uniquely short lived cells, neutrophils are now recognized as a heterogeneous, functionally diverse cell type with important implications in homeostatic and disease conditions (Ng et al., 2019). Furthermore, the long-term belief that neutrophils are eliminated in the bone marrow, liver, and spleen after less than a day in the bloodstream has been challenged by recent evidence that they redistribute and are found in most healthy tissues at varying numbers (Hidalgo et al., 2019). In accordance with their newly discovered heterogeneity, neutrophils play crucial roles not only in extracellular bacterial and fungal infections but also in the pathogenesis of a broad range of diseases, including autoimmunity, chronic inflammation, cancer and viral infections (Hedrick and Malanchi, 2022; Herrero-Cervera et al., 2022; Johansson and Kirsebom, 2021). As their defense mechanisms are rather brute and unspecific, neutrophils need to be tightly regulated to avoid bystander damage to host tissues. A drastic example is the excessive neutrophil activation in pneumonia, which can cause severe tissue damage and, in extreme cases, become the primary source of morbidity and mortality (Narasaraju et al., 2011; Pechous, 2017). In addition to the damage directly caused by their effector mechanisms, neutrophils can also suppress the adaptive immune response. So-called granulocytic myeloid-derived suppressor cells (MDSC) (Bronte et al., 2016) have been observed in cancer (Rodriguez et al., 2009), chronic non-communicable diseases (Tay et al., 2020) and viral infections (Goh et al., 2016; Vollbrecht et al., 2012) where they inhibit lymphocyte proliferation and function via depletion of arginine or engagement of inhibitory receptors, such as PD-1 (Cloke et al., 2012). Interestingly, the suppressive phenotype of these neutrophils coincides with a shift in their density profile that causes them to co-segregate with mononuclear cells after density gradient centrifugation of blood, which has coined the term low-density neutrophils (LDN) (Hassani et al., 2020). Acute pathological insults, such as severe infections, trauma or sepsis, cause a dramatic increase in demand of neutrophils and trigger a hematopoietic response program referred to as emergency granulopoiesis to enhance the *de novo* production of neutrophils and replenish the circulating pool (Manz and Boettcher, 2014; Schultze et al., 2019). This mechanism results in the egress of immature and mature neutrophils from the bone marrow, which are often linked to hyperinflammation and immunosuppression and are increasingly correlated with disease severity and treatment response in many pathologies (Kotliar et al., 2020; Mare et al., 2015; De Santo et al., 2008).

Circulating monocytes and tissue resident macrophages belong to the mononuclear phagocyte system (Hume, 2006; Hume et al., 2019). While most long-lived, tissue-resident macrophages are derived from embryonic precursors in the yolk sac and fetal liver (Ginhoux and Jung, 2014), monocytes, like granulocytes, are short-lived and originate from hematopoietic stem cells (HSC) in the bone marrow (Laurenti and Göttgens, 2018). Macrophages are a heterogeneous family of innate immune cells residing in almost all tissues, including brain microglia, liver Kupffer cells and lung alveolar and interstitial macrophages, and serve functions of tissue homeostasis and immune defense (Lavin et al.,

2014). In the case of an infection, macrophages sense microbial signals as pathogen-associated molecular patterns (PAMPs) or tissue damage in the form of danger-associated molecular patterns (DAMPs) via a set of pattern recognition receptors (PRRs), phagocytose pathogens and cellular debris and release a plethora of molecules that kill pathogens, initiate inflammation, recruit additional effector cells and promote tissue repair (Lavin et al., 2015). Macrophages are plastic cells capable to adjust to the tissue microenvironment and contextual signals, such as cytokines or metabolic cues (Mass et al., 2016; Thion et al., 2018; Xue et al., 2014). In contrast, monocytes are blood-circulating innate immune cells classically divided into three subsets based on their respective expression of CD14 and CD16: classical CD14⁺CD16⁻, non-classical CD14⁺CD16⁺, and intermediate CD14⁺CD16⁺. Under pathological conditions, such as viral infections or chronic inflammation, monocytes are activated and recruited by inflammatory cytokines and, like neutrophils, infiltrate affected tissues. Once in the tissue, they acquire inflammatory macrophage and DC-like phenotypes to fulfil pro- and anti-inflammatory effector functions to help resolve inflammation (Kapellos et al., 2019) and induce adaptive immune responses as professional antigen-presenting cells (Jakubzick et al., 2017).

It has long been debated whether monocyte-derived cells persist in tissues and take over DC and macrophage functions once inflammation has subsided. In recent years, the concept of niche competition was developed by Martin Guilliams and colleagues proposing that tissue infiltrating monocytes can indeed differentiate into self-maintaining macrophages, but only if a niche is available, e.g. after macrophage death during infection (Guilliams and Scott, 2017; Guilliams et al., 2020). Using diphtheria toxin-mediated depletion of liver-resident Kupffer cells to generate niche availability, Scott et al. showed that circulating monocytes engraft in the liver, gradually adopt the transcriptional profile of their depleted counterparts and become long-lived self-renewing cells (Scott et al., 2016). However, the lack of distinct marker genes for embryonically seeded macrophages or monocyte-derived macrophage-like cells and the apparent difficulties in cell depletion and fate mapping hamper the investigation of such mechanisms in humans (Guilliams and Scott, 2022).

In (Bassler et al., 2019), we have extensively reviewed recent advances in the understanding of the cellular ontogeny, activation, differentiation, and tissue-specific functions of circulating monocytes and tissue resident macrophages and dendritic cells with a focus on discoveries made thanks to the new developments in the field of single-cell omics.

2.4. The COVID-19 pandemic and pathology of SARS-CoV-2

In December 2019, a cluster of pneumonia cases with unknown cause in Wuhan, China, was reported by the Chinese Center for Disease Control and Prevention. Soon after, in January of 2020, a novel betacoronavirus was identified as the causative infectious agent (Tan et al., 2020) and quickly gained worldwide attention due to its rapid national and international spread. The newly discovered enveloped, single-stranded RNA betacoronavirus belongs to a large family of coronaviruses that includes seven human pathogens. It was named Severe Acute Respiratory Syndrome Coronavirus 2 (SARS-CoV-2) and the disease it causes has been termed Coronavirus Disease 2019 (COVID-19). The World Health Organization (WHO) declared the outbreak a public health emergency of international concern on 30 January 2020 with 7,818 confirmed cases globally, affecting 19 countries on the date of the declaration (Novel Coronavirus (2019-nCoV) Situation Report-10) and recognized the spread of COVID-19 as a pandemic on 11 March 2020. As of October 2022, COVID-19 has claimed more than 6.5 million lives, sickened more than 600 million people, and caused devastating socioeconomic consequences worldwide.

SARS-CoV-2 primarily enters host cells via the angiotensin-converting enzyme 2 (ACE2) receptor and uses the human protease TMPRSS2 as an entry activator (Hoffmann et al., 2020). These genes are co-

expressed on a range of cells including nasal and bronchial epithelial cells, supporting the initially localized infection by SARS-CoV-2, but also on enterocytes, cardiomyocytes, vascular and testicular cells, placental trophoblasts, bile duct cells as well as macrophages (Hikmet et al., 2020; Song et al., 2020b; Sungnak et al., 2020; Ziegler et al., 2020). The use of single-cell transcriptomics data across tissues and demographics has been instrumental to investigate SARS-CoV-2 tropism (Muus et al., 2021; Sungnak et al., 2020).

COVID-19 is characterized primarily by respiratory clinical manifestations ranging from mild common cold symptoms, including cough, shortness of breath and fever, in most cases to the development of pneumonia, hypoxemia, acute respiratory distress syndrome (ARDS) and multi-organ failure in a subset of patients (Lamers and Haagmans, 2022). Although acute respiratory manifestations are the most common feature of severe COVID-19, many non-respiratory effects have been reported in the acute phase of the disease including fatigue, myalgias, nausea, vomiting, diarrhea, headache and olfactory dysfunction (Osuchowski et al., 2021). In addition to respiratory disease, cardiovascular complications, including coagulopathy and endotheliitis with diffuse microcirculatory injury, are key occurrences in severe COVID-19 (Osuchowski et al., 2021; Varga et al., 2020). Furthermore, a significant proportion of patients develops protracted complications, including fatigue and neurological sequelae, after SARS-CoV-2 infection often referred to as 'post-COVID-19 syndrome' or 'long-COVID' (Kedor et al., 2022; Mehandru and Merad, 2022). The risk factors for severe disease include age and various comorbidities, such as diabetes, hypertension, obesity and chronic kidney disease, as well as genetic polymorphisms (Beck and Aksentijevich, 2020; Merad et al., 2022; Zhang et al., 2020b).

The immediate response and continued efforts of the medical and scientific community to this health crisis were unprecedented and produced remarkable insights into the immunopathology of COVID-19 as well as preventive and therapeutic management strategies at an extraordinary pace, most notably the exceptional success of the vaccine development (Tregoning et al., 2021). However, while these impressive advances have unraveled mechanism of protective immunity in mild forms and the derailment of the immune response in severe COVID-19, questions remain about the clinical complexities of diverse disease phenotypes and the underlying molecular mechanisms, particularly with regard to the emergence of new variants of concern as the virus evolves.

The complex clinical manifestations of COVID-19 suggest that SARS-CoV-2 can cause a dysregulated host response with far-reaching immune-inflammatory derangements in severe disease. This notion is supported by stark changes in peripheral immune activity (Chen et al., 2020a; Qin et al., 2020), increased levels of acute phase reactants and pro-inflammatory cytokines (Lucas et al., 2020; Mehta et al., 2020), neutrophilia and emergence of immature and suppressive neutrophils (Falck-Jones et al., 2021; Schulte-Schrepping et al., 2020b; Silvin et al., 2020), lymphopenia (Cao, 2020) as well as myeloid inflammation (Mann et al., 2020; Schulte-Schrepping et al., 2020b). After an initial phase of viral replication leading to direct virus-mediated tissue damage, recruitment of effector immune cells by infected cells and specialized immune sentinels that recognize viral genomic RNA via pattern recognition receptors or cytosolic RNA sensors causes a local and systemic immune response that determines disease progression and severity (Osuchowski et al., 2021). While early and efficient activation of the immune system is crucial for controlling the virus, a prolonged immune response may lead to progressive tissue damage ultimately resulting in a deleterious hyperinflammation characterized by the dysregulation of tissue repair mechanisms and fibrosis (Gustine and Jones, 2021).

High-throughput transcriptional profiling on single-cell level has been applied by many laboratories and consortia at large scale to decipher the immune response in COVID-19 and shed light upon many features of the systemic as well as tissue-specific pathomechanisms of SARS-CoV-2 infection

(Arunachalam et al., 2020; Bernardes et al., 2020; Chua et al., 2020; Combes et al., 2021; Delorey et al., 2021; Georg et al., 2022; Grant et al., 2021; Lee et al., 2020; Liao et al., 2020; Melms et al., 2021; Notarbartolo et al., 2021; Ren et al., 2021; Schulte-Schrepping et al., 2020b; Silvin et al., 2020; Sinha et al., 2022; Stephenson et al., 2021; Su et al., 2020; Szabo et al., 2021; van der Wijst et al., 2021; Wauters et al., 2021; Wilk et al., 2020, 2021; Zhang et al., 2020a). Indeed, the large number of single-cell omics studies in patients with COVID-19 may have provided the most detailed cellular atlas of any human disease to date.

Given the clear relevance of the cellular and humoral adaptive immune response for acute control, long-term immunity and vaccination strategies, a lot of effort was put into the investigation of the dynamics and derangements of T and B cell responses in COVID-19. As the work presented in this thesis primarily focusses on the myeloid immune compartment and its role in SARS-CoV-2 infection and COVID-19, we refer the reader to relevant review articles for further reading (Moss, 2022; Sette and Crotty, 2021).

2.4.1. Understanding the myeloid cell response in COVID-19 pathogenesis

The lungs and airways are a major portal of entry for viral infections and represent a prime site for immunological recognition and activation. Hence, efficient but balanced immune mechanisms in the respiratory tract are critical. The innate immune system functions as the first line of host defense against SARS-CoV-2 by limiting its proliferation, identifying, and removing infected cells, and coordinating the development of adaptive immunity (Schultze and Aschenbrenner, 2021).

Macrophages are the most abundant innate immune cell type in the lung under homeostatic conditions and, in addition to mucus and the epithelial barrier, they are the first defenders against the pathogen entering the respiratory system. Upon viral recognition, lung macrophages, together with epithelial cells, produce high levels of cellular mediators, including IL-1b, IL-6, IL-8, IL-17, CCL2, CCL3 and CCL7, which rapidly recruits monocytes and neutrophils into the lung (Chua et al., 2020; Kox et al., 2020; Monneret et al., 2020). Furthermore, alveolar macrophages are major producers of antiviral type I interferons (IFN) in viral respiratory infections (Kumagai et al., 2007). The role of type I IFNs in COVID-19 has been a topic of debate due to limited detection and transient peaks of gene expression and plasma protein levels (Arunachalam et al., 2020; Hadjadj et al., 2020; Lucas et al., 2020), but the observation of enriched inborn errors of type I IFN immunity (Zhang et al., 2020b) and the presence of neutralizing autoantibodies against type I IFN (Bastard et al., 2020, 2021) in patients with life-threatening COVID-19 has underpinned their importance in effectively combatting SARS-CoV-2.

From the very start of the COVID-19 pandemic, clinical reports indicated neutrophilia and quantitative alterations of the monocyte compartment in the peripheral blood of COVID-19 patients suggesting the critical involvement of neutrophils and monocytes in the pathology of this new disease (Chen et al., 2020b; Qin et al., 2020; Song et al., 2020a; Zhao et al., 2020). This early evidence immediately raised the question of whether the quantitative observations were associated with phenotypic shifts in the neutrophil and monocyte compartment potentially opening routes of therapeutic intervention. Therefore, we set out to perform an in-depth study to longitudinally profile the systemic immune cell status in patients with varying disease severity of COVID-19. In (Schulte-Schrepping et al., 2020b), we reported profound alterations of the myeloid compartment with inflammatory monocytes characterized by an interferon-stimulated gene signature in mild COVID-19 opposed to dysfunctional HLA-DR^{lo} monocytes in severe disease. The loss of major histocompatibility complex (MHC) class II expression on monocytes is an established sign of immunosuppression and has been confirmed in multiple independent studies and functionally validated (Falck-Jones et al., 2021; Giamarellos-

Bourboulis et al., 2020; Payen et al., 2020; Silvin et al., 2020; Spinetti et al., 2020). As the primary site of infection and inflammation in COVID-19, understanding the role of monocytes in the lung is critical. Again, single-cell transcriptomics has been instrumental in understanding the infiltration and adaptation of monocytes in the inflammatory milieu of COVID-19 and consistently demonstrated the accumulation of proinflammatory monocyte-derived macrophage-like cells in the lungs of patients with severe disease (Liao et al., 2020; Wauters et al., 2021). Wendisch et al. have extended the description of these cells to include a profibrotic transcriptional phenotype in COVID-19 ARDS (Wendisch et al., 2021).

In addition to the changes in the monocyte compartment, we observed signs of emergency myelopoiesis with the appearance of immature and dysfunctional neutrophils in severe COVID-19 (Schulte-Schrepping et al., 2020b). To understand these observations in the context of other respiratory diseases, we compared COVID-19 blood bulk transcriptomes with those of a large collection of over 3,100 samples derived from 12 different viral infections, inflammatory diseases, and independent control samples, which revealed highly specific neutrophil activation-associated transcriptome signatures for COVID-19 (Aschenbrenner et al., 2021). Considering the high risk of tissue damage posed by excessively activated and dysregulated neutrophils, our reports stimulated follow-up studies confirming our observations on transcriptional level (Combes et al., 2021; Wilk et al., 2021) and performing functional assays supporting the adverse effects of neutrophils in COVID-19 (Arcanjo et al., 2020; Leppkes et al., 2020; Siemińska et al., 2021; Veras et al., 2020). Consequently, evaluation of precise and timely therapeutic intervention in the neutrophil response presents a promising strategy that is being pursued in numerous studies (Earhart et al., 2020; Sinha et al., 2022; Thierry, 2020).

Another important deviation observed in COVID-19 is the intersection between the innate and adaptive immune system. Effective control of viral infections depends on both the innate and adaptive arm of the immune system and their seamless cooperation. APCs, such as DCs, macrophages and monocytes, bridge the two arms of the immune system by presenting antigens to antigen-specific lymphocyte and relaying environmental cues to activate and modulate their response. In this process, APCs are essential to rate and modulate the intensity of the required immune response by processing and integrating the situation-dependent information encoded by soluble mediators and cell-to-cell interactions (Bedoui et al., 2016). Together with colleagues at the Department of Microbiology and Immunology in Melbourne, Australia, we have set out to elucidate the intricacies of this process of signal integration in APCs and assess its relevance for COVID-19. Using transcriptional signatures derived from mouse *in vitro* studies delineating the influence of cellular and soluble signals in APCs, we showed significant differences in APCs of mild versus severe COVID-19 and linked these effects to phenotypic alterations in the CD8⁺ T cell response (unpublished work, currently in revision at Nature Immunology).

3. Aim of the thesis

In this thesis, I present my research to decipher the systemic immune response in COVID-19 using single-cell transcriptomics and place it in the context of recent developments and persisting challenges in the field of single-cell omics and their application to COVID-19. My work is presented as a cumulative thesis consisting of three publications:

In the first publication, I present an optimized workflow for the clinical application of single-cell transcriptomics and proteomics on potentially infectious samples derived from patients suffering from infectious diseases that enabled safe and reproducible research on COVID-19 (De Domenico et al., 2020). In the second publication, I describe our findings on alterations in the myeloid cell compartment in COVID-19. In a longitudinal, two-cohort study combining single-cell transcriptomics and proteomics of blood samples from patients with different COVID-19 disease severities, we examined changes in the systemic immune cell composition and activation and reported features of a dysregulated myeloid cell compartment in severe disease (Schulte-Schrepping et al., 2020b). In the third publication, we extended these investigations on the myeloid cell compartment in COVID-19 and investigated the potential consequences of its derailment on the priming of the adaptive immune response against SARS-CoV-2. In doing so, we found that antigen-presenting cells from patients with severe COVID-19 exhibit molecular alterations in the consolidation process of type 1 IFN signals and CD4⁺ T cell help, which in turn impair the CD8⁺ T cell immunity against SARS-CoV-2 (Gressier et al., in revision).

In summary, the research presented in this thesis provided insights into the role of the innate immune system in COVID-19, in particular in monocytes and neutrophils, which were followed up in numerous studies that expanded the knowledge of the involvement of the myeloid immune compartment in the pathogenesis of COVID-19.

4. Publications

4.1. Optimized workflow for single-cell transcriptomics on infectious diseases including COVID-19

De Domenico E*, Bonaguro L*, **Schulte-Schrepping J***, Becker M, Händler K, Schultze JL., „**Optimized workflow for single-cell transcriptomics on infectious diseases including COVID-19.**”, STAR Protoc. 2020 Dec 16;1(3):100233. doi: 10.1016/j.xpro.2020.100233. eCollection 2020 Dec 18.

Clinical studies on human samples require careful design to produce valuable scientific insights with medical benefits while preserving the rights and privacy of the patients and ensuring the well-being of the researchers during the study – the latter being particularly important when working on human pathogens. Hence, in the face of a newly emerging pathogen such as SARS-CoV-2, special precautions needed to be taken with regard to the experimental procedures when examining potentially infectious materials due to the lack of knowledge on disease transmissibility, infectivity, and molecular pathogenicity of the infectious agent. In addition, optimized SOPs are essential to ensure robust data acquisition with limited technical variability and high reproducibility, particularly when applying high-resolution omics technologies in clinical studies, while their open exchange and mutual validation in the scientific community is a prerequisite for rapid and reliable gain of knowledge.

In (De Domenico et al., 2020) we present a complete and safe workflow for performing flow cytometry and scRNA-seq experiments using the micro-well based BD Rhapsody platform on blood samples of patients infected with SARS-CoV-2 from cell isolation to data analysis. The protocol is not specific to SARS-CoV-2, but applicable to blood samples derived from patients infected with a range of similar human RNA viruses, including other coronavirus or influenza virus genera, and thus will be of relevance beyond the COVID-19 pandemic.

We present an extensive depiction of the recommended safety measures along the complete workflow, including the preparation of the working area and the required devices and materials, as well as the necessary cleaning steps, to prevent any risk for infection and guarantee the physical integrity of the experimenter. In addition to these general precautions, the publication provides a comprehensive, stepwise description of the scRNA-seq protocol using the BD Rhapsody platform including cell purification and processing, sample multiplexing and quantification of surface protein expression using oligo-coupled antibodies (BD AbSeq), as well as library production, quality assessment and sequencing. In addition to the predominant investigation of mononuclear cells in the peripheral blood, the presented workflow also includes a detailed description of the application of scRNA-seq to whole blood samples after red blood cell (RBC) lysis, allowing the analyses to be extended beyond peripheral blood mononuclear cells (PBMC) to all immune cells present in the peripheral blood, including polymorphonuclear granulocytes.

To facilitate troubleshooting for users of the protocol, we describe the limitations of the scRNA-seq approach and list potential experimental issues along with their respective solutions.

Furthermore, since bioinformatics remains a major gatekeeper to broader application of omics protocols, we also provide basic recommendations and ready-to-use code to help the interested reader and user of the protocol to easily enter the field of single-cell transcriptomics analysis. The section for processing and downstream analysis of multiplexed scRNA-seq data includes information on read alignment and quantification, sample de-multiplexing, quality control and filtering, normalization, dimensionality reduction, clustering, and differential gene expression analysis

comparing different cell types and states as well as cells derived from samples of different disease severities or disease phases.

In addition to the scRNA-seq workflow, we provide guidelines for multi-color flow cytometry analyses of potentially infectious blood samples, including safety measures, marker panels, and gating strategies, for quantitative analysis of cellular sample composition and validation of phenotypic and functional observations derived from the sequencing-based single-cell transcriptomics and proteomics analyses.

The workflow described in (De Domenico et al., 2020) was applied to study differences in immune cell composition and phenotypes in mild and severe COVID-19 over the course of the disease in a cohort of 17 COVID-19 patients and 13 control individuals sampled in Bonn, Germany, from April to July 2020. The resulting data have been extensively analyzed in multiple studies focusing on different aspects of the immunology and immunopathology of COVID-19, yielding insights into the dysregulation of monocyte and neutrophil subsets in progressive severe disease (Schulte-Schrepping et al., 2020b), interferon-induced alterations of megakaryocytes and erythroid cells (Bernardes et al., 2020), impaired NK cell function (Krämer et al., 2021), as well as the presence of CD16⁺ highly cytotoxic T cells in severe COVID-19 (Georg et al., 2022).

For this publication, I was responsible for designing the experimental scRNA-seq approach and developing the safety precautions to work with potentially infected human samples. In addition, I compiled the recommendations for the bioinformatics processing and downstream analyses, as well as the corresponding code, and contributed to the writing and editing of the manuscript.

4.2. Severe COVID-19 is marked by a dysregulated myeloid cell compartment

Schulte-Schrepping J*, Reusch N*, Paclik D*, Baßler K*, Schlickeiser S*, Zhang B*, Krämer B*, Krammer T*, Brumhard S*, Bonaguro L*, De Domenico E*, Wendisch D*, Grasshoff M, Kapellos TS, Beckstette M, Pecht T, Saglam A, Dietrich O, Mei HE, Schulz AR, Conrad C, Kunkel D, Vafadarnejad E, Xu C-J, Horne A, Herbert M, Drews A, Thibeault C, Pfeiffer M, Hippenstiel S, Hocke A, Müller-Redetzky H, Heim K-M, Machleidt F, Uhrig A, Bosquillon de Jarcy L, Jürgens L, Stegemann M, Glösenkamp CR, Volk H-D, Goffinet C, Landthaler M, Wyler E, Georg P, Schneider M, Dang-Heine C, Neuwinger N, Kappert K, Tauber R, Corman V, Raabe R, Kaiser KM, To Vinh M, Rieke G, Meisel C, Ulas T, Becker M, Geffers R, Witzernath M, Drosten C, Suttorp N, von Kalle C, Kurth F, Händler K, Schultze JL, Aschenbrenner AC, Li Y, Nattermann J, Sawitzki B, Saliba A-E, Sander LE, Deutsche COVID-19 OMICS Initiative (DeCOI), **"Severe COVID-19 Is Marked by a Dysregulated Myeloid Cell Compartment"**, Cell. 2020 Aug 5; S0092-8674(20)30992-2. doi: 10.1016/j.cell.2020.08.001.

The COVID-19 pandemic has confronted humanity with an enormous medical crisis and has demanded unprecedented efforts from the scientific community to elucidate the underlying molecular pathomechanisms in order to win the race for a stable health care situation and economy against the new pathogen. The use of high-resolution, state-of-the-art omics methods has proven highly useful in identifying disease-relevant features of the immune response to SARS-CoV-2 in an unbiased fashion and thus narrowing down potential targets for therapeutic intervention and prevention of severe disease progression in record time.

In (Schulte-Schrepping et al., 2020b), we have reported a dual-center, two-cohort study combining single-cell transcriptomics and proteomics of whole blood and peripheral blood mononuclear cells with the aim to determine changes in the immune cell composition and activation states in mild compared to severe COVID-19 over time. In total, we have profiled 242 samples from 109 individuals, including 161 COVID-19 samples from 53 patients, using a range of high-resolution and high-throughput methods for unbiased immune profiling, including two different platforms for scRNA-seq, mass cytometry, and multi-color flow cytometry. We analyzed a total of 24 million cells by their expression of protein markers as well as more than 328.000 single-cell transcriptomes. The comparative analysis of two clinical cohorts collected at a similar time during the first wave of the pandemic from April to July 2020 at two German university medical centers in Berlin and Bonn, respectively, and their analysis using two different technological platforms for single-cell transcriptomics allowed for instantaneous cross-validation of the findings and avoidance of technical artefacts distorting the interpretations. This approach of validation cohorts in single-cell omics studies contrasted with the prevailing strategy of computational data integration and batch removal but proved highly effective for the in-depth interrogation of predominant disease-relevant immunological alterations and increased the robustness of the observations.

Although this large dataset contains information on all immune cell types present in peripheral blood, in this initial study we focused our analyses on the most profound alterations induced by SARS-CoV-2 infection in the peripheral blood observed in the myeloid cell compartment. In addition to the previously reported lymphopenia and neutrophilia resulting in a left shift in the neutrophil to lymphocyte ratio (NLR) and the loss of non-classical CD16⁺ monocytes in COVID-19 (Hadjadj et al., 2020; Merad and Martin, 2020), we described severity-specific phenotypic alterations in classical CD14⁺ monocytes as well as quantitative and qualitative changes in neutrophils.

HLA-DR^{hi}CD11c^{hi}CD14⁺ inflammatory monocytes with an anti-viral interferon-stimulated gene signature, similar to the phenotype seen in patients with flu-like illness, were elevated at early time points in mild COVID-19 and receded during the natural course of the disease. In contrast, severe COVID-19 was marked by the presence of dysfunctional HLA-DR^{lo} monocytes expressing S100 alarmins and genes of anti-inflammatory function, such as CD162 and PLAC8.

Furthermore, the neutrophil compartment was profoundly affected in severe COVID-19 with the occurrence of immature neutrophil precursors indicative of emergency myelopoiesis as well as suppressive-like mature neutrophil subsets. The identification and transcriptional interrogation of LDN in the PBMC fraction after density gradient centrifugation in samples derived from severe COVID-19 patients, particularly at later stages of the disease, revealed stark phenotypic alterations in the neutrophil compartment similar to what has been previously described in the contexts of other severe infections and sepsis (Manz and Boettcher, 2014; Schultze et al., 2019). Applying scRNA-seq to whole blood samples allowed for a comprehensive examination of the neutrophil compartment and delineation of its heterogeneity in relation to COVID-19 disease severity at unparalleled resolution at the time of this study and revealed dysfunctional mature neutrophils expressing PD-L1 and exhibiting impaired oxidative burst responses in severe disease. Our work on the role of neutrophils in COVID-19 has been followed up and consolidated in several subsequent clinical scRNA-seq studies that confirmed the disease-specific shifts in this cellular compartment and further assessed their predictive and therapeutic potential for COVID-19 mortality (Combes et al., 2021; Sinha et al., 2022; Wilk et al., 2021).

The reduced HLA-DR expression, an antigen-presenting MHC class II molecule, on monocytes is a well-established marker of immune suppression, and has been consistently reported in severe COVID-19 across a multitude of studies (Giamarellos-Bourboulis et al., 2020; Payen et al., 2020; Silvin et al., 2020; Spinetti et al., 2020). Furthermore, this observation was strongly associated with COVID-19 severity, highlighted by the markedly lower expression in patients admitted to the ICU versus non-ICU patients as well as in non-survivors versus survivors (Wang et al., 2020). Moreover, the presence of HLA-DR^{lo} monocytes in severe COVID-19 was found to be positively correlated with levels of immunosuppressive soluble factors, including IL-10, TGF- β , VEGFA, and AREG, indicating their suppressive phenotype (Kvedaraite et al., 2021), which was corroborated by functional assessment of their capacity to suppress T cell proliferation (Falck-Jones et al., 2021).

For this publication, I was responsible for designing and implementing the experimental approach for scRNA-seq in the Bonn cohort. In addition, I led the analysis of the scRNA-seq data created for the second cohort collected in Bonn, Germany, and oversaw the concerted analysis of all scRNA-seq data including both cohorts. In particular, I was responsible for data acquisition and quality control, clustering and cell type annotation as well as the delineation of disease severity-specific alterations of gene expression in the monocyte compartment. Furthermore, I took the lead in writing and revising the manuscript, which was then published by Cell in September 2020.

4.3. Effective CD8⁺ T cell immunity against SARS-CoV-2 depends on the integration of type 1 IFN signals and CD4⁺ T cell help by antigen-presenting cells

Gressier E*, **Schulte-Schrepping J***, Petrov L, Brumhard S, Stubbemann P, Hiller A, Obermayer B, Spitzer J, Kostevc T, Whitney PG, Bachem PG, Odainic A, van de Sandt C, Nguyen THO, Ashhurst T, Wilson K, Oates CVL, Gearing LJ, Meischel T, Hochheiser K, Greyer M, Clarke M, Kreutzenbeck M, Gabriel SS, Kastenmüller W, Kurts C, Londrigan SL, Kallies A, Kedzierska K, Hertzog PJ, Latz E, Chen YCE, Radford KJ, Chopin M, Schroeder J, Kurth F, Gebhardt R, Sander LE, Sawitzki B, Schultze JL, Schmidt SV, Bedoui S, „**CD4⁺ T cell calibration of antigen-presenting cells optimizes antiviral CD8⁺ T cell immunity**”, *Nat Immunol* (2023). doi: 10.1038/s41590-023-01517-x

CD4⁺ T cells, also known as helper T cells (T_H cells), play important roles in the development of CD8⁺ cytotoxic T lymphocyte (CTL) responses critical for the control of bacterial and viral pathogens and memory formation. Among other functions, they catalyze the activation of APCs via CD40L-CD40 interactions to enable their autonomous priming of CD8⁺ T cell responses – a process termed APC licensing (Schoenberger et al., 1998). In addition to the activation signal from CD4⁺ T cells, APCs integrate additional signals, such as inflammatory cytokines, into the information they relay to CD8⁺ T cells (Greyer et al., 2016). Although it is well established that the combination and integration of these signals by APCs adapts the CD8⁺ T cell response to the circumstances of a particular infection, little is known about the underlying molecular mechanisms that control signal integration in APCs (Borst et al., 2018; Wu and Murphy, 2022).

As APCs present antigenic peptides to antigen-specific CD4⁺ T cells via MHC class II molecules (Roche and Furuta, 2015) and the expression of MHC class II molecules in human APCs is known to be positively regulated by IFN (Keskinen et al., 1997), an interesting question arises with regard to COVID-19 immunopathology: Does the reduction in expression of MHC class II molecules on APCs together with the impaired IFN response in severe COVID-19 (Bastard et al., 2021; Hadjadj et al., 2020; Zhang et al., 2020b) affect the interaction with CD4⁺ T cells during APC licensing and what might be the consequences for the CD8⁺ T cell response to SARS-CoV-2?

To investigate the potentially impaired signal transmission of CD4⁺ T cell help to CD8⁺ CTL via APCs in COVID-19, we collaborated with a team of researchers at the Department of Microbiology and Immunology in Melbourne, Australia, led by Elise Gressier and Sammy Bedoui – designated experts in the field of T cell help and CTL priming (Bedoui et al., 2016). In a previous study, they had shown that CD8⁺ T cell priming in a model of HSV-1 skin infection depended on APCs receiving both CD4⁺ T cell help and additional innate stimulation in form of type I IFN signals (Greyer et al., 2016). Moreover, they reported that the dependency on the help signal in this process was modulated by the intensity of the innate signal, extending previous reports that type I IFN can effectively replace the requirement of T cell help in specific infections (Wiesel et al., 2011). In a follow-up experiment, they extended this model using time-resolved transcriptomic profiling of murine APCs in presence or absence of type 1 interferon and CD40 stimulation mimicking T cell help. This approach allowed for the dissection of transcriptional response patterns and regulatory networks underlying the signal integration and consolidation process in APCs for effective and balanced CD8⁺ T cell activation in mice. While type 1 IFN stimulation caused a substantial transcriptional response in APCs, CD40 stimulation alone induced only minor transcriptional changes. Most of the interferon-responsive genes were unchanged by the additional CD40 stimulation, however, a subset of genes increased in expression upon the combinatorial stimulation. Furthermore, a distinct set of genes with known roles in the interplay

between APCs and T cells, such as *Ccl5*, *Cd83* and *Cxcl16*, was dependent on the combinatorial stimulation of type I IFNs and CD40 stimulation and not induced by neither stimulus alone. To better elucidate the interdependencies and dynamics of the two stimuli, our collaborators performed further experiments to determine whether type I IFNs and CD40 stimulation acted simultaneously or whether their molecular integration required a specific order. By performing sequential transcriptome measurements with differing order of the two signals they found that the type I IFN signal needed to precede the triggering of CD40 to condition APCs for an efficient response to CD4⁺ T cell help.

Loss of MHC class II antigen presentation (Schulte-Schrepping et al., 2020b), imbalances in provision of type 1 IFN (Hadjadj et al., 2020) and low avidity CD4⁺ T cell responses (Bacher et al., 2020) in severe COVID-19 raise the possibility that this signal integration process in APCs may be of relevance for an effective CD8⁺ T cell response during SARS-CoV-2 infections. Therefore, we applied the transcriptional signatures observed in the murine APC model to scRNA-seq data of PBMC samples derived from COVID-19 patients with varying disease severities (Figure 5). As the primary site of T-cell activation, human lymph nodes would need to be examined at early time points post-infection during acute COVID-19 to assess the precise mechanisms of T-cell priming. Since this is difficult to realize, we are providing a compromise, which is a limitation of human immunology at the moment, and examined signs of these processes in peripheral blood as a surrogate tissue, fully aware of the fact that this organ is not the prime tissue for early interactions between APCs and T cells. Yet both cell compartments (APCs and T cells) are accessible in peripheral blood and can interact *in vitro* (Tavukcuoglu et al., 2021; Winheim et al., 2021).

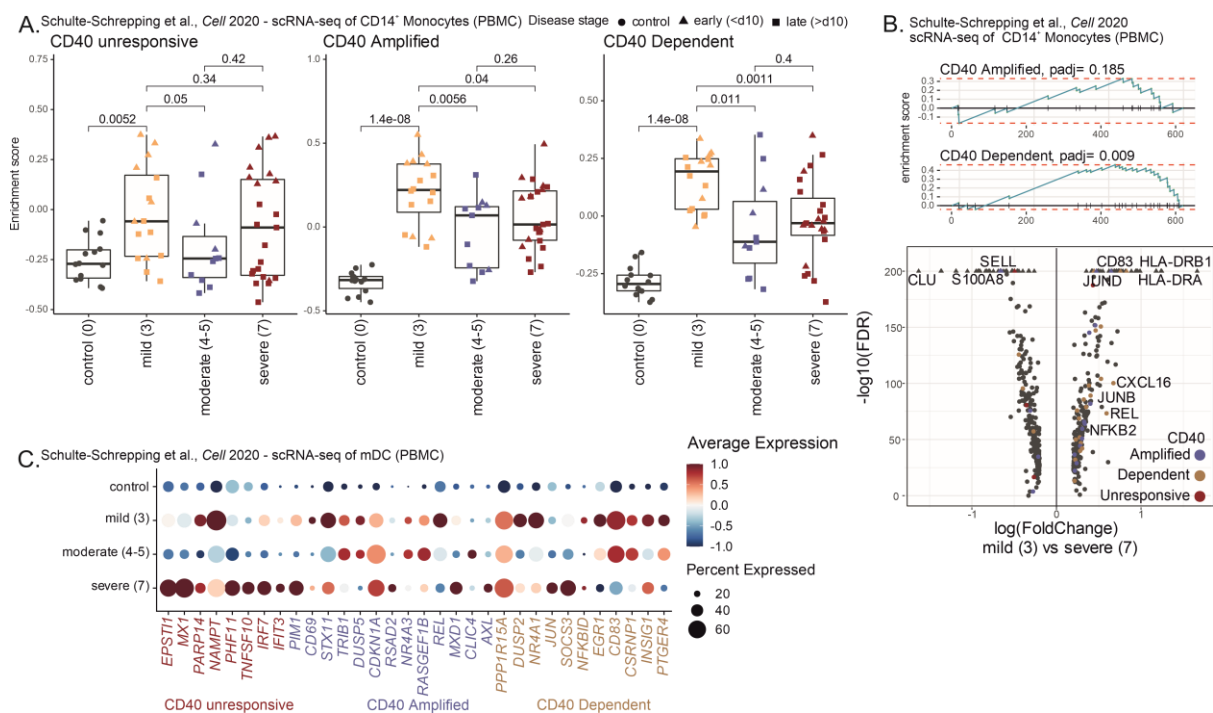


Figure 5: Combinatorial transcriptome responses to type 1 IFN and CD40 stimulation by monocytes and DCs correlate with milder outcomes of COVID-19

Re-analysis of scRNA-seq data of CD14⁺ monocytes and DCs subsetted from PBMCs derived from patients with mild (WHO 3, 16 samples), moderate (WHO 4-5, 11 samples) or severe (WHO 7, 23 samples) COVID-19 and healthy controls. A. Single-sample GSEA of the “CD40 unresponsive”, “CD40 amplified” and “CD40 dependent” gene signatures derived from *in vitro* stimulation experiments of murine APCs in monocytes from COVID-19 and control samples stratified by disease severity plotted as box plots of the enrichment scores. Wilcoxon rank-sum

test p-value is shown. B. Volcano plot (bottom) showing the differentially expressed genes in monocytes from mild COVID-19 compared to severe cases. Genes are colored according to their presence in the “CD40 unresponsive”, “CD40 amplified” or “CD40 combinatorial” signatures. GSEA enrichment plots (top) showing the enrichment curves of the “CD40 amplified” and “CD40 dependent” signature in the differentially expressed genes in monocytes from mild COVID-19 compared to severe cases. D. Dot plot visualizing the expression of genes differentially expressed in DCs comparing disease severities present in the “CD40 unresponsive”, “CD40 amplified” and “CD40 dependent” signatures.

CD14⁺ classical monocytes from patients with mild COVID-19 cases were significantly enriched for the transcriptional response signatures amplified by or dependent on CD40 stimulation in combination with type I IFN signal, whereas this enrichment was significantly lower in monocytes from patients with severe COVID-19 (Figure 5A). Differential gene expression analysis comparing monocytes from mild and severe cases of COVID-19 further revealed the distinct induction of CD40 amplified and dependent genes in mild COVID-19 (Figure 5B). The unbiased scRNA-seq PBMC dataset enabled us to confirm these findings in DCs, albeit in a more limited fashion due to low cell numbers in the blood. We found that transcription of genes depending on consecutive type I IFN and CD40 stimulation increased in DCs from COVID-19 patients with mild disease, while DCs from patients with severe COVID-19 showed increased expression of IFN-induced genes that were unresponsive to CD40 triggering (Figure 5C).

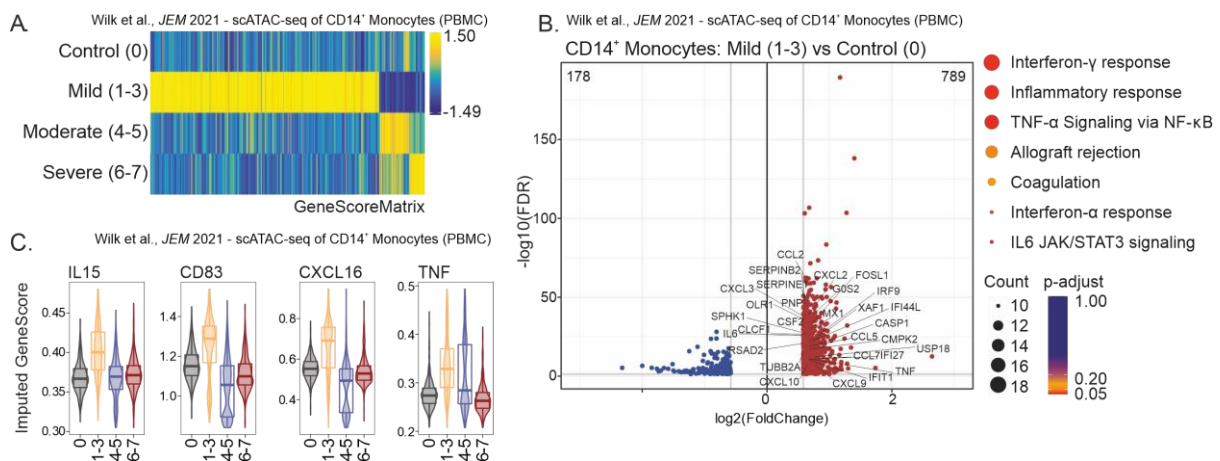


Figure 6: Open chromatin profiles in monocytes and DCs support the combinatorial transcriptome responses to type 1 IFN and CD40 stimulation in milder cases of COVID-19

Re-analysis of scATAC-seq data of CD14⁺ classical monocytes subsetted from PBMC derived from patients with mild (WHO 1-3), moderate (WHO 4-5) or severe (WHO 6-7) COVID-19 and healthy controls (Wilk et al., 2021). A. Heatmap showing GeneScores for disease-specific, significantly differentially accessible genes (FDR≤0.01 & Log₂FC≥0.58) across the indicated disease severities. B. Volcano Plot visualizing -log₁₀(FDR) and log₂ fold changes of significantly differentially accessible genes in CD14⁺ monocytes from mild COVID-19 patients compared to controls and respective significantly enriched HALLMARK terms for 789 genes with increased accessibility. C. Violin plots of imputed GeneScores of IL15, CD83, CXCL16 and TNF in CD14⁺ monocytes grouped according to COVID-19 severity.

This type I IFN and T cell help-dependent gene expression pattern was also reflected in the chromatin conformation of APCs from patients with mild COVID-19. The analysis of published scATAC-seq data from PBMCs of COVID-19 patients (Wilk et al., 2021) showed that CD14⁺ classical monocytes from patients with mild disease had significantly increased accessibility across more than 300 genes (Figure 6A). HALLMARK enrichment analysis of significantly more accessible genes in APCs from mild COVID-

19 patients compared to healthy control cells revealed ‘Interferon response’ as the major pathway of differentially regulated genes in mild COVID-19 (Figure 6B), but the set of genes also included key genes regulated by the combinatorial signal, such as *IL15*, *CD83*, *TNFA* and *CXCL16* (Figure 6C).

Subsequently, we investigated whether the observed alterations in APCs ultimately affect CD8⁺ T cell phenotypes in COVID-19 of different disease severities. We first assessed all CD8⁺ T cells of each disease severity for gene signatures reflecting priming of CD8⁺ T cells in the presence or absence of T cell help (Ahrends et al., 2017). Comparing the resulting enrichment scores across disease severities showed that ‘unhelped’ transcriptional profiles were significantly more pronounced in CD8⁺ T cells from patients with moderate and severe COVID-19 compared to mild cases (Figure 7A). Next, to resolve the relative composition of the CD8⁺ T cell phenotypes across the different disease severities, we performed clustering analysis and observed that mild and moderate COVID-19 cases were enriched in CD8⁺ T cell subsets with transcriptional profiles indicative of early effector cells and established memory T cells, including genes such as *IL7R*, *CD69*, *JUNB* and *JUND* (cluster 1 & 3 in Figure 7B-C). By contrast, CD8⁺ T cells with characteristics of terminal differentiation, such as expression of *CX3CR1* and *ISG15* (see cluster 5) dominated in patients with severe COVID-19. To further link the relative compositional changes in CD8⁺ T cell subsets across COVID-19 disease severities to the provision of CD4⁺ T cell help to APCs, we performed signature enrichments of the aforementioned ‘helped’ and ‘unhelped’ transcriptional signatures using AUCell across all cells of the respective subsets, which showed significant loss of the ‘helped’ signature and a corresponding gain in the ‘unhelped’ signature in CD8⁺ T cells of cluster 5 predominantly present in patients with severe COVID-19.

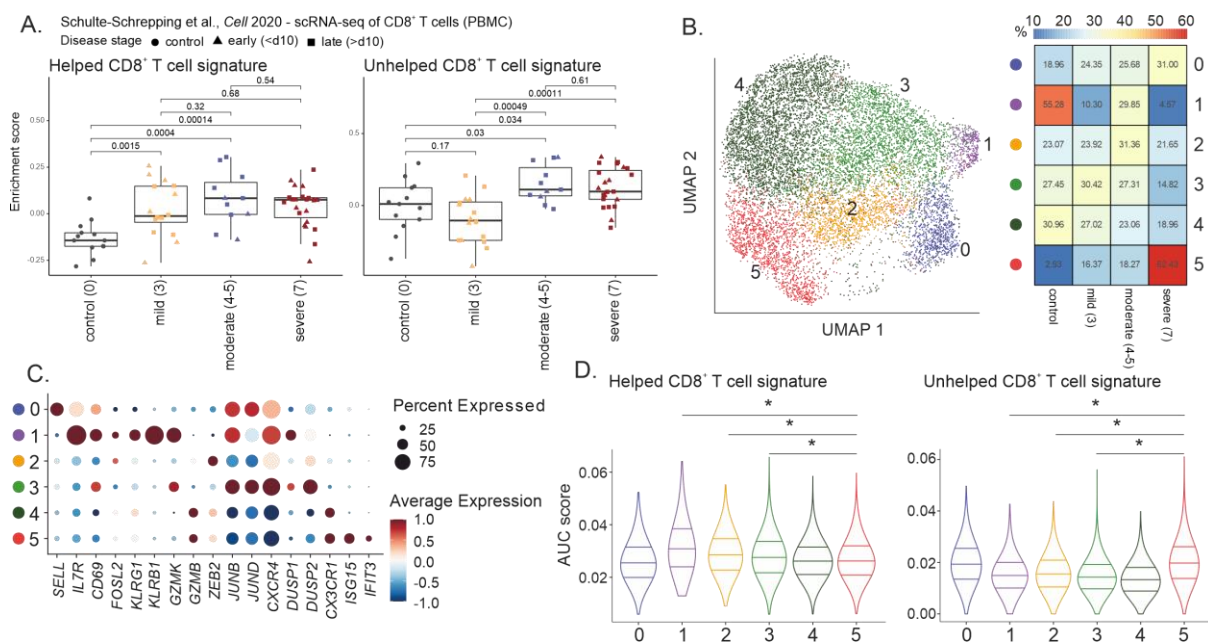


Figure 7: Severe outcomes of COVID-19 are associated with ‘unhelped’ CD8⁺ T cells

A. Single-sample GSVA of the “helped” and “unhelped” T cell signature derived from RNA-seq analysis of CD8⁺ T cells primed in the presence or absence of CD4⁺ T cell responses (Ahrends et al., 2017) in CD8⁺ T cells from COVID-19 and control samples stratified by disease severity plotted as box plots of the enrichment scores. Wilcoxon rank-sum test p-value is shown. B. UMAP visualization (left) of 6 clusters of the CD8⁺ T cell data and heatmap (right) visualizing the respective proportionate cluster occupancy per disease severity. C. Dot plot visualizing the expression of key genes associated with the respective clusters. E. AUCell enrichment of gene signatures for helped and unhelped T cells derived from RNA-seq analysis of CD8⁺ T cells primed in the presence or absence of CD4⁺ T cell responses in CD8⁺ T cells grouped according to the clustering, plotted as violin plots of

AUC scores. Benjamini-Hochberg corrected Dunn's Multiple Comparison Test has been used to infer statistical significance.

The study was designed to dissect how APCs molecularly integrate stimulation via type I IFN and CD40 from CD4⁺ T cells and identified that APCs require IFN-dependent rewiring of the signaling cascade downstream of CD40 for efficient provision of costimulatory molecules and soluble mediators upon receipt of T cell help. The activity of this carefully sequenced integration process in APCs from patients infected with SARS-CoV-2 correlated with milder forms of COVID-19 and consequent alterations of the CD8⁺ T cell responses in COVID-19.

For this publication, I performed all single-cell transcriptomics and epigenomics analyses and contributed to the writing and reviewing of the manuscript.

Methods

ScRNA-seq data production and analysis

ScRNA-seq data of PBMC from COVID-19 patients and controls collected from April to July 2020 in Bonn, Germany, was used as previously reported in (Schulte-Schrepping et al., 2020b). Samples were classified by disease severity according to WHO ordinal scale (WHO 3 mild; WHO 4–5, moderate; WHO 7 severe) and by the time after onset of first symptoms (early: day 0–10, late: > day 11) at the date of sampling. Details about sample procurement and processing, sequencing and data analysis have been described in (Schulte-Schrepping et al., 2020b) and an extensive description of the protocol has also been published in (De Domenico et al., 2020). Processed and annotated scRNA-seq data was downloaded from https://beta.fastgenomics.org/p/schulte-schrepping_covid19. The data was imported into R version 4.0.3 and analyzed using Seurat v3.9.9.

Subset analysis of CD14⁺ monocytes and mDCs

For the analysis of the myeloid DCs (mDCs) and classical CD14⁺ monocyte compartments, cells classified as mDCs, pDCs, classical monocytes, non-classical monocytes according to the original annotation provided were selected from the PBMC data set. These cells were subjected to Seurat v4 reference mapping following the developers vignette using the multimodal PBMC reference dataset (Hao et al., 2021). Only those cells classified as DC or monocyte subsets were selected to remove any possible cellular contaminations in the data set. Subsequently, the remaining 37.100 cells were re-clustered after scaling regressing for UMI count per cell, identification of variable genes and PCA in this cellular subspace using the Louvain algorithm with a resolution of 0.2 based on the first 10 principal components. Clusters representing mDCs or classical CD14⁺ monocytes were then subsetted, respectively, and the resulting 31.736 monocytes and 722 DCs were analysed in detail, including re-scaling, identification of variable genes, PCA and subsequent UMAP based on the first 10 principal components. Single sample gene set variation analysis (GSVA) using the “CD40 unresponsive”, “CD40 amplified” and “CD40 dependent” signatures derived from the described murine bulk RNA-seq analysis was performed using GSVA v1.38.244. For this, aggregated expression values of all cells of each sample were calculated using the AggregateExpression function in Seurat and used as input for the sample specific analysis. Of note, the CD40 unresponsive type I IFN response signature was intersected with the top 100 IFN response genes derived from an integrated analysis of 8 microarray data sets on IFN response of myeloid cells listed in the Interferome data base (<http://www.interferome.org/>) ranked by their combined log₂ fold changes in order to reduce the signature to a length comparable to the “CD40 amplified” and “CD40 dependent” signatures. Disease severity-specific marker gene analysis was performed using the Wilcoxon rank sum test with the

following cutoffs: genes had to be expressed in more than 10 % of the cells of the respective condition and exceed a logarithmic fold change cutoff of at least 0.2. Gene set enrichment analyses of “CD40 unresponsive”, “CD40 amplified” and “CD40 dependent” gene signatures in the differentially expressed genes in monocytes from mild COVID-19 compared to severe cases were performed using the fgsea packages v1.16.0.

Subset analysis of CD8⁺ T cells

For the analysis of the CD8⁺ T cell compartment, cells classified as T cells according to the original annotation (Schulte-Schrepping et al., 2020b) provided were selected from the PBMC data set. These cells were subjected to Seurat v4 reference mapping following the developers vignette using the multimodal PBMC reference dataset (Hao et al., 2021). Only those cells classified as T cells were selected to remove any possible cellular contaminations in the T cell data set. Subsequently, the remaining 45.516 cells were re-clustered after scaling regressing for UMI count per cell, identification of variable genes and PCA in this cellular subspace using the Louvain algorithm with a resolution of 0.2 based on the first 10 principal components. The cluster representing the CD8⁺ T cells was then subsetted and the resulting 12.386 cells were analyzed in detail, including re-scaling, identification of variable genes, PCA and subsequent UMAP based on the first 10 principal components. Ribosomal protein coding genes (RPL/RPS), mitochondrial genes (MT-) and haemoglobin genes (HBA1, HBA2, HBB) were excluded from the set of variable features to remove potential sources of technical differences. Single sample GSVA using the “helped” and “unhelped” T cell signature derived from RNA-seq analysis of CD8⁺ T cells primed in the presence or absence of CD4⁺ T cell help (Ahrends et al., 2017) was performed using GSVA v1.38.244. For this, aggregated expression values of all CD8⁺ T cells of each sample were calculated using the AggregateExpression function in Seurat and used as input for the sample specific analysis. Clustering of the CD8⁺ T cells was performed using the Louvain algorithm with a resolution of 0.4 based on the first 10 principal components and cells identified as $\gamma\delta$ T cells were removed. To investigate proportional cluster occupancy per disease severity, cell counts per condition were normalized before calculation of per-cluster percentages. Single-cell gene set enrichment analysis across cells of each CD8⁺ T cell subcluster using the “helped” and “unhelped” T cell signature derived from RNA-seq analysis of CD8⁺ T cells primed in the presence or absence of CD4⁺ T cell responses (Ahrends et al., 2017) was performed using AUCell v1.12.045.

Analysis of scATAC-seq data from Wilk et al., JEM 2021

Single-cell ATAC sequencing data of PBMC from COVID-19 patients and controls produced using the Chromium Next GEM Single Cell ATAC Reagent Kits version 1.1 (10x Genomics; PN-1000175) was used as previously published (Wilk et al., 2021). Processed and annotated scATAC-seq data from Wilk et al. was downloaded from GEO under GSE174072 and https://github.com/ajwilk/COVID_scMultiome and imported to R version 4.1.0. After creation of Arrow files and a respective ArchRproject using the R package ArchR version 1.0.1, the resulting single-cell data was filtered based on the published cell annotation and subsetted to CD14⁺ monocytes. Imputation weights on GeneScores were calculated using MAGIC implemented in ArchR’s addImputeWeights function. Severity-specific accessible genes were identified using the Wilcoxon Rank Sum test comparing gene scores of monocytes from mild cases of COVID-19 with cells from control donors with the following cutoffs: FDR \leq 0.05 & Log2FC \geq 0.58. HALLMARK enrichment analyses were performed using clusterProfiler version 4.0.5 (Wu et al., 2021) and the HALLMARK gene set v6.2.

5. Conclusion

In this thesis, I summarized recent developments in the field of omics for systems immunology, depicted challenges and considerations for their application to clinical questions and demonstrated their enormous potential at the example of COVID-19.

5.1. Dissecting the innate immune system in COVID-19 – cell by cell

The massive body of research produced over the course of the COVID-19 pandemic has left no doubt about the central role of the innate immune system in the pathology of this disease. While certainly indispensable for protection against the infection, its hyperactivation and dysregulation presents a dangerous threat in COVID-19. As outlined in this work, single-cell transcriptomics has contributed significantly to this understanding and accelerated the gain of knowledge through unbiased and comprehensive immunoprofiling (Tian et al., 2022).

To contribute to the robust, reproducible and safe research on COVID-19, we have developed and published an optimized workflow for handling potentially infectious samples derived from COVID-19 patients for single-cell transcriptomics and proteomics (De Domenico et al., 2020). Application of this protocol has yielded a valuable data set contributing to our understanding of the role of monocyte and neutrophil subsets in severe COVID-19 (Schulte-Schrepping et al., 2020b) as well as alterations of megakaryocytes and erythroid cells (Bernardes et al., 2020), functionally impaired NK cells (Krämer et al., 2021), and highly cytotoxic T cells (Georg et al., 2022). Furthermore, the data set has been used in external studies on COVID-19 (Schimke et al., 2022) and for other research purposes (Montaldo et al., 2022).

Because the innate and adaptive immune responses are inextricably linked through the processes of antigen presentation and lymphocyte priming and recruitment, it is crucial to understand how the respective alterations of the two domains affect each other in COVID-19. In Gressier et al., we reveal a carefully orchestrated consolidation process, whereby APCs integrate innate signals, such as type I IFNs, and CD4⁺ T cell help to produce a discrete set of costimulatory molecules and soluble mediators that are relevant to adapt the CD8⁺ T cell responses to the challenge of SARS-CoV-2.

To put our findings on of the role of monocytes and macrophages in COVID-19 in the context of subsequent studies, we reviewed the respective literature with a particular focus on observations gained by using high-resolution single-cell omics technologies (Knoll et al., 2021). In addition, we summarized the involvement of neutrophils in the pathogenesis of COVID-19 and highlighted several promising therapeutic attempts to target neutrophils and their reactivity in patients with COVID-19 in (Reusch et al., 2021).

In an exceptionally short time, we have gained great insight into the immunopathology of SARS-Cov-2 infection, but much remains to be done to paint a comprehensive picture of COVID-19 and to place the disease within the spectrum of human infectious diseases. Furthermore, despite great successes in the design of effective vaccines, including revolutionary progress in mRNA vaccine platforms (Hogan and Pardi, 2021), and treatment strategies using antiviral drugs, monoclonal antibodies or steroids (van de Veerdonk et al., 2022), COVID-19 continues to present a major health challenge with thousands of daily deaths demanding alternative treatment strategies. Intranasal vaccines (Madhavan et al., 2022) and other preventive therapeutics for immunocompromised individuals or those who or are not able to be fully vaccinated due to a history of severe adverse reactions are currently under development (Robinson et al., 2022). In addition, the long-term effects of COVID-19 are an increasing challenge and require therapeutic strategies. Approaches currently under investigation target

different proposed pathomechanisms, including antifibrotic medication due to the observation of fibrotic lung changes, anticoagulants as well as statins for their anti-inflammatory properties (Chaudhary et al., 2020; Mullard, 2021).

The derailment of the myeloid cell compartment in COVID-19 has brought the hematopoietic system to the spotlight. Acute infections, such as COVID-19, present a challenge for the hematopoietic stem and progenitor cell (HSPC) pool, and we and others have found that such immunological challenges to the HSPC pool can have both beneficial (Kalafati et al., 2020; Kaufmann et al., 2018) and maladaptive (Li et al., 2022; Ochando et al., 2022) long-term effects on myelopoiesis and the response to subsequent triggers (Mitroulis et al., 2018). The concept of ‘trained immunity’ primarily describes a beneficial enhanced responsiveness of the innate immune system as a consequence of previous immune activation based on epigenetic reprogramming (Cirovic et al., 2020), but conditioning of the innate immune system may also have deleterious effects (Netea et al., 2020). As in the acute response to viral infection, innate immune responses require balance and control.

From the beginning of the pandemic, it has been discussed that the mechanisms of trained immunity might potentially protect against severe COVID-19. *Bacillus Calmette–Guérin* (BCG) is a live attenuated vaccine that was developed against tuberculosis and has been the most widely used vaccine in the world (O’Neill and Netea, 2020). Beyond its primary purpose of protecting against tuberculosis, it has been shown to reduce the incidence of respiratory infections (Stensballe et al., 2005; Wardhana et al., 2011) and has since been identified as a potent inducer of trained immunity (Cirovic et al., 2020; Kleinnijenhuis et al., 2014). Therefore, the potential effect of BCG vaccination as a driver of protective trained immunity against COVID-19 has been investigated since the beginning of the pandemic with ambiguous results that require further studies (Brueggeman et al., 2022; Escobar et al., 2020; O’Neill and Netea, 2020; Tsilika et al., 2022).

However, what if we reverse these roles and consider SARS-CoV-2 to be the training agent itself? Several observations suggest this possibility. Influenza, for example, has been shown to induce prolonged antibacterial protection against *Streptococcus pneumoniae* due to a population of monocyte-derived alveolar macrophages in mice (Aegerter et al., 2020). On the other hand, long-lasting defects of monocytes and macrophages have been described after the resolution of bacterial infection and sepsis due to metabolic and epigenetic alterations (Cheng et al., 2016; Roquilly et al., 2020). For mild and asymptomatic COVID-19, features of long-term immunosuppression associated with regulatory neutrophil phenotypes have been described in convalescent individuals (Siemińska et al., 2021). Furthermore, it has been shown that after COVID-19 HSPCs retain epigenomic alterations that vary with disease severity, persist for months to a year, and are associated with increased myeloid cell differentiation and inflammatory or antiviral programs (Cheong et al., 2022). In this light, understanding the long-term effects of COVID-19 on the HSPC pool in the bone marrow in more detail certainly presents a pressing issue, particularly in the context of long-COVID.

Notably, not only severe acute threats are of concern in this context. Chronic inflammatory diseases as well as unhealthy lifestyles and malnutrition have also been described to impact myelopoiesis (Cabezas-Wallscheid et al., 2017; Christ et al., 2018; Kastrup and Grønbæk, 2021; Sanchez-Pino et al., 2022; Zhao and Baltimore, 2015). As long-lived humans in the changing environments of our fast-paced world, we are exposed to numerous such challenges throughout our lives and, consequently, our HSPCs are repeatedly challenged to ensure the supply of functional innate immune cells. How does the human hematopoietic system cope with these constant, life-long challenges given its finite number of stem cells, what are the dynamics and secondary effects of its memory and what are the mechanisms keeping the system from failing during aging? Given the complex biographies of humans and the difficulties of collecting and analyzing human bone marrow, these questions seem

unanswerable, but controlled experiments in animal models combined with high-resolution single-cell omics screens of human samples in conjunction with detailed clinical records will be vital to understand immune-mediated pathologies during aging – and the extensive and well-documented challenge of the human population with a newly emerging pathogen during the COVID-19 pandemic may present a unique scientific chance in this regard.

5.2. Future perspectives of single-cell omics in medicine

Our continuous work on the clinical application of single-cell omics since its introduction (Baßler et al., 2022) has allowed us to readily apply the technology in response to the challenge of COVID-19. The pandemic has forced us to accelerate the technology dramatically and implement its application to large clinical cohorts at unforeseen speed. Clearly, research on COVID-19 must continue to improve our understanding of its immunopathology and treatment, particularly with respect to vaccine efficacy and emerging variants of concern. But the impact of the pandemic on single-cell omics goes well beyond COVID-19 research.

High-resolution omics technologies will inevitably become widely used in clinical research and practice. Their diagnostic potential is unquestioned and with falling prices for reagents and sequencing, the hurdles for their translation become smaller and smaller. Studies applying single-cell omics to diseases other than COVID-19 are continuously increasing in numbers and growing in terms of patient cohorts and information content. Their potential for virtually all fields of medicine have recently been underpinned by large efforts in cancer (Barkley et al., 2022; Luo et al., 2022), cardiomyopathies (Reichart et al., 2022), infections (Oelen et al., 2022), chronic inflammatory and autoimmune diseases (Jaeger et al., 2021; Perez et al., 2022) as well as neurodegenerative diseases (Kamath et al., 2022; Yang et al., 2022). In addition, multi-omics approaches are being increasingly used. For example, the combined application of transcriptomics and immune repertoire profiling to clinical cohorts of patients with various cancer types has been effective to map a pan-cancer single-cell landscape of tumor-infiltrating T cells (Zheng et al., 2021). Moreover, recent developments in the fields of spatial transcriptomics (Moses and Pachter, 2022) and epigenomics (Lu et al., 2022), CRISPR screens (Ferrari et al., 2022) and temporal sequencing of living cells (Chen et al., 2022) make undeniably clear how technological improvements will continue to enhance data quality and content, paving the way for discoveries.

Despite all the great progress, we still have much to learn about how to optimally utilize these techniques in the clinical setting. The highly modular workflows demand more efforts to benchmark, standardize and disseminate protocols in order to improve robustness and reproducibility. With highly optimized experimental and computational SOPs and transparent and detailed reporting of standardized medical meta information of the patient cohorts, the use of such techniques will substantially enhance medical practice and contribute to the patients' benefits. Particularly in combination with artificial intelligence and machine learning approaches making use of the vast amount of data, these approaches hold great potential for disease risk prediction and differential diagnosis improving the experiences of both clinicians and patients (Rajpurkar et al., 2022; Warnat-Herresthal et al., 2020).

Furthermore, automation of sample processing and data generation will be key to further advance the use of omics in clinical practice and establish easy-to-use, reliable, and trusted applications. A single benchtop device performing sample collection by capillary blood draw from the fingertip, single cell purification and isolation, and transcriptome and epigenome library preparation all in one run

presents a futuristic, but not impossible, avenue towards fast and comprehensive assessment of a patients' immune status and might one day become a standard procedure in diagnostics. Of course, such an automation approach could also be further developed to include stimulation assays to assess the response capacities of the immune system or for processing different types of tissue samples to expand the potential applications beyond the systemic immune cell status.

But even the largest amounts of data are worthless if they cannot be analyzed, condensed, and understood. Therefore, in addition to all the necessary technical improvements, the medical community must invest in the education and training of personnel to be equipped to work with such new kinds of data and ultimately evaluate and make medical use of the information. Clearly, all these developments can only be initiated and supported by the research community but must be adapted by industry to create evaluated products generating useful and understandable readouts. The potential of these approaches is too valuable to be wasted by faulty or inaccurate attempts and therefore requires very careful implementation in order not to risk people's trust.

Beyond the experimental challenges, data protection and privacy regulations complicate the use of omics data in clinical trials across different institutions and countries, making it difficult to realize their full potential. To facilitate the integration of any medical data from any data owner worldwide without violating privacy laws, we introduced Swarm Learning for decentralized and confidential clinical machine learning as a means of disease classification and diagnosis. The approach unites edge computing with blockchain-based peer-to-peer networking and coordination to maintain confidentiality and circumvent the need for data sharing and central data storage (Warnat-Herresthal et al., 2021). This approach has been shown to outperform classifiers developed at individual sites across a range of diseases, including COVID-19, tuberculosis, leukemia and lung pathologies and holds great promise to accelerate the introduction of precision medicine.

In view of future pandemics, the scientific community must be prepared to react quickly and efficiently (Schultze et al., 2022), and advancing such powerful experimental methods and analytical approaches for robust clinical routine application could make a significant contribution to this preparation.

6. References

- Aderem, A. (2005). Systems biology: its practice and challenges. *Cell* 121, 511–513.
- Aegerter, H., Kulikauskaite, J., Crotta, S., Patel, H., Kelly, G., Hessel, E.M., Mack, M., Beinke, S., and Wack, A. (2020). Influenza-induced monocyte-derived alveolar macrophages confer prolonged antibacterial protection. *Nat. Immunol.* 21, 145–157.
- Ahrends, T., Spanjaard, A., Pilzecker, B., Bąbala, N., Bovens, A., Xiao, Y., Jacobs, H., and Borst, J. (2017). CD4+ T cell help confers a cytotoxic T cell effector program including coinhibitory receptor downregulation and increased tissue invasiveness. *Immunity* 47, 848–861.e5.
- Arcanjo, A., Logullo, J., Menezes, C.C.B., de Souza Carvalho Giangiarulo, T.C., Dos Reis, M.C., de Castro, G.M.M., da Silva Fontes, Y., Todeschini, A.R., Freire-de-Lima, L., Decoté-Ricardo, D., et al. (2020). The emerging role of neutrophil extracellular traps in severe acute respiratory syndrome coronavirus 2 (COVID-19). *Sci. Rep.* 10, 19630.
- Arunachalam, P.S., Wimmers, F., Mok, C.K.P., Perera, R.A.P.M., Scott, M., Hagan, T., Sigal, N., Feng, Y., Bristow, L., Tak-Yin Tsang, O., et al. (2020). Systems biological assessment of immunity to mild versus severe COVID-19 infection in humans. *Science* 369, 1210–1220.
- Aschenbrenner, A.C., Mouktaroudi, M., Krämer, B., Oestreich, M., Antonakos, N., Nuesch-Germano, M., Gkizeli, K., Bonaguro, L., Reusch, N., Baßler, K., et al. (2021). Disease severity-specific neutrophil signatures in blood transcriptomes stratify COVID-19 patients. *Genome Med.* 13, 7.
- Bacher, P., Rosati, E., Esser, D., Martini, G.R., Saggau, C., Schiminsky, E., Dargvainiene, J., Schröder, I., Wieters, I., Khodamoradi, Y., et al. (2020). Low-Avidity CD4+ T Cell Responses to SARS-CoV-2 in Unexposed Individuals and Humans with Severe COVID-19. *Immunity* 53, 1258–1271.e5.
- Barkley, D., Moncada, R., Pour, M., Liberman, D.A., Dryg, I., Werba, G., Wang, W., Baron, M., Rao, A., Xia, B., et al. (2022). Cancer cell states recur across tumor types and form specific interactions with the tumor microenvironment. *Nat. Genet.* 54, 1192–1201.
- Bassler, K., Schulte-Schrepping, J., Warnat-Herresthal, S., Aschenbrenner, A.C., and Schultze, J.L. (2019). The Myeloid Cell Compartment-Cell by Cell. *Annu. Rev. Immunol.* 37, 269–293.
- Baßler, K., Fujii, W., Kapellos, T.S., Dudkin, E., Reusch, N., Horne, A., Reiz, B., Luecken, M.D., Osei-Sarpong, C., Warnat-Herresthal, S., et al. (2022). Alveolar macrophages in early stage COPD show functional deviations with properties of impaired immune activation. *Front. Immunol.* 13, 917232.
- Bastard, P., Rosen, L.B., Zhang, Q., Michailidis, E., Hoffmann, H.-H., Zhang, Y., Dorgham, K., Philippot, Q., Rosain, J., Béziat, V., et al. (2020). Autoantibodies against type I IFNs in patients with life-threatening COVID-19. *Science* 370.
- Bastard, P., Gervais, A., Le Voyer, T., Rosain, J., Philippot, Q., Manry, J., Michailidis, E., Hoffmann, H.-H., Eto, S., Garcia-Prat, M., et al. (2021). Autoantibodies neutralizing type I IFNs are present in ~4% of uninfected individuals over 70 years old and account for ~20% of COVID-19 deaths. *Sci. Immunol.* 6.
- Beck, D.B., and Aksentijevich, I. (2020). Susceptibility to severe COVID-19. *Science* 370, 404–405.
- Bedoui, S., Heath, W.R., and Mueller, S.N. (2016). CD4(+) T-cell help amplifies innate signals for primary CD8(+) T-cell immunity. *Immunol. Rev.* 272, 52–64.

- Bennett, L., Palucka, A.K., Arce, E., Cantrell, V., Borvak, J., Banchereau, J., and Pascual, V. (2003). Interferon and granulopoiesis signatures in systemic lupus erythematosus blood. *J. Exp. Med.* 197, 711–723.
- Bernardes, J.P., Mishra, N., Tran, F., Bahmer, T., Best, L., Blase, J.I., Bordoni, D., Franzenburg, J., Geisen, U., Josephs-Spaulding, J., et al. (2020). Longitudinal Multi-omics Analyses Identify Responses of Megakaryocytes, Erythroid Cells, and Plasmablasts as Hallmarks of Severe COVID-19. *Immunity* 53, 1296–1314.e9.
- Bonaguro, L., Schulte-Schrepping, J., Ulas, T., Aschenbrenner, A.C., Beyer, M., and Schultze, J.L. (2022). A guide to systems-level immunomics. *Nat. Immunol.*
- Borst, J., Ahrends, T., Bąbka, N., Melief, C.J.M., and Kastenmüller, W. (2018). CD4+ T cell help in cancer immunology and immunotherapy. *Nat. Rev. Immunol.* 18, 635–647.
- Bronte, V., Brandau, S., Chen, S.-H., Colombo, M.P., Frey, A.B., Greten, T.F., Mandruzzato, S., Murray, P.J., Ochoa, A., Ostrand-Rosenberg, S., et al. (2016). Recommendations for myeloid-derived suppressor cell nomenclature and characterization standards. *Nat. Commun.* 7, 12150.
- Brueggeman, J.M., Zhao, J., Schank, M., Yao, Z.Q., and Moorman, J.P. (2022). Trained Immunity: An Overview and the Impact on COVID-19. *Front. Immunol.* 13, 837524.
- Byron, S.A., Van Keuren-Jensen, K.R., Engelthaler, D.M., Carpten, J.D., and Craig, D.W. (2016). Translating RNA sequencing into clinical diagnostics: opportunities and challenges. *Nat. Rev. Genet.* 17, 257–271.
- Cabezas-Wallscheid, N., Buettner, F., Sommerkamp, P., Klimmeck, D., Ladel, L., Thalheimer, F.B., Pastor-Flores, D., Roma, L.P., Renders, S., Zeisberger, P., et al. (2017). Vitamin A-Retinoic Acid Signaling Regulates Hematopoietic Stem Cell Dormancy. *Cell* 169, 807–823.e19.
- Cao, X. (2020). COVID-19: immunopathology and its implications for therapy. *Nat. Rev. Immunol.* 20, 269–270.
- Cao, J., Packer, J.S., Ramani, V., Cusanovich, D.A., Huynh, C., Daza, R., Qiu, X., Lee, C., Furlan, S.N., Steemers, F.J., et al. (2017). Comprehensive single-cell transcriptional profiling of a multicellular organism. *Science* 357, 661–667.
- Chappell, L., Russell, A.J.C., and Voet, T. (2018). Single-cell (multi)omics technologies. *Annu. Rev. Genomics. Hum. Genet.* 19, 15–41.
- Chaudhary, S., Natt, B., Bime, C., Knox, K.S., and Glassberg, M.K. (2020). Antifibrotics in COVID-19 Lung Disease: Let Us Stay Focused. *Front Med (Lausanne)* 7, 539.
- Chen, G., Wu, D., Guo, W., Cao, Y., Huang, D., Wang, H., Wang, T., Zhang, X., Chen, H., Yu, H., et al. (2020a). Clinical and immunological features of severe and moderate coronavirus disease 2019. *J. Clin. Invest.* 130, 2620–2629.
- Chen, G., Wu, D., Guo, W., Cao, Y., Huang, D., Wang, H., Wang, T., Zhang, X., Chen, H., Yu, H., et al. (2020b). Clinical and immunologic features in severe and moderate forms of Coronavirus Disease 2019. *medRxiv*.
- Chen, W., Guillaume-Gentil, O., Rainer, P.Y., Gäbelein, C.G., Saelens, W., Gardeux, V., Klaeger, A., Dainese, R., Zachara, M., Zambelli, T., et al. (2022). Live-seq enables temporal transcriptomic recording of single cells. *Nature* 608, 733–740.

Cheng, S.-C., Scicluna, B.P., Arts, R.J.W., Gresnigt, M.S., Lachmandas, E., Giamarellos-Bourboulis, E.J., Kox, M., Manjeri, G.R., Wagenaars, J.A.L., Cremer, O.L., et al. (2016). Broad defects in the energy metabolism of leukocytes underlie immunoparalysis in sepsis. *Nat. Immunol.* 17, 406–413.

Cheong, J.G., Ravishankar, A., Sharma, S., Parkhurst, C., Nehar-Belaid, D., Ma, S., Paddock, L., Fatou, B., Karakaslar, E., Thibodeau, A., et al. (2022). Epigenetic Memory of COVID-19 in Innate Immune Cells and Their Progenitors. *BioRxiv*.

Christ, A., Günther, P., Lauterbach, M.A.R., Duester, P., Biswas, D., Pelka, K., Scholz, C.J., Oosting, M., Haendler, K., Baßler, K., et al. (2018). Western Diet Triggers NLRP3-Dependent Innate Immune Reprogramming. *Cell* 172, 162–175.e14.

Chua, R.L., Lukassen, S., Trump, S., Hennig, B.P., Wendisch, D., Pott, F., Debnath, O., Thürmann, L., Kurth, F., Völker, M.T., et al. (2020). COVID-19 severity correlates with airway epithelium-immune cell interactions identified by single-cell analysis. *Nat. Biotechnol.* 38, 970–979.

Cirovic, B., de Bree, L.C.J., Groh, L., Blok, B.A., Chan, J., van der Velden, W.J.F.M., Bremmers, M.E.J., van Crevel, R., Händler, K., Picelli, S., et al. (2020). BCG vaccination in humans elicits trained immunity via the hematopoietic progenitor compartment. *Cell Host Microbe* 28, 322–334.e5.

Cloke, T., Munder, M., Taylor, G., Müller, I., and Kropf, P. (2012). Characterization of a novel population of low-density granulocytes associated with disease severity in HIV-1 infection. *PLoS One* 7, e48939.

Cloonan, N., Forrest, A.R.R., Kolle, G., Gardiner, B.B.A., Faulkner, G.J., Brown, M.K., Taylor, D.F., Steptoe, A.L., Wani, S., Bethel, G., et al. (2008). Stem cell transcriptome profiling via massive-scale mRNA sequencing. *Nat. Methods* 5, 613–619.

Combes, A.J., Courau, T., Kuhn, N.F., Hu, K.H., Ray, A., Chen, W.S., Chew, N.W., Cleary, S.J., Kushnoor, D., Reeder, G.C., et al. (2021). Global absence and targeting of protective immune states in severe COVID-19. *Nature* 591, 124–130.

Delorey, T.M., Ziegler, C.G.K., Heimberg, G., Normand, R., Yang, Y., Segerstolpe, Å., Abbondanza, D., Fleming, S.J., Subramanian, A., Montoro, D.T., et al. (2021). COVID-19 tissue atlases reveal SARS-CoV-2 pathology and cellular targets. *Nature* 595, 107–113.

DeRisi, J., Penland, L., Brown, P.O., Bittner, M.L., Meltzer, P.S., Ray, M., Chen, Y., Su, Y.A., and Trent, J.M. (1996). Use of a cDNA microarray to analyse gene expression patterns in human cancer. *Nat. Genet.* 14, 457–460.

De Domenico, E., Bonaguro, L., Schulte-Schrepping, J., Becker, M., Händler, K., and Schultze, J.L. (2020). Optimized workflow for single-cell transcriptomics on infectious diseases including COVID-19. *STAR Protocols* 1, 100233.

Dong, X., Zhang, L., Milholland, B., Lee, M., Maslov, A.Y., Wang, T., and Vijg, J. (2017). Accurate identification of single-nucleotide variants in whole-genome-amplified single cells. *Nat. Methods* 14, 491–493.

Earhart, A.P., Holliday, Z.M., Hofmann, H.V., and Schrum, A.G. (2020). Consideration of dornase alfa for the treatment of severe COVID-19 ARDS. *New Microbes New Infect.* 100689.

Erle, D.J., and Yang, Y.H. (2003). Asthma investigators begin to reap the fruits of genomics. *Genome Biol.* 4, 232.

- Escobar, L.E., Molina-Cruz, A., and Barillas-Mury, C. (2020). BCG vaccine protection from severe coronavirus disease 2019 (COVID-19). *Proc. Natl. Acad. Sci. USA* 117, 17720–17726.
- Evrard, M., Kwok, I.W.H., Chong, S.Z., Teng, K.W.W., Becht, E., Chen, J., Sieow, J.L., Penny, H.L., Ching, G.C., Devi, S., et al. (2018). Developmental analysis of bone marrow neutrophils reveals populations specialized in expansion, trafficking, and effector functions. *Immunity* 48, 364–379.e8.
- Evrony, G.D., Hinch, A.G., and Luo, C. (2021). Applications of Single-Cell DNA Sequencing. *Annu. Rev. Genomics. Hum. Genet.* 22, 171–197.
- Falck-Jones, S., Vangeti, S., Yu, M., Falck-Jones, R., Cagigi, A., Badolati, I., Österberg, B., Lautenbach, M.J., Åhlberg, E., Lin, A., et al. (2021). Functional monocytic myeloid-derived suppressor cells increase in blood but not airways and predict COVID-19 severity. *J. Clin. Invest.* 131.
- Ferrari, S., Jacob, A., Cesana, D., Laugel, M., Beretta, S., Varesi, A., Unali, G., Conti, A., Canarutto, D., Albano, L., et al. (2022). Choice of template delivery mitigates the genotoxic risk and adverse impact of editing in human hematopoietic stem cells. *Cell Stem Cell* 29, 1428–1444.e9.
- Georg, P., Astaburuaga-García, R., Bonaguro, L., Brumhard, S., Michalick, L., Lippert, L.J., Kostevc, T., Gäbel, C., Schneider, M., Streitz, M., et al. (2022). Complement activation induces excessive T cell cytotoxicity in severe COVID-19. *Cell* 185, 493–512.e25.
- Giamarellos-Bourboulis, E.J., Netea, M.G., Rovina, N., Akinosoglou, K., Antoniadou, A., Antonakos, N., Damoraki, G., Gkavogianni, T., Adami, M.-E., Katsaounou, P., et al. (2020). Complex Immune Dysregulation in COVID-19 Patients with Severe Respiratory Failure. *Cell Host Microbe* 27, 992–1000.e3.
- Gierahn, T.M., Wadsworth, M.H., Hughes, T.K., Bryson, B.D., Butler, A., Satija, R., Fortune, S., Love, J.C., and Shalek, A.K. (2017). Seq-Well: portable, low-cost RNA sequencing of single cells at high throughput. *Nat. Methods* 14, 395–398.
- Ginhoux, F., and Jung, S. (2014). Monocytes and macrophages: developmental pathways and tissue homeostasis. *Nat. Rev. Immunol.* 14, 392–404.
- Goh, C.C., Roggerson, K.M., Lee, H.-C., Golden-Mason, L., Rosen, H.R., and Hahn, Y.S. (2016). Hepatitis C Virus-Induced Myeloid-Derived Suppressor Cells Suppress NK Cell IFN- γ Production by Altering Cellular Metabolism via Arginase-1. *J. Immunol.* 196, 2283–2292.
- Grant, R.A., Morales-Nebreda, L., Markov, N.S., Swaminathan, S., Querrey, M., Guzman, E.R., Abbott, D.A., Donnelly, H.K., Donayre, A., Goldberg, I.A., et al. (2021). Circuits between infected macrophages and T cells in SARS-CoV-2 pneumonia. *Nature* 590, 635–641.
- Greyer, M., Whitney, P.G., Stock, A.T., Davey, G.M., Tebartz, C., Bachem, A., Mintern, J.D., Strugnell, R.A., Turner, S.J., Gebhardt, T., et al. (2016). T cell help amplifies innate signals in CD8(+) dcs for optimal CD8(+) T cell priming. *Cell Rep.* 14, 586–597.
- GTE Consortium (2013). The Genotype-Tissue Expression (GTEx) project. *Nat. Genet.* 45, 580–585.
- Guilliams, M., and Scott, C.L. (2017). Does niche competition determine the origin of tissue-resident macrophages? *Nat. Rev. Immunol.* 17, 451–460.
- Guilliams, M., and Scott, C.L. (2022). Liver macrophages in health and disease. *Immunity* 55, 1515–1529.

- Guilliams, M., Thierry, G.R., Bonnardel, J., and Bajenoff, M. (2020). Establishment and maintenance of the macrophage niche. *Immunity* 52, 434–451.
- Guo, L., Yi, X., Chen, L., Zhang, T., Guo, H., Chen, Z., Cheng, J., Cao, Q., Liu, H., Hou, C., et al. (2022). Single-Cell DNA Sequencing Reveals Punctuated and Gradual Clonal Evolution in Hepatocellular Carcinoma. *Gastroenterology* 162, 238–252.
- Gustine, J.N., and Jones, D. (2021). Immunopathology of Hyperinflammation in COVID-19. *Am. J. Pathol.* 191, 4–17.
- Hadjadj, J., Yatim, N., Barnabei, L., Corneau, A., Boussier, J., Smith, N., Péré, H., Charbit, B., Bondet, V., Chenevier-Gobeaux, C., et al. (2020). Impaired type I interferon activity and inflammatory responses in severe COVID-19 patients. *Science* 369, 718–724.
- Hao, Y., Hao, S., Andersen-Nissen, E., Mauck, W.M., Zheng, S., Butler, A., Lee, M.J., Wilk, A.J., Darby, C., Zager, M., et al. (2021). Integrated analysis of multimodal single-cell data. *Cell* 184, 3573–3587.e29.
- Hassani, M., Hellebrekers, P., Chen, N., van Aalst, C., Bongers, S., Hietbrink, F., Koenderman, L., and Vrisekoop, N. (2020). On the origin of low-density neutrophils. *J. Leukoc. Biol.* 107, 809–818.
- Hedrick, C.C., and Malanchi, I. (2022). Neutrophils in cancer: heterogeneous and multifaceted. *Nat. Rev. Immunol.* 22, 173–187.
- Heng, T.S.P., Painter, M.W., and Immunological Genome Project Consortium (2008). The Immunological Genome Project: networks of gene expression in immune cells. *Nat. Immunol.* 9, 1091–1094.
- Herrero-Cervera, A., Soehnlein, O., and Kenne, E. (2022). Neutrophils in chronic inflammatory diseases. *Cell Mol Immunol.*
- Hidalgo, A., Chilvers, E.R., Summers, C., and Koenderman, L. (2019). The neutrophil life cycle. *Trends Immunol.* 40, 584–597.
- Hikmet, F., Méar, L., Edvinsson, Å., Micke, P., Uhlén, M., and Lindskog, C. (2020). The protein expression profile of ACE2 in human tissues. *Mol. Syst. Biol.* 16, e9610.
- Hoffmann, M., Kleine-Weber, H., Schroeder, S., Krüger, N., Herrler, T., Erichsen, S., Schiergens, T.S., Herrler, G., Wu, N.-H., Nitsche, A., et al. (2020). SARS-CoV-2 Cell Entry Depends on ACE2 and TMPRSS2 and Is Blocked by a Clinically Proven Protease Inhibitor. *Cell* 181, 271–280.e8.
- Hogan, M.J., and Pardi, N. (2021). mRNA Vaccines in the COVID-19 Pandemic and Beyond. *Annu. Rev. Med.*
- Hume, D.A. (2006). The mononuclear phagocyte system. *Curr. Opin. Immunol.* 18, 49–53.
- Hume, D.A., Irvine, K.M., and Pridans, C. (2019). The Mononuclear Phagocyte System: The Relationship between Monocytes and Macrophages. *Trends Immunol.* 40, 98–112.
- Hunt, S., Bennett, A.T.D., Cuthill, I.C., and Griffiths, R. (1998). Blue tits are ultraviolet tits. *Proc. R. Soc. Lond. B* 265, 451–455.
- Islam, S., Kjällquist, U., Moliner, A., Zajac, P., Fan, J.-B., Lönnerberg, P., and Linnarsson, S. (2011). Characterization of the single-cell transcriptional landscape by highly multiplex RNA-seq. *Genome Res.* 21, 1160–1167.

Jaeger, N., Gamini, R., Cella, M., Schettini, J.L., Bugatti, M., Zhao, S., Rosadini, C.V., Esaulova, E., Di Luccia, B., Kinnett, B., et al. (2021). Single-cell analyses of Crohn's disease tissues reveal intestinal intraepithelial T cells heterogeneity and altered subset distributions. *Nat. Commun.* 12, 1921.

Jaitin, D.A., Kenigsberg, E., Keren-Shaul, H., Elefant, N., Paul, F., Zaretsky, I., Mildner, A., Cohen, N., Jung, S., Tanay, A., et al. (2014). Massively parallel single-cell RNA-seq for marker-free decomposition of tissues into cell types. *Science* 343, 776–779.

Jakubzick, C.V., Randolph, G.J., and Henson, P.M. (2017). Monocyte differentiation and antigen-presenting functions. *Nat. Rev. Immunol.* 17, 349–362.

Jia, Q., Chu, H., Jin, Z., Long, H., and Zhu, B. (2022). High-throughput single-cell sequencing in cancer research. *Signal Transduct. Target. Ther.* 7, 145.

Jiang, P., Zhang, Z., Hu, Y., Liang, Z., Han, Y., Li, X., Zeng, X., Zhang, H., Zhu, M., Dong, J., et al. (2022). Single-cell ATAC-seq maps the comprehensive and dynamic chromatin accessibility landscape of CAR-T cell dysfunction. *Leukemia*.

Johansson, C., and Kirsebom, F.C.M. (2021). Neutrophils in respiratory viral infections. *Mucosal Immunol.*

Kaastrup, K., and Grønbaek, K. (2021). The Impact of Sedentary Lifestyle, High-fat Diet, Tobacco Smoke, and Alcohol Intake on the Hematopoietic Stem Cell Niches. *HemaSphere* 5, e615.

Kalafati, L., Kourtzelis, I., Schulte-Schrepping, J., Li, X., Hatzioannou, A., Grinenko, T., Hagag, E., Sinha, A., Has, C., Dietz, S., et al. (2020). Innate Immune Training of Granulopoiesis Promotes Anti-tumor Activity. *Cell* 183, 771–785.e12.

Kamath, T., Abdulraouf, A., Burris, S.J., Langlieb, J., Gazestani, V., Nadaf, N.M., Balderrama, K., Vanderburg, C., and Macosko, E.Z. (2022). Single-cell genomic profiling of human dopamine neurons identifies a population that selectively degenerates in Parkinson's disease. *Nat. Neurosci.* 25, 588–595.

Kapellos, T.S., Bonaguro, L., Gemünd, I., Reusch, N., Saglam, A., Hinkley, E.R., and Schultze, J.L. (2019). Human monocyte subsets and phenotypes in major chronic inflammatory diseases. *Front. Immunol.* 10, 2035.

Kaufmann, E., Sanz, J., Dunn, J.L., Khan, N., Mendonça, L.E., Pacis, A., Tzelepis, F., Pernet, E., Dumaine, A., Grenier, J.-C., et al. (2018). BCG Educates Hematopoietic Stem Cells to Generate Protective Innate Immunity against Tuberculosis. *Cell* 172, 176–190.e19.

Kawai, J., Shinagawa, A., Shibata, K., Yoshino, M., Itoh, M., Ishii, Y., Arakawa, T., Hara, A., Fukunishi, Y., Konno, H., et al. (2001). Functional annotation of a full-length mouse cDNA collection. *Nature* 409, 685–690.

Kazer, S.W., Aicher, T.P., Muema, D.M., Carroll, S.L., Ordovas-Montanes, J., Miao, V.N., Tu, A.A., Ziegler, C.G.K., Nyquist, S.K., Wong, E.B., et al. (2020). Integrated single-cell analysis of multicellular immune dynamics during hyperacute HIV-1 infection. *Nat. Med.* 26, 511–518.

Kedor, C., Freitag, H., Meyer-Arndt, L., Wittke, K., Hanitsch, L.G., Zoller, T., Steinbeis, F., Haffke, M., Rudolf, G., Heidecker, B., et al. (2022). A prospective observational study of post-COVID-19 chronic fatigue syndrome following the first pandemic wave in Germany and biomarkers associated with symptom severity. *Nat. Commun.* 13, 5104.

Keren-Shaul, H., Spinrad, A., Weiner, A., Matcovitch-Natan, O., Dvir-Szternfeld, R., Ulland, T.K., David, E., Baruch, K., Lara-Astaiso, D., Toth, B., et al. (2017). A Unique Microglia Type Associated with Restricting Development of Alzheimer's Disease. *Cell* 169, 1276–1290.e17.

Keskinen, P., Ronni, T., Matikainen, S., Lehtonen, A., and Julkunen, I. (1997). Regulation of HLA class I and II expression by interferons and influenza A virus in human peripheral blood mononuclear cells. *Immunology* 91, 421–429.

Kleinnijenhuis, J., Quintin, J., Preijers, F., Benn, C.S., Joosten, L.A.B., Jacobs, C., van Loenhout, J., Xavier, R.J., Aaby, P., van der Meer, J.W.M., et al. (2014). Long-lasting effects of BCG vaccination on both heterologous Th1/Th17 responses and innate trained immunity. *J Innate Immun* 6, 152–158.

Knoll, R., Schultze, J.L., and Schulte-Schrepping, J. (2021). Monocytes and Macrophages in COVID-19. *Front. Immunol.* 12, 720109.

Kotliar, D., Lin, A.E., Logue, J., Hughes, T.K., Khoury, N.M., Raju, S.S., Wadsworth, M.H., Chen, H., Kurtz, J.R., Dighero-Kemp, B., et al. (2020). Single-Cell Profiling of Ebola Virus Disease In Vivo Reveals Viral and Host Dynamics. *Cell* 183, 1383–1401.e19.

Kox, M., Waalders, N.J.B., Kooistra, E.J., Gerretsen, J., and Pickkers, P. (2020). Cytokine Levels in Critically Ill Patients With COVID-19 and Other Conditions. *JAMA*.

Krämer, B., Knoll, R., Bonaguro, L., ToVinh, M., Raabe, J., Astaburuaga-García, R., Schulte-Schrepping, J., Kaiser, K.M., Rieke, G.J., Bischoff, J., et al. (2021). Early IFN- α signatures and persistent dysfunction are distinguishing features of NK cells in severe COVID-19. *Immunity* 54, 2650–2669.e14.

Kumagai, Y., Takeuchi, O., Kato, H., Kumar, H., Matsui, K., Morii, E., Aozasa, K., Kawai, T., and Akira, S. (2007). Alveolar macrophages are the primary interferon-alpha producer in pulmonary infection with RNA viruses. *Immunity* 27, 240–252.

Kvedaraite, E., Hertwig, L., Sinha, I., Ponzetta, A., Hed Myrberg, I., Lourda, M., Dzidic, M., Akber, M., Klingström, J., Folkesson, E., et al. (2021). Major alterations in the mononuclear phagocyte landscape associated with COVID-19 severity. *Proc. Natl. Acad. Sci. USA* 118.

Kwok, I., Becht, E., Xia, Y., Ng, M., Teh, Y.C., Tan, L., Evrard, M., Li, J.L.Y., Tran, H.T.N., Tan, Y., et al. (2020). Combinatorial Single-Cell Analyses of Granulocyte-Monocyte Progenitor Heterogeneity Reveals an Early Uni-potent Neutrophil Progenitor. *Immunity* 53, 303–318.e5.

Lähnemann, D., Köster, J., Szczurek, E., McCarthy, D.J., Hicks, S.C., Robinson, M.D., Vallejos, C.A., Campbell, K.R., Beerwinkler, N., Mahfouz, A., et al. (2020). Eleven grand challenges in single-cell data science. *Genome Biol.* 21, 31.

Lamers, M.M., and Haagmans, B.L. (2022). SARS-CoV-2 pathogenesis. *Nat. Rev. Microbiol.* 20, 270–284.

Laurenti, E., and Göttgens, B. (2018). From haematopoietic stem cells to complex differentiation landscapes. *Nature* 553, 418–426.

Lavin, Y., Winter, D., Blecher-Gonen, R., David, E., Keren-Shaul, H., Merad, M., Jung, S., and Amit, I. (2014). Tissue-resident macrophage enhancer landscapes are shaped by the local microenvironment. *Cell* 159, 1312–1326.

Lavin, Y., Mortha, A., Rahman, A., and Merad, M. (2015). Regulation of macrophage development and function in peripheral tissues. *Nat. Rev. Immunol.* 15, 731–744.

- Lee, J.S., Park, S., Jeong, H.W., Ahn, J.Y., Choi, S.J., Lee, H., Choi, B., Nam, S.K., Sa, M., Kwon, J.-S., et al. (2020). Immunophenotyping of COVID-19 and influenza highlights the role of type I interferons in development of severe COVID-19. *Sci. Immunol.* 5.
- Leppkes, M., Knopf, J., Naschberger, E., Lindemann, A., Singh, J., Herrmann, I., Stürzl, M., Staats, L., Mahajan, A., Schauer, C., et al. (2020). Vascular occlusion by neutrophil extracellular traps in COVID-19. *EBioMedicine* 58, 102925.
- Li, X., Wang, H., Yu, X., Saha, G., Kalafati, L., Ioannidis, C., Mitroulis, I., Netea, M.G., Chavakis, T., and Hajishengallis, G. (2022). Maladaptive innate immune training of myelopoiesis links inflammatory comorbidities. *Cell* 185, 1709–1727.e18.
- Liao, M., Liu, Y., Yuan, J., Wen, Y., Xu, G., Zhao, J., Cheng, L., Li, J., Wang, X., Wang, F., et al. (2020). Single-cell landscape of bronchoalveolar immune cells in patients with COVID-19. *Nat. Med.* 26, 842–844.
- Lu, T., Ang, C.E., and Zhuang, X. (2022). Spatially resolved epigenomic profiling of single cells in complex tissues. *Cell*.
- Lucas, C., Wong, P., Klein, J., Castro, T.B.R., Silva, J., Sundaram, M., Ellingson, M.K., Mao, T., Oh, J.E., Israelow, B., et al. (2020). Longitudinal analyses reveal immunological misfiring in severe COVID-19. *Nature* 584, 463–469.
- Ludwig, L.S., Lareau, C.A., Ulirsch, J.C., Christian, E., Muus, C., Li, L.H., Pelka, K., Ge, W., Oren, Y., Brack, A., et al. (2019). Lineage Tracing in Humans Enabled by Mitochondrial Mutations and Single-Cell Genomics. *Cell* 176, 1325–1339.e22.
- Luecken, M.D., Büttner, M., Chaichoompu, K., Danese, A., Interlandi, M., Mueller, M.F., Strobl, D.C., Zappia, L., Dugas, M., Colomé-Tatché, M., et al. (2022). Benchmarking atlas-level data integration in single-cell genomics. *Nat. Methods* 19, 41–50.
- Luo, H., Xia, X., Huang, L.-B., An, H., Cao, M., Kim, G.D., Chen, H.-N., Zhang, W.-H., Shu, Y., Kong, X., et al. (2022). Pan-cancer single-cell analysis reveals the heterogeneity and plasticity of cancer-associated fibroblasts in the tumor microenvironment. *Nat. Commun.* 13, 6619.
- Macosko, E.Z., Basu, A., Satija, R., Nemes, J., Shekhar, K., Goldman, M., Tirosh, I., Bialas, A.R., Kamitaki, N., Martersteck, E.M., et al. (2015). Highly Parallel Genome-wide Expression Profiling of Individual Cells Using Nanoliter Droplets. *Cell* 161, 1202–1214.
- Madhavan, M., Ritchie, A.J., Aboagye, J., Jenkin, D., Provstgaard-Morys, S., Tarbet, I., Woods, D., Davies, S., Baker, M., Platt, A., et al. (2022). Tolerability and immunogenicity of an intranasally-administered adenovirus-vectored COVID-19 vaccine: An open-label partially-randomised ascending dose phase I trial. *EBioMedicine* 104298.
- Mann, E.R., Menon, M., Knight, S.B., Konkel, J.E., Jagger, C., Shaw, T.N., Krishnan, S., Rattray, M., Ustianowski, A., Bakerly, N.D., et al. (2020). Longitudinal immune profiling reveals key myeloid signatures associated with COVID-19. *Sci. Immunol.* 5.
- Manz, M.G., and Boettcher, S. (2014). Emergency granulopoiesis. *Nat. Rev. Immunol.* 14, 302–314.
- Mare, T.A., Treacher, D.F., Shankar-Hari, M., Beale, R., Lewis, S.M., Chambers, D.J., and Brown, K.A. (2015). The diagnostic and prognostic significance of monitoring blood levels of immature neutrophils in patients with systemic inflammation. *Crit. Care* 19, 57.

- Martin, J.C., Chang, C., Boschetti, G., Ungaro, R., Giri, M., Grout, J.A., Gettler, K., Chuang, L.-S., Nayar, S., Greenstein, A.J., et al. (2019). Single-Cell Analysis of Crohn's Disease Lesions Identifies a Pathogenic Cellular Module Associated with Resistance to Anti-TNF Therapy. *Cell* 178, 1493–1508.e20.
- Mass, E., Ballesteros, I., Farlik, M., Halbritter, F., Günther, P., Crozet, L., Jacome-Galarza, C.E., Händler, K., Klughammer, J., Kobayashi, Y., et al. (2016). Specification of tissue-resident macrophages during organogenesis. *Science* 353.
- Mathew, N.R., Jayanthan, J.K., Smirnov, I.V., Robinson, J.L., Axelsson, H., Nakka, S.S., Emmanouilidi, A., Czarnewski, P., Yewdell, W.T., Schön, K., et al. (2021). Single-cell BCR and transcriptome analysis after influenza infection reveals spatiotemporal dynamics of antigen-specific B cells. *Cell Rep.* 35, 109286.
- Meers, M.P., Llagas, G., Janssens, D.H., Codomo, C.A., and Henikoff, S. (2022). Multifactorial profiling of epigenetic landscapes at single-cell resolution using Multi-Tag. *Nat. Biotechnol.*
- Mehandru, S., and Merad, M. (2022). Pathological sequelae of long-haul COVID. *Nat. Immunol.* 23, 194–202.
- Mehta, P., McAuley, D.F., Brown, M., Sanchez, E., Tattersall, R.S., Manson, J.J., and HLH Across Speciality Collaboration, UK (2020). COVID-19: consider cytokine storm syndromes and immunosuppression. *Lancet* 395, 1033–1034.
- Melms, J.C., Biermann, J., Huang, H., Wang, Y., Nair, A., Tagore, S., Katsyv, I., Rendeiro, A.F., Amin, A.D., Schapiro, D., et al. (2021). A molecular single-cell lung atlas of lethal COVID-19. *Nature* 595, 114–119.
- Merad, M., and Martin, J.C. (2020). Pathological inflammation in patients with COVID-19: a key role for monocytes and macrophages. *Nat. Rev. Immunol.* 20, 355–362.
- Merad, M., Blish, C.A., Sallusto, F., and Iwasaki, A. (2022). The immunology and immunopathology of COVID-19. *Science* 375, 1122–1127.
- Mereu, E., Lafzi, A., Moutinho, C., Ziegenhain, C., McCarthy, D.J., Álvarez-Varela, A., Batlle, E., Sagar, Grün, D., Lau, J.K., et al. (2020). Benchmarking single-cell RNA-sequencing protocols for cell atlas projects. *Nat. Biotechnol.* 38, 747–755.
- Mitroulis, I., Ruppova, K., Wang, B., Chen, L.-S., Grzybek, M., Grinenko, T., Eugster, A., Troullinaki, M., Palladini, A., Kourtzelis, I., et al. (2018). Modulation of myelopoiesis progenitors is an integral component of trained immunity. *Cell* 172, 147–161.e12.
- Monneret, G., Benlyamani, I., Gossez, M., Bermejo-Martin, J.F., Martín-Fernandez, M., Sesques, P., Wallet, F., and Venet, F. (2020). COVID-19: What type of cytokine storm are we dealing with? *J. Med. Virol.*
- Montaldo, E., Lusito, E., Bianchessi, V., Caronni, N., Scala, S., Basso-Ricci, L., Cantaffa, C., Masserdotti, A., Barilaro, M., Barresi, S., et al. (2022). Cellular and transcriptional dynamics of human neutrophils at steady state and upon stress. *Nat. Immunol.* 23, 1470–1483.
- Morabito, S., Miyoshi, E., Michael, N., Shahin, S., Martini, A.C., Head, E., Silva, J., Leavy, K., Perez-Rosendahl, M., and Swarup, V. (2021). Single-nucleus chromatin accessibility and transcriptomic characterization of Alzheimer's disease. *Nat. Genet.* 53, 1143–1155.
- Moses, L., and Pachter, L. (2022). Museum of spatial transcriptomics. *Nat. Methods* 19, 534–546.

- Moss, P. (2022). The T cell immune response against SARS-CoV-2. *Nat. Immunol.* 23, 186–193.
- Mullard, A. (2021). Long COVID's long R&D agenda. *Nat. Rev. Drug Discov.*
- Muus, C., Luecken, M.D., Eraslan, G., Sikkema, L., Waghray, A., Heimberg, G., Kobayashi, Y., Vaishnav, E.D., Subramanian, A., Smillie, C., et al. (2021). Single-cell meta-analysis of SARS-CoV-2 entry genes across tissues and demographics. *Nat. Med.* 27, 546–559.
- Narasaraju, T., Yang, E., Samy, R.P., Ng, H.H., Poh, W.P., Liew, A.-A., Phoon, M.C., van Rooijen, N., and Chow, V.T. (2011). Excessive neutrophils and neutrophil extracellular traps contribute to acute lung injury of influenza pneumonitis. *Am. J. Pathol.* 179, 199–210.
- Nauseef, W.M., and Borregaard, N. (2014). Neutrophils at work. *Nat. Immunol.* 15, 602–611.
- Netea, M.G., Domínguez-Andrés, J., Barreiro, L.B., Chavakis, T., Divangahi, M., Fuchs, E., Joosten, L.A.B., van der Meer, J.W.M., Mhlanga, M.M., Mulder, W.J.M., et al. (2020). Defining trained immunity and its role in health and disease. *Nat. Rev. Immunol.* 20, 375–388.
- Ng, L.G., Ostuni, R., and Hidalgo, A. (2019). Heterogeneity of neutrophils. *Nat. Rev. Immunol.* 19, 255–265.
- Notarbartolo, S., Ranzani, V., Bandera, A., Gruarin, P., Bevilacqua, V., Putignano, A.R., Gobbin, A., Galeota, E., Manara, C., Bombaci, M., et al. (2021). Integrated longitudinal immunophenotypic, transcriptional and repertoire analyses delineate immune responses in COVID-19 patients. *Sci. Immunol.* 6.
- O'Neill, L.A.J., and Netea, M.G. (2020). BCG-induced trained immunity: can it offer protection against COVID-19? *Nat. Rev. Immunol.* 20, 335–337.
- Ochando, J., Mulder, W.J.M., Madsen, J.C., Netea, M.G., and Duivenvoorden, R. (2022). Trained immunity - basic concepts and contributions to immunopathology. *Nat. Rev. Nephrol.*
- Oelen, R., de Vries, D.H., Brugge, H., Gordon, M.G., Vochteloo, M., single-cell eQTLGen consortium, BIOS Consortium, Ye, C.J., Westra, H.-J., Franke, L., et al. (2022). Single-cell RNA-sequencing of peripheral blood mononuclear cells reveals widespread, context-specific gene expression regulation upon pathogenic exposure. *Nat. Commun.* 13, 3267.
- Osuchowski, M.F., Winkler, M.S., Skirecki, T., Cajander, S., Shankar-Hari, M., Lachmann, G., Monneret, G., Venet, F., Bauer, M., Brunkhorst, F.M., et al. (2021). The COVID-19 puzzle: deciphering pathophysiology and phenotypes of a new disease entity. *Lancet Respir. Med.* 9, 622–642.
- Ounzain, S., Micheletti, R., Beckmann, T., Schroen, B., Alexanian, M., Pezzuto, I., Crippa, S., Nemir, M., Sarre, A., Johnson, R., et al. (2015). Genome-wide profiling of the cardiac transcriptome after myocardial infarction identifies novel heart-specific long non-coding RNAs. *Eur. Heart J.* 36, 353–68a.
- Pai, J.A., and Satpathy, A.T. (2021). High-throughput and single-cell T cell receptor sequencing technologies. *Nat. Methods* 18, 881–892.
- Papalex, E., and Satija, R. (2018). Single-cell RNA sequencing to explore immune cell heterogeneity. *Nat. Rev. Immunol.* 18, 35–45.
- Papayannopoulos, V. (2018). Neutrophil extracellular traps in immunity and disease. *Nat. Rev. Immunol.* 18, 134–147.

Payen, D., Cravat, M., Maadadi, H., Didelot, C., Prosic, L., Dupuis, C., Losser, M.-R., and De Carvalho Bittencourt, M. (2020). A Longitudinal Study of Immune Cells in Severe COVID-19 Patients. *Front. Immunol.* 11, 580250.

Pechous, R.D. (2017). With friends like these: the complex role of neutrophils in the progression of severe pneumonia. *Front. Cell Infect. Microbiol.* 7.

Perez, R.K., Gordon, M.G., Subramaniam, M., Kim, M.C., Hartoularos, G.C., Targ, S., Sun, Y., Ogorodnikov, A., Bueno, R., Lu, A., et al. (2022). Single-cell RNA-seq reveals cell type-specific molecular and genetic associations to lupus. *Science* 376, eabf1970.

Qin, C., Zhou, L., Hu, Z., Zhang, S., Yang, S., Tao, Y., Xie, C., Ma, K., Shang, K., Wang, W., et al. (2020). Dysregulation of Immune Response in Patients With Coronavirus 2019 (COVID-19) in Wuhan, China. *Clin. Infect. Dis.* 71, 762–768.

Quackenbush, J. (2006). Microarray analysis and tumor classification. *N. Engl. J. Med.* 354, 2463–2472.

Rajpurkar, P., Chen, E., Banerjee, O., and Topol, E.J. (2022). AI in health and medicine. *Nat. Med.* 28, 31–38.

Reichart, D., Lindberg, E.L., Maatz, H., Miranda, A.M.A., Viveiros, A., Shvetsov, N., Gärtner, A., Nadelmann, E.R., Lee, M., Kanemaru, K., et al. (2022). Pathogenic variants damage cell composition and single cell transcription in cardiomyopathies. *Science* 377, eabo1984.

Ren, X., Wen, W., Fan, X., Hou, W., Su, B., Cai, P., Li, J., Liu, Y., Tang, F., Zhang, F., et al. (2021). COVID-19 immune features revealed by a large-scale single-cell transcriptome atlas. *Cell* 184, 1895–1913.e19.

Reusch, N., De Domenico, E., Bonaguro, L., Schulte-Schrepping, J., Baßler, K., Schultze, J.L., and Aschenbrenner, A.C. (2021). Neutrophils in COVID-19. *Front. Immunol.* 12, 652470.

Robinson, P.C., Liew, D.F.L., Tanner, H.L., Grainger, J.R., Dwek, R.A., Reisler, R.B., Steinman, L., Feldmann, M., Ho, L.-P., Hussell, T., et al. (2022). COVID-19 therapeutics: Challenges and directions for the future. *Proc. Natl. Acad. Sci. USA* 119, e2119893119.

Roche, P.A., and Furuta, K. (2015). The ins and outs of MHC class II-mediated antigen processing and presentation. *Nat. Rev. Immunol.* 15, 203–216.

Rodriguez, P.C., Ernstoff, M.S., Hernandez, C., Atkins, M., Zabaleta, J., Sierra, R., and Ochoa, A.C. (2009). Arginase I-producing myeloid-derived suppressor cells in renal cell carcinoma are a subpopulation of activated granulocytes. *Cancer Res.* 69, 1553–1560.

Roquilly, A., Jacqueline, C., Davieau, M., Mollé, A., Sadek, A., Fourgeux, C., Rooze, P., Broquet, A., Misme-Aucouturier, B., Chaumette, T., et al. (2020). Alveolar macrophages are epigenetically altered after inflammation, leading to long-term lung immunoparalysis. *Nat. Immunol.* 21, 636–648.

Rosenberg, A.B., Roco, C.M., Muscat, R.A., Kuchina, A., Sample, P., Yao, Z., Graybuck, L.T., Peeler, D.J., Mukherjee, S., Chen, W., et al. (2018). Single-cell profiling of the developing mouse brain and spinal cord with split-pool barcoding. *Science* 360, 176–182.

Rozenblatt-Rosen, O., Stubbington, M.J.T., Regev, A., and Teichmann, S.A. (2017). The Human Cell Atlas: from vision to reality. *Nature* 550, 451–453.

Saelens, W., Cannoodt, R., Todorov, H., and Saey, Y. (2019). A comparison of single-cell trajectory inference methods. *Nat. Biotechnol.* 37, 547–554.

Sanchez-Pino, M.D., Richardson, W.S., Zabaleta, J., Puttalingaiah, R.T., Chapple, A.G., Liu, J., Kim, Y., Ponder, M., DeArmitt, R., Baiamonte, L.B., et al. (2022). Increased inflammatory low-density neutrophils in severe obesity and effect of bariatric surgery: Results from case-control and prospective cohort studies. *EBioMedicine* 77, 103910.

De Santo, C., Salio, M., Masri, S.H., Lee, L.Y.-H., Dong, T., Speak, A.O., Porubsky, S., Booth, S., Veerapen, N., Besra, G.S., et al. (2008). Invariant NKT cells reduce the immunosuppressive activity of influenza A virus-induced myeloid-derived suppressor cells in mice and humans. *J. Clin. Invest.* 118, 4036–4048.

Satpathy, A.T., Saligrama, N., Buenrostro, J.D., Wei, Y., Wu, B., Rubin, A.J., Granja, J.M., Lareau, C.A., Li, R., Qi, Y., et al. (2018). Transcript-indexed ATAC-seq for precision immune profiling. *Nat. Med.* 24, 580–590.

Schafflick, D., Xu, C.A., Hartlehnert, M., Cole, M., Schulte-Mecklenbeck, A., Lautwein, T., Wolbert, J., Heming, M., Meuth, S.G., Kuhlmann, T., et al. (2020). Integrated single cell analysis of blood and cerebrospinal fluid leukocytes in multiple sclerosis. *Nat. Commun.* 11, 247.

Schena, M., Shalon, D., Davis, R.W., and Brown, P.O. (1995). Quantitative monitoring of gene expression patterns with a complementary DNA microarray. *Science* 270, 467–470.

Schimke, L.F., Marques, A.H.C., Baiocchi, G.C., de Souza Prado, C.A., Fonseca, D.L.M., Freire, P.P., Rodrigues Praça, D., Salerno Filgueiras, I., Coelho Salgado, R., Jansen-Marques, G., et al. (2022). Severe COVID-19 Shares a Common Neutrophil Activation Signature with Other Acute Inflammatory States. *Cells* 11.

Schoenberger, S.P., Toes, R.E., van der Voort, E.I., Offringa, R., and Melief, C.J. (1998). T-cell help for cytotoxic T lymphocytes is mediated by CD40-CD40L interactions. *Nature* 393, 480–483.

Schulte-Schrepping, J., Ferreira, H.J., Saglam, A., Hinkley, E., and Schultze, J.L. (2020a). Advances in single-cell epigenomics of the immune system. In *Epigenetics of the immune system*, (Elsevier), pp. 185–216.

Schulte-Schrepping, J., Reusch, N., Paclik, D., Baßler, K., Schlickeiser, S., Zhang, B., Krämer, B., Krammer, T., Brumhard, S., Bonaguro, L., et al. (2020b). Severe COVID-19 Is Marked by a Dysregulated Myeloid Cell Compartment. *Cell* 182, 1419–1440.e23.

Schultze, J.L., and Aschenbrenner, A.C. (2021). COVID-19 and the human innate immune system. *Cell* 184, 1671–1692.

Schultze, J.L., Mass, E., and Schlitzer, A. (2019). Emerging Principles in Myelopoiesis at Homeostasis and during Infection and Inflammation. *Immunity* 50, 288–301.

Schultze, J.L., Gabriel, M., and Nicotera, P. (2022). Time for a voluntary crisis research service. *Cell Death Differ.* 29, 888–890.

Scott, C.L., Zheng, F., De Baetselier, P., Martens, L., Saeys, Y., De Prijck, S., Lippens, S., Abels, C., Schoonooghe, S., Raes, G., et al. (2016). Bone marrow-derived monocytes give rise to self-renewing and fully differentiated Kupffer cells. *Nat. Commun.* 7, 10321.

Sette, A., and Crotty, S. (2021). Adaptive immunity to SARS-CoV-2 and COVID-19. *Cell* 184, 861–880.

Shalek, A.K., Satija, R., Shuga, J., Trombetta, J.J., Gennert, D., Lu, D., Chen, P., Gertner, R.S., Gaublotte, J.T., Yosef, N., et al. (2014). Single-cell RNA-seq reveals dynamic paracrine control of cellular variation. *Nature* 510, 363–369.

Shendure, J., Porreca, G.J., Reppas, N.B., Lin, X., McCutcheon, J.P., Rosenbaum, A.M., Wang, M.D., Zhang, K., Mitra, R.D., and Church, G.M. (2005). Accurate multiplex polony sequencing of an evolved bacterial genome. *Science* 309, 1728–1732.

Siemińska, I., Węglarczyk, K., Surmiak, M., Kurowska-Baran, D., Sanak, M., Siedlar, M., and Baran, J. (2021). Mild and Asymptomatic COVID-19 Convalescents Present Long-Term Endotype of Immunosuppression Associated With Neutrophil Subsets Possessing Regulatory Functions. *Front. Immunol.* 12, 748097.

Silvin, A., Chapuis, N., Dunsmore, G., Goubet, A.-G., Dubuisson, A., Derosa, L., Almire, C., Hénon, C., Kosmider, O., Droin, N., et al. (2020). Elevated Calprotectin and Abnormal Myeloid Cell Subsets Discriminate Severe from Mild COVID-19. *Cell* 182, 1401–1418.e18.

Sinha, S., Rosin, N.L., Arora, R., Labit, E., Jaffer, A., Cao, L., Farias, R., Nguyen, A.P., de Almeida, L.G.N., Dufour, A., et al. (2022). Dexamethasone modulates immature neutrophils and interferon programming in severe COVID-19. *Nat. Med.* 28, 201–211.

Smillie, C.S., Biton, M., Ordovas-Montanes, J., Sullivan, K.M., Burgin, G., Graham, D.B., Herbst, R.H., Rogel, N., Slyper, M., Waldman, J., et al. (2019). Intra- and Inter-cellular Rewiring of the Human Colon during Ulcerative Colitis. *Cell* 178, 714–730.e22.

Song, C.-Y., Xu, J., He, J.-Q., and Lu, Y.-Q. (2020a). COVID-19 early warning score: a multi-parameter screening tool to identify highly suspected patients. *medRxiv*.

Song, X., Hu, W., Yu, H., Zhao, L., Zhao, Y., Zhao, X., Xue, H.-H., and Zhao, Y. (2020b). Little to no expression of angiotensin-converting enzyme-2 on most human peripheral blood immune cells but highly expressed on tissue macrophages. *Cytometry A*.

Spinetti, T., Hirzel, C., Fux, M., Walti, L.N., Schober, P., Stueber, F., Luedi, M.M., and Schefold, J.C. (2020). Reduced Monocytic Human Leukocyte Antigen-DR Expression Indicates Immunosuppression in Critically Ill COVID-19 Patients. *Anesth. Analg.* 131, 993–999.

Stensballe, L.G., Nante, E., Jensen, I.P., Kofoed, P.-E., Poulsen, A., Jensen, H., Newport, M., Marchant, A., and Aaby, P. (2005). Acute lower respiratory tract infections and respiratory syncytial virus in infants in Guinea-Bissau: a beneficial effect of BCG vaccination for girls community based case-control study. *Vaccine* 23, 1251–1257.

Stephenson, E., Reynolds, G., Botting, R.A., Calero-Nieto, F.J., Morgan, M.D., Tuong, Z.K., Bach, K., Sungnak, W., Worlock, K.B., Yoshida, M., et al. (2021). Single-cell multi-omics analysis of the immune response in COVID-19. *Nat. Med.*

Su, Y., Chen, D., Yuan, D., Lausted, C., Choi, J., Dai, C.L., Voillet, V., Duvvuri, V.R., Scherler, K., Troisch, P., et al. (2020). Multi-Omics Resolves a Sharp Disease-State Shift between Mild and Moderate COVID-19. *Cell* 183, 1479–1495.e20.

Sungnak, W., Huang, N., Bécavin, C., Berg, M., Queen, R., Litvinukova, M., Talavera-López, C., Maatz, H., Reichart, D., Sampaziotis, F., et al. (2020). SARS-CoV-2 entry factors are highly expressed in nasal epithelial cells together with innate immune genes. *Nat. Med.* 26, 681–687.

Svensson, V., Vento-Tormo, R., and Teichmann, S.A. (2018). Exponential scaling of single-cell RNA-seq in the past decade. *Nat. Protoc.* 13, 599–604.

Szabo, P.A., Dogra, P., Gray, J.I., Wells, S.B., Connors, T.J., Weisberg, S.P., Krupka, I., Matsumoto, R., Poon, M.M.L., Idzikowski, E., et al. (2021). Longitudinal profiling of respiratory and systemic immune

responses reveals myeloid cell-driven lung inflammation in severe COVID-19. *Immunity* 54, 797–814.e6.

Tan, W., Zhao, X., Ma, X., Wang, W., Niu, P., Xu, W., Gao, G.F., and Wu, G. (2020). A Novel Coronavirus Genome Identified in a Cluster of Pneumonia Cases - Wuhan, China 2019-2020. *China CDC Wkly* 2, 61–62.

Tang, F., Barbacioru, C., Wang, Y., Nordman, E., Lee, C., Xu, N., Wang, X., Bodeau, J., Tuch, B.B., Siddiqui, A., et al. (2009). mRNA-Seq whole-transcriptome analysis of a single cell. *Nat. Methods* 6, 377–382.

Tavukcuoglu, E., Horzum, U., Cagkan Inkaya, A., Unal, S., and Esendagli, G. (2021). Functional responsiveness of memory T cells from COVID-19 patients. *Cell Immunol.* 365, 104363.

Tay, S.H., Celhar, T., and Fairhurst, A.-M. (2020). Low-Density Neutrophils in Systemic Lupus Erythematosus. *Arthritis Rheumatol.* 72, 1587–1595.

Tedore, C., and Nilsson, D.-E. (2019). Avian UV vision enhances leaf surface contrasts in forest environments. *Nat. Commun.* 10, 238.

Thierry, A.R. (2020). Anti-protease Treatments Targeting Plasmin(ogen) and Neutrophil Elastase May Be Beneficial in Fighting COVID-19. *Physiol. Rev.* 100, 1597–1598.

Thion, M.S., Low, D., Silvin, A., Chen, J., Grisel, P., Schulte-Schrepping, J., Blecher, R., Ulas, T., Squarzone, P., Hoeffel, G., et al. (2018). Microbiome Influences Prenatal and Adult Microglia in a Sex-Specific Manner. *Cell* 172, 500–516.e16.

Tian, Y., Carpp, L.N., Miller, H.E.R., Zager, M., Newell, E.W., and Gottardo, R. (2022). Single-cell immunology of SARS-CoV-2 infection. *Nat. Biotechnol.* 40, 30–41.

Tirosh, I., Izar, B., Prakadan, S.M., Wadsworth, M.H., Treacy, D., Trombetta, J.J., Rotem, A., Rodman, C., Lian, C., Murphy, G., et al. (2016). Dissecting the multicellular ecosystem of metastatic melanoma by single-cell RNA-seq. *Science* 352, 189–196.

Tregoning, J.S., Flight, K.E., Higham, S.L., Wang, Z., and Pierce, B.F. (2021). Progress of the COVID-19 vaccine effort: viruses, vaccines and variants versus efficacy, effectiveness and escape. *Nat. Rev. Immunol.* 21, 626–636.

Tsilika, M., Taks, E., Dolianitis, K., Kotsaki, A., Leventogiannis, K., Damoulari, C., Kostoula, M., Paneta, M., Adamis, G., Papanikolaou, I., et al. (2022). ACTIVATE-2: A Double-Blind Randomized Trial of BCG Vaccination Against COVID-19 in Individuals at Risk. *Front. Immunol.* 13, 873067.

van de Veerdonk, F.L., Giamarellos-Bourboulis, E., Pickkers, P., Derde, L., Leavis, H., van Crevel, R., Engel, J.J., Wiersinga, W.J., Vlaar, A.P.J., Shankar-Hari, M., et al. (2022). A guide to immunotherapy for COVID-19. *Nat. Med.* 28, 39–50.

van der Wijst, M.G.P., Vazquez, S.E., Hartoularos, G.C., Bastard, P., Grant, T., Bueno, R., Lee, D.S., Greenland, J.R., Sun, Y., Perez, R., et al. (2021). Type I interferon autoantibodies are associated with systemic immune alterations in patients with COVID-19. *Sci. Transl. Med.* 13, eabh2624.

Varga, Z., Flammer, A.J., Steiger, P., Haberecker, M., Andermatt, R., Zinkernagel, A.S., Mehra, M.R., Schuepbach, R.A., Ruschitzka, F., and Moch, H. (2020). Endothelial cell infection and endotheliitis in COVID-19. *Lancet* 395, 1417–1418.

Veras, F.P., Pontelli, M.C., Silva, C.M., Toller-Kawahisa, J.E., de Lima, M., Nascimento, D.C., Schneider, A.H., Caetité, D., Tavares, L.A., Paiva, I.M., et al. (2020). SARS-CoV-2-triggered neutrophil extracellular traps mediate COVID-19 pathology. *J. Exp. Med.* 217, e20201129.

Vollbrecht, T., Stirner, R., Tufman, A., Roider, J., Huber, R.M., Bogner, J.R., Lechner, A., Bourquin, C., and Draenert, R. (2012). Chronic progressive HIV-1 infection is associated with elevated levels of myeloid-derived suppressor cells. *AIDS* 26, 31–37.

Wang, F., Hou, H., Yao, Y., Wu, S., Huang, M., Ran, X., Zhou, H., Liu, Z., and Sun, Z. (2020). Systemically comparing host immunity between survived and deceased COVID-19 patients. *Cell Mol Immunol* 17, 875–877.

Wang, Y., Yuan, P., Yan, Z., Yang, M., Huo, Y., Nie, Y., Zhu, X., Qiao, J., and Yan, L. (2021). Single-cell multiomics sequencing reveals the functional regulatory landscape of early embryos. *Nat. Commun.* 12, 1247.

Wang, Z., Gerstein, M., and Snyder, M. (2009). RNA-Seq: a revolutionary tool for transcriptomics. *Nat. Rev. Genet.* 10, 57–63.

Wardhana, Datau, E.A., Sultana, A., Mandang, V.V.V., and Jim, E. (2011). The efficacy of Bacillus Calmette-Guerin vaccinations for the prevention of acute upper respiratory tract infection in the elderly. *Acta Med. Indones.* 43, 185–190.

Warnat-Herresthal, S., Perrakis, K., Taschler, B., Becker, M., Baßler, K., Beyer, M., Günther, P., Schulte-Schrepping, J., Seep, L., Klee, K., et al. (2020). Scalable Prediction of Acute Myeloid Leukemia Using High-Dimensional Machine Learning and Blood Transcriptomics. *iScience* 23, 100780.

Warnat-Herresthal, S., Schultze, H., Shastry, K.L., Manamohan, S., Mukherjee, S., Garg, V., Sarveswara, R., Händler, K., Pickkers, P., Aziz, N.A., et al. (2021). Swarm Learning for decentralized and confidential clinical machine learning. *Nature* 594, 265–270.

Wauters, E., Van Mol, P., Garg, A.D., Jansen, S., Van Herck, Y., Vanderbeke, L., Bassez, A., Boeckx, B., Malengier-Devlies, B., Timmerman, A., et al. (2021). Discriminating mild from critical COVID-19 by innate and adaptive immune single-cell profiling of bronchoalveolar lavages. *Cell Res.* 0, 1–19.

Wendisch, D., Dietrich, O., Mari, T., von Stillfried, S., Ibarra, I.L., Mittermaier, M., Mache, C., Chua, R.L., Knoll, R., Timm, S., et al. (2021). SARS-CoV-2 infection triggers profibrotic macrophage responses and lung fibrosis. *Cell* 184, 6243–6261.e27.

Wiesel, M., Kratky, W., and Oxenius, A. (2011). Type I IFN substitutes for T cell help during viral infections. *J. Immunol.* 186, 754–763.

Wilk, A.J., Rustagi, A., Zhao, N.Q., Roque, J., Martínez-Colón, G.J., McKechnie, J.L., Ivison, G.T., Ranganath, T., Vergara, R., Hollis, T., et al. (2020). A single-cell atlas of the peripheral immune response in patients with severe COVID-19. *Nat. Med.* 26, 1070–1076.

Wilk, A.J., Lee, M.J., Wei, B., Parks, B., Pi, R., Martínez-Colón, G.J., Ranganath, T., Zhao, N.Q., Taylor, S., Becker, W., et al. (2021). Multi-omic profiling reveals widespread dysregulation of innate immunity and hematopoiesis in COVID-19. *J. Exp. Med.* 218.

Winheim, E., Rinke, L., Lutz, K., Reischer, A., Leutbecher, A., Wolfram, L., Rausch, L., Kranich, J., Wrátil, P.R., Huber, J.E., et al. (2021). Impaired function and delayed regeneration of dendritic cells in COVID-19. *PLoS Pathog.* 17, e1009742.

Winterbourn, C.C., Kettle, A.J., and Hampton, M.B. (2016). Reactive oxygen species and neutrophil function. *Annu. Rev. Biochem.* 85, 765–792.

Wu, R., and Murphy, K.M. (2022). DCs at the center of help: Origins and evolution of the three-cell-type hypothesis. *J. Exp. Med.* 219.

Wu, T., Hu, E., Xu, S., Chen, M., Guo, P., Dai, Z., Feng, T., Zhou, L., Tang, W., Zhan, L., et al. (2021). clusterProfiler 4.0: A universal enrichment tool for interpreting omics data. *Innovation (Camb)* 2, 100141.

Xue, J., Schmidt, S.V., Sander, J., Draffehn, A., Krebs, W., Quester, I., De Nardo, D., Gohel, T.D., Emde, M., Schmidleithner, L., et al. (2014). Transcriptome-based network analysis reveals a spectrum model of human macrophage activation. *Immunity* 40, 274–288.

Yang, A.C., Vest, R.T., Kern, F., Lee, D.P., Agam, M., Maat, C.A., Losada, P.M., Chen, M.B., Schaum, N., Khoury, N., et al. (2022). A human brain vascular atlas reveals diverse mediators of Alzheimer's risk. *Nature* 603, 885–892.

Zappia, L., and Theis, F.J. (2021). Over 1000 tools reveal trends in the single-cell RNA-seq analysis landscape. *Genome Biol.* 22, 301.

Zhang, J.-Y., Wang, X.-M., Xing, X., Xu, Z., Zhang, C., Song, J.-W., Fan, X., Xia, P., Fu, J.-L., Wang, S.-Y., et al. (2020a). Single-cell landscape of immunological responses in patients with COVID-19. *Nat. Immunol.* 21, 1107–1118.

Zhang, Q., Bastard, P., Liu, Z., Le Pen, J., Moncada-Velez, M., Chen, J., Ogishi, M., Sabli, I.K.D., Hodeib, S., Korol, C., et al. (2020b). Inborn errors of type I IFN immunity in patients with life-threatening COVID-19. *Science* 370.

Zhao, J.L., and Baltimore, D. (2015). Regulation of stress-induced hematopoiesis. *Curr Opin Hematol* 22, 286–292.

Zhao, Z., Xie, J., Yin, M., Yang, Y., He, H., Jin, T., Li, W., Zhu, X., Xu, J., Zhao, C., et al. (2020). Clinical and Laboratory Profiles of 75 Hospitalized Patients with Novel Coronavirus Disease 2019 in Hefei, China. *medRxiv*.

Zheng, L., Qin, S., Si, W., Wang, A., Xing, B., Gao, R., Ren, X., Wang, L., Wu, X., Zhang, J., et al. (2021). Pan-cancer single-cell landscape of tumor-infiltrating T cells. *Science* 374, abe6474.

Ziegler, C.G.K., Allon, S.J., Nyquist, S.K., Mbanjo, I.M., Miao, V.N., Tzouanas, C.N., Cao, Y., Yousif, A.S., Bals, J., Hauser, B.M., et al. (2020). SARS-CoV-2 Receptor ACE2 Is an Interferon-Stimulated Gene in Human Airway Epithelial Cells and Is Detected in Specific Cell Subsets across Tissues. *Cell* 181, 1016–1035.e19.

7. Appendix A-C

Appendix A:

Optimized workflow for single-cell transcriptomics on infectious diseases including COVID-19

De Domenico E*, Bonaguro L*, **Schulte-Schrepping J***, Becker M, Händler K, Schultze JL., *STAR Protoc.* 2020 Dec 16;1(3):100233. doi: 10.1016/j.xpro.2020.100233. eCollection 2020 Dec 18.

Appendix B:

Severe COVID-19 Is Marked by a Dysregulated Myeloid Cell Compartment

Schulte-Schrepping J*, Reusch N*, Paclik D*, Baßler K*, Schlickeiser S*, Zhang B*, Krämer B*, Krammer T*, Brumhard S*, Bonaguro L*, De Domenico E*, Wendisch D*, Grasshoff M, Kapellos TS, Beckstette M, Pecht T, Saglam A, Dietrich O, Mei HE, Schulz AR, Conrad C, Kunkel D, Vafadarnejad E, Xu C-J, Horne A, Herbert M, Drews A, Thibeault C, Pfeiffer M, Hippenstiel S, Hocke A, Müller-Redetzky H, Heim K-M, Machleidt F, Uhrig A, Bosquillon de Jarcy L, Jürgens L, Stegemann M, Glösenkamp CR, Volk H-D, Goffinet C, Landthaler M, Wyler E, Georg P, Schneider M, Dang-Heine C, Neuwinger N, Kappert K, Tauber R, Corman V, Raabe R, Kaiser KM, To Vinh M, Rieke G, Meisel C, Ulas T, Becker M, Geffers R, Witzernath M, Drosten C, Suttorp N, von Kalle C, Kurth F, Händler K, Schultze JL, Aschenbrenner AC, Li Y, Nattermann J, Sawitzki B, Saliba A-E, Sander LE, Deutsche COVID-19 OMICS Initiative (DeCOI), *Cell* 2020 Aug 5; S0092-8674(20)30992-2. doi: 10.1016/j.cell.2020.08.001.

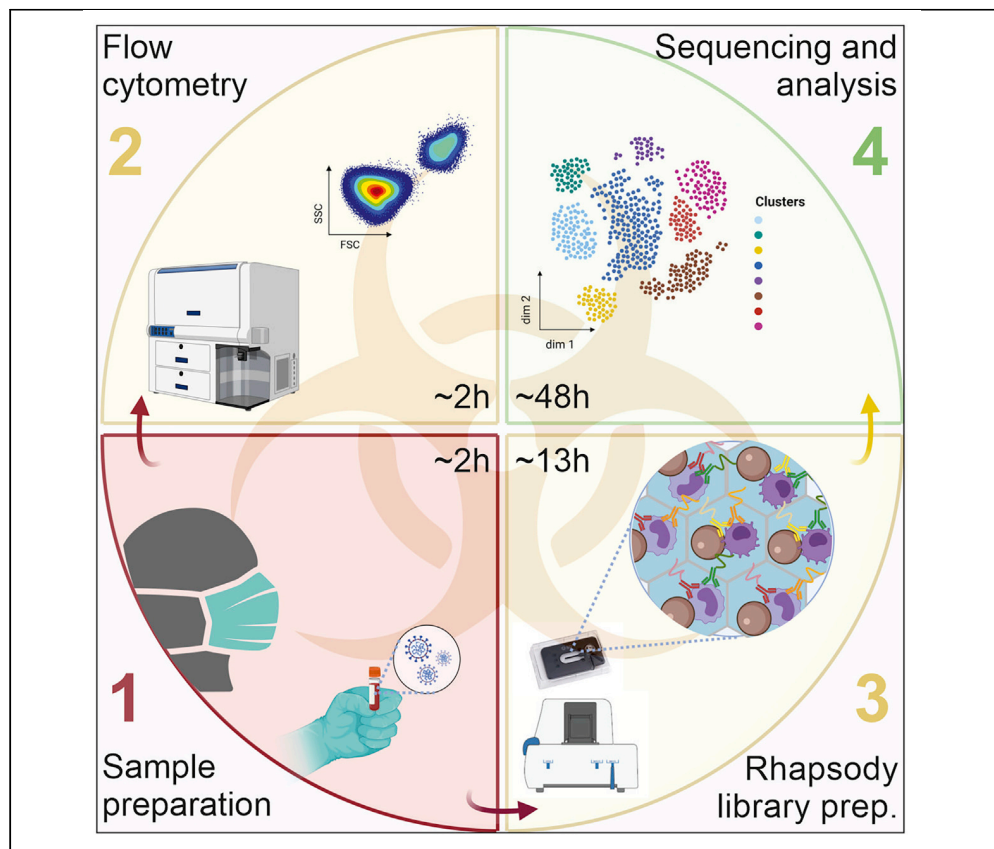
Appendix C:

CD4+ T cell calibration of antigen-presenting cells optimizes antiviral CD8+ T cell immunity

Gressier E*, **Schulte-Schrepping J***, Petrov L, Brumhard S, Stubbemann P, Hiller A, Obermayer B, Spitzer J, Kostevc T, Whitney PG, Bachem PG, Odainic A, van de Sandt C, Nguyen THO, Ashhurst T, Wilson K, Oates CVL, Gearing LJ, Meischel T, Hochheiser K, Greyer M, Clarke M, Kreutzenbeck M, Gabriel SS, Kastenmüller W, Kurts C, Londrigan SL, Kallies A, Kedzierska K, Hertzog PJ, Latz E, Chen YCE, Radford KJ, Chopin M, Schroeder J, Kurth F, Gebhardt R, Sander LE, Sawitzki B, Schultze JL, Schmidt SV, Bedoui S, *Nat Immunol* **24**, 979–990 (2023). doi: 10.1038/s41590-023-01517-x

Protocol

Optimized workflow for single-cell transcriptomics on infectious diseases including COVID-19



In December 2019, a new coronavirus, SARS-CoV-2, which causes the respiratory illness that led to the COVID-19 pandemic, was reported. In the face of such a new pathogen, special precautions must be taken to examine potentially infectious materials due to the lack of knowledge on disease transmissibility, infectivity, and molecular pathogenicity. Here, we present a complete and safe workflow for performing scRNA-seq experiments on blood samples of infected patients from cell isolation to data analysis using the micro-well based BD Rhapsody platform.

Elena De Domenico,
Lorenzo Bonaguro,
Jonas
Schulte-Schrepping,
Matthias Becker,
Kristian Händler,
Joachim L. Schultze
j.schultze@uni-bonn.de

HIGHLIGHTS

Complete, safe protocol for handling potentially infectious blood samples for scRNA-seq

scRNA-seq application including sample multiplexing and AbSeq protein quantification

Guidelines for flow cytometry analyses of potentially infectious blood samples

Recommendations and code for processing and analysis of multiplexed scRNA-seq data

De Domenico et al., STAR Protocols 1, 100233
December 18, 2020 © 2020 The Author(s).
<https://doi.org/10.1016/j.xpro.2020.100233>

Protocol

Optimized workflow for single-cell transcriptomics on infectious diseases including COVID-19

Elena De Domenico,^{1,2,4,5} Lorenzo Bonaguro,^{2,3,4} Jonas Schulte-Schrepping,^{2,3,4} Matthias Becker,^{1,2} Kristian Händler,^{1,2} and Joachim L. Schultze^{1,2,3,6,*}

¹German Center for Neurodegenerative Diseases (DZNE), PRECISE Platform for Genomics and Epigenomics at DZNE, and University of Bonn, Bonn, Germany

²Systems Medicine, German Center for Neurodegenerative Diseases (DZNE), Bonn, Germany

³Genomics and Immunoregulation, Life & Medical Sciences (LIMES) Institute, University of Bonn, Bonn, Germany

⁴These authors contributed equally

⁵Technical contact

⁶Lead contact

*Correspondence: j.schultze@uni-bonn.de
<https://doi.org/10.1016/j.xpro.2020.100233>

SUMMARY

In December 2019, a new coronavirus, SARS-CoV-2, which causes the respiratory illness that led to the COVID-19 pandemic, was reported. In the face of such a new pathogen, special precautions must be taken to examine potentially infectious materials due to the lack of knowledge on disease transmissibility, infectivity, and molecular pathogenicity. Here, we present a complete and safe workflow for performing scRNA-seq experiments on blood samples of infected patients from cell isolation to data analysis using the micro-well based BD Rhapsody platform.

For complete information on the use and execution of this protocol, please refer to Schulte-Schrepping et al. (2020).

BEFORE YOU BEGIN**Study subject details and written informed consent**

The original study following this protocol, Schulte-Schrepping et al. (2020), was approved by the Institutional Review board of the University Hospital Bonn (073/19 and 134/20). After providing written informed consent, control donors and COVID-19 patients were included in the study. In patients who were not able to consent at the time of study enrollment, consent was obtained after recovery.

Prepare working area

This protocol must be performed in a Biosafety level 2 laboratory. The initial part of the protocol must be done in a laminar flow hood and special precautions must be taken to avoid any potential risk working with samples from COVID-19 patients. It is important to realize that as soon as samples from COVID-19 patients are handled under the hood everything is considered potentially contaminated and should be treated as such. In order to minimize handling of potentially contaminated materials outside of the hood it is critical to organize the working area (Figure 1) and disinfect both hands and materials with Sterillium and Terralin respectively before taking them out of the hood.

Prepare cell culture hood and materials

Refer to “Materials and equipment” for the list of materials to be prepared before the experiment.





Figure 1. Working area

Prepare solutions

Refer to “[Materials and equipment](#)” for the list of buffers and solutions to be prepared before the experiment. Prepare all necessary buffers and working dilutions in advance to avoid possible contaminations of the stock solutions.

General precautions

Up to the cell lyses the samples are considered infected and potentially infectious. Therefore, special precautions need to be taken when steps must be performed outside of the laminar flow hood. In this section we present how to safely perform cell counting and centrifugation steps.

1. Spinning samples

- a. Have a centrifuge bucket and lid ready in the hood

Note: Everything inside the bucket is possibly contaminated. Do not open it outside of the hood. Leave the balance bucket outside the hood to avoid contaminations.

- b. Close your tube and place it in the centrifuge bucket, close the lid
- c. Disinfect your hands with Sterillium and wipe the outside of the bucket with Terralin PAA
- d. You can now spin outside the hood
- e. Bring closed bucket back under the hood for subsequent sample processing

2. Counting cells

- a. Prepare Eppendorf tubes with ready to use Trypan blue solution (0.4%) according to the desired ratio (1:10) outside of the hood beforehand and place them in the hood
- b. Mix the cell sample with the Trypan blue solution (0.4%) according to the chosen ratio (1:10) under the cell culture hood
- c. Load cell suspension on a single-use counting chamber
- d. Place the counting chambers in the 4-well dish
- e. Close the 4-well dish with its lid and seal the dish with tape ([Figure 2](#))
- f. Disinfect your hands with Sterillium and wipe the plate with Terralin PAA
- g. You can now count your cells outside hood

Note: Do not take the counting chamber out of the plate at any time outside of the hood. The cell counting procedure at the microscope can be performed leaving the counting chamber inside the plate ([Figure 3](#)).

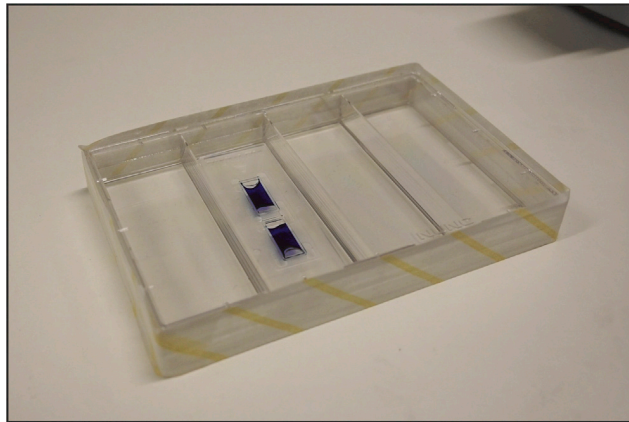


Figure 2. Counting chamber in the 4-well dish

- h. After cell counting, bring back the plate under the hood
3. Clean up
 - a. Disinfect all materials that must be moved out of the hood with Terralin PAA before discarding them
 - b. Prepare a decontamination bath with Terralin PAA for decontaminating the centrifuge buckets and lids for at least 10 min
- △ **CRITICAL: Open bucket under water in the decontamination bath so that the Terralin PAA covers all surfaces.**
- c. Discard the liquid waste flask in a labeled autoclave bag and close the bag properly for autoclaving
 - d. Leave the 2 liter Terralin PAA cylinder flask with the used serological pipettes under the hood for 24 h. After decontamination, the pipettes can be discarded in a bag for autoclaving and the Terralin PAA can be discarded safely into a sink

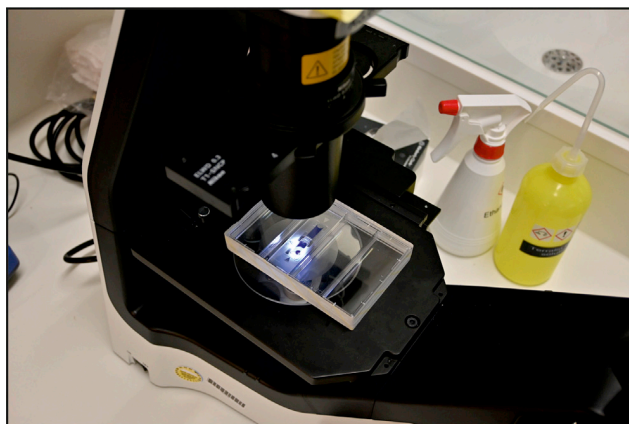


Figure 3. Microscope setup for cell counting

KEY RESOURCES TABLE

REAGENT or RESOURCE	SOURCE	IDENTIFIER
Antibodies		
HLA-DR BV421 (L243)	BioLegend	Cat# 307635; RRID:AB_10897449
CD4 BV510 (OKT4)	BioLegend	Cat# 317444; RRID:AB_2561866
CD16 BV605 (3G8)	BioLegend	Cat# 302039; RRID:AB_2561354
CD45 BV711 (HI30)	BioLegend	Cat# 304050; RRID:AB_2563466
CD8 BV785 (SK1)	BioLegend	Cat# 344740; RRID:AB_2566202
CD66b FITC (G10F5)	BioLegend	Cat# 305104; RRID:AB_314496
CD14 PerCp-Cy5.5 (MφP9)	Becton Dickinson	Cat# 562692; RRID:AB_2737726
CD56 PE (MY31)	Becton Dickinson	Cat# 345810; RRID:AB_396511
CD3 PE/Dazzle (UCHT1)	BioLegend	Cat# 300450; RRID:AB_2563618
CD11c PE/Cy5 (B-Iy6)	Becton Dickinson	Cat# 551077; RRID:AB_394034
Siglec8 PE/Cy7 (7C9)	BioLegend	Cat# 347112; RRID:AB_2629720
CD203c APC (NP4D6)	BioLegend	Cat# 324609; RRID:AB_2099774
CD1c AlexaFluor700 (L161)	BioLegend	Cat# 331530; RRID:AB_2563657
CD19 APC/Fire 750 (HIB19)	BioLegend	Cat# 302258; RRID:AB_2629691
Chemicals, peptides, and recombinant proteins		
BD Horizon brilliant stain buffer	Becton Dickinson	Cat# 563794
RBC lysis buffer 10×	BioLegend	Cat# 420301
Trypan blue	Invitrogen	Cat# T10282
Pierce 16% formaldehyde (w/v), methanol-free	Thermo Fisher	Cat# 28908
RPMI 1640 medium	Gibco	Cat# 11875093
Fetal bovine serum	PAN Biotec	Cat# 3302
Pancoll human, density: 1.077 g/mL	Pan Biotec	Cat# P04-601000
Dulbecco's phosphate buffered saline, MO	Sigma-Aldrich	Cat# D8537
FcR blocking reagent, human	Miltenyi	Cat# 130-059-901
Nuclease-free water	Invitrogen	Cat# AM9937
Sterillium	PAUL HARTMANN	Cat# 9800081
Terralin PAA 160 mL (2 × 80 mL)	Schülke	Cat# 126203
Critical commercial assays		
Human single-cell multiplexing kit	Becton Dickinson	Cat# 633781
SPRIselect reagent	Beckman Coulter	Cat# B23318
LIVE/DEAD fixable yellow dead cell stain kit, for 405 nm excitation	Invitrogen	Cat# L34959
BD Rhapsody WTA amplification kit	Becton Dickinson	Cat# 633801
BD Rhapsody cartridge kit	Becton Dickinson	Cat# 633733
BD cartridge reagent kit	Becton Dickinson	Cat# 633731
BD Rhapsody cDNA kit	Becton Dickinson	Cat# 633773
High sensitivity D5000 ScreenTape	Agilent	Cat# 5067-5592
Qubit dsDNA HS assay kit	Thermo Fisher	Cat# Q32854
NovaSeq 6000 S1 reagent kit (100 cycle)	Illumina	Cat# 200012865
NovaSeq 6000 S2 reagent kit (100 cycle)	Illumina	Cat# 20012862
NovaSeq 6000 S2 reagent kit (200 cycles)	Illumina	Cat# 20040326

(Continued on next page)

Continued

REAGENT or RESOURCE	SOURCE	IDENTIFIER
Deposited data		
scRNA-seq raw data	Schulte Schrepping et al., 2020	EGAS00001004571
Processed scRNA-seq count data and code	Schulte Schrepping et al., 2020	https://beta.fastgenomics.org/p/schulte-schrepping_covid19
Software and algorithms		
Bcl2fastq2	Illumina	v2.20
STAR	Dobin et al., 2013	v2.6.1b
Cutadapt	Martin, 2011	v1.16
Dropseq-tools	https://github.com/broadinstitute/Drop-seq/	v2.0.0
Picard	https://github.com/broadinstitute/picard	v2.23.7
R	www.cran.r-project.org	v3.6.2
Seurat (R package)	Butler et al., 2018 ; Stuart et al., 2019	v3.1.2 (CRAN)
Biological samples		
Blood samples from COVID-19 patients	University Hospital Bonn (for details see Schulte Schrepping et al., 2020)	N/A
Other		
Falcon tube (50 mL)	Corning	Cat# CLS430290-500EA
Falcon tube (15 mL)	Corning	Cat# CLS430053-500EA
Improved Neubauer hemocytometer	INCYTO	Cat# DHC-N01-5
Cryovials	Sarstedt	Cat# 72.379.002
4-well dish	Thermo Fisher Scientific	Cat# 267061
Serological pipettes (5, 10, 25 mL)	Santa Cruz	Cat# sc-200283 sc-200281, sc-200283
Thermo Scientific Megafuge 40R with TX-1000 rotor	Thermo Fisher Scientific	N/A
Slide coat TX-1000 buckets with TX-1000 ClickSeal biocontainment lids	Thermo Fisher Scientific	N/A
Adapter BIOFlex HC (15 mL/50 mL)	Thermo Fisher Scientific	N/A
BD Rhapsody Express Single-Cell Analysis System Package	Becton Dickinson	Cat# 633707
TapeStation 4200 system	Agilent	Cat# G2991AA
Invitrogen Qubit fluorometer	Thermo Fisher Scientific	Cat# Q33240
Eppendorf ThermoMixer C	Eppendorf	Cat# 5382000015
Magnetic separation stand (0.2 mL; 5 mL)	V&P Scientific	Cat# VP 772F4-1, VP 772FB-1A, VP 772FB-1
DynaMag-2 magnet	Thermo Fisher Scientific	Cat# 12321D
BD LSRII/Symphony	Becton Dickinson	Special order research product
Light-transmission microscope	Major supplier	N/A
Thermocycler	Major supplier	N/A
Minifuge for PCR TubeStrips	Major supplier	N/A
Illumina NovaSeq 6000	Illumina	Cat# 20012850
Illumina NextSeq 500	Illumina	Cat# SY-415-1001

MATERIALS AND EQUIPMENT

Preparation of buffers and solutions

- **Complete RPMI:** Supplement RPMI1640 medium with 10% FCS (store at 4°C, up to 4 weeks).
- **PFA:** 16% Methanol-free PFA is diluted to a final concentration of 4% in sterile PBS (prepare freshly if possible or store small aliquots at –20°C).

- **RBC lysis Buffer:** 10× RBC lysis buffer stock solution (BioLegend) is diluted to a final concentration of 1× in sterile nuclease-free ddH₂O (prepare freshly).

Preparation of materials and equipment

Here, a list of required materials and equipment is described:

- Reservoirs filled with Terralin PAA solution to rinse tips before discarding into waste bins
- 2 liter Terralin PAA cylinder flask to discard serological pipettes
- Empty waste flask for liquid waste
- Waste bucket with double bag
- Sterillium bottle for disinfection of gloves/hands
- Terralin PAA squeeze bottle to disinfect surfaces and materials
- Stack of dust-free paper towels
- 1,000 μL, 200 μL and 10 μL filter tips and pipettes
- 50 mL Falcons
- Single-use counting chambers
- Cryovials
- 4-well dish
- Pre-cut stripes of tape to seal 4-well dish for counting
- Electric pipette
- 25 mL, 10 mL, and 5 mL serological pipettes
- Aliquots of the media and buffers needed
 - cell culture medium (RPMI1640+10%FBS)
 - PBS
 - BD stain buffer (on ice)
 - BD sample tags (on ice)
 - Trypan blue

Note: Prepare aliquots before starting to work with the samples to avoid contamination of the stock solutions. Volumes of aliquots should be scaled according to number of samples.

- Thermo Scientific Megafuge 40R with TX-1000 rotor
- Slide coat TX-1000 buckets with TX-1000 ClickSeal biocontainment lids and 50 mL and 15 mL Adapter BIOFlex HC

Alternatives: Any refrigerated centrifuge with swinging bucket rotor and buckets with biocontainment lids can be used.

- BD Rhapsody Express instrument
- BD Rhapsody P1200M and P5000M pipettes
- TapeStation 4200 system

Alternatives: The 2100 Bioanalyzer (Agilent technologies) can alternatively be used for fragment distribution analyses.

- Invitrogen Qubit Fluorometer
- Eppendorf ThermoMixer C

Alternatives: Any programmable thermomixer can be used.

- Magnetic separation stands for 5 mL, 1.5 mL and 0.2 mL
- 3-laser flow cytometer (e.g., BD LSRII/Symphony)
- Light-transmission microscope

- Thermocycler
- Minifuge for PCR TubeStrips
- Illumina NovaSeq 6000/NextSeq500

STEP-BY-STEP METHOD DETAILS

Note: If both peripheral blood mononuclear cells (PBMC) isolation and red blood cell lysis are performed from the same sample in parallel, it is necessary to split the samples in 2 aliquots. The respective volumes depend on the starting material and should be adjusted to the required material for downstream applications.

Red blood cell (RBC) lysis

⌚ Timing: 30 min

In this section, the RBC lysis procedure to prepare whole blood samples for scRNA-seq and FACS from blood of COVID-19 patients is described.

1. Preparation of the RBC lysis solution
 - a. Dilute 1:9 the 10× RBC lysis buffer (BioLegend) in sterile ddH₂O freshly before use
2. Red blood cell lysis
 - a. Transfer the blood tube in the biological hood and gently transfer 1 mL of blood to a 50 mL Falcon
 - b. Using a serological pipette carefully add 10 mL of 1× RBC lysis buffer
 - c. Shortly vortex the Falcon and incubate for 10 min between 20°C–22°C
 - d. Dilute the cell solution in RBC lysis buffer by adding 40 mL of PBS
 - e. Centrifuge the cell suspension at 300 × g for 10 min, 4°C, following the above-mentioned safety instructions
 - f. Remove the supernatant and resuspend the cell pellet in the desired volume of PBS
 - g. Count the cells following the above-mentioned safety instructions

PBMC purification using density-gradient centrifugation

⌚ Timing: 1 h

In this section the procedure to purify PBMC from blood of COVID-19 patients is described. Special emphasis will be paid on the necessary steps to avoid contamination of the working area and infection of the experimenter.

3. Preparation of the necessary materials
 - a. For each sample prepare and label two 50 mL Falcons, fill one of the tubes with 10 mL of Pancoll pre-warmed to between 20°C–22°C and one with 20 mL PBS
 - b. Label the tubes with all necessary information (PBS, Pancoll, sample ID, etc.)
4. Pancoll density-gradient centrifugation
 - a. Move the blood tube under the laminar flow hood
 - b. Transfer the content (maximum 20 mL) to a new 50 mL Falcon and add an equal volume of PBS
 - c. Gently overlay the diluted blood onto 10 mL Pancoll (pre-filled tubes) following the manufacturer's protocol
 - d. Centrifuge at 700 × g 25 min, 20°C, without breaks, following the above-mentioned safety instructions

- e. After centrifugation, take the Falcon out of the centrifugation bucket under the hood and carefully collect the PBMC fraction into a 50 mL Falcon pre-filled with PBS using a serological pipette

Note: PBS volume should be two volumes of the expected PBMC fraction; final volume should be adjusted accordingly.

△ CRITICAL: Prevent mixing of the density phases to avoid contamination of the PBMC fraction with erythrocytes and granulocytes.

- f. Centrifuge cells at $300 \times g$ for 10 min, 4°C , following the above-mentioned safety instructions
- g. Remove supernatant and resuspend the PBMC in the desired volume of complete RPMI
- h. Count the cells following the above-mentioned safety instructions

Cryopreservation of PBMC samples (optional)

In this section we describe how to store PBMC samples for long-term sample acquisition and processing for scRNA-seq. Cells are stored in DMSO-supplemented freezing media in liquid nitrogen.

5. Preparation of required media and equipment
 - a. $2\times$ freezing medium: RPMI1640 supplemented with 40% FBS and 20% DMSO
 - b. Resuspension medium: RPMI1640 supplemented with 40% FBS
 - c. Chill a cell freezing container in a 4°C refrigerator
 - d. Cryovials
6. Cryopreservation Protocol
 - a. Prepare and label cryovials, open them, and place them on ice in the hood
 - b. Centrifuge the purified PBMC at $300 \times g$ for 5 min, 4°C , following the above-mentioned safety instructions
 - c. Resuspend the cell pellet in an appropriate volume of chilled resuspension medium to achieve a cell concentration of $\sim 2\text{--}10 \times 10^6$ cells/mL (maintain the cells on ice)
 - d. Gently add an equivalent volume of chilled $2\times$ freezing medium to achieve a cell concentration of $\sim 1\text{--}5 \times 10^6$ cells/mL
 - e. Gently mix the cells
 - f. Dispense 1 mL aliquots of the cell suspension into the cryovials on ice
 - g. Close the cryovials with the corresponding lid
 - h. Remove the chilled cell freezing container from the 4°C refrigerator and place it in the hood
 - i. Wipe each cryovial with Terralin PAA and place inside the cell freezing container
 - j. Wipe the outside of the cell freezing container with Terralin PAA
 - k. Move the container out of the hood and place it in a -80°C freezer for minimum 12 h, ensure that the bottom and top vents of the container are not obstructed to allow adequate air flow
 - l. Transfer the cryovials to liquid nitrogen for long-term storage
7. Thawing procedure:
 - a. Remove cryovial(s) from liquid nitrogen storage and transport immediately on ice in the hood
 - b. Thaw the samples in a reservoir containing water at 37°C for 2–3 min
 - c. Gently transfer thawed cell suspension into an empty 50 mL Falcon using a 1 mL pipette tip (If possible, use wide-bore tips for the complete thawing procedure)
 - d. Rinse the cryovial with 1 mL warm complete RPMI and add the medium dropwise to the 50 mL Falcon containing the cell suspension while gently shaking the Falcon

Note: Dropwise addition of medium allows the cells sufficient time for a gradual loss of DMSO and therefore prevents osmotic lysis.

- e. Serially dilute the cells with complete RPMI a total of 4 times by 1:1 volume addition with approximately 1 min wait between additions (final volume: 32 mL)
- f. Put all 50 mL Falcons in a centrifuge bucket inside the hood and close the lid

- g. Centrifuge cells at $300 \times g$ for 5 min between 20 and 22°C, following the above-mentioned safety instructions
- h. Remove most of the supernatant, leaving ~1 mL and resuspend cell pellet in this volume using a 1 mL pipette tip
- i. Add an additional 4 mL complete growth medium to achieve a total volume of ~5 mL
- j. Proceed to count viable cells as described above and adjust the cell concentration according to the downstream protocol

Oligo-coupled antibody-based sample multiplexing (and optionally AbSeq)

⌚ Timing: from 1 h to 3 h

In this section the staining with universal antibodies conjugated to unique polyadenylated DNA barcodes (sample tags) is described. The use of sample tags allows multiplexing of up to 12 samples reducing potential technical batch effects. Furthermore, multiplexing of samples significantly reduces the time and costs of the library preparation and sequencing processes. After the sample tag labeling, an optional step can be introduced to detect surface protein expression. This protocol is termed AbSeq by BD and is based on a second staining using currently up to 100 selected antibodies conjugated to oligonucleotides (Ab-Oligos) (Figure 4). Cells can be either co-labeled with sample tag and Ab-Oligos concurrently in the same tube or labeled sequentially. The latter allows reducing the cost per sample considerably, but increases both time and the risk to lose cells during the additional washing steps. It is, therefore, critical to take these considerations into account for the experimental design. Here we describe the sequential labeling approach. Considering the potential loss of cells during the extra wash steps, starting with 1 million cells is recommended, but the following protocol also works with low-abundance samples (< 100,000 cells).

8. Labeling samples with sample tag-coupled antibodies
 - a. Transfer 20,000– 2×10^6 cells into 200–500 μL of BD Stain Buffer in a 5 mL Eppendorf tube
 - b. Proceed to spin samples at $300 \times g$ for 5 min, 4°C following the above-mentioned safety instructions
 - c. Resuspend the cell pellet in 190 μL of BD Stain Buffer
 - d. For each sample, transfer the cell suspension to the respective sample tag tube previously aliquoted (see Note) and mix by pipetting only

Note: The original BD Rhapsody protocol uses the whole volume of 20 μL of each sample tag-coupled antibody mix for labeling the samples. However, using 10 μL yielded comparable results.

- e. Incubate the cell suspension between 20°C and 22°C for 20 min
- f. Add 200 μL of BD Stain Buffer to the cell suspension and mix by pipetting
- g. Proceed to spin samples at $300 \times g$ for 5 min, 4°C following the above-mentioned safety instructions
- h. Carefully remove the supernatant with a pipette leaving a small amount of medium to ensure the cell pellet is not disturbed
- i. Resuspend the pellet in 500 μL of BD Stain Buffer
- j. Repeat step 8g and centrifuge the cell suspension at $300 \times g$ for 5 min, 4°C following the above-mentioned safety instructions
- k. Remove the supernatant leaving a small amount of medium and resuspend the pellet in 300 μL of BD Sample Buffer

Note: For low-abundance samples leave ~50 μL of supernatant and resuspend the cells in a total volume of 100 μL .

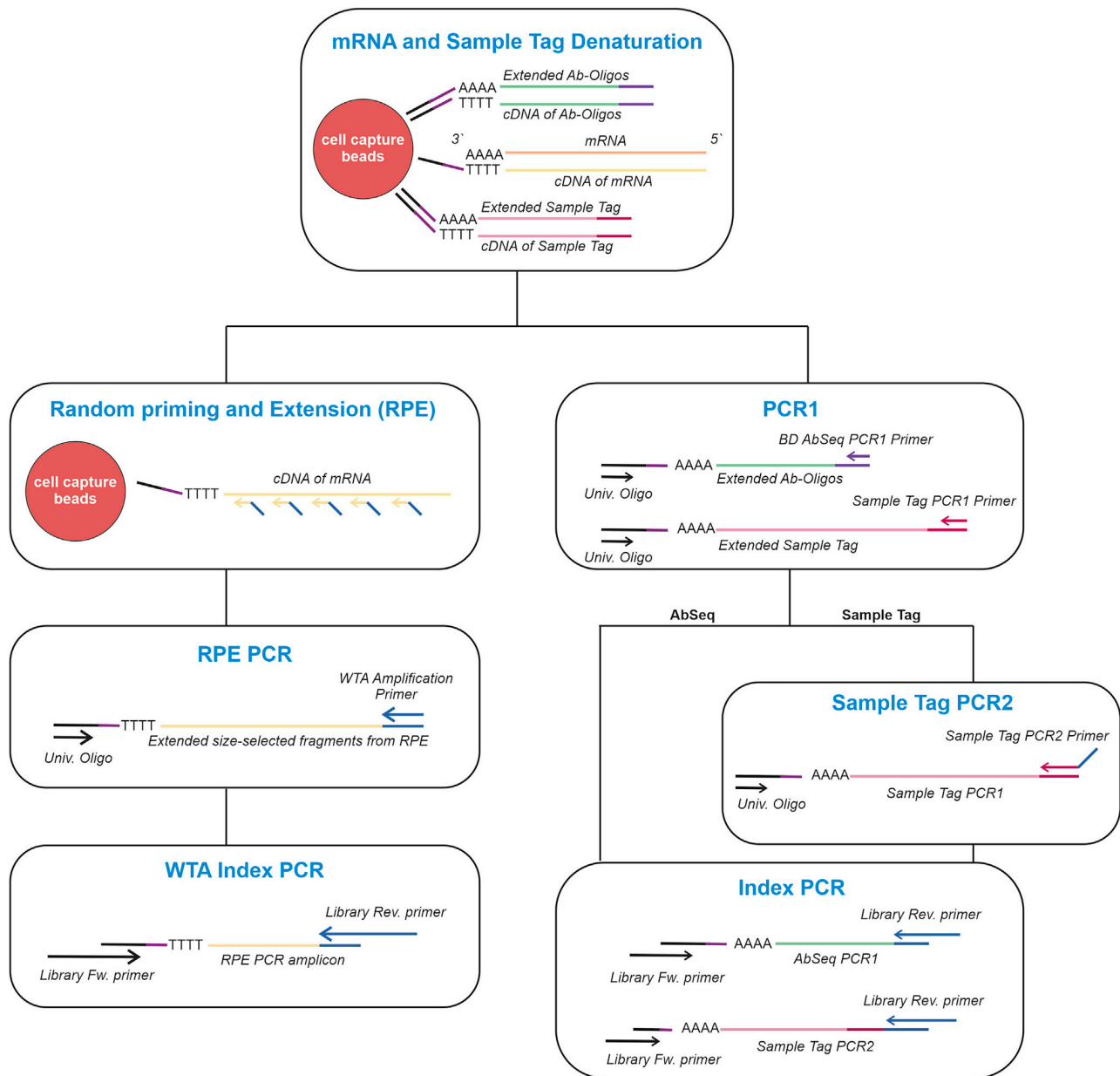


Figure 4. Schematic overview for the combination of WTA, sample tag, and AbSeq

Note: For low-abundance samples, a co-labeling approach as mentioned above could be used to decrease the potential risk of cell loss. It is important, however, to consider that this approach substantially increases the cost for the AB-labeling per sample. For more details, please refer to the BD protocol. (<http://static.bdbiosciences.com/documents/BD-AbSeq-Ab-Oligos-Single-Cell-Multiplexing-Kit-User-Guide.pdf>)

△ CRITICAL: If the Ab-oligo labeling step follows, samples need to be resuspended in BD Stain Buffer, otherwise resuspend in BD Sample Buffer.

9. Pooling samples

- a. Count the cell number of each sample after labeling as described above
- b. Pool the cells of all samples at equal numbers and adjust the volume with BD Sample Buffer to a final volume of 610 μL

Note: If Ab-Oligo staining is not performed, proceed immediately with the single-cell capture step.

△ CRITICAL: Accurate cell counting is critical for obtaining an equal distribution of cells between the different samples in the final cell mixture.

10. *Optional:* Ab-Oligo Labeling

- a. After Oligo-coupled antibody-based sample multiplexing, centrifuge the cell mixture at $300 \times g$ for 5 min, 4°C following the above-mentioned safety instructions
- b. To block non-specific AB binding sites, remove the supernatant, add 100 μL blocking buffer (95 μL BD Stain Buffer + 5 μL human FcR blocking reagent) and incubate the cell suspension for 10 min between 20°C and 22°C
- c. Add 100 μL of the antibody mix to the cell suspension and incubate the cell suspension for 40 min on ice

Note: BD AbSeq oligo-coupled antibodies are optimized for use at a final concentration of 1:100. Thus, 2 μL of each antibody are mixed and depending on the numbers of antibodies used stain buffer is added to reach a volume of 100 μL of the antibody mix. At this point the mix is added to the cell suspension in blocking buffer reaching a final volume of 200 μL .

- d. Add 1 mL of Stain Buffer and proceed to spin the samples at $300 \times g$ for 5 min, 4°C , following the above-mentioned safety instructions
- e. Repeat the wash step two more times
- f. Resuspend the cell pellet in 300 μL of BD Sample Buffer
- g. Count the cells as described above
- h. Considering the number of cells to load on the BD Rhapsody cartridge, adjust the volume with Sample Buffer to obtain a final volume of 610 μL

BD Rhapsody single-cell capture and cDNA synthesis

⌚ **Timing:** ~ 2 h

This section describes cell loading and capturing of single cells onto the BD Rhapsody Cartridge (RC) and subsequently cDNA synthesis and exonuclease treatment. The critical step here is to define the desired number of cells to load on the RC. BD estimates a multiplet rate of 4.7% when loading 20,000 cells. Using the oligo-coupled antibody-based sample multiplexing strategy enables to efficiently identify doublets in the data *in silico* thus allowing to super-load a higher number of cells thereby substantially increasing the number of singlets (Stoeckius et al., 2018). On average, we observe a doublet rate ranging roughly from 20 to 40 % when super-loading the cartridges with 60,000 cells and end up with approximately 15–20k cells. The inevitable increase in doublets of course also leads to higher sequencing cost for the informative cells as the doublets take up a substantial part of the reads. But as clinical samples are precious and sequencing costs decrease continuously, this is the preferred approach to get as much information per sample with as little batch effects as possible.

11. Prepare the following items before starting the experiment:
 - a. Set two thermomixers at 37°C and 80°C , respectively
 - b. Thaw all the reagents from the BD Rhapsody cDNA kit and place them on ice. Remove the enzymes from -20°C only right before use

- c. Place Sample Buffer, 1 M DTT, Lysis Buffer, and Cell capture beads from the BD Rhapsody Cartridge Reagent kit on ice
- d. Prepare Cell Capture Beads by placing the Cell Capture Bead tube on the magnet for 1 min and remove the storage buffer. Afterward, remove the tube from the magnet and resuspend the beads in 750 μL of cold BD Sample Buffer
- e. Prepare Lysis Buffer by adding 75 μL 1 M DTT to one 15 mL Lysis Buffer bottle
- f. Ensure that the waste collector and a labeled 5 mL LoBind tube are inserted in the designated slots of the BD Rhapsody Express instrument (Figure 5). The waste collector located inside the instrument must be pre-filled with 1,400 μL absolute ethanol
- g. Move the left slider on top of the instrument in the middle in position 0 and the slider on the front to WASTE
- h. Prepare a Terralin PAA bottle and a respiratory protection mask (FFP2 or FFP3) next to the BD Rhapsody express instrument for the case of contamination

△ CRITICAL: In order to assure no potential contamination, the cell loading step has to be carried out under the laminar flow hood. Once the cells are loaded on the RC, it can be brought outside the hood to proceed with the protocol.

Note: For operations on the BD Rhapsody Express instrument only electronic BD Rhapsody P1200M and P5000M pipettes can be used. The flow rate in these pipettes is optimized for each different step. For more details on how to use the BD Rhapsody express instrument please consult the BD user guide (<http://static.bdbiosciences.com/documents/BD-Rhapsody-Single-Cell-Analysis-System-Instrument.pdf>).

12. Priming of the RC

Note: All buffers used in this step need to be equilibrated between 20°C and 22°C.

- a. Place the RC into the BD Rhapsody Express instrument assuring that the RC barcodes faces out
- b. Set the P1200M pipette to “Prime/Treat” mode
- c. Load 700 μL of absolute ethanol onto the RC
- d. Remove the ethanol from the RC loading 700 μL of air
- e. Load 700 μL of Cartridge Wash Buffer 1 (CWB1) and leave it for 1 min at between 20°C and 22°C
- f. Remove the CWB1 from the RC loading 700 μL of air and subsequently load 700 μL of CWB1 once more leaving it for 10 min between 20°C and 22°C

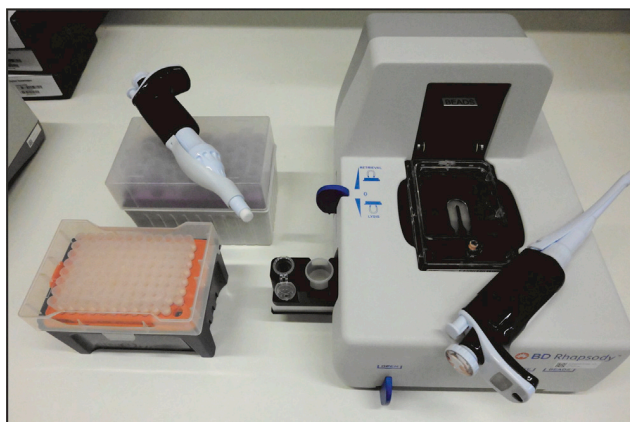


Figure 5. BD Rhapsody Express instrument

- g. Load the RC with 700 μ L of air to empty it and immediately load 700 μ L Cartridge Wash Buffer
2

Note: The RC can be primed up to 4 h and stored at a temperature between 20°C and 22°C before cell loading.

13. Cell Loading onto the RC and bead retrieval
 - a. With the RC placed on the BD Rhapsody Express instrument empty the RC by loading air into it with the P1200M set in "Prime/Treat" mode
 - b. Bring the RC and P1200M pipette set in "Cell Load" mode under the laminar flow hood

Note: Please consider that in "Cell Load" mode, it is required to press the button of the P1200M a first time to aspirate 40 μ L of air, and then after immersing the tip in cold cell suspension to press once more in order to fill the tip and aspirate 575 μ L of solution.

- c. Mix the cell suspension by pipetting with a normal 1,000 μ L pipette and then immediately load 575 μ L cell suspension on the RC using the P1200M pipette
- d. Incubate the RC at 20°C–22°C for 15 min

Note: At this step, if working with two cartridges in parallel, proceed with cell loading into the second one. We recommend waiting until almost the end of the incubation of step 13d. This allows processing the first cartridge until step (14g) during the incubation time of the second one.

- e. In the meantime:
 - i. Disinfect your hands and wipe the outside of RC and the P1200M carefully with Terralin PAA assuring that the entire surface has been decontaminated
 - ii. Transfer both the P1200AM and the RC outside of the hood and place the latter into the Rhapsody Express instrument
- f. Set the P1200M pipette in "Prime/Treat" mode and load the RC with air to remove cells in excess

Note: The diluted cell solution will be discarded directly into the waste collector pre-filled with absolute ethanol. The final concentration of ethanol inside the container is sufficient to neutralize the virus and the waste can be considered virus free.

- g. Set the P1200M pipette in "Bead Load" mode
- h. Resuspend the BD beads by pipetting with a normal 1,000 μ L pipette and then immediately aspirate 630 μ L bead suspension and load on the RC using the P1200M pipette in "Bead Load" mode
- i. Incubate the RC at 20°C–22°C for 3 min
- j. Shake the RC at 20°C–22°C for 15 s using a plate mixer or Thermo mixer at 1,000 rpm to re-suspend the beads in excess before to remove them
- k. Return the RC on the BD Rhapsody Express instrument and wait 30 s
- l. Set the P1200M pipette in "Wash" mode and load the RC with air and cold Sample Buffer in the following order
 - i. Air
 - ii. Cold Sample Buffer
 - iii. Air
 - iv. Cold Sample Buffer
- m. Move the left slider on the BD Express instrument to **LYSIS** and set the P1200M in "Lysis" mode
- n. Load 550 μ L Lysis Buffer + DTT on the RC and incubate at 20°C–22°C for 2 min
- o. Set the P5000M pipette in "Retrieval" mode
- p. Move the front slider on the BD Express instrument to **BEADS** and the left slider on **RETRIEVAL**

- q. Move the retrieval magnet in down position and leave it for 30 s
- r. Aspirate 5,000 μ L Lysis Buffer + DTT with the P5000M pipette
- s. Place the P5000M pipette in position to seal against the gasket of the RC
- t. Move the left slider to the middle position (0) and immediately load 4,950 μ L Lysis Buffer with DTT
- u. Move the front slider on the BD Express instrument to **OPEN** and collect the 5 mL LoBind Tube

14. Washing of the cell capture beads

- a. Place the 5 mL LoBind tube on a large magnetic stand for 5 mL Eppendorf tubes
- b. After 1 min remove all but \sim 1 mL of supernatant without disturbing the beads
- c. Removing the tube from the magnet, gently pipet the beads and transfer them to a new 1.5 mL LoBind Tube
- d. Place the tube on the magnetic stand holding 1.5 mL tubes for about 2 min and remove supernatant

Δ CRITICAL: Avoid leaving Lysis Buffer in the tube. Lysis Buffer might inhibit the reverse transcription reaction.

- e. Remove the tube from the magnet and gently resuspend the beads with 1 mL of cold Bead Wash Buffer (BWB)
- f. Place the tube on the magnet for \sim 2 min and remove the supernatant
- g. Repeat the washing step once more and proceed with the reverse transcriptase reaction

Note: Beads can sit in BWB on ice for up to 30 min before proceeding with the next steps. If working with two cartridges, at this time the second cell incubation in RC of step 13d should be finished and can be further processed. In this way. It is possible to proceed with the Reverse transcription and Exonuclease I treatment with both samples together

15. Reverse transcription and treatment with Exonuclease I on the cell capture beads

- a. Prepare the cDNA mix (Table 1) and assure that a Thermomixer is set to 37°C and 1,200 rpm

Table 1. cDNA mix

Components	1 \times library (μ L)
RT buffer	40
dNTP	20
RT 0.1 DTT	10
Bead RT/PCR enhancer	12
RNase inhibitor	10
Reverse transcriptase	10
Nuclease-free water	98
Total	200

- b. Place the tube containing the Cell Capture Beads on the magnetic stand for \sim 2 min and remove the supernatant
- c. Pipet 200 μ L cDNA mix into the tube containing the Cell Capture Beads
- d. On a thermomixer incubate the samples at 1,200 rpm and 37°C for 20 min
- e. In the meantime, prepare the Exonuclease I mix (Table 2) and assure that a thermomixer is set at 80°C without shaking
- f. Place the tube with the Cell Capture Beads incubated with the cDNA mix on the magnet for \sim 2 min and remove the supernatant

Table 2. Exonuclease I mix

Components	1 × library (μL)
10× exonuclease I buffer	20
Exonuclease	10
Nuclease-free water	170
Total	200

- g. Remove tube from the magnet and pipet 200 μL of Exonuclease I Mix onto the beads and gently pipet the mix
- h. Incubate the bead suspension first in a thermomixer at 1,200 rpm and 37°C for 30 min and then at 80°C for 20 min (no shaking)
- i. Place tube with the Cell Capture Beads on the magnet for ~1 min and remove the supernatant
- j. Resuspend the beads in 200 μL of cold Resuspension Buffer

▮▮ **Pause Point:** At this point, the cDNA sample can be stored at 2°C to 8°C for ≤3 months.

BD Rhapsody 3' whole transcriptome analysis (WTA)

⌚ **Timing:** ~8 h

This section describes the workflow to prepare single-cell whole transcriptome mRNA, sample tag, and optionally AbSeq libraries. After a first denaturation step in which sample tag sequences (and AbSeq sequences) are denatured off the beads, it is possible to generate the different sequencing libraries (WTA, sample tag, and AbSeq) by several PCR steps. BD provides the protocol for performing WTA analysis either with sample tag or AbSeq. Here, we further describe an optional extension that allows to process the 3 different products together (Figure 6).

16. Prepare the following items before starting the experiment:
 - a. Thaw all the reagents from the BD Rhapsody WTA amplification kit and place them on ice. Remove the enzymes from –20°C only right before use
 - b. Set three thermomixers at 95°C, 37°C and 25°C, respectively
 - c. Save the program shown in Table 3 on the thermomixer

Table 3. Extension reaction program

Temperature	Rpm	Time
25°C	1,200	10 min
37°C	1,200	15 min
45°C	1,200	10 min
55°C	1,200	10 min

⚠ **CRITICAL:** The ramp rates of the thermomixer must be set to maximum to assure that the device reaches the desired temperature in the shortest time possible.

Note: We recommend saving the program (Table 3) in the same thermomixer that is set at 25°C from step 17f.iii. This allows to prevent that the sample handling time is unnecessarily extended.

17. Random Priming Extension (RPE) on the cell capture beads

Library preparation workflow

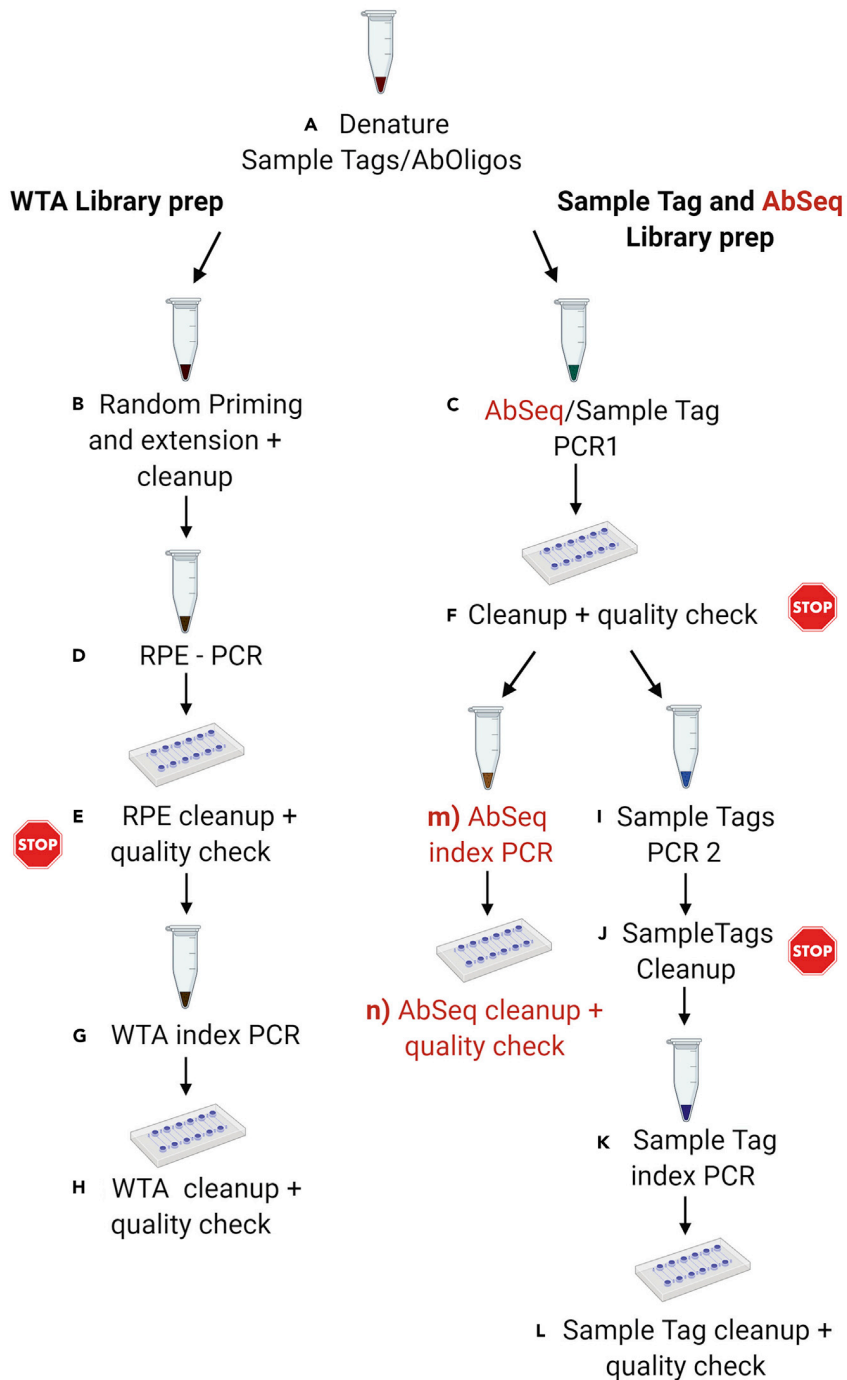


Figure 6. Library preparation workflow

- Prepare the Random Primer Mix (Table 4) and keep at 20°C–22°C
- Place the Exonuclease I-treated beads on the magnet for ~2 min, remove the supernatant and resuspend the beads in 75 µL Elution Buffer
- Heat the beads in a thermomixer at 95°C for 5 min without shaking (Figure 6A)

Table 4. Random primer mix

Component	1 × library (μL)
WTA extension buffer	20
WTA extension primers	20
Nuclease-free water	134

- d. Put the tube on the magnet for ~2 min, remove the supernatant and transfer it (AbSeq/sample tag solution) to a new labeled tube. Keep the supernatant at 4°C for later processing
- e. Resuspend the beads in 174 μL of Random Primers Mix (Figure 6B)
- f. Incubate the tube in the following order
 - i. 95°C for 5 min (no shaking)
 - ii. 37°C, 1,200 rpm for 5 min
 - iii. 25°C, 1,200 rpm for 15 min
- g. In the meantime, proceed to prepare the Extension Enzyme Mix (Table 5)

Table 5. Extension enzyme mix

Component	1 × library (μL)
10 mM dNTP	8
Bead RT/PCR enhancer	12
WTA extension enzyme	6

- h. After the incubations, add 26 μL of Extension Enzyme Mix into the tube containing the beads and place it in the thermomixer with the pre-saved Extension Reaction Program (see “Before you begin” section at the start of this step)

Note: While the program is running it is possible to proceed with the sample tag (optional AbSeq) PCR 1 step (Figure 6C).

- i. Place the tube containing the Random Primer Extension product on the magnet (from step 17h), remove the supernatant and resuspend the beads in 205 μL of Elution Buffer
- j. Denature the products off the beads by incubating the sample at 95°C for 5 min (no shaking)
- k. Briefly centrifuge the sample and then resuspend the beads by placing the tube in a thermomixer at any temperature for 30 s at 1,200 rpm
- l. Place the tube on a magnet and transfer the supernatant containing the Random Primer Extension products in a new tube and proceed with step 18
- m. Pipette 200 μL of cold bead resuspension buffer in the tube with the beads

Note: At this step, the beads can be stored at 4°C for up to 3 months.

18. Random Primer Extension Product purification (Figure 6B)
 - a. Before to start freshly prepare 80% ethanol, vortex the SPRIselect beads until they are fully resuspended and label a new 1.5 mL tube as Random Primer Extension Purified Product
 - b. Pipet 360 μL of the beads into the tube containing 200 μL of Random Primer Extension product (from step 17l) and gently mix
 - c. Incubate at 20°C–22°C for 10 min
 - d. Place the suspension on the magnet for 5 min until the sample becomes clear and remove the supernatant
 - e. Add 1 mL of 80% ethanol into the tube sitting on the magnet
 - f. Wait 30 s and then remove the supernatant
 - g. Repeat steps 18e and 18f once more

- h. Assure to remove all the supernatant and drops of ethanol on the wall of the tube and air dry the sample at 20°C–22°C for 5 min
- i. Resuspend the beads in 40 µL of Elution Buffer and incubate at 20°C–22°C for 2 min
- j. Place the tube on the magnet until the solution is clear and transfer the supernatant in the new labeled tube

19. RPE PCR (Figure 6D)

- a. Prepare the RPE PCR Mix (Table 6)

Table 6. RPE PCR mix

Component	1 × library (µL)
PCR master mix	60
Universal oligo	10
WTA amplification primer	10
Total	80

- b. Add 80 µL of the RPE PCR mix to 40 µL of the Random Primer Extension Purified Product from step 18j
- c. Pipette around 60 µL of the reaction in two 0.2 mL PCR tubes and run the following PCR program (Table 7)

Table 7. RPE PCR program

Step	Temperature	Time	Cycles
Hot start	95°C	3 min	1
Denaturation	95°C	30 s	12–13 (for more than 10K cells use 12 cycles)
Annealing	60°C	1 min	
Extension	72°C	1 min	
Final extension	72°C	2 min	1
Hold	4°C	∞	1

Note: Splitting the reaction in two tubes assures that the entire volume in each tube is reaching the same temperature increasing the efficiency of the PCR reaction.

Note: Suggested PCR cycles need to be optimized for different cell types and cell number.

- d. After the PCR, briefly centrifuge the tubes, combine the two reactions in one 1.5 mL tube and proceed to purify the product with SPRIselect beads

20. RPE PCR product purification (Figure 6E)

- a. Before to start freshly prepare 80% ethanol, vortex the SPRIselect beads until they are fully resuspended and label a new 1.5 mL tube as Random Primer Extension Purified Product
- b. Pipet 120 µL of the beads into the tube containing 120 µL of RPE PCR product and gently mix
- c. Incubate at 20°C–22°C for 5 min
- d. Place the suspension on the magnet for 3 min until the sample becomes clear and remove the supernatant
- e. Add 300 µL of 80% ethanol into the tube sitting on the magnet
- f. Wait 30 s and then remove the supernatant
- g. Repeat steps 20e and 20f once more
- h. Assure to remove all the supernatant and drops that could be on the wall of the tube and air dry the sample at 20°C–22°C for 5 min
- i. Resuspend the beads in 40 µL of Elution Buffer and incubate at 20°C–22°C for 2 min
- j. Place on the magnet until the solution is clear and transfer the supernatant in the new labeled tube

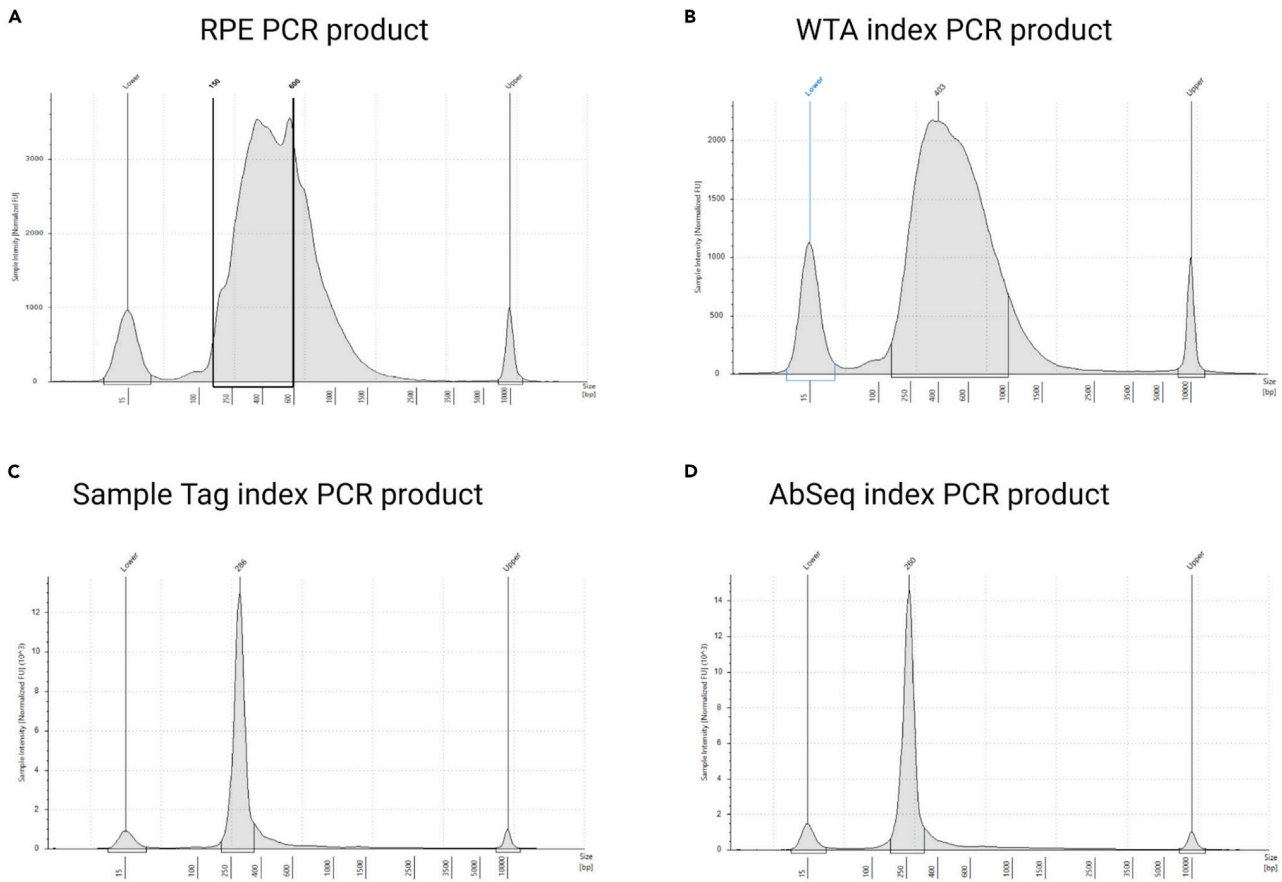


Figure 7. TapeStation profiles

k. Quantify the concentration and check the fragment distribution using the TapeStation System

△ **CRITICAL:** The TapeStation profile should be a broad peak from ~200 bp to 2,000 bp (Figure 7A). For proceeding with the WTA index PCR step set a region between 150 bp and 600 bp and consider this concentration to calculate how much template to add.

21. Sample tag PCR 1 (Figure 6C)

a. Prepare the sample tag PCR 1 Mix (Table 8)

Table 8. Sample tag PCR 1 mix

Component	1× library (μL)
PCR master mix	100
Universal oligo	20
Bead RT/PCR enhancer	12
Sample Tag PCR 1 primer	1
Total	133

b. In a 1.5 mL tube mix 133 μL of sample tag PCR 1 mix with 67 μL of the sample tag product from step 17d.

- c. Split the PCR 1 mix in four 0.2 mL PCR tubes and run the following program (Table 9)

Table 9. Sample tag PCR 1 program

Step	Temperature	Time	Cycles
Hot start	95°C	3 min	1
Denaturation	95°C	30 s	11–15 (for more than 10K cells use 11cycles)
Annealing	60°C	3 min	
Extension	72°C	1 min	
Final extension	72°C	5 min	1
Hold	4°C	∞	1

Note: Suggested PCR cycles need to be optimized for different cell types and cell number.

- d. After the PCR, combine the 4 reactions in one 1.5 mL tube and proceed to purify the product with SPRIselect beads

22. Sample tag PCR 1 purification (Figure 6F)

- Before to start freshly prepare 80% ethanol, vortex the SPRIselect beads until they are fully resuspended and label a new 1.5 mL tube as sample tag PCR1 purified product
- Pipet 360 μ L of the SPRIselect beads into the tube containing 200 μ L of sample tag PCR1 and gently mix
- Incubate at 20°C–22°C for 5 min
- Place the suspension on the magnet for 5 min until the sample becomes clear and remove the supernatant
- Add 600 μ L of 80% ethanol into the tube sitting on the magnet
- Wait 30 s and then remove the supernatant
- Repeat steps 22e and 22f once more
- Assure to remove all the supernatant and drops of ethanol on the wall of the tube and air dry the sample at 20°C–22°C for 5 min
- Resuspend the beads in 30 μ L of Elution Buffer and incubate at 20°C–22°C for 2 min
- Place the tube on the magnet until the solution is clear and transfer the supernatant in the new labeled tube

Pause Point: After the purification steps both the RPE PCR and sample tag PCR 1 products can be stored at 4°C if the protocol is continued within 24 h or can be stored at –20°C for up to 6 months.

23. WTA Index PCR (Figure 6G)

- Considering the concentration of the 150–600 bp region, dilute the RPE PCR product to a concentration of 2 nM using Elution Buffer.
- Prepare the WTA Index PCR mix as described below (Table 10)

Table 10. WTA index PCR mix

Component	1× library (μ L)
PCR master mix	25
Library forward primer	5
Library reverse primer (1–4)	5
Nuclease-free water	5
Total	40

△ **CRITICAL:** In the BD Rhapsody WTA Amplification four different Library Reverse primers are present. When preparing multiple libraries, for each of them different reverse primers should be used to allow combined sequencing.

- c. Combine 10 μL of 2 nM template with 40 μL of the WTA Index PCR mix
- d. Run the following program (Table 11)

Table 11. WTA index PCR program

Step	Temperature	Time	Cycles
Hot start	95°C	3 min	1
Denaturation	95°C	30 s	8–9 (for less than 2 nM use 9 cycles)
Annealing	60°C	30 s	
Extension	72°C	30 s	
Final extension	72°C	1 min	1
Hold	4°C	∞	1

- e. After PCR, briefly centrifuge the tube for collecting all the sample at the bottom of the tube
- f. Add 60 μL of nuclease-free water to the WTA index PCR product, pipet and then transfer 100 μL into a new 0.2 mL PCR tube

24. WTA index PCR product purification (dual-sided cleanup) (Figure 6H)

- a. Before to start freshly prepare 80% ethanol, vortex the SPRIselect beads until they are fully resuspended, prepare a new 0.2 mL PCR tube for the second clean up and label a new 1.5 mL tube as WTA index PCR Purified Product.
- b. Pipet 60 μL of the beads into the tube containing 100 μL of the WTA Index PCR product (from step 23f) and gently mix
- c. Incubate at 20°C–22°C for 5 min
- d. Place the suspension on the magnet for 2 min
- e. In the meantime, pipet 15 μL of SPRIselect beads in a new 0.2 mL PCR tube
- f. Transfer 160 μL of the supernatant from step 24d in the tube containing 15 μL of beads and gently pipet
- g. Incubate at 20°C–22°C for 5 min
- h. Place the tube on the magnet for 2 min until the suspension becomes clear and remove the supernatant
- i. Add 300 μL of 80% ethanol into the tube sitting on the magnet
- j. Wait 30 s and then remove the supernatant
- k. Repeat steps 24i and 24j once more
- l. Assure to remove all the supernatant and drops of ethanol on the wall of the tube and air dry the sample at 20°C–22°C for 2 min
- m. Resuspend the beads in 30 μL of Elution Buffer and incubate at 20°C–22°C for 2 min
- n. Place the tube on the magnet until the solution is clear and transfer the supernatant in the new labeled tube
- o. Quantify the concentration with a Qubit Fluorometer and check the fragment distribution with the TapeStation System (Figure 7B)

Note: The fragment distribution should show a peak between 250 and 1,000 bp (Figure 7B). If lower peaks are shown or the concentration is too low refer to the troubleshooting section (see below).

△ **CRITICAL:** If a peak at ~ 165 bp is shown in the TapeStation, profile a second purification is recommended using a beads ratio of 0.75 (following the steps from 24f to 24o).

25. Sample tag PCR 2 (Figure 6I)
a. Prepare the sample tag PCR 2 Mix (Table 12)

Table 12. Sample tag PCR 2 mix

Component	1 × library (μL)
PCR master mix	25
Universal oligo	2
Sample tag PCR 2 primer	3
Nuclease-free water	15
Total	45

- b. In a 1.5 mL tube mix 45 μL of sample tag PCR 2 mix with 5 μL of the sample tag PCR 1 product from step 22j
c. Run the following program (Table 13)

Table 13. Sample tag PCR 2 program

Step	Temperature	Time	Cycles
Hot start	95°C	3 min	1
Denaturation	95°C	30 s	10
Annealing	60°C	3 min	
Extension	72°C	1 min	
Final extension	72°C	5 min	1
Hold	4°C	∞	1

- d. After the PCR, proceed to purify the product with SPRIselect beads
26. Sample tag PCR 2 purification (Figure 6J)
- Before to start freshly, prepare 80% ethanol, vortex the SPRIselect beads until they are fully resuspended and label a new 1.5 mL tube as sample tag PCR2 purified product
 - Pipet 60 μL of the beads into the tube containing 50 μL of sample tag PCR 2 product and gently mix
 - Incubate at 20°C–22°C for 5 min
 - Place the suspension on the magnet for 3 min until the sample becomes clear and remove the supernatant
 - Add 200 μL of 80% ethanol into the tube sitting on the magnet
 - Wait 30 s and then remove the supernatant
 - Repeat steps 26e and 26f once more
 - Assure to remove all the supernatant and drops of ethanol on the wall of the tube and air dry the sample at 20°C–22°C for 3 min
 - Resuspend the beads in 30 μL of Elution Buffer and incubate at 20°C–22°C for 2 min
 - Place on the magnet until the solution is clear and transfer the supernatant in a new labeled tube
 - Measure the concentration with a Qubit fluorometer

Pause Point: After the purification steps both the WTA Index and sample tag PCR 2 products can be store at 4°C if the protocol is continued within 24 h or can be stored at –20°C for up to 6 months.

27. Sample tag index PCR (Figure 6K)

- a. Prepare the sample tag index PCR mix as described below (Table 14):

Table 14. Sample tag index PCR mix

Component	1 × library (μL)
PCR master mix	25
Library forward primer	2
Library reverse primer (1–4)	2
Nuclease-free water	18
Total	47

△ **CRITICAL:** When preparing libraries from multiple RC, for each of them different reverse primers must be used. However, for one RC the same index for both the WTA and sample tag can be used.

- b. Combine 3 μL of 1 ng/μL of template with 47 μL of the sample tag index PCR mix
c. Run the following program (Table 15)

Table 15. Sample tag index PCR program

Step	Temperature	Time	Cycles
Hot start	95°C	5 min	1
Denaturation	95°C	30 s	6–8 (for concentrations between 0.5 and 1.1 ng/μL use 6 cycles)
Annealing	60°C	30 s	
Extension	72°C	30 s	
Final extension	72°C	1 min	1
Hold	4°C	∞	1

Note: Suggested PCR cycles need to be optimized for different cell types and cell number

- d. After PCR, briefly centrifuge the tube for collecting the entire sample at the bottom of the tube and proceed with the purification.
28. Sample tag index PCR product purification (Figure 6L)
- Before to start, freshly prepare 80% ethanol, vortex the SPRIselect beads until they are fully resuspended and label a new 1.5 mL tube as sample tag index purified product
 - Pipet 40 μL of the beads into the tube containing 50 μL of sample tag index PCR product and gently mix
 - Incubate at 20°C–22°C for 5 min
 - Place the suspension on the magnet for 3 min until the sample becomes clear and remove the supernatant
 - Add 200 μL of 80% ethanol into the tube sitting on the magnet
 - Wait 30 s and then remove the supernatant
 - Repeat steps 28e and 28f once more
 - Assure to remove all the supernatant and drops of ethanol on the wall of the tube and air dry the sample at 20°C–22°C for 3 min
 - Resuspend the beads in 30 μL of Elution Buffer and incubate at 20°C–22°C for 2 min
 - Place the tube on the magnet until the solution is clear and transfer the supernatant in a new labeled tube
 - Quantify the concentration with a Qubit Fluorometer and check the fragment distribution with TapeStation System (Figure 7C)

Note: The sample tag should show a unique peak at ~290 bp. If other peaks are shown or the concentration is too low refer to the troubleshooting section (see below).

29. Optional: AbSeq Library

Note: If the samples have been stained with oligo-coupled AbSeq antibodies as well, an AbSeq library needs to be prepared together with the WTA and sample tag library. In this case, the protocol mainly deviates in one step, the sample tag PCR 1 step (step 21), as primers specifically targeting the AbSeq oligo peptides are added to the PCR 1 mix.

- a. AbSeq/sample tag PCR 1 ([Figure 6C](#))
 - i. Prepare the AbSeq/sample tag PCR 1 Mix ([Table 16](#))

Table 16. AbSeq/sample tag PCR 1 mix

Component	1× library (μL)
PCR master mix	117.5
Universal oligo	23.5
Bead RT/PCR enhancer	14.1
Sample tag PCR 1 primer	1.1
AbSeq PCR 1 primer	11.8
Total	168

- ii. In a 1.5 mL tube mix 168 μL of AbSeq/sample tag PCR 1 mix with 67 μL of the AbSeq/sample tag product from step 17d.
- iii. Split the PCR 1 mix in four 0.2 mL PCR tubes and run the following program ([Table 17](#))

Table 17. AbSeq/sample tag PCR 1 program

Step	Temperature	Time	Cycles
Hot start	95°C	3 min	1
Denaturation	95°C	30 s	11–15 (for more than 10K cells use 11cycles)
Annealing	60°C	3 min	
Extension	72°C	1 min	
Final extension	72°C	5 min	1
Hold	4°C	∞	1

Note: Suggested PCR cycles need to be optimized for different cell types and cell number.

- iv. After the PCR, combine the 4 reactions in one 1.5 mL tube and proceed to purify the product with SPRIselect beads
- b. AbSeq/sample tag PCR 1 Purification ([Figure 6F](#))
 - i. Before to start, freshly prepare 80% ethanol, vortex the SPRIselect beads until they are fully resuspended and label a new 1.5 mL tube as AbSeq/sample tag PCR1 purified product
 - ii. Pipet 423 μL of beads in 235 μL of AbSeq/sample tag product and incubate 5 min at 20°C–22°C
 - iii. Place the tube on the magnets, wait 5 min, and remove supernatant
 - iv. Wash twice with 600 μL of 80% ethanol
 - v. Assure to remove all the supernatant and drops of ethanol on the wall of the tube and air dry the sample at 20°C–22°C for 5 min.
 - vi. Resuspend in 30 μL Elution Buffer and incubate 2 min at 20°C–22°C
 - vii. Place the tube on the magnet and pipette the eluate in a new tube

- viii. Quantify on the Qubit fluorometer
- ix. Dilute an aliquot of AbSeq/sample tag product to 1 ng/ μ L and proceed to index PCR of the AbSeq product (Figure 6M). For the sample tag use undiluted PCR 1 product and proceed with the sample tag PCR 2 step (step 25) as described above

Note: The diluted AbSeq sample can be stored at 4°C for 24 h to run the indexing PCR later together with the sample tag PCR 2 product. The conditions for indexing both the AbSeq and the sample tag libraries are the same (see step 27).

- x. Once the AbSeq index PCR has been run, purify the product as described for sample tag (see step 28) and check fragment size (Figure 6N). The product should show only a peak around 260 bp (Figure 7D). Refer to the troubleshooting sections (see below) if the concentration is too low or other peaks are detectable.

Multi-color flow cytometry

⌚ Timing: ~2 h depending on sample number

This section describes all important steps and details for sample preparation and recording of flow cytometric data from COVID-19 blood samples. Representative data and a gating strategy are shown in Figure 8. For more elaborate analyses we refer the reader to Schulte-Schrepping et al. (2020). Emphasis will be put on the procedure applied to avoid possible contamination of the scientist during both the preparation of the samples and the final recording of the data.

- 30. Prepare the staining solution adding the necessary microliters for the respective components (Antibodies-human FcR Blocking reagent-BD Horizon Brilliant Stain Buffer-PBS) to reach the desired concentration in a final volume of 100 μ L per sample as indicated in the Table 18

Table 18. Pipetting scheme for flow cytometry antibody staining

Antibody (clone)	Dilution (2 \times master mix)	μ L to add for each sample
HLA-DR BV421 (L243)	1:50	2
CD4 BV510 (OKT4)	1:50	2
CD16 BV605 (3G8)	1:50	2
CD45 BV711 (HI30)	1:50	2
CD8 BV785 (SK1)	1:50	2
CD66b FITC (G10F5)	1:50	2
CD14 PerCp-Cy5.5 (M ϕ P9)	1:50	2
CD56 PE (MY31)	1:12.5	8
CD3 PE/Dazzle (UCHT1)	1:50	2
CD11c PE/Cy5 (B-Iy6)	1:25	4
Siglec8 PE/Cy7 (7C9)	1:50	2
CD203c APC (NP4D6)	1:50	2
CD1c AlexaFluor700 (L161)	1:50	2
CD19 APC/Fire 750 (HIB19)	1:25	4
LIVE/DEAD fixable yellow dead cell stain	1:50 (1:10 pre-dilution in PBS)	2
BD Horizon brilliant stain buffer	1:5	20
FcR blocking reagent, human	1:50	2
PBS		38
Total		100

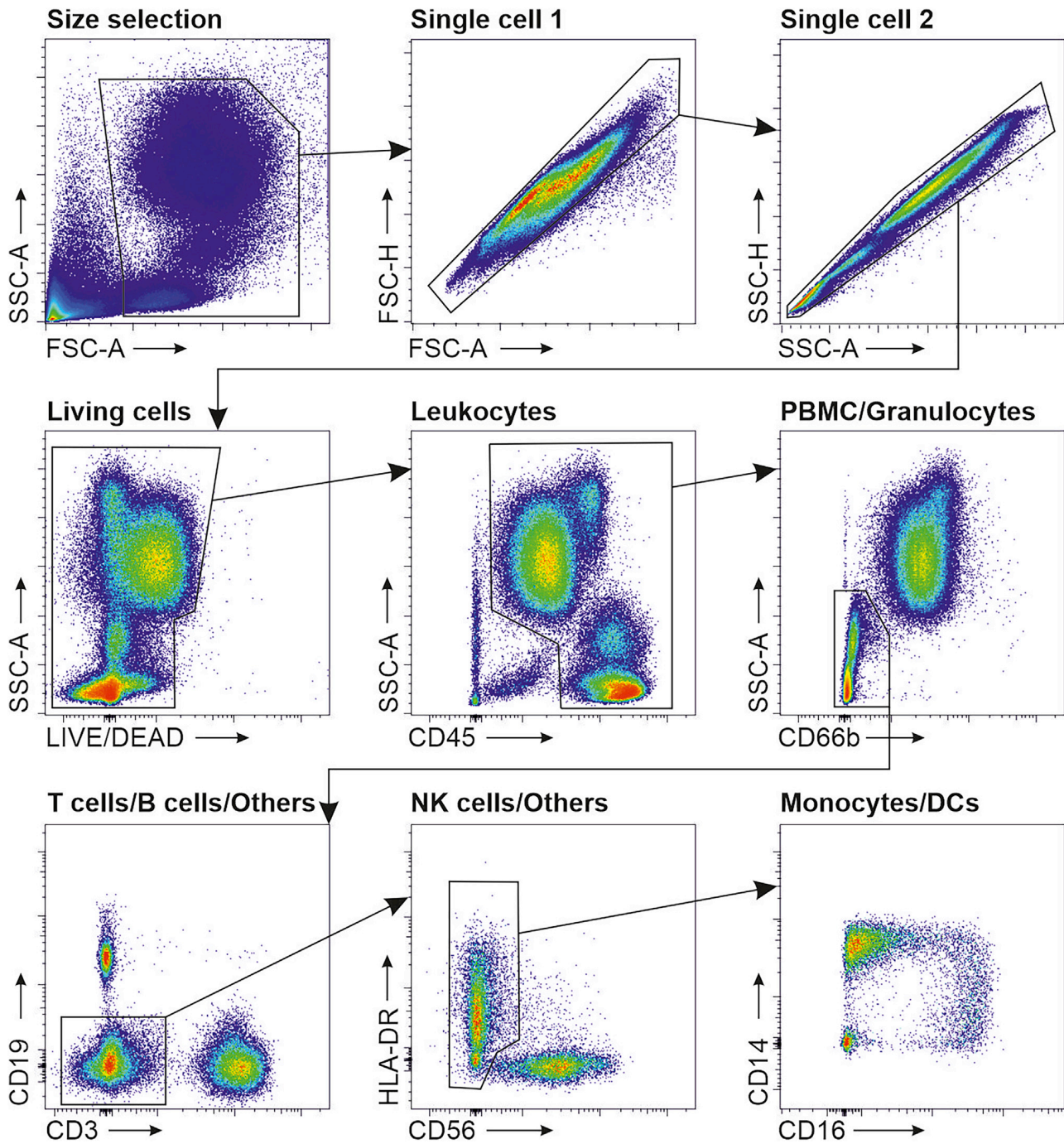


Figure 8. Visualization of representative flow cytometry data and gating strategy

Note: For LIVE/DEAD Fixable Yellow Dead Cell Stain a pre-dilution 1:10 in PBS is required.

31. Labeling with fluorescently labeled antibodies
 - a. Count the cell suspension and aliquot at least 2 million cells of each sample (see Cell counting section for details); if the number of available cells is lower see [Troubleshooting](#) section

Note: Flow cytometric analysis can be performed with a lower number of cells; however, this results in reduced statistical power for low represented cell types.

Optional: Add 10 μL counting beads to the cell suspension before counting; this will allow you to retrieve the absolute number of cells for each milliliter of blood.

- b. Centrifuge samples for 5 min at $300 \times g$, 4°C in 15 mL Falcon tubes following the above-mentioned safety instructions
- c. After centrifugation, remove the supernatant entirely and resuspend the cells in 100 μL of PBS
- d. Add 100 μL of staining solution and incubate at 4°C for 30 min
- e. After antibody incubation, wash the cell suspension with 1 mL of PBS and centrifuge for 5 min at $300 \times g$, 4°C following the above-mentioned safety instructions
- f. Remove the supernatant and resuspend the cells carefully in 500 μL of methanol-free PFA (4% in PBS)
- g. Incubate for 5 min at 20°C – 22°C
- h. Wash samples in 1 mL of PBS following centrifugation for 5 min at $300 \times g$, 4°C . Repeat this step twice
- i. Remove the supernatant and resuspend PFA fixed cell pellet in 500 μL PBS
- j. Store samples protected from light until flow cytometric analysis

Note: PFA-treated samples can be considered virus free.

32. Flow cytometric analysis

- a. Before starting the measurement exchange the waste tank of the instrument and use an auto-clave-grade waste canister

Note: According to the technology in use, assess daily the performance of the instrument to ensure the highest quality possible from the analysis. For example, for BD instruments CS&T beads or Rainbow (8-peak) beads can be used for routine performance check.

- b. Acquire a minimum of 100,000 events in the living/CD45+ cells gate for each sample

Note: According to the stability of the used instrument and the consistency in the experimental procedure, the voltage setting of the instrument for the measured parameters can be kept the same over different experiments. The daily performance check will give important information in this regard.

Note: We provide one possible workflow for flow cytometric analysis, variations are possible according to the procedure established in each facility. For detailed information, we refer to [Cossarizza et al. \(2019\)](#).

33. Cleaning of the instrument after measurement

- a. For washing the instrument, set the flow cytometer to the highest acquisition speed for sample acquisition
- b. 10 min flow with FACS Rinse
- c. 10 min flow with FACS Clean
- d. 10 min flow with ddH₂O (autoclaved water can be cleaned from debris with a 0.2 μm filter just before use)
- e. Waste canister is removed and autoclaved

Note: Data analysis will not be part of this protocol since the focus here is on the preparation of potentially harmful samples. For guideline on data analysis, we refer to [Cossarizza et al. \(2019\)](#).

Sequencing and sequencing depth estimation

⌚ Timing: 18 h

This step elutes on multiplexing for sequencing, settings of the sequencer, as well as estimated read numbers per pool.

34. Pooling of BD Rhapsody libraries for sequencing
 - a. Pool WTA, AbSeq and sample tag libraries of the same cartridge (with the same index) at a molar ratio of 1:1:0.1 (Library Pool)

Note: Molarity is calculated by average fragment size of each library determined by the D5000 assay on a TapeStation4200 system and concentration by Qubit HS dsDNA assay.

- b. Pool an equal number of moles per each library pool normalizing them for the expected number of beads retrieved from each cartridge (theoretically this number should correspond to the actual number of capture single cells)
35. Perform Sequencing on a NovaSeq6000 System (Illumina) using v1 S2 200 cycle kits
 - a. Pool Rhapsody Cartridge libraries to aim for 50,000 reads for WTA, 50,000 reads for AbSeq, and 5,000 reads for sample tag per cell, allowing for a total of ~38,000 cells on a S2 flow cell
 - b. PE R1 75 cycles, i7 8 cycles, R2 75 cycles mode
 - c. Final clustering concentration of 220 pM

Data pre-processing

⌚ Timing: 24 h, depends on sequencing depth and sample size

This section describes the computational steps required for pre-processing and alignment of multiplexed BD Rhapsody WTA scRNA-seq data, optionally with AbSeq data. The protocol is based on the Drop-seq tools initially developed for processing of drop-seq data (Macosko et al., 2015) and has been developed into a Snakemake workflow for simple and reproducible use (<https://github.com/Hoohm/dropSeqPipe>). In brief, the two reads of the paired-end sequencing stored in fastq format after demultiplexing of bcl files are transformed into BAM format and the cell barcode and UMI sequence of read 1 are stored as tags in the BAM file containing the read 2 information. Afterwards, the read 2 sequences, treated as single-end reads, are transformed back to fastq format, cleaned and trimmed of 5' adapter and 3' polyA sequences and aligned against the reference sequences. After alignment, the BAM tags from the unaligned BAM file are merged with the aligned reads to recover cell barcode and UMI information. Next, additional annotation is added to the reads depending on their genomic location, e.g., their overlap with genes or exons, to enable subsequent gene expression quantification (Figure 9).

36. Mapping
 - a. Demultiplex bcl files using Bcl2fastq2 from Illumina
 - b. For mapping of cDNA, sample tag and optionally AbSeq reads, prepare a suitable reference genome by adding sample tag sequences and antibody-coupled oligo sequences as additional chromosomes to the reference genome of choice in *fasta* format. Additionally, a corresponding annotation file in *gtf* format must be prepared by adding the necessary information to the gene annotation file of choice
 - c. Build a STAR index from the custom reference genome and annotation file.
 - d. Filter the input reads for valid Rhapsody barcodes

Note: As cell barcodes in the BD Rhapsody system are produced as random combinations of 3 from a pool of 96 possible sequences with standardized spacer sequences in between, a

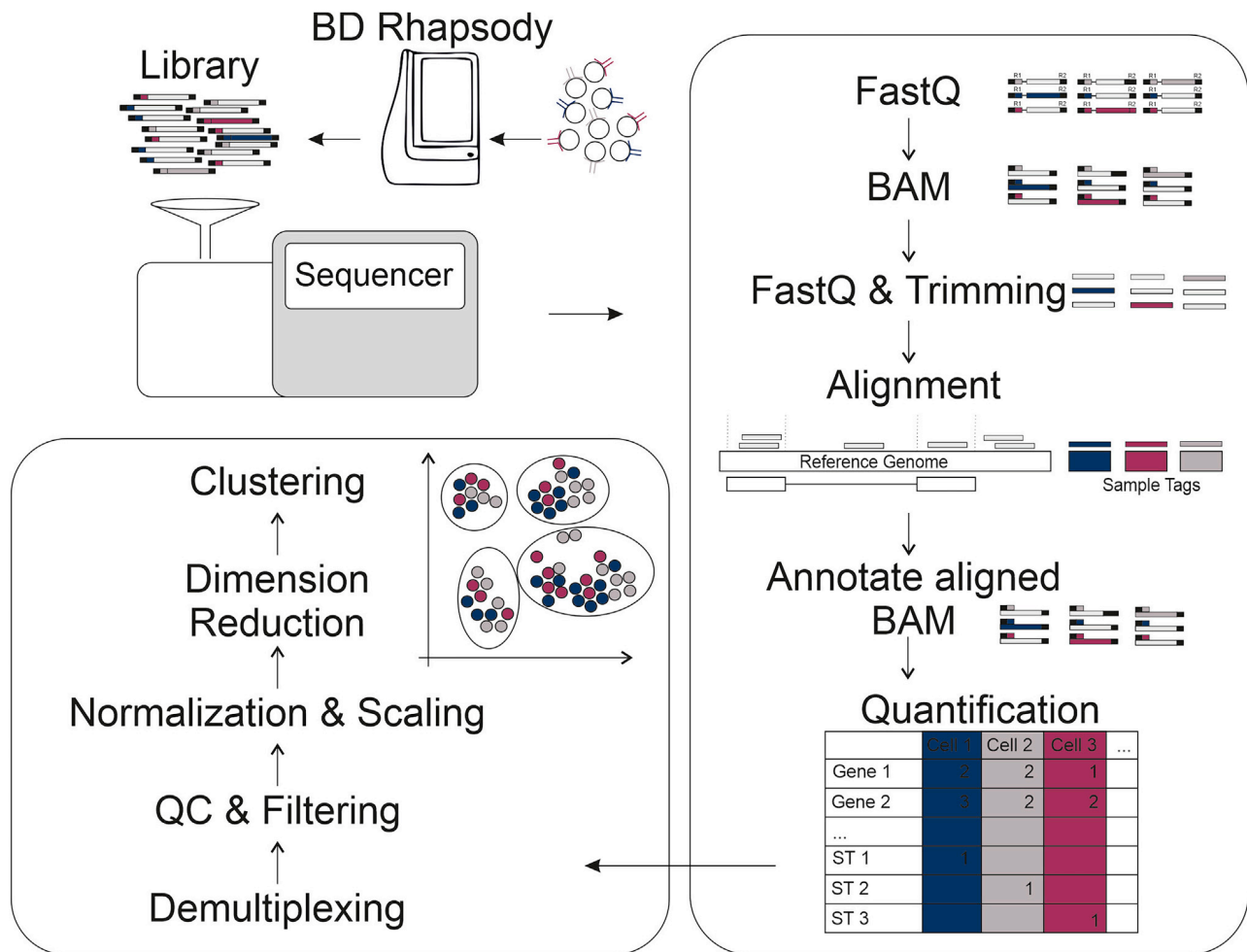


Figure 9. Schematic overview of the scRNA-seq analysis

whitelist of the 884.736 possible cell barcodes is available and can be used to eliminate reads with wrong cell barcodes upfront. This allows to skip time-consuming error repair and barcode correction steps.

- e. Next, using the above-mentioned pipeline, cDNA, sample tag and AbSeq reads are processed, trimmed using *Cutadapt* (Martin, 2011) and mapped to the custom reference genome using *STAR* (Dobin et al., 2013)

37. Quantification

- a. To estimate gene expression abundances, BAM records are annotated depending on their genomic location and overlap with genic regions
- b. Expression values are extracted from the BAM files using the picard *DigitalExpression* module and stored as gene expression matrix including gene expression, sample tag, and optionally AbSeq counts

Downstream data analysis

This section describes the essential downstream analysis steps for the resulting gene expression count data using the R software package *Seurat* (Butler et al., 2018), including de-multiplexing, quality control, normalization, dimension reduction, clustering and differential gene testing (Figure 9). The following section is based on tutorials and vignettes published by the developer team of *Seurat*

available at <https://satijalab.org/seurat/>. In addition, the following R packages are required for the analysis: *dplyr*, *Matrix*, and *ggplot2*. For the analysis of AbSeq data, we would like to refer the reader to the respective tutorial by the developer team of *Seurat*: https://satijalab.org/seurat/v3.2/multimodal_vignette.html.

38. Downstream analysis

- a. Import scRNA-seq UMI count matrices data to R and divide gene expression, sample tag and, if available, AbSeq counts into separate matrices.
 - i. Data import

```
""{r}
dir <- "path/to/directory/" # set the path to the directory containing the gene expression quantifi-
cation output

mtx <- readMM(paste(dir, "umi/matrix.mtx", sep="/"))
genes <- read.delim(paste(dir, "umi/genes.tsv", sep="/"), header = F, stringsAsFactors = F)
bc <- read.delim(paste(dir, "umi/barcodes.tsv", sep="/"), header = F, stringsAsFactors = F)
mtx@Dimnames[[1]] <- as.character(genes$V1)
mtx@Dimnames[[2]] <- as.character(bc$V1)
""
```

Note: To speed up downstream processing, we can filter cell barcodes with less than a set number of UMIs.

```
""{r}
mtx <- mtx[,colSums(mtx)>250]
""
```

- ii. Separate sample tag quantifications and gene expression to new matrices

```
""{r}
sampletags <- c("SampleTag1", "SampleTag2", "SampleTag3", "SampleTag4", "SampleTag5",
"SampleTag6", "SampleTag7", "SampleTag8", "SampleTag9", "SampleTag10", "SampleTag11",
"SampleTag12")

# Separate the sample tag counts
mtx_sampletag <- mtx[mtx@Dimnames[[1]] %in% sampletags,]

# Separate AbSeq counts (optional)
mtx_AbSeq <- mtx[mtx@Dimnames[[1]] %in%
mtx@Dimnames[[1]][grep("^AB_", mtx@Dimnames[[1]])],]

# Separate the gene expression counts
mtx_counts <- mtx[!mtx@Dimnames[[1]] %in% c(sampletags,
mtx@Dimnames[[1]][grep("^AB_", mtx@Dimnames[[1]])],]
""
```

- b. Create a *Seurat* object using the gene expression count matrix and add the sample tag quantifications as a separate assay to the object.
 - i. Create *Seurat* object

```
""{r}
seurat <- CreateSeuratObject(counts = mtx_counts,
```

```

    assay = "RNA",
    min.cells = 5,
    min.features = 250,
    project = "Multiplexed BD Rhapsody WTA")
'''

```

ii. Add sample tag data as a separate assay to the Seurat object

```

'''{r}
seurat[["HTO"]] <- CreateAssayObject(counts = mtx_sampletag[,mtx_sampletag@Dimnames[[2]] %
in% Cells(seurat)])

```

```

# Optional: Filter cells with less than 1 tag reads
seurat <- subset(seurat, subset = nCount_HTO > 0)
'''

```

c. Perform standard quality control and filtering of cells.
i. Quality Control

```

'''{r}
seurat[["percent.mito"]] <- PercentageFeatureSet(seurat, pattern = "^MT-")

```

```

VlnPlot(object = seurat,
        features = "nFeature_RNA",
        pt.size = 0,
        group.by = "orig.ident") +
theme(legend.position="none")

```

```

VlnPlot(object = seurat,
        features = "nCount_RNA",
        log = TRUE,
        pt.size = 0,
        group.by = "orig.ident")+
theme(legend.position="none")

```

```

VlnPlot(object = seurat,
        features = "nCount_HTO",
        log = TRUE,
        pt.size = 0,
        group.by = "orig.ident")+
theme(legend.position="none")

```

```

VlnPlot(object = seurat,
        features = "percent.mito",
        pt.size = 0,
        group.by = "orig.ident")+
theme(legend.position="none")
'''

```

ii. Filter cells

Filter cells according to selected quality criteria, including the information content per cell, i.e., the number of detected features and the percentage of reads from mitochondrial genes.


```
""{r}
seurat <- subset(x = seurat, subset = nFeature_RNA > 250 &
                nFeature_RNA < 5000 &
                nCount_RNA > 500 &
                percent.mito < 25)
""
```

- d. Demultiplex cells from different samples based on the sample tag counts.
 - i. Sample tag-based demultiplexing

```
""{r}
# Normalize HTO data, here we use centered log-ratio (CLR) transformation
seurat <- NormalizeData(seurat, assay = "HTO", normalization.method = "CLR")

# Demultiplex
seurat <- HTODemux(seurat, assay = "HTO", positive.quantile = 0.99)

# Visualize demultiplexing results
ggplot(seurat@meta.data, aes(x = hash.ID, fill = hash.ID)) +
  geom_text(stat = 'count', aes(label = ..count..), vjust = 0) +
  geom_bar()

# Filter singlets
seurat_singlet <- subset(seurat, subset = HTO_classification.global == "Singlet")
""
```

- e. Perform normalization, scaling, variable gene selection, and dimension reduction on the data to get a global representation of the data structure.
 - i. Data normalization and dimension reduction

```
""{r}
# Normalization
seurat_singlet <- NormalizeData(object = seurat_singlet,
                               normalization.method = "LogNormalize",
                               scale.factor = 1e4)

# Define variable genes
seurat_singlet <- FindVariableFeatures(object = seurat_singlet,
                                     assay = "RNA",
                                     selection.method = 'vst')

# Scaling
seurat_singlet <- ScaleData(object = seurat_singlet,
                           vars.to.regress = c("nCount_RNA"))

# PCA
seurat_singlet <- RunPCA(object = seurat_singlet,
                        features = VariableFeatures(object = seurat_singlet))

# UMAP
seurat_singlet <- RunUMAP(seurat_singlet, reduction.use = "pca", dims = 1:20, seed.use = 42)

DimPlot(object = seurat_singlet,
```



```
reduction = 'umap',  
label = FALSE,  
group.by = "hash.ID")  
""
```

- f. Cluster the cells and determine cluster marker genes to understand the cluster identity and cell type composition.
 - i. Clustering

```
""{r}  
seurat_singlet <- FindNeighbors(object = seurat_singlet, dims = 1:20, reduction="pca", force.re-  
calc = TRUE)  
seurat_singlet <- FindClusters(object = seurat_singlet, resolution = 0.5, algorithm = 1)
```

```
DimPlot(object = seurat_singlet,  
reduction = 'umap',  
label = TRUE,  
group.by = "RNA_snn_res.0.5")  
""
```

- ii. Cluster marker gene identification

```
""{r}  
Idents(seurat_singlet) <- "RNA_snn_res.0.5"  
cluster.markers.wilcox <- FindAllMarkers(object = seurat_singlet,  
only.pos = TRUE,  
min.pct = 0.2,  
logfc.threshold = 0.25,  
min.diff.pct = 0.1,  
test.use = "wilcox")
```

```
top <- cluster.markers.wilcox %>% group_by(cluster) %>% top_n(n = 5, wt = avg_logFC)
```

```
DotPlot(seurat_singlet,  
group.by = "RNA_snn_res.0.5",  
features = unique(top$gene))  
""
```

EXPECTED OUTCOMES

After demultiplexing, stringent quality control and filtering of low-quality cells, we expect to retrieve approximately 15,000 to 20,000 high quality single-cell transcriptomes per BD Rhapsody cartridge super-loaded with 60,000 cells. In case of successful oligo-coupled antibody-based sample multiplexing, we expect the cells to be equally originating from the 12 originally multiplexed samples and representing all major cell types present in the human peripheral blood at physiological or pathological proportions. For more detailed information on the quality of the data, the possible downstream analyses and *in silico* applications and their biological meaningfulness, we would like to refer the reader to [Schulte-Schrepping et al., \(2020\)](#).

LIMITATIONS

One of the limitations is the lack of BD imaging. The imaging functionality of the BD Rhapsody system cannot be used following the strict safety instructions described above.

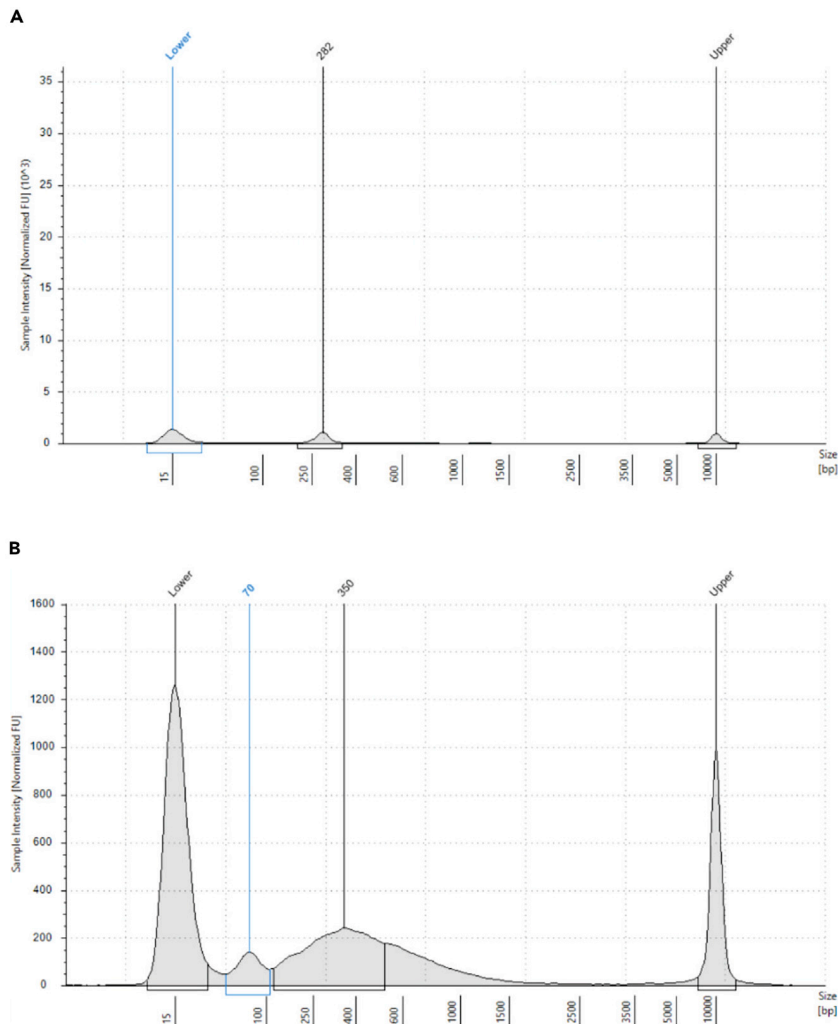


Figure 10. TapeStation profile with low DNA concentration or unexpected peak

Moreover, due to the size of the microwells in the BD cartridge, this system is not suitable for large cell types. A substantial decline in the number of recovered cells has been already recorded for cells with a diameter bigger than 20 μm . In this case additional cells can be loaded into the cartridge to offset the losses observed.

In addition, no multi-omic solution (e.g., scRNA-seq and scATAC-seq) from BD is available at this point in time. Further developments, however, are expected for this platform as well.

TROUBLESHOOTING

Problem 1

Product concentration lower than required in one of the quality control steps (steps 24, 26, 28, 29; [Figure 10A](#))

Potential solution

If the library concentration in one of the QC steps is too low, it is possible to repeat the step optimizing the number of PCR cycles. Note that increasing the number of PCR cycles will reduce the complexity of the final library impacting the sequencing performance. Therefore, it is recommended

to start with one or just few cycles. It is also possible to re- start the entire procedure using the exonuclease-treated beads.

Problem 2

Unexpected peak in the TapeStation profile after SPRIbead cleaning steps (steps 24, 28, 29; Figure 10B)

Potential solution

Poor bead cleaning procedure can result in peaks with smaller size (<165 bp). In this case, it is possible to repeat the bead cleaning step using the same ratio. However, it is important to consider that repeating a cleaning step will entail the loss of a certain amount of sample product. Therefore, sample concentration should also be taken into account before repeating this step.

Problem 3

Low number of cells for flow cytometry after RCB lysis (step 31).

Potential solution

If the number of cells is > 0.5 million, continue with the procedure as described, pay special attention in all washing steps to avoid excessive loss of cells. If the number is lower, check temperature and concentration of the RBC lysis buffer, wrong concentration or too high temperature of the buffer can be a common cause of loss of cells during the purification procedure.

RESOURCE AVAILABILITY

Lead contact

Further information and requests for resources and reagents should be directed to and will be fulfilled by the Lead Contact, Joachim L. Schultze (j.schultze@uni-bonn.de).

Materials availability

This study did not generate new unique reagents.

Data and code availability

ScRNA-seq data generated using this protocol and published in [Schulte-Schrepping et al. \(2020\)](#) are deposited at the European Genome-phenome Archive (EGA) under access number EGAS00001004571, which is hosted by the EBI and the CRG. Furthermore, respective count data has been uploaded to the online analysis platform FASTGenomics for easy access and direct use under https://beta.fastgenomics.org/p/schulte-schrepping_covid19.

ACKNOWLEDGMENTS

J.L.S. was funded by the BMBF-funded excellence project Diet–Body–Brain (DietBB) under grant number 01EA1809A and by EU project SYSCID under grant number 733100.

AUTHOR CONTRIBUTIONS

Writing and reviewing, E.D.D., L.B., J.S.-S., K.H., M.B., and J.L.S.

DECLARATION OF INTERESTS

The authors declare no competing interests.

REFERENCES

- Butler, A., Hoffman, P., Smibert, P., Papalexi, E., and Satija, R. (2018). Integrating single-cell transcriptomic data across different conditions, technologies, and species. *Nat. Biotechnol.* 36, 411–420.
- Cossarizza, A., Chang, H.-D., Radbruch, A., Acs, A., Adam, D., Adam-Klages, S., Agace, W.W., Aghaeepour, N., Akdis, M., Allez, M., et al. (2019). Guidelines for the use of flow cytometry and cell sorting in immunological studies (second edition). *Eur. J. Immunol.* 49, 1457–1973.
- Dobin, A., Davis, C.A., Schlesinger, F., Drenkow, J., Zaleski, C., Jha, S., Batut, P.,

Chaisson, M., and Gingeras, T.R. (2013). STAR: ultrafast universal RNA-seq aligner. *Bioinformatics* 29, 15–21.

Macosko, E.Z., Basu, A., Satija, R., Nemesh, J., Shekhar, K., Goldman, M., Tirosh, I., Bialas, A.R., Kamitaki, N., Martersteck, E.M., et al. (2015). Highly parallel genome-wide expression profiling of individual cells using nanoliter droplets. *Cell* 161, 1202–1214.

Martin, M. (2011). Cutadapt removes adapter sequences from high-throughput sequencing reads. *EMBnet. J.* 17, 10.

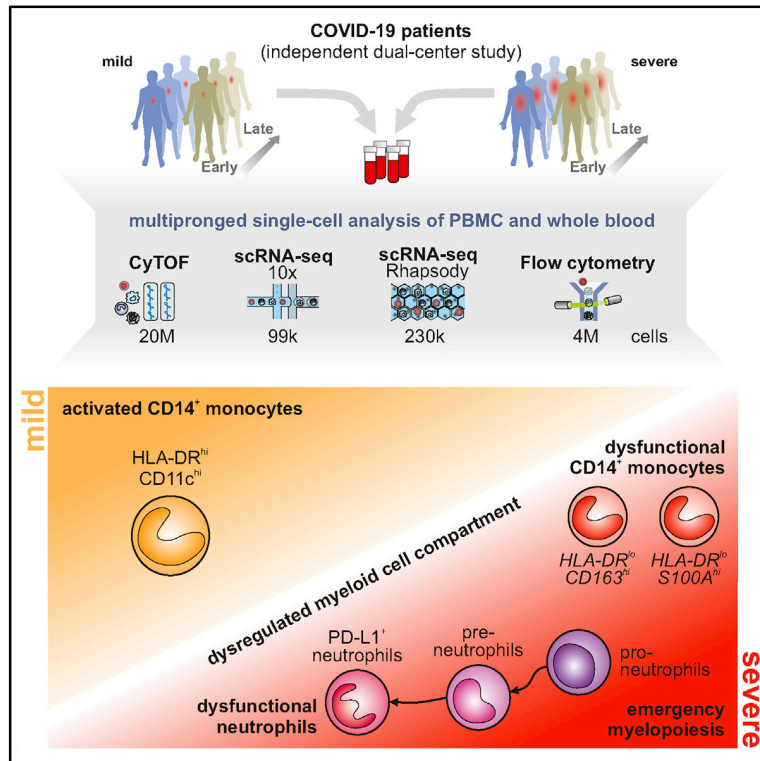
Schulte-Schrepping, J., Reusch, N., Paclik, D., Baßler, K., Schlickeiser, S., Zhang, B., Krämer, B., Krammer, T., Brumhard, S., Bonaguro, L., et al. (2020). Severe COVID-19 is marked by a dysregulated myeloid cell compartment. *Cell* 182, 1419–1440.e23.

Stoeckius, M., Zheng, S., Houck-Loomis, B., Hao, S., Yeung, B.Z., Mauck, W.M., Smibert, P., and Satija, R. (2018). Cell Hashing with barcoded antibodies enables multiplexing and doublet detection for single cell genomics. *Genome Biol.* 19, 224.

Stuart, T., Butler, A., Hoffman, P., Hafemeister, C., Papalexi, E., Mauck, W.M., Hao, Y., Stoeckius, M., Smibert, P., and Satija, R. (2019). Comprehensive integration of single-cell data. *Cell* 177, 1888–1902.e21.

Severe COVID-19 Is Marked by a Dysregulated Myeloid Cell Compartment

Graphical Abstract



Authors

Jonas Schulte-Schrepping, Nico Reusch, Daniela Paclik, ..., Antoine-Emmanuel Saliba, Leif Erik Sander, Deutsche COVID-19 OMICS Initiative (DeCOI)

Correspondence

j.schultze@uni-bonn.de

In Brief

Analysis of patients with mild and severe COVID-19 reveals the presence of dysfunctional neutrophils in the latter that is linked to emergency myelopoiesis.

Highlights

- SARS-CoV-2 infection induces profound alterations of the myeloid compartment
- Mild COVID-19 is marked by inflammatory $HLA-DR^{hi}CD11c^{hi}CD14^{+}$ monocytes
- Dysfunctional $HLA-DR^{lo}CD163^{hi}$ and $HLA-DR^{lo}S100A^{hi}CD14^{+}$ monocytes in severe COVID-19
- Emergency myelopoiesis with immature and dysfunctional neutrophils in severe COVID-19



Article

Severe COVID-19 Is Marked by a Dysregulated Myeloid Cell Compartment

Jonas Schulte-Schrepping,^{1,23} Nico Reusch,^{1,23} Daniela Paclik,^{2,23} Kevin Baßler,^{1,23} Stephan Schlickeiser,^{2,3,23} Bowen Zhang,^{4,23} Benjamin Krämer,^{5,23} Tobias Krammer,^{6,23} Sophia Brumhard,^{7,23} Lorenzo Bonaguro,^{1,23} Elena De Domenico,^{8,23} Daniel Wendisch,^{7,23} Martin Grasshoff,⁴ Theodore S. Kapellos,¹ Michael Beckstette,⁴ Tal Pecht,¹ Adem Saglam,⁸ Oliver Dietrich,⁶ Henrik E. Mei,⁹ Axel R. Schulz,⁹ Claudia Conrad,⁷ Désirée Kunkel,¹⁰ Ehsan Vafadarnejad,⁶ Cheng-Jian Xu,^{4,11} Arik Horne,¹ Miriam Herbert,¹ Anna Drews,⁸ Charlotte Thibeault,⁷ Moritz Pfeiffer,⁷ Stefan Hippenstiel,^{7,12} Andreas Hocke,^{7,12} Holger Müller-Redetzky,⁷ Katrin-Moira Heim,⁷ Felix Machleidt,⁷ Alexander Uhrig,⁷ Laure Bosquillon de Jarcy,⁷ Linda Jürgens,⁷ Miriam Stegemann,⁷ Christoph R. Glösenkamp,⁷ Hans-Dieter Volk,^{2,3,13} Christine Goffinet,^{14,15} Markus Landthaler,¹⁶ Emanuel Wyler,¹⁶ Philipp Georg,⁷ Maria Schneider,² Chantip Dang-Heine,¹⁷ Nick Neuwinger,^{13,18} Kai Kappert,^{13,18} Rudolf Tauber,^{13,18} Victor Corman,¹⁴ Jan Raabe,⁵ Kim Melanie Kaiser,⁵ Michael To Vinh,⁵ Gereon Rieke,⁵ Christian Meisel,^{2,13} Thomas Ulas,⁸

(Author list continued on next page)

¹Life and Medical Sciences (LIMES) Institute, University of Bonn, Germany

²Institute of Medical Immunology, Charité, Universitätsmedizin Berlin, Berlin, Germany

³BIH Center for Regenerative Therapies, Charité, Universitätsmedizin Berlin, and Berlin Institute of Health (BIH) Berlin, Germany

⁴Centre for Individualised Infection Medicine (CiIM) and TWINCORE, joint ventures between the Helmholtz-Centre for Infection Research (HZI) and the Hannover Medical School (MHH), Hannover, Germany

⁵Department of Internal Medicine I, University Hospital Bonn, Bonn, Germany

⁶Helmholtz Institute for RNA-based Infection Research (HIRI), Helmholtz-Center for Infection Research (HZI), Würzburg, Germany

⁷Department of Infectious Diseases and Respiratory Medicine, Charité, Universitätsmedizin Berlin, Berlin, Germany

⁸German Center for Neurodegenerative Diseases (DZNE), PRECISE Platform for Genomics and Epigenomics at DZNE, and University of Bonn, Bonn, Germany

⁹Mass Cytometry Lab, DRFZ Berlin, a Leibniz Institute, Berlin, Germany

¹⁰Flow and Mass Cytometry Core Facility, Charité, Universitätsmedizin Berlin, and Berlin Institute of Health (BIH), Berlin, Germany

¹¹Department of Internal Medicine and Radboud Center for Infectious Diseases, Radboud University Medical Center, Nijmegen, the Netherlands

¹²German Center for Lung Research (DZL)

¹³Department of Immunology, Labor Berlin-Charité Vivantes, Berlin, Germany

¹⁴Institute of Virology, Charité Universitätsmedizin Berlin, Berlin, Germany

(Affiliations continued on next page)

SUMMARY

Coronavirus disease 2019 (COVID-19) is a mild to moderate respiratory tract infection, however, a subset of patients progress to severe disease and respiratory failure. The mechanism of protective immunity in mild forms and the pathogenesis of severe COVID-19 associated with increased neutrophil counts and dysregulated immune responses remain unclear. In a dual-center, two-cohort study, we combined single-cell RNA-sequencing and single-cell proteomics of whole-blood and peripheral-blood mononuclear cells to determine changes in immune cell composition and activation in mild versus severe COVID-19 (242 samples from 109 individuals) over time. HLA-DR^{hi}CD11c^{hi} inflammatory monocytes with an interferon-stimulated gene signature were elevated in mild COVID-19. Severe COVID-19 was marked by occurrence of neutrophil precursors, as evidence of emergency myelopoiesis, dysfunctional mature neutrophils, and HLA-DR^{lo} monocytes. Our study provides detailed insights into the systemic immune response to SARS-CoV-2 infection and reveals profound alterations in the myeloid cell compartment associated with severe COVID-19.

INTRODUCTION

Clinical presentations of COVID-19 are highly variable, and while the majority of patients experiences mild to moderate symptoms, 10%–20% of patients develop pneumonia and severe disease (Huang et al., 2020a; Wang et al., 2020; Zhou et al., 2020a). Clinical

deterioration with respiratory failure and acute respiratory distress syndrome (ARDS) typically develops in the second week of disease. This kinetic may suggest a role for secondary immune responses in the development of severe COVID-19 (Ong et al., 2020). However, the exact mechanisms that govern the pathophysiology of the different disease courses of COVID-19 remain ill-defined.



Matthias Becker,⁸ Robert Geffers,¹⁹ Martin Witzenrath,^{7,12} Christian Drosten,^{14,20} Norbert Suttorp,^{7,12} Christof von Kalle,¹⁷ Florian Kurth,^{7,21,22} Kristian Händler,⁸ Joachim L. Schultze,^{1,8,23,24,25,*} Anna C. Aschenbrenner,^{1,11,23,24} Yang Li,^{4,11,23,24} Jacob Nattermann,^{5,20,23,24} Birgit Sawitzki,^{2,23,24} Antoine-Emmanuel Saliba,^{6,23,24} and Leif Erik Sander^{7,12,23,24} Deutsche COVID-19 OMICS Initiative (DeCOI)

¹⁵Berlin Institute of Health (BIH), Berlin, Germany

¹⁶Berlin Institute for Medical Systems Biology, Max-Delbrück-Center for Molecular Medicine in the Helmholtz Association, Berlin, Germany

¹⁷Clinical Study Center (CSC), Charité, Universitätsmedizin Berlin, and Berlin Institute of Health, Berlin, Germany

¹⁸Institute of Laboratory Medicine, Clinical Chemistry, and Pathobiochemistry, Charité, Universitätsmedizin Berlin, Berlin, Germany

¹⁹Genome Analytics, Helmholtz-Center for Infection Research (HZI), Braunschweig, Germany

²⁰German Center for Infection Research (DZIF)

²¹Department of Tropical Medicine, Bernhard Nocht Institute for Tropical Medicine, Hamburg, Germany

²²I. Department of Medicine, University Medical Center, Hamburg-Eppendorf, Hamburg, Germany

²³These authors contributed equally

²⁴Senior author

²⁵Lead Contact

*Correspondence: j.schultze@uni-bonn.de

<https://doi.org/10.1016/j.cell.2020.08.001>

Single-cell studies of bronchoalveolar lavage samples have suggested a complex dysregulation of the pulmonary immune response in severe COVID-19 (Chua et al., 2020; Liao et al., 2020). Overall, systemic inflammation is linked to an unfavorable clinical course of disease and the development of severe COVID-19 (Giamarellos-Bourboulis et al., 2020; Lucas et al., 2020; Ong et al., 2020). SARS-CoV-2 infection induces specific T cell and B cell responses, which is reflected by elevation of SARS-CoV-2 peptide-specific T cells (Braun et al., 2020; Grifoni et al., 2020) and the production of SARS-CoV-2-specific antibodies (Long et al., 2020; Ni et al., 2020; Robbiani et al., 2020). Patients with severe COVID-19 have high systemic levels of inflammatory cytokines, particularly interleukin (IL)-6 and IL-1 β (Chen et al., 2020; Giamarellos-Bourboulis et al., 2020; Lucas et al., 2020; Ong et al., 2020), whereas interferon (IFN) responses appear blunted, as shown by whole blood transcriptomics (Hadjadj et al., 2020) and plasma profiling (Trouillet-Assant et al., 2020). A number of studies and regular clinical observations indicate an increase of neutrophils and a decrease of non-classical (CD14^{lo}CD16^{hi}) monocytes in severe COVID-19 (Hadjadj et al., 2020; Merad and Martin, 2020; Sanchez-Cerrillo et al., 2020). Profound immune dysregulation is commonly observed in severe infections and sepsis, characterized by a progression from hyperinflammatory states to immunosuppression (Remy et al., 2020; Ritchie and Sinaganayagam, 2020), and similar mechanisms have been proposed for severe COVID-19 (Giamarellos-Bourboulis et al., 2020). Yet, comprehensive insights into the immunopathology of severe COVID-19 are still missing. Exacerbated immune responses played a major role in the pathophysiology of SARS, leading to severe lung injury and respiratory failure (Perلمان and Dandekar, 2005). Mitigation of immunodysregulation is therefore viewed as a major therapeutic avenue for the treatment and prevention of severe COVID-19 (Dimopoulos et al., 2020; Jamilloux et al., 2020). In support of this view, a recent multicenter study reported that dexamethasone treatment significantly reduced mortality in hospitalized patients with COVID-19, particularly in patients on mechanical ventilation (Horby et al., 2020). Previous studies of peripheral blood mononuclear cell (PBMC) transcriptomes in a small number of patients with COVID-19 revealed changes in several cellular compartments, including monocytes, natural killer (NK) cells, dendritic cells (DCs), and T cells (Lee et al., 2020; Wilk et al., 2020).

The heterogeneity of clinical manifestations and the complexity of immune responses to COVID-19 highlight the need for detailed analyses using high-resolution techniques and well-characterized clinical cohorts. We hypothesized that distinct responses, particularly within the innate immune system, underlie the different clinical trajectories of COVID-19 patients (Chua et al., 2020; Kuri-Cervantes et al., 2020; Mathew et al., 2020; McKechnie and Blish, 2020). Here, we used single-cell transcriptomics and single-cell proteomics to analyze immune responses in blood samples in two independent cohorts of COVID-19 patients.

Activated HLA-DR^{hi}CD11c^{hi}CD14⁺ monocytes were increased in patients with mild COVID-19, similar to patients with SARS-CoV-2 negative flu-like illness (“FLI”). In contrast, monocytes characterized by low expression of *HLA-DR*, and marker genes indicative of anti-inflammatory functions (e.g., *CD163* and *PLA2G8*) appeared in patients with severe COVID-19. The granulocyte compartment was profoundly altered in severe COVID-19, marked by the appearance of neutrophil precursors due to emergency myelopoiesis, dysfunctional neutrophils expressing PD-L1, and exhibiting an impaired oxidative burst response. Collectively, our study links highly dysregulated myeloid cell responses to severe COVID-19.

RESULTS

Dual Center Cohort Study to Assess Immunological Alterations in COVID-19 Patients

In order to probe the divergent immune responses in mild versus severe COVID-19, we analyzed blood samples collected from independent patient cohorts at two university medical centers in Germany. Samples from the Berlin cohort (cohort 1) (Kurth et al., 2020), were analyzed by mass cytometry (CyTOF) and single-cell RNA-sequencing (scRNA-seq) using a droplet-based single-cell platform (10x Chromium), while samples from the Bonn cohort (cohort 2) were analyzed by multi-color flow cytometry (MFCF) and on a microwell-based scRNA-seq system (BD Rhapsody). We analyzed a total of 24 million cells by their protein markers and >328,000 cells by scRNA-seq in 242 samples from 53 COVID-19 patients and 56 controls, including 8 patients with FLI (Figures 1A, 1B, and S1A; Table S1).

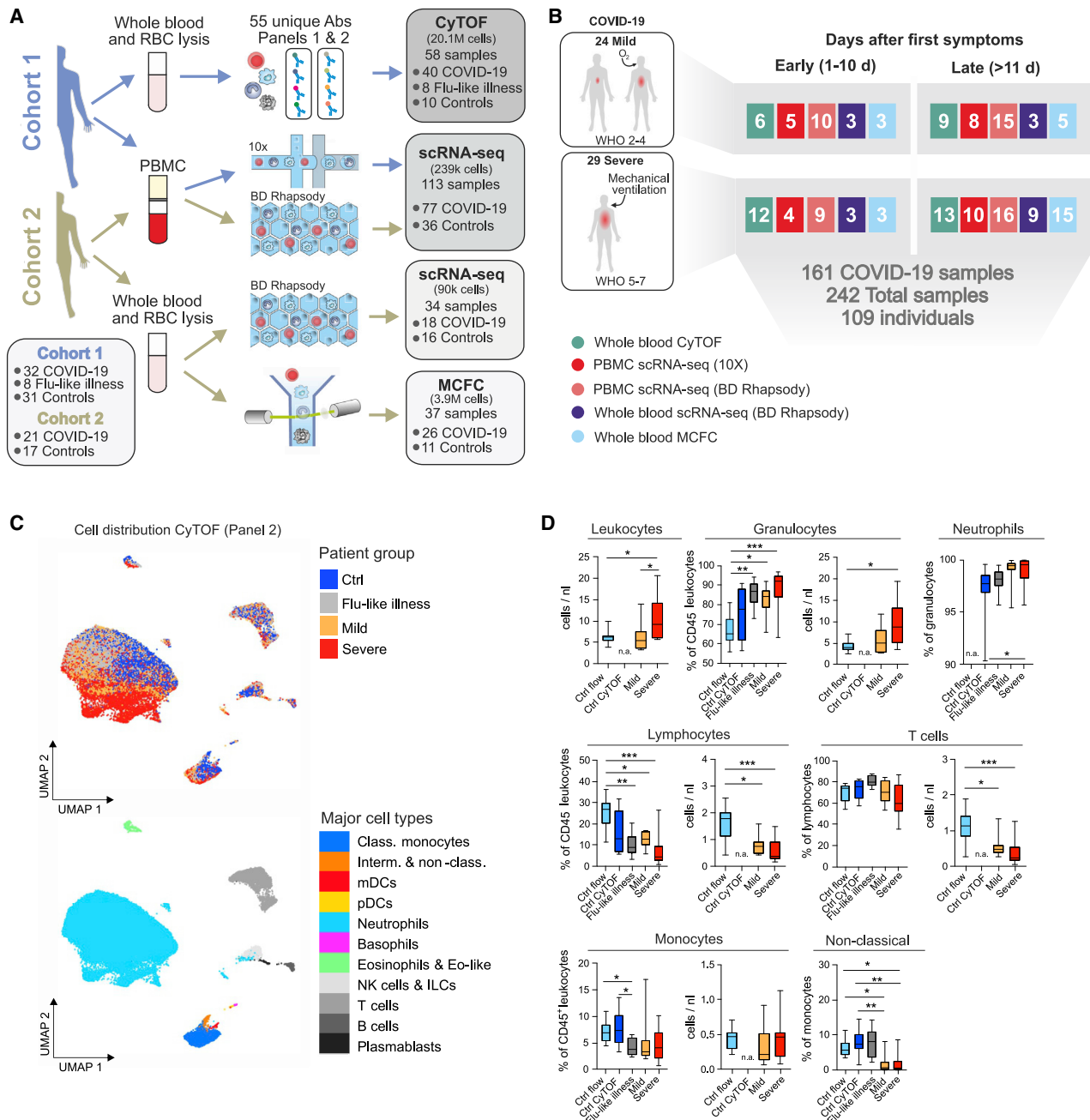


Figure 1. Cohort Definition and Single-Cell Multi-omics Analysis Strategy

(A) Pipeline for control and COVID-19 blood samples of the two cohorts (see also Table S1). Whole blood samples were subjected to red blood cell (RBC) lysis and processed for CyTOF mass cytometry (two antibody panels), multi-color flow cytometry (MCFC), or scRNA-seq (BD Rhapsody). PBMCs were isolated by density centrifugation and processed directly or after frozen storage, labeled with cell hashing antibodies and loaded on droplet-based (10x) or microwell-based (BD Rhapsody) scRNA-seq platforms. Box (bottom left): number of subjects in each cohort. Boxes (on the right): number of samples analyzed with each technique. (B) Number of samples per technique summarized across cohorts, divided by disease severity according to WHO ordinal scale and by the time after onset of first symptoms (early: days 0–10, late: >day 11).

(C) UMAP of CD45⁺ leukocytes, down-sampled to 70,000 cells, from mass cytometry using antibody panel 2 (30 markers, Table S2). Cells are colored according to donor origin (blue, age-matched controls; gray, FLI; yellow, mild COVID-19; red, severe COVID-19) and major lineage subtypes.

(D) Box and whisker (10–90 percentile) plots of major cell lineage composition in whole blood from FLI (n = 8), COVID-19 patients with mild (n = 8) or severe disease (n = 9), age-matched controls measured by mass cytometry (ctrl CyTOF, n = 9) or by flow cytometry (ctrl flow, n = 19) (Kverneland et al., 2016). Kruskal-Wallis and Dunn's multiple comparison test *p < 0.05, **p < 0.01, ***p < 0.001, ****p < 0.0001. n.a., not available.

See also Figure S1 and Table S3.

We first characterized alterations of the major leukocyte lineages by mass cytometry on whole blood samples from 20 COVID-19 patients collected between day 4 and day 29 after symptom onset and compared them to 10 age- and gender-matched controls and 8 FLI patients. We designed two antibody panels to specifically capture alterations in mononuclear leukocytes (lymphocytes, monocytes, and DCs, panel 1), and in granulocytes (Table S2, panel 2). High-resolution SPADE analysis was performed with 400 target nodes and individual nodes were aggregated into cell subsets based on lineage-specific markers, such as CD14 for monocytes and CD15 for neutrophils (Figure S1B). Uniform manifold approximation and projection (UMAP) analysis revealed distinct clustering of samples from COVID-19 patients, FLI, and healthy controls, with marked changes of the monocyte and granulocyte compartment (Figure 1C). Leukocyte lineages were compared in the earliest available samples in COVID-19 patients (days 4–13), FLI, and controls (Figure 1D; Table S1). Because leukocyte counts were not available for all control samples, we compared the control samples for CyTOF (“ctrl CyTOF”) to data from our recently published healthy control cohorts (“ctrl flow”) (Kverneland et al., 2016; Sawitzki et al., 2020). The proportions of all major lineages were highly similar, irrespective of the methodology (Figure 1D). Cell counts of the published cohort could therefore be used as a reference to report absolute cell counts for leukocyte lineages in COVID-19 samples. In line with recent reports (Barnes et al., 2020; Xia et al., 2020), we observed elevated leukocytes and increased proportions of neutrophils in patients with severe COVID-19 (Figure 1D), whereas only proportional increases in neutrophils were evident in FLI and mild COVID-19 patients (Figure 1D). Total lymphocytes and T cells were strongly reduced in all COVID-19 and FLI patients, whereas non-classical monocytes were specifically depleted in COVID-19 (Figure 1D). Increased neutrophils in severe COVID-19 and loss of non-classical monocytes in both mild and severe disease were validated in cohort 2 by MCFC (Figure S1C; Tables S1 and S3).

Thus, SARS-CoV-2 infection is associated with lymphopenia and profound alterations of the myeloid compartment.

Severity-Dependent Alterations of the Myeloid Cell Compartment in COVID-19

Given the dramatic changes in various immune cell populations (Figures 1C and 1D), we next assessed their composition and activation state by droplet-based scRNA-seq in 27 samples from 18 COVID-19 patients (8 mild and 10 severe, cohort 1, Table S1)

collected between day 3 and day 20 after symptom onset. A total of 48,266 single-cell transcriptomes of PBMCs were analyzed together with 50,783 PBMCs from publicly available control datasets (21 control donors, Table S1). UMAP and high-resolution cell type classification identified all cell types expected in the mononuclear compartment of blood with a high granularity in the monocytes, identifying five distinct clusters (clusters 0–4) (Figures 2A and S2A; Table S4). Monocytes in clusters 0–3 expressed *CD14*, and cluster 4 comprised the non-classical monocytes marked by *FCGR3A* (encoding CD16a) and low expression of *CD14*. Separate visualization of cells in mild and severe cases revealed highly disease severity-specific clusters (Figure 2B). A distinct subset of *CD14*⁺ monocytes (cluster 1) (Figure 2A) marked by high expression of *HLA-DRA*, *HLA-DRB1*, and co-stimulatory molecule *CD83* (Figure S2D), the engagement of which has been linked to prolonged expansion of antigen-specific T cells (Hirano et al., 2006), was selectively detected in mild COVID-19 (Figure 2C). In addition, we identified another closely related *CD14*⁺*HLA-DR*^{hi} monocyte population (cluster 2), which was characterized by high expression of IFN-stimulated genes (ISGs). However, upon closer analysis, this cluster was found to originate from a single donor with mild COVID-19 (Figures 2A–2C and S2D). Both cluster 1 and cluster 2 expressed high levels of ISGs *IFI6* and *ISG15* (Figure S2D). In patients with severe COVID-19, monocytes showed low expression of *HLA-DR* and high expression of alarmins *S100A8/9/12* (cluster 3, Figures 2A–2C and S2D). The most prominent change in severe COVID-19 was the appearance of two distinct cell populations (cluster 5+6), absent in PBMCs of patients with mild COVID-19 and control donors (Figure 2A). Published markers (Kwok et al., 2020; Ng et al., 2019) identified clusters 5 and 6 as neutrophils and immature neutrophils, respectively (Figures 2A and 2B). Immature neutrophils (cluster 6) expressed *CD24*, *PGLYRP1*, *DEFA3*, and *DEFA4*, whereas neutrophil cluster 5 expressed *FCGR3B* (CD16b), *CXCL8*, and *LCN2* (lipocalin 2) (Figures 2C and S2A). Their migration within the PBMC fraction on a density gradient marked these cells as low-density neutrophils (LDNs).

In the second cohort, PBMCs from 17 COVID-19 patients (8 mild, 9 severe, Table S1), sampled between 2 and 25 days after symptom onset, and 13 controls, were collected for scRNA-seq on a microwell-based platform (BD Rhapsody). High-quality single-cell transcriptomes for 139,848 PBMCs were assessed and their population structure was visualized using UMAP (Figure 2D; Table S4). Data-driven cell-type classification (Aran et al., 2019) and cluster-specific marker gene expression identified all cell

Figure 2. scRNA-Seq of PBMC from Patients of the Two Independent Cohorts

(A) UMAP visualization of scRNA-seq profiles (10x, cohort 1) of 99,049 PBMC from 49 samples (8 mild, 10 severe patients, different time points) and 22 control samples colored according to cell type classification (Louvain clustering), reference-based cell-type annotation, and marker gene expression (Table S4).

(B) UMAP shown in (A) colored according to disease severity (yellow, mild COVID-19; red, severe COVID-19).

(C) Dot plots of the intersection of the top 20 marker genes sorted by average log fold change determined for the indicated myeloid cell subsets in the PBMC datasets of both cohorts.

(D) UMAP visualization of scRNA-seq profiles (BD Rhapsody, cohort 2) of 139,848 PBMCs (50 samples of 8 mild, 9 severe COVID-19; 14 samples of 13 controls; different time points), coloring as in (A) (see also Figure S2A and Table S4).

(E) Box and whisker plots (25–75 percentile) of percentages of cell subsets of total PBMC (per patient). Boxes are colored according to disease group and dots according to the respective cohort of the sample. Dirichlet-multinomial regression adjusted with the Benjamini-Hochberg method, **p* < 0.05, ***p* < 0.01, ****p* < 0.001.

See also Table S1.

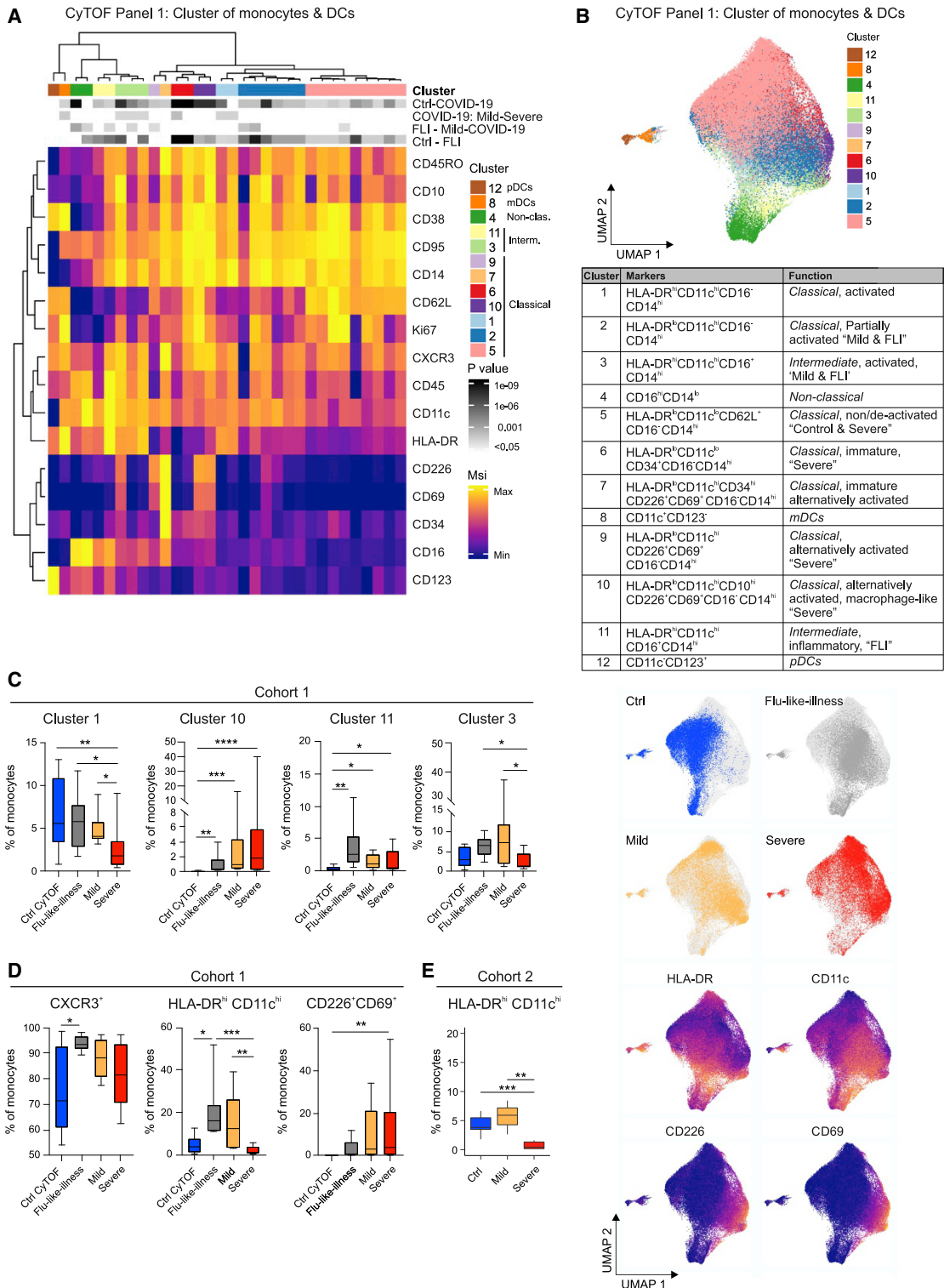


Figure 3. CD11c^{lo} and HLA-DR^{lo} but CD226⁺CD69⁺ Monocytes in Severe COVID-19

(A) Heatmap of CyTOF data (antibody panel 1, cohort 1) covering monocytes and DCs. Main cell, as defined by the numbers 1 to 12, and individual cell clusters are displayed in columns and marker identity is indicated in rows. MSI, marker staining intensity respective expression level, significance level for the following comparisons: (1) controls (ctrl, n = 9) versus COVID-19 (mild and severe, n = 17, first row), (2) mild (n = 8) versus severe (n = 9, second row), (3) FLI (n = 8) versus

(legend continued on next page)

types expected in the PBMC compartment and revealed additional clusters and substructures (Figures 2D and S2B). Similar to cohort 1, monocytes exhibited significant plasticity and were subclassified into 5 clusters (Figure 2D, clusters 0–4). Disease-severity-associated changes seen in cohort 1 were validated in cohort 2 (Figure 2E). Immature and mature neutrophil clusters were detected in both cohorts (clusters 5–6) and showed near identical marker gene expression (Figure 2C). Similar to cohort 1, a prominent shift in subpopulation occupancy was observed in the monocyte clusters (Figures 2D and 2E).

Based on the union of the top 50 genes for monocyte and neutrophil clusters, we found a high correlation between the independently defined functional states within the monocyte compartment, and mature and immature neutrophils in cohort 1 and cohort 2 (Figure S2C). Violin plot representation of important marker genes illustrated distinct phenotypic states and underscored the high similarity of the two cohorts (Figure S2D).

Disease-severity-dependent alterations of the monocyte compartment and the appearance of two LDN populations were detected in two cohorts of COVID-19 patients.

Predominance of HLA-DR^{hi}CD11c^{hi} Inflammatory Monocytes in Mild and HLA-DR^{lo}CD11c^{lo}CD226⁺CD69⁺ Monocytes in Severe COVID-19

The monocyte compartment is particularly affected by COVID-19, indicated by a loss of CD14^{lo}CD16^{hi} non-classical monocytes (Figures 1C and 1D). Disease-severity-dependent shifts in monocyte activation were identified by scRNA-seq (Figure 2). We further explored the phenotypic alterations of the monocyte compartment using mass cytometry (Table S2, panel 1) on whole blood samples from COVID-19 patients with a mild or severe disease (n = 8+9), patients with FLI (n = 8), and age- and gender-matched controls (n = 9, all collected within cohort 1, Table S1). Unsupervised cluster analysis using 15 surface antigens and the proliferation marker Ki67 separated the monocyte and DC compartment into 12 main cell clusters (Figures 3A and 3B). Classical CD14^{hi}CD16⁻ monocytes displayed high heterogeneity and separated into seven main subclusters. Most classical monocytes showed high expression of activation markers CD38, CD95, and CXCR3. The four most prevalent clusters (1, 2, 5, and 6) varied according to CD62L, HLA-DR,

CD11c, and Ki67 expression, with CD62L and HLA-DR showing a reverse expression pattern (Figure 3A). Cluster 1 displayed an activated inflammatory phenotype with high co-expression of CD11c and HLA-DR (Bernardo et al., 2018; Janols et al., 2014). In addition, we observed classical monocyte cell clusters (7, 9, and 10) with high CD226 and CD69 but low HLA-DR expression and thus signs of altered or alternative activation (Davison et al., 2017; Raymond et al., 2004; Vo et al., 2016). Among the HLA-DR^{lo} clusters, particularly cluster 7 showed high expression of CD34 indicative of a more immature phenotype. In contrast, the majority of CD14^{hi}CD16⁺ intermediate monocyte cell clusters showed high CD11c and HLA-DR expression.

Monocytes from COVID-19 patients separated from those of FLI patients and controls (Figure 3B), mainly based on elevated CD226 and CD69 expression in COVID-19. Monocytes in mild and severe COVID-19 clustered separately, and monocytes from mild COVID-19 clustered closer to monocytes in FLI. FLI patients and mild COVID-19 contained higher proportions of HLA-DR^{hi}CD11c^{hi} cells (clusters 3 and 11), and total HLA-DR^{hi}CD11c^{hi} monocytes were higher compared to controls and severe COVID-19, reflecting blunted monocyte activation in severe COVID-19, reminiscent of observations in sepsis (Janols et al., 2014) (Figures 3A, 3C, and 3D). Increased levels of activated HLA-DR^{hi}CD11c^{hi} monocytes in mild COVID-19 patients were confirmed by MCFC in cohort 2 (Figure 3E). In severe COVID-19, we detected increased expression of CD226 and CD69 (cluster 10) and/or decreased expression of HLA-DR, and total CD226⁺CD69⁺ monocytes were elevated compared to controls. Cluster 10 expressed high levels of CD10, which is induced during macrophage differentiation (Huang et al., 2020b). Thus, an alternative activation pattern of classical monocytes appeared to be COVID-19-specific and was associated with severe disease. Besides activated lymphocytes, monocytes also upregulate CD69 expression (Davison et al., 2017), which promotes tissue infiltration and retention (Cibrián and Sánchez-Madrid, 2017). Similarly, CD226 expression on alternatively activated monocytes might also promote diapedesis and tissue infiltration (Raymond et al., 2004). Together, this activation pattern may contribute to the reduction of circulating monocytes in COVID-19.

mild COVID-19 (n = 8, third row), as well as (4) controls (ctrl, n = 9) versus FLI (n = 8) are indicated using a gray scale on top of the heatmap (p value scale next to heatmap). COVID-19 samples collected between days 4 and 13 post-symptom onset (= first day of sample collection per patient). Abundance testing via generalized mixed effects models and multiple comparison adjustment using the Benjamini-Hochberg procedure and a false discovery rate (FDR) cutoff of 5% across all clusters/subsets and between-group comparisons.

(B) UMAP of monocytes and DCs, down-sampled to 70,000 cells, (39 markers, Table S2). Cells are colored according to main cell clusters (1 to 12, colors as in A) as defined in the table, donor origin (blue, controls; gray, FLI; yellow, mild COVID-19; red, severe COVID-19) and expression intensity of HLA-DR, CD11c, CD226, and CD69.

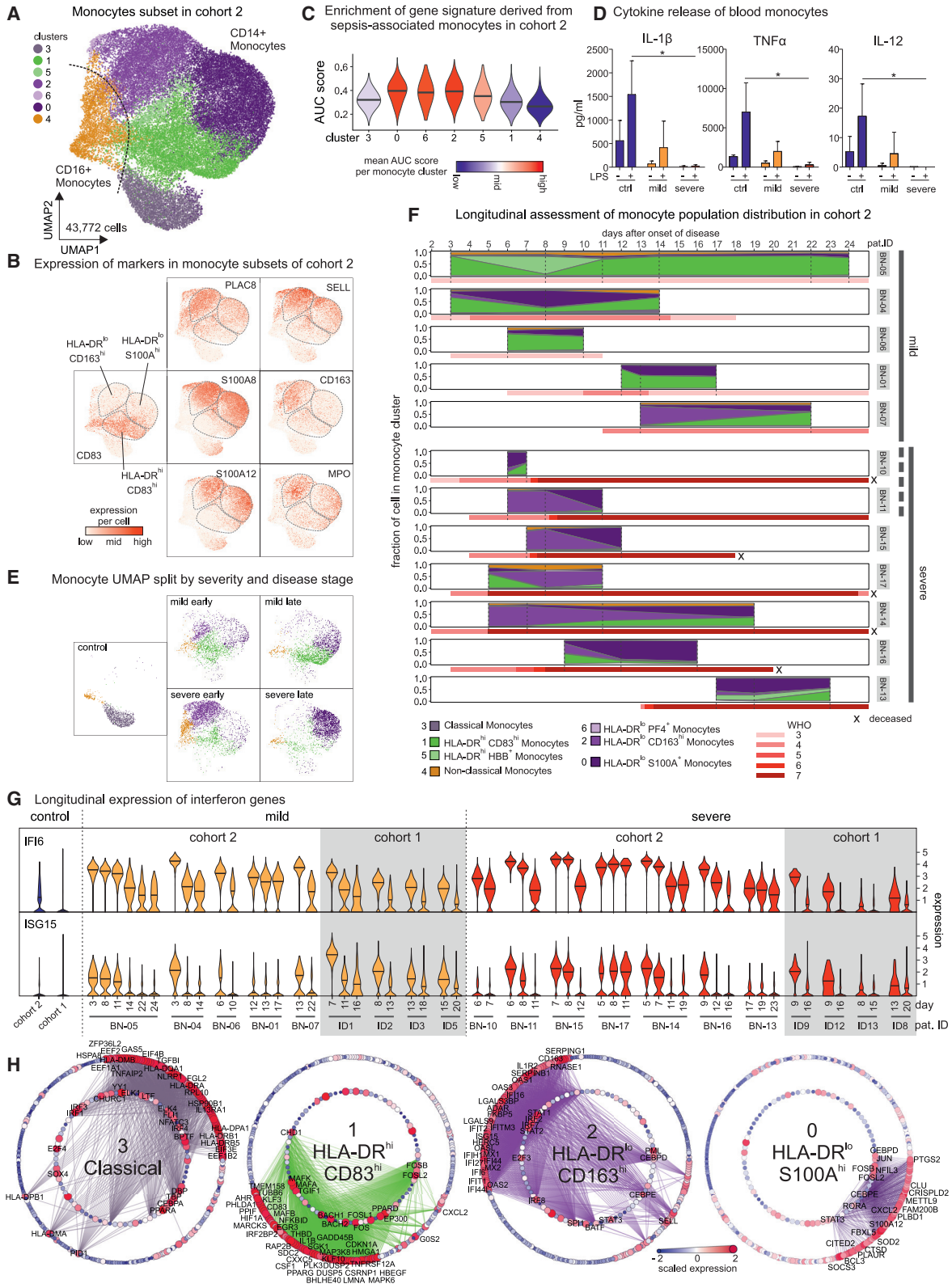
(C) Box and whisker (10–90 percentile) plots of main monocyte clusters 1, 10 (CD14^{hi}CD16⁻ classical monocytes), 11, and 3 (CD14^{hi}CD16⁺ intermediate monocytes) determined by mass cytometry (whole blood, cohort 1): controls (n = 9), FLI patients (n = 8), COVID-19 patients (mild, n = 8; severe, n = 9). Abundance testing via R multcomp and lsmeans packages adjusted using the Benjamini-Hochberg procedure and an FDR-cutoff of 5% across all clusters/subsets and between-group comparisons.

(D) Box and whisker (10–90 percentile) plots of CXCR3⁺, HLA-DR^{hi}CD11c^{hi}, and CD226⁺CD69⁺ monocytes measured by mass cytometry (whole blood, cohort 1): controls (n = 9), FLI patients (n = 8), and COVID-19 patients (mild, n = 8; severe, n = 9). Kruskal-Wallis and Dunn's multiple comparison tests.

(E) Boxplot of HLA-DR^{hi}CD11c^{hi} monocytes (cohort 2) measured by flow cytometry: COVID-19 (mild, n = 3; severe, n = 7) and age-matched controls (n = 11). Unpaired t test.

*p < 0.05, **p < 0.01, ***p < 0.001, ****p < 0.0001.

See also Tables S1 and S3.



(legend on next page)

HLA-DR^{lo} Monocytes Persist in Severe COVID-19

Next, we dissected COVID-19-associated phenotypic alterations of monocytes by scRNA-seq. Marker genes of the monocyte clusters derived from Figure 2A showed that mild COVID-19 associated clusters 1 and 2 were characterized by an ISG-driven transcriptional program (Figure S3A), and gene ontology enrichment analysis (GOEA) assigned these clusters to “type I interferon signaling pathway” (Figure S3B). A monocyte cluster marked by low expression of *HLA-DR* and high expression of *S100A12* and *CXCL8* (cluster 3, *HLA-DR^{lo}S100A^{hi}*) was strongly associated with severe COVID-19 (Figures 2B, S2D, and S3A). For further in-depth analysis, we subclustered the monocyte compartment of the PBMC dataset of cohort 2 (Figures 2D and S3C; Table S1) resulting in 7 subclusters (Figure 4A). Cluster 1 was marked by high expression of *HLA-DRA* and *HLA-DRB1* and co-stimulatory molecule *CD83* and was therefore designated *HLA-DR^{hi}CD83^{hi}*-activated inflammatory monocytes (Figures 4A, 4B, S3D, and S3E). We identified two major clusters (0 and 2) and a smaller cluster (6) with low *HLA-DR* expression, which were associated with severe COVID-19 (Figures 4B, S3D, and S3E). Low *HLA-DR* expression is an established surrogate marker of monocyte dysfunction (Venet et al., 2020) which results in reduced responsiveness to microbial stimuli (Veglia et al., 2018), suggesting that clusters 0 and 6 are composed of dysfunctional monocytes. Genes of the *S100A* family were expressed in both *HLA-DR^{lo}* clusters (Figure 4B), albeit to a higher degree in cluster 0 (*HLA-DR^{lo}S100A^{hi}*, e.g., *S100A12*) (Figures S2D and S3E; Table S4). Cluster 2 monocytes expressed high levels of *SELL* (CD62L) and *CD163* (*HLA-DR^{lo}CD163^{hi}*) (Figure 4B), associated with anti-inflammatory macrophage functions (Fischer-Riepe et al., 2020; MacParland et al., 2018), as well as pre-maturation markers like *MPO* and *PLAC8* (Figure 4B), recently linked to immature monocyte states in sepsis patients (Reyes et al., 2020). In line with these findings, clusters 0, 2, and 6 were significantly enriched in a gene signature derived from sepsis-associated monocytes (Figure 4C) (Reyes et al.,

2020). Moreover, blood monocytes isolated from COVID-19 patients showed a blunted cytokine response to LPS stimulation, particularly monocytes from patients with severe COVID-19 (Figure 4D). Accordingly, *HLA-DR^{lo}* monocyte clusters (0, 2, and 6) were detected almost exclusively in severe COVID-19 (Figure 4E). We next analyzed time-dependent cluster occupancies per patient in cohort 2 (Figures 4E and 4F). Activated *HLA-DR^{hi}CD83^{hi}* monocytes (cluster 1) were found in all cases of mild COVID-19, even at late time points (Figures 4E and 4F). In contrast, *HLA-DR^{lo}CD163^{hi}* monocytes (cluster 2) were present mainly early in severe disease, while *HLA-DR^{lo}S100A^{hi}* monocytes (cluster 0) dominated the late phase of disease (Figures 4E and 4F). Violin plots of *ISG* (Figure S3D) and visualization of marker genes (Figure S3E) indicated differential expression patterns of IFN signature genes in individual monocyte clusters. To reveal the kinetics of ISG expression, we plotted the expression of *ISG15* and *IFI6* in the complete monocyte population for all patients that had been sampled at least twice (Figure 4G). Expression levels were highest at early time points and consistently decreased over time, clearly indicating that the IFN response in COVID-19 is inversely linked to disease severity and time (Figures S3F and S3G). In contrast, decreased expression of *HLA-DRA* and *HLA-DRB1* in severe COVID-19 is evident early on and sustained over time.

Transcription factor prediction indicated a STAT signaling-driven gene expression program in monocytes in COVID-19 (Figure 4H), with additional regulation by CEBPD and CEBPE, which have been implicated in gene expression programs of sepsis-associated monocytes (Reyes et al., 2020). STAT3 was predicted as a specific regulator of genes enriched in *HLA-DR^{lo}CD163^{hi}* and *HLA-DR^{lo}S100A^{hi}* monocytes (clusters 2 and 0), in line with their immunosuppressive phenotype.

Taken together, dynamic changes of monocyte phenotypes were associated with COVID-19 disease severity and time after onset of disease.

Figure 4. Disease-Related Longitudinal Changes in Monocyte Transcriptomes

- (A) UMAP visualization of monocytes (43,772 cells; from Figure 2C, cohort 2); 46 samples from controls (n = 6) and COVID-19 (mild, n = 7; severe, n = 8). Cells are colored according to the identified monocyte clusters (Louvain clustering, Table S4).
- (B) Visualization of scaled expression of selected genes (monocyte markers, Figures 2 and S3E) using the UMAP defined in (A). Three main clusters defining monocytes in COVID-19 (*HLA-DR^{lo}CD163^{hi}*, *HLA-DR^{lo}S100A^{hi}*, and *HLA-DR^{hi}CD83^{hi}* monocytes) indicated by dashed areas.
- (C) AUCCell-based enrichment of a gene signature from sepsis-associated monocytes (MS1 cells) (Reyes et al., 2020), violin plots of the area under the curve (AUC) scores. Horizontal lines: median of the respective AUC scores per cluster.
- (D) Cytokine detection of IL-1 β , tumor necrosis factor alpha (TNF)- α , and IL-12 in supernatants of purified monocytes (controls, ctrl, n = 3; COVID-19, mild, n = 3, and severe, n = 3) after 8 h *in vitro* incubation with or without 1 ng/mL LPS. Mean \pm standard deviation. Kruskal-Wallis test adjusted with Benjamini-Hochberg method, *p < 0.05.
- (E) Mapping of monocytes derived from COVID-19 patients (mild early, mild late, severe early, and severe late) onto UMAP from (A), coloring according to monocyte cluster identity.
- (F) Cluster occupancy over time for patients with longitudinal scRNA-seq data (mild, n = 5; severe, n = 7), coloring according to (A). Vertical dashed lines: time points of sampling. Red bar, WHO ordinal scale; X, patient deceased. Patient IDs on the right side, grouping according to disease severity. Bold dotted line (right): patients classified as mild at initial sampling developing severe disease over time.
- (G) Time-dependent change of *IFI6* and *ISG15* expression (violin-plots) in monocytes of cohort 1 (mild [yellow], n = 4; severe [red], n = 4), cohort 2 (mild [yellow], n = 5; severe [red], n = 7), and controls (cohort 1, n = 22, cohort 2, n = 6).
- (H) Network representation of marker genes and their predicted upstream transcriptional regulators for monocyte clusters 0, 1, 2, and 3. Edges: predicted transcriptional regulation. Transcription factors (TFs, inner circle) and predicted target genes (outer circle) represented as nodes sized and colored according to the scaled expression level across all clusters. Selected TFs and genes labeled based on connectivity and literature mining. Numbers in the center refer to clusters defined in (A).

See also Figure S1 and Tables S1 and S4.

Low-Density Neutrophils Emerge in Severe COVID-19 Patients Indicative of Emergency Myelopoiesis

PBMCs derived from blood samples of patients with severe COVID-19 contained two distinct clusters of LDNs (Figures 2A, clusters 5 and 6, and 2D, clusters 5 and 6). LDNs were slightly more frequent in cohort 1, and we analyzed these cells in more detail. Subsampling of all LDNs (Figure 5A; Table S1) and re-clustering the cells revealed 8 transcriptionally distinct cell clusters (Figures 5A and 5B; Table S4). Based on published markers for pro- and pre-neutrophils, and mature neutrophils (Kwok et al., 2020; Ng et al., 2019; Scapini et al., 2016) we identified clusters 4 and 6 as *CD81*⁺*SPN*(*CD43*)⁺*FUT4*(*CD15*)⁺*CD63*⁺*CEACAM8*(*CD66b*)⁺ pro-neutrophils, clusters 3 and 5 as *ITGAM*(*CD11b*)⁺*CEACAM8*(*CD66b*)⁺*CD101*^{+/-} pre-neutrophils, and the remaining clusters as mature neutrophils (Figure S4A). Accordingly, pro- and pre-neutrophils were enriched for transcriptional signatures of neutrophil progenitors derived from published single-cell data (Figure 4C) (Pellin et al., 2019; Popescu et al., 2019), and pro-neutrophils in clusters 4 and 6 showed the highest proportion of cells with a proliferative signature (Figure S4B). Clusters 0, 1, and 2 (originally in cluster 4 in Figure 2A) expressed mature neutrophil markers *FCGR3B* (*CD16*) and *MME* (*CD10*) (Figure S4A).

Differential gene expression analysis for each cluster revealed extensive phenotypic heterogeneity within the LDN compartment (Figure 5B). LDNs mainly arise under pathological conditions, such as severe infection and sepsis in the context of emergency myelopoiesis (Schultze et al., 2019), and they have been associated with dysfunctional immune responses, marked by combined immunosuppression and inflammation (Silvestre-Roig et al., 2019). While LDN in cluster 1 expressed numerous ISGs (*ISG15*, *IFITM1/3*, and *RSAD2*), cluster 4 (pro-neutrophils) expressed genes (e.g., *MPO*, *ELANE*, and *PRTN3*) that are involved in neutrophil extracellular trap formation (Stiel et al., 2018; Thomas et al., 2014; You et al., 2019) among other functions and that have been associated with sepsis (Ahmad et al., 2019; Carbon et al., 2019; Silvestre-Roig et al., 2019). Both pre-neutrophil clusters expressed *PADI4*, another co-factor in NETosis (Leshner et al., 2012) (Figure 5D). NETs have recently been implicated in the pathogenesis of COVID-19 (Barnes et al., 2020; Zuo et al., 2020). Both pre-neutrophils (clusters 3 and 5) and pro-neutrophils expressed genes including *CD24*, *OLFM4*, *LCN2*, and *BPI*, previously associated with poor outcome in sepsis (Figures 5B and S4A) (Kangelaris et al., 2015).

All LDNs also expressed high levels of alarmins *S100A8* and *S100A9* (Figure 5D), whereas other *S100* genes (e.g., *S100A4* and *S100A12*) were strongly induced in selected neutrophil clusters. Finally, known inhibitors of T cell activation, namely *CD274* (PD-L1) and *Arginase 1* (*ARG1*) (Bronte et al., 2003; Li et al., 2018) were highly expressed in neutrophils in COVID-19 patients (Figure 5E). *ARG1*⁺ neutrophils in sepsis patients were shown to deplete arginine and constrain T cell function in septic shock (Darcy et al., 2014) and were predictive of the development of nosocomial infections (Uhel et al., 2017). Mature *CD274*(PD-L1)⁺ neutrophils (cluster 0) have been attributed suppressive functions in various conditions including HIV-1 infection (Bowers et al., 2014), cancer (Chun et al., 2015) and in lymph nodes (Cas-

tell et al., 2019), spleen (Langereis et al., 2017), and blood after LPS exposure (de Kleijn et al., 2013). *ARG1*⁺ cells were mainly immature neutrophils (clusters 3–6) and did not overlap with *CD274* (PD-L1) expressing cells, indicating different populations of dysfunctional and potentially suppressive neutrophils in severe COVID-19.

LDNs recovered from PBMC fractions of COVID-19 patients revealed the presence of dysfunctional neutrophils and pointed toward multiple potentially deleterious pathways activated in severe COVID-19.

Persistent Increase of Activated Neutrophil Precursors and PD-L1⁺ Neutrophils in Severe COVID-19

Alterations of the neutrophil compartment were further interrogated by mass cytometry of whole blood samples of COVID-19 patients (n = 8 mild + 9 severe, cohort 1), FLI patients (n = 8), and age- and gender-matched controls (n = 9) (Table S1), using a panel designed to detect myeloid cell maturation and activation states as well as markers of immunosuppression or dysfunction (Table S2). Unsupervised clustering analysis of all neutrophils in all samples revealed 10 major clusters (Figure 6A) of immature (clusters 2, 5, 6, and 7), mature (clusters 1, 3, and 4), and remaining clusters of low abundance (clusters 8, 9, and 10). Based on their differential expression of *CD11b*, *CD16*, *CD24*, *CD34*, and *CD38*, clusters 5 and 6 were identified as pro-neutrophils and cluster 2 as pre-neutrophils (Kwok et al., 2020; Ng et al., 2019). The fourth immature cell cluster (7) showed very low expression of *CD11b* and *CD16*, reminiscent of pro-neutrophils, but lacking *CD34*, *CD38*, and *CD24* (Figure 6A), suggesting a hitherto unappreciated pro-neutrophil-like population. The mature neutrophils segregated into non-activated (cluster 1), partially activated (cluster 3), and highly activated cells (cluster 4), based on the loss of *CD62L* and up-regulation of *CD64*, as well as signs of proliferative activity (*Ki67*⁺) (Figure 6A).

Neutrophils from COVID-19 patients clearly separated from those of controls and also FLI patients in UMAP analysis (Figure 6B), and neutrophils in patients with severe COVID-19 were distinct from those of patients with mild disease (Figure 6B). Cells from control donors accumulated in areas enriched for mature non-activated cells (cluster 1) and immature pre-neutrophil-like cells (cluster 2). In contrast, neutrophils from FLI patients were mainly mature non-activated (cluster 1) and mature highly activated (cluster 4) cells. Neutrophils from COVID-19, particularly from patients with severe disease, primarily occupied immature pre- and pro-neutrophil-like clusters. Plotting cell cluster-specific surface marker expression onto the UMAPs (Figure 6C) as well as statistical analyses of cell cluster distribution and surface marker expression among different patient groups supported these observations (Figures 6D and 6E). Samples from FLI patients contain a high proportion of highly activated mature neutrophils, but barely any immature neutrophils. In contrast, severe COVID-19 is associated with the appearance of immature pre- and pro-neutrophils (Figures 6D and 6E). Interestingly, immature cell clusters in severe COVID-19 showed signs of recent activation like upregulation of *CD64* (Mortaz et al., 2018), *RANK*, and *RANKL* (Riegel et al., 2012), as well as reduced *CD62L* expression (Mortaz et al., 2018). In addition to loss of

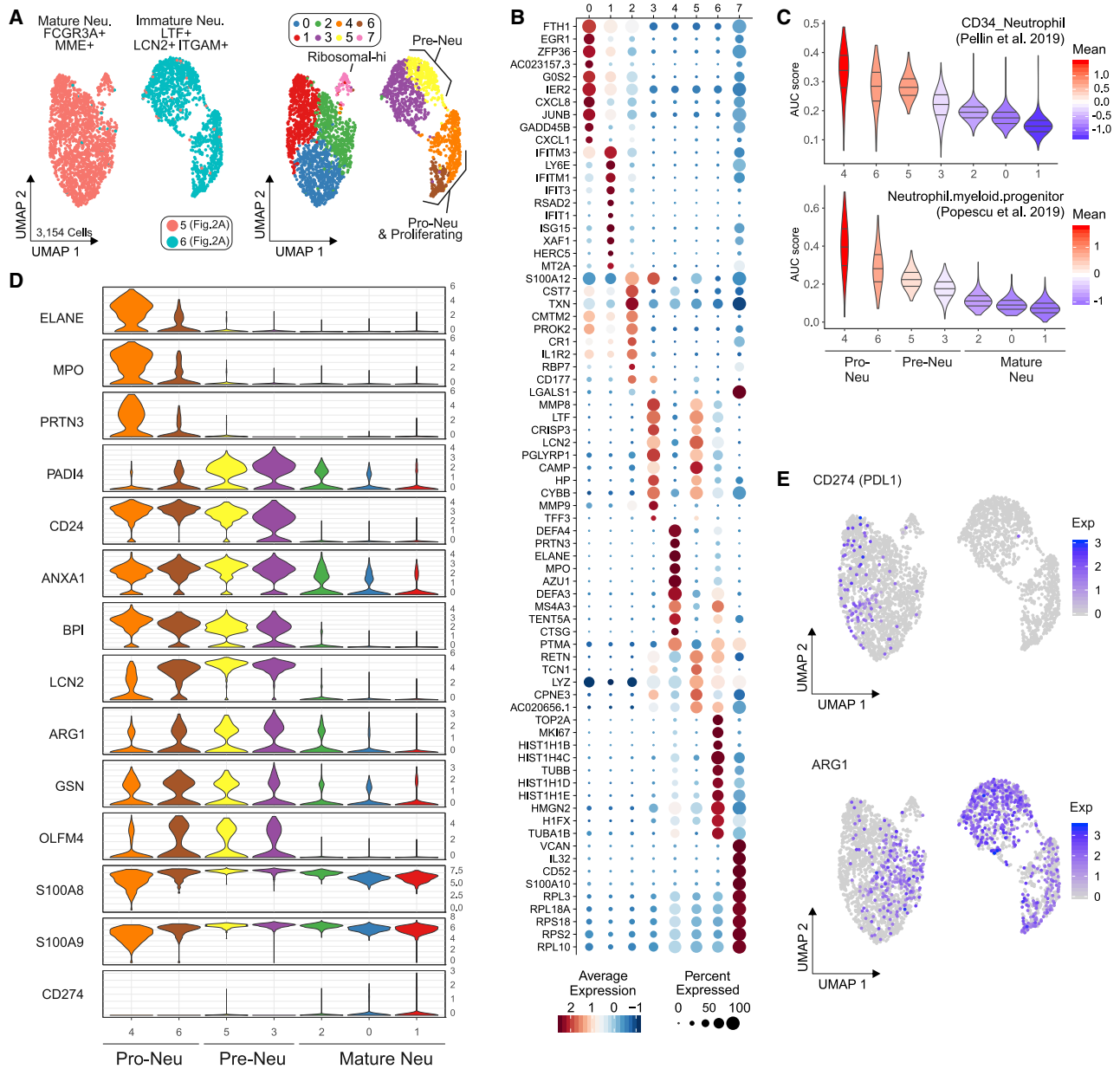


Figure 5. Immature and Dysfunctional Low-Density Neutrophils Emerge in PBMC

(A) UMAP representation and clustering of low-density neutrophils (LDNs, 3,154 cells) in PBMCs (cohort 1, clusters 5/6, Figure 2A) from 21 samples (6 mild, 10 severe COVID-19). Left panel: cluster affiliation in Figure 2A. Right panel: data-driven clustering and cell type nomenclature based on marker genes (Table S4). (B) Dot plot of the top 10 marker genes sorted by average log fold change associated with the neutrophil clusters identified in (A).

(C) Signature enrichment scores of single-cell data from neutrophil progenitors (Pellin et al., 2019; Popescu et al., 2019) in LDN clusters, plotted as violin plots. The lines in the violin plots represent the median of the respective AUC scores per cluster and the 0.25 and 0.75 quantiles. The ribosomal^{hi}-specific cluster 7 was excluded from this analysis.

(D) Violin plots of expression of selected activation genes across the neutrophil clusters identified in (A). The panel of genes was chosen based on their described role in neutrophil extracellular trap formation (*PRTN3*, *ELANE*, *MPO*, and *PADI4*) and neutrophil activation and dysregulation (*CD24*, *OLFM4*, *LCN2*, *BPI*, *CD274* [PD-L1], *Arginase 1* [*ARG1*], and *ANXA1*).

(E) Expression of *ARG1* and *CD274*(PD-L1) projected on the UMAP from (A).

See also Figure S4 and Table S1.

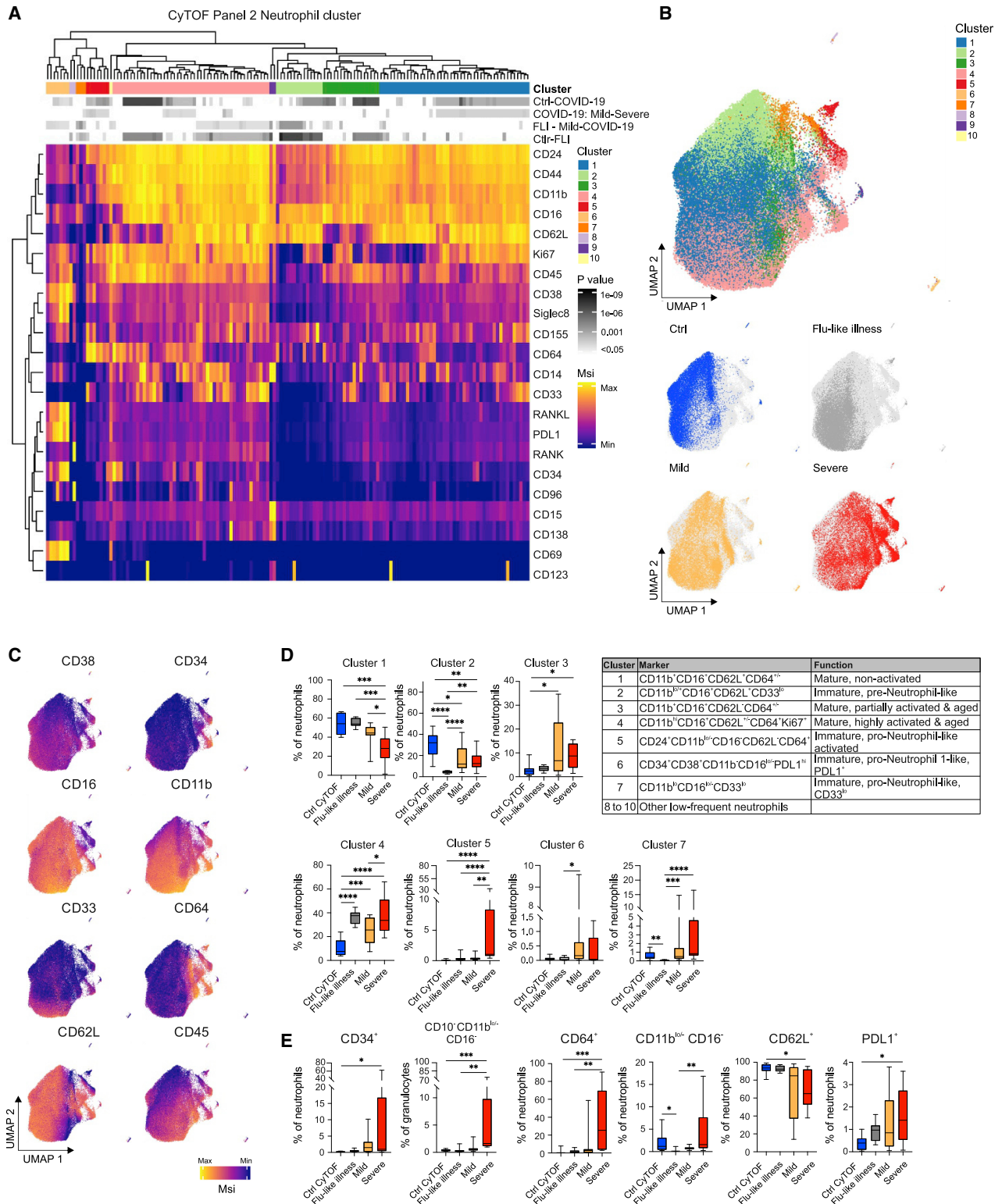


Figure 6. Appearance of Immature and PD-L1⁺ Neutrophils in Severe COVID-19

(A) Heatmap revealing differences in marker expression determined by mass cytometry (antibody panel 2, cohort 1) of main neutrophil cell cluster (1 to 10). Main individual neutrophil cell clusters are displayed in columns and marker identity is indicated in rows. MSI, marker staining intensity respective expression level.

(legend continued on next page)

CD62L, immature and mature neutrophils from severe COVID-19 showed elevated PD-L1 expression compared to control samples (Figure 6E). Indeed, CD62L downregulation and high PD-L1 expression has been frequently associated with suppressive function of neutrophils and granulocytic myeloid-derived suppressor cells (gMDSs) (Bronte et al., 2016; Cassetta et al., 2019; Kamp et al., 2012; Pillay et al., 2012; Tak et al., 2017; Testa et al., 2004; Younos et al., 2015). Interestingly, a recent study described a high abundance of similar immature and dysfunctional CD64⁺ and PD-L1⁺ neutrophils in sepsis patients (Meghraoui-Kheddar et al., 2020).

Thus, SARS-CoV-2 infection induces major alterations in the neutrophil compartment. While neutrophils in FLI patients display a mature activated phenotype, a release of immature neutrophils with phenotypic signs of immunosuppression and dysfunction is a hallmark of severe COVID-19.

We next assessed the dynamics of the changes within the myeloid cell compartment over time. We grouped samples according to collection time as “early” (within the first 10 days) or late (during the following 20 days) after onset of symptoms. In both cohorts, we observed a tendency toward (cohort 1) or significantly higher (cohort 2) proportions of granulocytes in severe versus mild COVID-19 patients, both at early and late time points (Figure S5A). We observed a persistent release of immature neutrophils (e.g., cluster 6) in severe COVID-19 (Figure S5B) showing high expression of CD64 and PD-L1, but downregulation of CD62L as a sign of activation, dysfunction, and immunosuppression (Figure S5C). In addition, severe COVID-19 patients show further increased frequencies of mature, partially activated neutrophils (cluster 3) at later time periods (Figure S5B). Thus, the neutrophil compartment of severe COVID-19 patients is characterized by a combination of persistent signs of inflammation and immunosuppression, which is reminiscent of long-term post-traumatic complications (Hesselink et al., 2019).

We also analyzed time-dependent phenotypic changes in the monocyte compartment by mass cytometry. Non-classical monocytes started to recover in COVID-19 patients during the later stages of the disease (Figure S5A). HLA-DR^{hi}CD11c^{hi} monocyte cell clusters also declined at later time points in mild COVID-19 (Figures S5D–S5F), which correlates well with the longitudinal changes of *IFI6* and *ISG15* as well as *HLA-DRA* and *HLA-DRB1* expression profiles (Figures 4G and S3F). In contrast,

overall proportions of HLA-DR^{hi}CD11c^{hi} monocytes in severe COVID-19 remained low throughout the course of the disease. Proportions of CD10^{hi} macrophage-like cluster 10 and CD226⁺CD69⁺ monocytes were generally higher at later stages in severe COVID-19, which resembled the kinetics of *HLA-DR^{lo}-S100A^{hi}* monocytes identified by scRNA-seq (Figure 4F). This indicates a prolonged alternative activation of monocytes in severe COVID-19 (Figure S5E).

Single-Cell Transcriptomes of Whole Blood Reveal Suppressible-like Neutrophils in Severe COVID-19

Whole blood CyTOF analysis (cohort 1) clearly indicated very distinct phenotypic alterations of the neutrophil compartment in mild and severe forms of COVID-19. To further delineate the underlying transcriptional programs, we performed scRNA-seq analysis on fresh whole blood samples of 23 individuals (34 samples, cohort 2, Table S1). Integrated visualization of all samples of cohort 2 (fresh/frozen PBMCs, fresh whole blood, 229,731 cells, Figure S6A) revealed the expected blood leukocyte distribution, including granulocytes (Figures 7A and S6A; Table S4). Cell-type distribution identified by scRNA-seq profiles (Figure S6B) strongly correlated with MCFC characterization of the same samples (Figure S6C). For further analysis of the granulocyte compartment, we first combined the whole blood samples with the fresh PBMCs to guide the clustering of all major immune cells resulting in a total of 122,954 cells (Figure 7A). From these samples, we identified all neutrophil clusters and extracted the cells derived from whole blood for subsampling, which revealed a structure of 9 clusters (n = 58,383 cells) (Figures 7B and 7C).

Using marker- and data-driven approaches as applied to LDN (Figure 5D and S4A), we identified *FUT4*(CD15)⁺*CD63*⁺*CD66b*⁺ pro-neutrophils, *ITGAM*(CD11b)⁺*CD101*⁺ pre-neutrophils, along with 7 mature neutrophil clusters (Figures 7B–7D and S6D; Table S4). Heterogeneous expression of various markers involved in mature neutrophil function including *CXCR2*, *FCGR2A* (CD32), *FCGR1A* (CD64), or *MME* (CD10), pointed toward distinct functionalities within the neutrophil compartment (Figures 7E, S6D, and S6E). Seven of the nine neutrophil clusters identified in whole blood in cohort 2 could also be mapped to the fresh PBMC transcriptomes in cohort 1 (Figure S6F), indicating that scRNA-seq of fresh PBMC in COVID-19 patients reveals relevant parts of the neutrophil space. The transcriptional phenotype of pro- and

Significance level for the following comparisons: (1) controls (ctrl, n = 9) versus COVID-19 (mild and severe, n = 17, first row), (2) mild (n = 8) versus severe (n = 9, second row), (3) FLI (n = 8) versus mild COVID-19 (n = 8, third row), as well as (4) controls (ctrl, n = 9) versus FLI (n = 8) are indicated using a gray scale on top of the heatmap (see also p value scale next to the heatmap). Samples of COVID-19 patients collected between day 4 and 13 post-symptom onset (= first day of sample collection per patient). Abundance testing via generalized mixed effects models and multiple comparison adjustment using the Benjamini-Hochberg procedure and an FDR-cutoff of 5% across all clusters/subsets and between-group comparisons

(B) UMAP of neutrophils, down-sampled to 70,000 cells (30 markers, Table S2). Cells are colored according to main cell clusters (1 to 10, see table). Donor origin (blue, controls; gray, FLI; yellow, mild COVID-19; red, severe COVID-19).

(C) UMAP (from (B)) with cells colored according to expression intensity of CD38, CD34, CD16, CD11b, CD33, CD64, CD62L, and CD45.

(D) Box and whisker (10–90 percentile) plots of main neutrophil cell clusters 1 to 7, reaching proportions of over 1%, measured by mass cytometry (whole blood, cohort 1): controls (n = 9), FLI (n = 8), and COVID-19 (mild, n = 8; severe, n = 9). Abundance testing via generalized mixed effects models and multiple comparison adjustment using the Benjamini-Hochberg procedure and an FDR-cutoff of 5% across all clusters/subsets and between-group comparisons.

(E) Box and whisker (10–90 percentile) plots of proportions of CD34⁺, CD11b^{lo/-}CD16⁻, CD64⁺, CD62L⁺, CD10⁻CD11b^{lo/-}CD16⁻ (reported from panel 1) and PD-L1⁺ neutrophils (whole blood, cohort 1): controls (n = 9), FLI (n = 8), and COVID-19 (mild, n = 8; severe, n = 9). Kruskal-Wallis and Dunn’s multiple comparison tests.

*p < 0.05, **p < 0.01, ***p < 0.001, ****p < 0.0001.

See also Figure S5 and Tables S1 and S3.

pre-neutrophils (cluster 8+9) was corroborated in cohort 2 (Figures 7B–7D and S6D).

Heatmap and UMAP visualization of the cell type distribution identified pro- and pre-neutrophils mainly at late time points in severe COVID-19 (Figures 7F and 7G). Furthermore, mature neutrophils with a high IFN-signature (cluster 1) were associated with severe COVID-19 (Figures 7E and S6G). This cluster was also enriched for markers identified by CyTOF as differentially expressed in patients with severe COVID-19 (Figure 6), such as elevated expression of *CD274* (PD-L1) and *FCGR1A* (CD64) (Figure 7H). In addition to *CD274*, cells in cluster 1 expressed genes indicative of a potentially suppressive or anti-inflammatory state, including *ZC3H12A* (Figure 7E), which is known to suppress hepatitis C virus replication and virus-induced pro-inflammatory cytokine production (Lin et al., 2014). Cluster 2 was also enriched for cells from COVID-19 patients, mainly from severe but also mild cases (Figures 7F and 7G).

Gene signatures from granulocytic MDSC (Bayik et al., 2020) and *CD274*(PD-L1)⁺ neutrophils after LPS exposure (de Kleijn et al., 2013), both shown to be immunosuppressive, were enriched in clusters 1, 2, and 6, which mainly harbor cells from severe COVID-19. This indicates a suppressive functionality of these cells in severe COVID-19 (Figure 7I). Predictions of transcription factor (TF)-based regulation of the cluster-specific gene signatures separated mature neutrophils from patients with severe COVID-19 (cluster 1) and control patients (cluster 0) (Figure 7J). IFN-response genes are mainly controlled by STAT and IRF TFs, whereas the transcriptional signature of cluster 0 is mainly driven by the CEBP TF family. The TF network underlying the transcriptional difference in pro-neutrophils is mainly driven by E2F family members and pre-neutrophils mainly depend on ETS TFs (Figure S6H).

Pseudotime analysis strongly supported the differentiation trajectory from pro-neutrophils (cluster 8) via pre-neutrophils (cluster 6) to mature neutrophils in cluster 2 and 1 (Figures S6I and S6J). Particularly *CD274* (PD-L1) was enriched in cluster 1 compared to cluster 2, supporting the potential of neutrophils to progress toward a suppressive phenotype in severe COVID-19 (Figure S6J). Interestingly, *CD177* is expressed in pre-neutrophils and persisting in cluster 1 further highlighting the newly emerging character of this cluster (Volkmann et al., 2020).

Finally, we studied whether the persistent emergence of immature, potentially dysfunctional neutrophils in severe COVID-19 patients can be captured under routine diagnostic conditions. Therefore, samples of 32 COVID-19 patients (Table S1, cohort 1) were characterized by routine hematology analyses using a clinical flow cytometry system (Sysmex analyzer). Indeed, the assumption of rescue myelopoiesis in severe COVID-19 was supported by significantly higher counts in the population of immature granulocytes (IG, representing promyelocytes, myelocytes, and metamyelocytes) in this patient group (Figure 7K). We also found significant differences in the neutrophil compartment, when analyzing the width of dispersion with respect to granularity, activity, and cell volume defined as NE-WX, NE-WY, and NE-WZ, respectively. As compared to patients with mild course, severely ill patients displayed increases in width of dispersion of activity and cell volume as surrogates for increased cellular heterogeneity, immaturity, and dysregulation in severe COVID-19 (Figure 7K), resembling previously described alterations in sepsis patients (Stiel et al., 2016). Furthermore, neutrophils of severe COVID-19 patients were partially dysfunctional, because their oxidative burst upon stimulation with standardized stimuli (*E. coli* or PMA) was strongly impaired in comparison to control and mild COVID-19

Figure 7. Immature and Dysfunctional Whole-Blood Neutrophils in Severe COVID-19

- (A) UMAP of 35 fresh blood samples from cohort 2 (122,954 cells, PBMCs, and whole blood): controls (n = 17), mild COVID-19 (early, n = 3; late, n = 3) and severe COVID-19 (early, n = 3, late = 9). Clusters defined by Louvain clustering. Cell types assigned based on reference-based cell type classification (Aran et al., 2019) and marker gene expression (Table S4).
- (B) UMAP visualization of neutrophils (58,383 cells; 34 whole blood samples, cohort 2): controls (n = 16), mild COVID-19 (early, n = 3; late, n = 3), and severe COVID-19 (early, n = 3; late, n = 9). Clusters defined by Louvain clustering (Table S4).
- (C) Nomenclature and marker genes for each neutrophil cluster from (B).
- (D) Dot plot of selected marker genes for each neutrophil cluster from (B).
- (E) Dot plot of genes from different functional classes (based on literature research). Clusters 8, 6, 1, and 2 are specific for severe COVID-19, cluster 0 represents homeostatic mature neutrophils from controls.
- (F) Heatmap divided by disease severity and stage (early versus late) showing the proportion of each patient group for each cluster.
- (G) Density plot of cell frequency by disease severity and stage (early versus late) overlaid on the UMAP of the neutrophil space.
- (H) UMAP visualization showing scaled expression of *CD274* (PD-L1) and *FCGR1A* (CD64).
- (I) Violin plots showing AUC_{Cell}-based enrichment as AUC scores of gene signature from granulocytic myeloid-derived suppressor cells (Bayik et al., 2020) and PD-L1^{hi} neutrophils after LPS exposure (de Kleijn et al., 2013) in neutrophil clusters from (B). Horizontal lines: median of the respective AUC scores per cluster and 0.25 and 0.75 quantiles.
- (J) Network representation of marker genes and their predicted upstream transcriptional regulators for neutrophil clusters 1 (mature/COVID-19 severe-specific) and 0 (mature/control-specific). Edges in cluster color: predicted transcriptional regulation. TFs (inner circle) and their predicted target genes (outer circle): nodes, sized, and colored according to scaled expression level across all clusters. Selected genes and TFs labeled based on connectivity and literature mining.
- (K) Box and whisker (10–90 percentile) plots representing the hematological analyses (whole blood, cohort 1): mild (n = 11), severe (n = 21) COVID-19. Analytes, measured by flow cytometry in white blood cell differential channel, included absolute counts of immature granulocytes (IG, dotted line: upper limit of reference range) and width of neutrophil cytometric dispersions (NE-WX, dispersion of side scatter; NE-WY, dispersion of side fluorescence light; NE-WZ, dispersion of forward scatter). Mann Whitney test applied to IG count analysis and mixed-effect-analysis and Sidak's multiple comparison test to NE-WX, NE-WY, and NE-WZ analyses.
- (L) Box and whisker (10–90 percentile) plots of *E. coli*- and PMA-induced neutrophil oxidative burst (reactive oxygen species [ROS] production) and phagocytosis of whole blood samples (cohort 1; mild, n = 10; severe [n = 8] COVID-19) in comparison to controls measured by flow cytometry. Dotted line: relative level of controls run in the assay. Mixed-effect-analysis and Sidak's multiple comparison test. **p < 0.01, ***p < 0.001, ****p < 0.0001. See also Figure S6 and Table S1.

neutrophils, whereas phagocytic activity was preserved (Figure 7L; Table S1).

Collectively, the neutrophil compartment in peripheral blood of severe COVID-19 patients is characterized by the appearance of LDN, *FUT4*(CD15)⁺*CD63*⁺*CD66b*⁺ pro-neutrophils, and *ITGAM*(CD11b)⁺*CD101*⁺ pre-neutrophils, reminiscent of emergency myelopoiesis, as well as *CD274*(PD-L1)⁺*ZC3H12A*⁺ mature neutrophils reminiscent of gMDSC-like cells, which might exert suppressive or anti-inflammatory functions.

DISCUSSION

SARS-CoV-2 infection generally causes mild disease in the majority of individuals, however, ~10%–20% of COVID-19 patients progress to severe disease with pneumonia and respiratory failure. The reported case-fatality rates among patients with critical illness and respiratory failure vary, with a mean of ~25% (Quah et al., 2020). Dysregulated immune responses have been described in patients with severe COVID-19 (Chua et al., 2020; Giamarellos-Bourboulis et al., 2020; Lucas et al., 2020; Merad and Martin, 2020; Messner et al., 2020; Wei et al., 2020; Zhou et al., 2020b). Hence, detailed knowledge of the cellular and molecular processes that drive progression from mild disease to potentially fatal courses of COVID-19 is urgently needed to identify predictive biomarkers and therapeutic targets.

Here, we employed four complementary technologies at single-cell resolution to assess alterations in the systemic immune response in mild or severe courses of COVID-19. We analyzed a total of 53 patients (161 samples) from two independent cohorts collected at two university medical centers in Germany (Kurth et al., 2020). Combining single-cell transcriptomics with single-cell proteomics, using different technological platforms in two independent patient cohorts, provided a detailed view of the systemic immune responses in COVID-19 and allowed for cross-validation and in-depth interrogation of key findings. The results were further supported by additional routine diagnostics lab measurements and functional assays, linking the results of the exploratory investigations to functional phenotypes and clinically relevant diagnostics.

This multipronged approach revealed drastic changes within the myeloid cell compartment during COVID-19, particularly in patients with a severe course of disease. Early activation of HLA-DR^{hi}CD11c^{hi}/HLA-DR^{hi}CD83^{hi} monocytes with a strong antiviral IFN-signature was a hallmark of mild COVID-19, which receded during the natural course of disease. In contrast, HLA-DR^{lo} dysfunctional monocytes along with clear evidence of emergency myelopoiesis with release of immature neutrophils including pro- and pre-neutrophils into the circulation marked severe COVID-19. Furthermore, we identified neutrophils in severe COVID-19 with transcriptional programs reminiscent of dysfunction and immunosuppression not observed in controls or patients with mild COVID-19. Thus, defective monocyte activation and dysregulated myelopoiesis may contribute to severe disease course and ARDS development (Middleton et al., 2020).

Previous immunophenotyping studies have reported an increase of inflammatory monocytes with a strong IFN-response in COVID-19 (Liao et al., 2020; Merad and Martin, 2020; Zhou et al., 2020b). Mononuclear phagocytes and neutrophils appear

to dominate inflammatory infiltrates in the lungs, and resident alveolar macrophages are replaced by inflammatory monocyte-derived macrophages in patients with severe COVID-19 (Chua et al., 2020; Liao et al., 2020). Here, we report substantial time- and disease severity-dependent alterations of the monocyte compartment in COVID-19. Marked depletion of CD14^{lo}CD16^{hi} non-classical monocytes observed in all COVID-19 patients, but not in patients with SARS-CoV-2 negative FLI (Figure 1D), is in line with previous reports on COVID-19, and other severe viral infections (Lüdtke et al., 2016; Naranjo-Gómez et al., 2019). Single-cell proteomics and transcriptomics revealed a transient increase in highly activated CD14⁺HLA-DR^{hi}CD11c^{hi} (*HLA-DRA*^{hi}*CD83*^{hi}) monocytes in mild COVID-19. This was similar in patients presenting with common cold or FLI, but absent in severe COVID-19 (Figures 3 and 4). In contrast, in severe COVID-19, monocytes showed low expression of HLA-DR, and high levels of *MAFB*, *PLBD1*, and *CD163*, all of which are associated with anti-inflammatory macrophage functions (Bronte et al., 2016; Cuevas et al., 2017; Fischer-Riepe et al., 2020; MacParland et al., 2018). Low HLA-DR expression on monocytes is an established surrogate marker of immunosuppression in sepsis (Venet et al., 2020). Elevated HLA-DR^{lo} monocytes have been associated with an increased risk of infectious complications after trauma (Hoffmann et al., 2017) and fatal outcome in septic shock (Monneret et al., 2006). Indeed, the HLA-DR^{lo}CD163⁺ monocytes showed enrichment of genes associated with poor prognosis in sepsis patients, including *PLAC8* (Maslove et al., 2019) and *MPO* (Schrijver et al., 2017) (Figure 4B). In line with this dysfunctional phenotype, *PLAC8* was recently shown to suppress production of IL-1 β and IL-18 (Segawa et al., 2018). In fact, we observed that inflammatory cytokine production, including IL-1 β release, was impaired in monocytes from patients with severe COVID-19 (Figure 4). CD14⁺HLA-DR^{lo} monocytes have also been implicated with immunosuppression in cancer patients (Bronte et al., 2016; Mengos et al., 2019; Meyer et al., 2014). While exhibiting anti-inflammatory features, especially in the early stages of severe disease (Figures S3C–S3F), persistently high expression of CD226 and CD69 may promote tissue infiltration and organ dysfunction (Davison et al., 2017; Reymond et al., 2004; Vo et al., 2016).

Acute pathological insults, such as trauma or severe infections, trigger a process referred to as emergency myelopoiesis to replenish functional granulocytes and other hematopoietic cells. Emergency myelopoiesis is characterized by the mobilization of immature myeloid cells, which are often linked to immunosuppressive functions (Loftus et al., 2018; Schultze et al., 2019). In fact, emergence of suppressive myeloid cells including neutrophils, often referred to as granulocytic MDSCs, has been observed during sepsis and severe influenza (Darcy et al., 2014; Loftus et al., 2018; Sander et al., 2010; De Santo et al., 2008). LDN in PBMC fractions in severe COVID-19 contained immature neutrophils, including pro- and pre-neutrophils, which was not observed in mild cases (Figure 5). These immature LDNs showed a surface marker and gene expression profile reminiscent of granulocytic MDSCs including genes such as *S100A12*, *S100A9*, *MMP8*, *ARG1* (Uhel et al., 2017), and *OLF4*, which has been recently associated with immunopathogenesis in sepsis (Alder et al., 2017). Emergence of pro-neutrophils in

severe COVID-19 was also detected by single-cell proteomics on whole blood samples. Strikingly, both immature and the mature neutrophils showed increased expression of CD64 and PD-L1 (Figures 6 and S5), similar to recently described alterations in sepsis (Meghraoui-Kheddar et al., 2020). In addition to the altered phenotype, we also observed an altered functionality. Neutrophils from patients with severe COVID-19 showed an impaired oxidative burst response, while their phagocytic capacity was preserved (Figure 7).

Single-cell transcriptomics of whole blood samples revealed mature activated neutrophils in both mild and severe COVID-19 (Figure 7B, cluster 2), however, expression of *CD274* (PD-L1) was only found in severe COVID-19 (cluster 1), and it increased in later stages of the disease. Expression of PD-L1 on neutrophils has been associated with T cell suppression (Bowers et al., 2014; Castell et al., 2019; de Kleijn et al., 2013; Langereis et al., 2017), suggesting that neutrophils in severe COVID-19 might exert suppressive functions. Furthermore, the expression of *CD177* on mature activated neutrophils and the identification of genes associated with anti-inflammatory functions (*CD274* and *ZC3H12A*) suggest a model in which neutrophils emerging prematurely from the bone marrow are programmed toward an anti-inflammatory or even suppressive phenotype in severe COVID-19. The transcriptional programs induced in immature neutrophils, including pro- and pre-neutrophils, as well as in COVID-19-associated mature neutrophil clusters, align with other observations in severe COVID-19 patients, including increased NET formation (Barnes et al., 2020; Zuo et al., 2020), coagulation (Klok et al., 2020; Pfeiler et al., 2014), and immunothrombosis (Stiel et al., 2018; Xu et al., 2020). In contrast, these transcriptional programs were not observed in patients with mild COVID-19 or in SARS-CoV-2 negative controls, even though the latter exhibited a range of comorbidities (e.g., COPD, type II diabetes).

Thus, defective or repressed monocyte activation combined with dysregulated myelopoiesis may cause a deleterious loop of continuous tissue inflammation and ineffective host defense.

Limitations of Study

The pathophysiological consequences of the dysfunctional phenotype of myeloid cells in severe COVID-19 remain unclear at this stage. It is, however, highly likely that they contribute to immunosuppression in critically ill patients, potentially leading to insufficient host defense, disbalanced inflammation, and increased susceptibility to superinfections. While our dual cohort study design provided robust and reproducible results concerning the alterations within the myeloid compartment in COVID-19, it is too early to speculate on the underlying mechanisms driving this response, such as genetics, lifestyle, comorbidities, environmental factors, or initial viral load (Ellinghaus et al., 2020). Utilizing the herein established transcriptional and functional phenotypes of the myeloid cell compartment, it will likely be possible to estimate the potential contribution of the causes mentioned above in larger clinical studies in the future and to address potential upstream events of immune dysregulation in preclinical model systems as they become available (Bao et al., 2020; Cohen, 2020). Indeed, in future studies it will be interesting to dissect whether the myeloid subsets in COVID-19 are anti-in-

flammatory or even capable of suppressing other immune cells, and which pathways might be mainly involved. Clearly, PD-L1 is a prime candidate (Bowers et al., 2014; Castell et al., 2019; de Kleijn et al., 2013; Langereis et al., 2017).

Collectively, our data link a striking appearance of immature and dysfunctional cells, in both the monocyte and neutrophil compartment, to disease severity in COVID-19. Consequently, the development of treatments and prevention strategies for severe COVID-19 may benefit from insights gained in other fields such as oncology, which have successfully applied therapies targeting suppressive myeloid cells.

STAR★METHODS

Detailed methods are provided in the online version of this paper and include the following:

- KEY RESOURCES TABLE
- RESOURCE AVAILABILITY
 - Lead Contact
 - Materials Availability
 - Data and Code Availability
- EXPERIMENTAL MODEL AND SUBJECT DETAILS
 - Cohort 1 / Berlin cohort
 - Cohort 2 / Bonn cohort
- METHOD DETAILS
 - Isolation of blood cells for scRNA-seq
 - Cohort 2 / Bonn cohort
 - Antibodies used for mass cytometry
 - Sample processing, antigen staining and data analysis of mass cytometry-based immune cell profiling
 - Blood processing for multi-color flow cytometry
 - *Ex vivo* functional analysis of neutrophils
 - *Ex vivo* functional analysis of monocytes
 - Hematological analyses of the granulocyte compartment
 - 10x Genomics Chromium single-cell RNA-seq
 - BD Rhapsody single-cell RNA-seq
- QUANTIFICATION AND STATISTICAL ANALYSIS
 - Data pre-processing of 10x Genomics Chromium scRNA-seq data
 - Data pre-processing of BD Rhapsody scRNA-seq data
 - ScRNA-seq data analysis of 10x Chromium data of cohort 1
 - Data quality control
 - Normalization
 - Data integration
 - Differential expression tests and cluster marker genes
 - Cluster annotation
 - GO enrichment analysis
 - Correlation analysis of marker genes for monocyte and neutrophils between cohort 1 and 2
 - Subset analysis of the neutrophils within the PBMC dataset of cohort 1
 - ScRNA-seq data analysis of Rhapsody data of cohort 2
 - scRNA-seq analysis of the complete BD Rhapsody dataset of cohort 2 including data from frozen and fresh PBMC and whole blood

- scRNA-seq analysis of fresh and frozen PBMC samples
- Quantification of the percentages of cell clusters in the PBMC scRNA-seq data of both cohorts separated by disease group
- Subset analysis of the monocytes within the PBMC dataset of cohort 2
- Time kinetics analysis of identified monocyte clusters
- Analysis of scRNA-seq data from fresh PBMC and whole blood samples of cohort 2
- Quantification of percentages of cell subsets in whole blood scRNA-seq data of cohort 2
- Confusion matrix
- GO enrichment
- Cell cycle state analysis of scRNA-seq data
- Trajectory analysis
- Transcription factor prediction analysis
- Mass cytometry data analysis
- Data Analysis of Flow Cytometry Data
- Data visualization

● ADDITIONAL RESOURCES

SUPPLEMENTAL INFORMATION

Supplemental Information can be found online at <https://doi.org/10.1016/j.cell.2020.08.001>.

CONSORTIA

The members of the Deutsche COVID-19 Omics Initiative (DeCOI) are Angel Angelov, Robert Bals, Alexander Bartholomäus, Anke Becker, Daniela Bezdán, Ezio Bonifacio, Peer Bork, Thomas Clavel, Maria Colome-Tatche, Andreas Diefenbach, Alexander Dilthey, Nicole Fischer, Konrad Förstner, Julia-Stefanie Frick, Julien Gagneur, Alexander Goesmann, Torsten Hain, Michael Hummel, Stefan Janssen, Jörn Kalinowski, René Kallies, Birte Kehr, Andreas Keller, Sarah Kim-Hellmuth, Christoph Klein, Oliver Kohlbacher, Jan O. Korbel, Ingo Kurth, Markus Landthaler, Yang Li, Kerstin Ludwig, Oliwia Makarewicz, Manja Marz, Alice McHardy, Christian Mertes, Markus Nöthen, Peter Nürnberg, Uwe Ohler, Stephan Ossowski, Jörg Overmann, Silke Peter, Klaus Pfeffer, Anna R. Poetsch, Alfred Pühler, Nikolaus Rajewsky, Markus Ralsler, Olaf Rieß, Stephan Ripke, Ulisses Nunes da Rocha, Philip Rosenstiel, Antoine-Emmanuel Saliba, Leif Erik Sander, Birgit Sawitzki, Philipp Schiffer, Eva-Christina Schulte, Joachim L. Schultze, Alexander Sczyrba, Oliver Stegle, Jens Stoye, Fabian Theis, Janne Vehreschild, Jörg Vogel, Max von Kleist, Andreas Walker, Jörn Walter, Dagmar Wieczorek, and John Ziebuhr.

ACKNOWLEDGMENTS

We thank Michael Kraut, Heidi Theis, Gudrun Hack, Claudia Finnemann, Magdalena Bürkle, Moritz Vollgraf, and Wibke Groenewald for perfect technical assistance. This work was supported by the German Research Foundation (DFG) (SFB-TR84 114933180 to L.E.S., S.H., A. Hocke, N.S., M.W., and C.D.; INST 37/1049-1, INST 216/981-1, INST 257/605-1, INST 269/768-1, INST 217/988-1, INST 217/577-1, and EXC2151/1 to J.L.S.; SFB TR57 and SPP1937 to J.N.; GRK2157 to A.-E.S.; and ME 3644/5-1 to H.E.M.); the Berlin University Alliance (BUA) (PreEP-Corona grant to L.E.S., V.C., and C.D.), the Berlin Institute of Health (BIH) (to L.E.S., A. Hocke, and C.D.); Helmholtz-Gemeinschaft Deutscher Forschungszentren, Germany (sparse2big to J.L.S.), EU projects SYSCID (733100 to J.L.S.), ERA CVD (00160389 to J.L.S.); the DZIF, Germany (TTU 04.816 and 04.817 to J.N.); the Hector Foundation (M89 to J.N.); the Helmholtz Association of German Research Centres (to A.-E.S.); the EU projects ONE STUDY (260687 to B.S.), BIO-DrIM (305147 to B.S.), and INsTRuCT (860003 to B.S.); the German Federal Ministry of Edu-

cation and Research, Germany (BMBF) (project RAPID to M.W., C.D., S.H., and A. Hocke, project SYMPATH to M.W. and N.S.); a Charité 3R project (to B.S. and S.H.); and Radboud University Medical Centre Hypatia Grant (2018 to Y.L.).

AUTHOR CONTRIBUTIONS

Conceptualization, J.S.-S., N.R., K.B., B.K., L.B., E.D.D., F.K., J.L.S., A.C.A., Y.L., J.N., B.S., A.-E.S., and L.E.S.; Methodology, J.S.-S., D.P., T.K., S.B., L.B., E.D.D., M.G., D.W., M. Beckstette, T.S.K., A.S., O.D., H.M., A.R.S., C.C., D.K., E.V., C.J.X., A.D., C.T., S.H., C.R.G., M.L., E.W., T.U., M. Becker, R.G., C.D.-H., C.v.K., and K.H.; Software/Data Analysis, J.S.-S., N.R., K.B., S.S., B.Z., T.K., L.B., A.S., T.U., and M. Becker.; Investigation, J.S.-S., K.B., T.P., A. Horne., M.H., J.L.S., A.C.A., M.W., Y.L., J.N., B.S., A.-E.S., and L.E.S.; Biospecimen/Enzyme Resources, B.K., S.B., M.P., S.H., H.M.-R., F.M., A.U., L.B.d.J., L.J., C.R.G., P.G., M.S., C.D.-H., N.N., K.K., R.T., V.C., J.R., K.M.K., M.T.V., G.R., F.K., J.N., and M.W.; Writing – Original Draft, J.S.-S., N.R., K.B., L.B., E.D.D., C.M., J.L.S., A.C.A., Y.L., J.N., B.S., A.-E.S., and L.E.S.; Writing – Review & Editing, J.S.-S., N.R., M.W., K.B., L.B., E.D.D., T.P., M. Becker, T.S.K., S.H., A. Hocke., M.S., H.-D.V., C.D.-H., N.S., C.v.K., F.K., J.L.S., A.C.A., Y.L., J.N., B.S., A.-E.S., and L.E.S.

DECLARATION OF INTERESTS

The authors declare no competing interests.

Received: May 27, 2020

Revised: July 13, 2020

Accepted: July 31, 2020

Published: August 5, 2020

REFERENCES

- Ahmad, S., Singh, P., Sharma, A., Arora, S., Shriwash, N., Rahmani, A.H., Almatroodi, S.A., Manda, K., Dohare, R., and Syed, M.A. (2019). Transcriptome meta-analysis deciphers a dysregulation in immune response-associated gene signatures during sepsis. *Genes (Basel)* *10*, 1005.
- Aibar, S., González-Blas, C.B., Moerman, T., Huynh-Thu, V.A., Imrichova, H., Hulselmans, G., Rambow, F., Marine, J.C., Geurts, P., Aerts, J., et al. (2017). SCENIC: single-cell regulatory network inference and clustering. *Nat. Methods* *14*, 1083–1086.
- Alder, M.N., Opoka, A.M., Lahni, P., Hildeman, D.A., and Wong, H.R. (2017). Olfactomedin-4 Is a Candidate Marker for a Pathogenic Neutrophil Subset in Septic Shock. *Crit. Care Med.* *45*, e426–e432.
- Angerer, P., Haghverdi, L., Büttner, M., Theis, F.J., Marr, C., and Büttner, F. (2016). destiny: diffusion maps for large-scale single-cell data in R. *Bioinformatics* *32*, 1241–1243.
- Aran, D., Looney, A.P., Liu, L., Wu, E., Fong, V., Hsu, A., Chak, S., Naikawadi, R.P., Wolters, P.J., Abate, A.R., et al. (2019). Reference-based analysis of lung single-cell sequencing reveals a transitional profibrotic macrophage. *Nat. Immunol.* *20*, 163–172.
- Ashburner, M., Ball, C.A., Blake, J.A., Botstein, D., Butler, H., Cherry, J.M., Davis, A.P., Dolinski, K., Dwight, S.S., Eppig, J.T., et al.; The Gene Ontology Consortium (2000). Gene ontology: tool for the unification of biology. *Nat. Genet.* *25*, 25–29.
- Bao, L., Deng, W., Huang, B., Gao, H., Liu, J., Ren, L., Wei, Q., Yu, P., Xu, Y., Qi, F., et al. (2020). The pathogenicity of SARS-CoV-2 in hACE2 transgenic mice. *Nature* *583*, 830–833.
- Barnes, B.J., Adrover, J.M., Baxter-Stoltzfus, A., Borczuk, A., Cools-Lartigue, J., Crawford, J.M., DaBler-Plenker, J., Guerci, P., Huynh, C., Knight, J.S., et al. (2020). Targeting potential drivers of COVID-19: Neutrophil extracellular traps. *J. Exp. Med.* *217*, e20200652.
- Bayik, D., Zhou, Y., Park, C., Hong, C., Vail, D., Silver, D.J., Lauko, A., Roversi, G., Watson, D.C., Lo, A., et al. (2020). Myeloid-derived suppressor cell subsets

- drive glioblastoma growth in a sex-specific manner. *Cancer Discov.* 10, 1210–1225.
- Bernardo, D., Marin, A.C., Fernández-Tomé, S., Montalban-Arques, A., Carrasco, A., Tristán, E., Ortega-Moreno, L., Mora-Gutiérrez, I., Díaz-Guerra, A., Caminero-Fernández, R., et al. (2018). Human intestinal pro-inflammatory CD11c^{high}CCR2⁺CX3CR1⁺ macrophages, but not their tolerogenic CD11c⁺CCR2⁺CX3CR1⁻ counterparts, are expanded in inflammatory bowel disease. *Mucosal Immunol.* 11, 1114–1126.
- Bowers, N.L., Helton, E.S., Huijbregts, R.P.H., Goepfert, P.A., Heath, S.L., and Hel, Z. (2014). Immune suppression by neutrophils in HIV-1 infection: role of PD-L1/PD-1 pathway. *PLoS Pathog.* 10, e1003993.
- Braun J., Loyal L., Frentsch M., Wendisch D., Georg P., Kurth F., Hippenstiel S., Dingeldey M., Kruse B., Faucher F., et al. (2020). SARS-CoV-2-reactive T cells in healthy donors and patients with COVID-19. *Nature*. Published online July 29, 2020. <https://doi.org/10.1038/s41586-020-2598-9>.
- Bronte, V., Serafini, P., Mazzoni, A., Segal, D.M., and Zanovello, P. (2003). L-arginine metabolism in myeloid cells controls T-lymphocyte functions. *Trends Immunol.* 24, 302–306.
- Bronte, V., Brandau, S., Chen, S.H., Colombo, M.P., Frey, A.B., Greten, T.F., Mandruzzato, S., Murray, P.J., Ochoa, A., Ostrand-Rosenberg, S., et al. (2016). Recommendations for myeloid-derived suppressor cell nomenclature and characterization standards. *Nat. Commun.* 7, 12150.
- Butler, A., Hoffman, P., Smibert, P., Papalexis, E., and Satija, R. (2018). Integrating single-cell transcriptomic data across different conditions, technologies, and species. *Nat. Biotechnol.* 36, 411–420.
- Carbon, S., Douglass, E., Dunn, N., Good, B., Harris, N.L., Lewis, S.E., Mungall, C.J., Basu, S., Chisholm, R.L., Dodson, R.J., et al.; The Gene Ontology Consortium (2019). The Gene Ontology Resource: 20 years and still GOing strong. *Nucleic Acids Res.* 47 (D1), D330–D338.
- Cassetta, L., Baekkevold, E.S., Brandau, S., Bujko, A., Cassatella, M.A., Dohoi, A., Krieg, C., Lin, A., Loré, K., Marini, O., et al. (2019). Deciphering myeloid-derived suppressor cells: isolation and markers in humans, mice and non-human primates. *Cancer Immunol. Immunother.* 68, 687–697.
- Castell, S.D., Harman, M.F., Morón, G., Maletto, B.A., and Pistoiresi-Palencia, M.C. (2019). Neutrophils which migrate to lymph nodes modulate CD4⁺ T cell response by a PD-L1 dependent mechanism. *Front. Immunol.* 10, 105.
- Chen, G., Wu, D., Guo, W., Cao, Y., Huang, D., Wang, H., Wang, T., Zhang, X., Chen, H., Yu, H., et al. (2020). Clinical and immunological features of severe and moderate coronavirus disease 2019. *J. Clin. Invest.* 130, 2620–2629.
- Chua, R.L., Lukassen, S., Trump, S., Hennig, B.P., Wendisch, D., Pott, F., Debnath, O., Thürmann, L., Kurth, F., Völker, M.T., et al. (2020). COVID-19 severity correlates with airway epithelium-immune cell interactions identified by single-cell analysis. *Nat. Biotechnol.* Published online June 26, 2020. <https://doi.org/10.1038/s41587-020-0602-4>.
- Chun, E., Lavoie, S., Michaud, M., Gallini, C.A., Kim, J., Soucy, G., Odze, R., Glickman, J.N., and Garrett, W.S. (2015). CCL2 Promotes Colorectal Carcinogenesis by Enhancing Polymorphonuclear Myeloid-Derived Suppressor Cell Population and Function. *Cell Rep.* 12, 244–257.
- Cibrián, D., and Sánchez-Madrid, F. (2017). CD69: from activation marker to metabolic gatekeeper. *Eur. J. Immunol.* 47, 946–953.
- Cohen, J. (2020). From mice to monkeys, animals studied for coronavirus answers. *Science* 368, 221–222.
- Cuevas, V.D., Anta, L., Samaniego, R., Orta-Zavalza, E., Vladimir de la Rosa, J., Baujat, G., Domínguez-Soto, Á., Sánchez-Mateos, P., Escribese, M.M., Castrillo, A., et al. (2017). MAFB Determines Human Macrophage Anti-inflammatory Polarization: Relevance for the Pathogenic Mechanisms Operating in Multicentric Carpotarsal Osteolysis. *J. Immunol.* 198, 2070–2081.
- Darcy, C.J., Minigo, G., Piera, K.A., Davis, J.S., McNeil, Y.R., Chen, Y., Volkheimer, A.D., Weinberg, J.B., Anstey, N.M., and Woodberry, T. (2014). Neutrophils with myeloid derived suppressor function deplete arginine and constrain T cell function in septic shock patients. *Crit. Care* 18, R163.
- Davison, G.M., Nkambule, B.B., Mkandla, Z., Hon, G.M., Kengne, A.P., Erasmus, R.T., and Matsha, T.E. (2017). Platelet, monocyte and neutrophil activation and glucose tolerance in South African Mixed Ancestry individuals. *Sci. Rep.* 7, 40329.
- de Kleijn, S., Langereis, J.D., Leentjens, J., Kox, M., Netea, M.G., Koenderman, L., Ferwerda, G., Pickkers, P., and Hermans, P.W.M. (2013). IFN- γ -stimulated neutrophils suppress lymphocyte proliferation through expression of PD-L1. *PLoS ONE* 8, e72249.
- De Santo, C., Salio, M., Masri, S.H., Lee, L.Y.H., Dong, T., Speak, A.O., Porubsky, S., Booth, S., Veerapen, N., Besra, G.S., et al. (2008). Invariant NKT cells reduce the immunosuppressive activity of influenza A virus-induced myeloid-derived suppressor cells in mice and humans. *J. Clin. Invest.* 118, 4036–4048.
- Dimopoulos, G., de Mast, Q., Markou, N., Theodorakopoulou, M., Komnos, A., Mouktaroudi, M., Netea, M.G., Spyridopoulos, T., Verheggen, R.J., Hoogerwerf, J., et al. (2020). Favorable Anakinra Responses in Severe Covid-19 Patients with Secondary Hemophagocytic Lymphohistiocytosis. *Cell Host Microbe* 28, 117–123.
- Dobin, A., Davis, C.A., Schlesinger, F., Drenkow, J., Zaleski, C., Jha, S., Batut, P., Chaisson, M., and Gingeras, T.R. (2013). STAR: ultrafast universal RNA-seq aligner. *Bioinformatics* 29, 15–21.
- Ellinghaus, D., Degenhardt, F., Bujanda, L., Buti, M., Albillos, A., Invernizzi, P., Fernández, J., Prati, D., Baselli, G., Asselta, R., et al. (2020). Genomewide Association Study of Severe Covid-19 with Respiratory Failure. *N. Engl. J. Med.* Published online June 17, 2020. <https://doi.org/10.1056/NEJMoa2020283>.
- Fischer-Riepe, L., Daber, N., Schulte-Schrepping, J., Vêras De Carvalho, B.C., Russo, A., Pohlen, M., Fischer, J., Chasan, A.I., Wolf, M., Ulas, T., et al. (2020). CD163 expression defines specific, IRF8-dependent, immune-modulatory macrophages in the bone marrow. *J. Allergy Clin. Immunol.* Published online March 19, 2020. <https://doi.org/10.1016/j.jaci.2020.02.034>.
- Giamarellos-Bourboulis, E.J., Netea, M.G., Rovina, N., Akinosoglou, K., Antoniadou, A., Antonakos, N., Damoraki, G., Gkavogianni, T., Adami, M.E., Katsounou, P., et al. (2020). Complex Immune Dysregulation in COVID-19 Patients with Severe Respiratory Failure. *Cell Host Microbe* 27, 992–1000.
- Grifoni, A., Weiskopf, D., Ramirez, S.I., Mateus, J., Dan, J.M., Moderbacher, C.R., Rawlings, S.A., Sutherland, A., Premkumar, L., Jodi, R.S., et al. (2020). Targets of T cell responses to SARS-CoV-2 coronavirus in humans with COVID-19 disease and unexposed individuals. *Cell* 181, 1489–1501.
- Gu, Z., Eils, R., and Schlesner, M. (2016). Complex heatmaps reveal patterns and correlations in multidimensional genomic data. *Bioinformatics* 32, 2847–2849.
- Hadjadj, J., Yatim, N., Barnabei, L., Corneau, A., Boussier, J., Smith, N., Pere, H., Charbit, B., Bondet, V., Chenevier-Gobeaux, C., Breillat, P., et al. (2020). Impaired type I interferon activity and exacerbated inflammatory responses in severe COVID-19 patients. *Science* 369, 718–724.
- Hafemeister, C., and Satija, R. (2019). Normalization and variance stabilization of single-cell RNA-seq data using regularized negative binomial regression. *Genome Biol.* 20, 296.
- Hesselink, L., Spijkerman, R., van Wesse, K.J.P., Koenderman, L., Leenen, L.P.H., Huber-Lang, M., and Hietbrink, F. (2019). Neutrophil heterogeneity and its role in infectious complications after severe trauma. *World J. Emerg. Surg.* 14, 24.
- Hirano, N., Butler, M.O., Xia, Z., Ansén, S., von Bergwelt-Baildon, M.S., Neuberger, D., Freeman, G.J., and Nadler, L.M. (2006). Engagement of CD83 ligand induces prolonged expansion of CD8⁺ T cells and preferential enrichment for antigen specificity. *Blood* 107, 1528–1536.
- Hoffmann, S., Harms, H., Ulm, L., Nabavi, D.G., Mackert, B.M., Schmehl, I., Jungehulsing, G.J., Montaner, J., Bustamante, A., Hermans, M., et al.; PREDICT Investigators (2017). Stroke-induced immunodepression and dysphagia independently predict stroke-associated pneumonia - The PREDICT study. *J. Cereb. Blood Flow Metab.* 37, 3671–3682.
- Horby, P., Lim, W.S., Emberson, J.R., Mafham, M., Bell, J.L., Linsell, L., Phil, D., Sta-Plin, N., Brightling, C., Med, F., et al. (2020). Dexamethasone in Hospitalized Patients with Covid-19 - Preliminary Report. *N. Engl. J. Med.* Published online July 17, 2020. <https://doi.org/10.1056/NEJMoa2021436>.

- Hothorn, T., Bretz, F., and Westfall, P. (2008). Simultaneous inference in general parametric models. *Biom. J. 50*, 346–363.
- Huang, C., Wang, Y., Li, X., Ren, L., Zhao, J., Hu, Y., Zhang, L., Fan, G., Xu, J., Gu, X., et al. (2020a). Clinical features of patients infected with 2019 novel coronavirus in Wuhan, China. *Lancet 395*, 497–506.
- Huang, X., He, C., Lin, G., Lu, L., Xing, K., Hua, X., Sun, S., Mao, Y., Song, Y., Wang, J., and Li, S. (2020b). Induced CD10 expression during monocyte-to-macrophage differentiation identifies a unique subset of macrophages in pancreatic ductal adenocarcinoma. *Biochem. Biophys. Res. Commun. 524*, 1064–1071.
- Jamilou, Y., Henry, T., Belot, A., Viel, S., Fauter, M., El Jammal, T., Walzer, T., François, B., and Sève, P. (2020). Should we stimulate or suppress immune responses in COVID-19? Cytokine and anti-cytokine interventions. *Autoimmun. Rev. 19*, 102567.
- Janky, R., Verfaillie, A., Imrichová, H., Van de Sande, B., Standaert, L., Christiaens, V., Hulselmans, G., Hertens, K., Naval Sanchez, M., Potier, D., et al. (2014). iRegulon: from a gene list to a gene regulatory network using large motif and track collections. *PLoS Comput. Biol. 10*, e1003731.
- Janols, H., Wullt, M., Bergenfelz, C., Björnsson, S., Lickei, H., Janciauskiene, S., Leandersson, K., and Bredberg, A. (2014). Heterogeneity among septic shock patients in a set of immunoregulatory markers. *Eur. J. Clin. Microbiol. Infect. Dis. 33*, 313–324.
- Kamp, V.M., Pillay, J., Lammers, J.-W.J., Pickkers, P., Ulfman, L.H., and Koenderman, L. (2012). Human suppressive neutrophils CD16bright/CD62Ldim exhibit decreased adhesion. *J. Leukoc. Biol. 92*, 1011–1020.
- Kanehisa, M. (2019). Toward understanding the origin and evolution of cellular organisms. *Protein Sci. 28*, 1947–1951.
- Kangelaris, K.N., Prakash, A., Liu, K.D., Aouizerat, B., Woodruff, P.G., Erle, D.J., Rogers, A., Seeley, E.J., Chu, J., Liu, T., et al. (2015). Increased expression of neutrophil-related genes in patients with early sepsis-induced ARDS. *Am. J. Physiol. Lung Cell. Mol. Physiol. 308*, L1102–L1113.
- Klok, F.A., Kruijff, M.J.H.A., van der Meer, N.J.M., Arbous, M.S., Gommers, D.A.M.P.J., Kant, K.M., Kaptein, F.H.J., van Paassen, J., Stals, M.A.M., Huisman, M.V., and Endeman, H. (2020). Incidence of thrombotic complications in critically ill ICU patients with COVID-19. *Thromb. Res. 191*, 145–147.
- Korsunsky, I., Millard, N., Fan, J., Slowikowski, K., Zhang, F., Wei, K., Baglaenko, Y., Brenner, M., Loh, P.R., and Raychaudhuri, S. (2019). Fast, sensitive and accurate integration of single-cell data with Harmony. *Nat. Methods 16*, 1289–1296.
- Kotecha, N., Krutzik, P.O., and Irish, J.M. (2010). Web-based analysis and publication of flow cytometry experiments. *Curr. Protoc. Cytom. Chapter 10*, Unit10.17.
- Kuri-Cervantes, L., Pampena, M.B., Meng, W., Rosenfeld, A.M., Ittner, C.A.G., Weisman, A.R., Agyekum, R., Mathew, D., Baxter, A.E., Vella, L., et al. (2020). Immunologic perturbations in severe COVID-19/SARS-CoV-2 infection. *bioRxiv*. <https://doi.org/10.1101/2020.05.18.101717>.
- Kurth, F., Roennefarth, M., Thibeault, C., Corman, V.M., Müller-Redetzky, H., Mittermaier, M., Ruwwe-Glösenkamp, C., Heim, K.M., Krannich, A., Zvorc, S., et al. (2020). Studying the pathophysiology of coronavirus disease 2019: a protocol for the Berlin prospective COVID-19 patient cohort (Pa-COVID-19). *Infection 48*, 619–626.
- Kverneland, A.H., Streitz, M., Geissler, E., Hutchinson, J., Vogt, K., Boës, D., Niemann, N., Pedersen, A.E., Schlickeiser, S., and Sawitzki, B. (2016). Age and gender leucocytes variances and references values generated using the standardized ONE-Study protocol. *Cytometry A 89*, 543–564.
- Kwok, I., Becht, E., Xia, Y., Ng, M., Teh, Y.C., Tan, L., Evrard, M., Li, J.L.Y., Tran, H.T.N., Tan, Y., et al. (2020). Combinatorial Single-Cell Analyses of Granulocyte-Monocyte Progenitor Heterogeneity Reveals an Early Uni-potent Neutrophil Progenitor. *Immunity S1074-7613*, 30235-1.
- Largeries, J.D., Pickkers, P., de Kleijn, S., Gerretsen, J., de Jonge, M.I., and Kox, M. (2017). Spleen-derived IFN- γ induces generation of PD-L1⁺-suppressive neutrophils during endotoxemia. *J. Leukoc. Biol. 102*, 1401–1409.
- Lee, J.S., Park, S., Jeong, H.W., Ahn, J.Y., Choi, S.J., Lee, H., Choi, B., Nam, S.K., Sa, M., Kwon, J.-S., et al. (2020). Immunophenotyping of COVID-19 and influenza highlights the role of type I interferons in development of severe COVID-19. *Sci. Immunol. 5*, eabd1554.
- Lenth, R.V. (2016). Least-squares means: The R package lsmeans. *J. Stat. Softw. 69*, 1–33.
- Leshner, M., Wang, S., Lewis, C., Zheng, H., Chen, X.A., Santy, L., and Wang, Y. (2012). PAD4 mediated histone hyperacetylation induces heterochromatin decondensation and chromatin unfolding to form neutrophil extracellular trap-like structures. *Front. Immunol. 3*, 307.
- Li, X.-K., Lu, Q.-B., Chen, W.-W., Xu, W., Liu, R., Zhang, S.-F., Du, J., Li, H., Yao, K., Zhai, D., et al. (2018). Arginine deficiency is involved in thrombocytopenia and immunosuppression in severe fever with thrombocytopenia syndrome. *Sci. Transl. Med. 10*, eaat4162.
- Liao, M., Liu, Y., Yuan, J., Wen, Y., Xu, G., Zhao, J., Cheng, L., Li, J., Wang, X., Wang, F., et al. (2020). Single-cell landscape of bronchoalveolar immune cells in patients with COVID-19. *Nat. Med. 26*, 842–844.
- Liberzon, A., Birger, C., Thorvaldsdóttir, H., Ghandi, M., Mesirov, J.P., and Tamayo, P. (2015). The Molecular Signatures Database (MSigDB) hallmark gene set collection. *Cell Syst. 1*, 417–425.
- Lin, R.-J., Chu, J.-S., Chien, H.-L., Tseng, C.-H., Ko, P.-C., Mei, Y.-Y., Tang, W.-C., Kao, Y.-T., Cheng, H.-Y., Liang, Y.-C., and Lin, S.Y. (2014). MCP1 suppresses hepatitis C virus replication and negatively regulates virus-induced proinflammatory cytokine responses. *J. Immunol. 193*, 4159–4168.
- Loftus, T.J., Mohr, A.M., and Moldawer, L.L. (2018). Dysregulated myelopoiesis and hematopoietic function following acute physiologic insult. *Curr. Opin. Hematol. 25*, 37–43.
- Long, Q.-X., Liu, B.-Z., Deng, H.-J., Wu, G.-C., Deng, K., Chen, Y.-K., Liao, P., Qiu, J.-F., Lin, Y., Cai, X.-F., et al. (2020). Antibody responses to SARS-CoV-2 in patients with COVID-19. *Nat. Med. 26*, 845–848.
- Lucas, C., Wong, P., Klein, J., Castro, T.B.R., Silva, J., Sundaram, M., Ellingson, M.K., Mao, T., Oh, J.E., Israelow, B., et al.; Yale IMPACT Team (2020). Longitudinal analyses reveal immunological misfiring in severe COVID-19. *Nature*. <https://doi.org/10.1038/s41586-020-2588-y>.
- Lüdtke, A., Ruibal, P., Becker-Ziaja, B., Rottstegge, M., Wozniak, D.M., Cabeza-Cabrero, M., Thorenz, A., Weller, R., Kerber, R., Idoyaga, J., et al. (2016). Ebola Virus Disease Is Characterized by Poor Activation and Reduced Levels of Circulating CD16⁺ Monocytes. *J. Infect. Dis. 214 (Suppl 3)*, S275–S280.
- MacParland, S.A., Liu, J.C., Ma, X.Z., Innes, B.T., Bartczak, A.M., Gage, B.K., Manuel, J., Khuu, N., Echeverri, J., Linares, I., et al. (2018). Single cell RNA sequencing of human liver reveals distinct intrahepatic macrophage populations. *Nat. Commun. 9*, 4383.
- Maier, M.J. (2014). DirichletReg: Dirichlet Regression for Compositional Data in R. <https://pub.wu.ac.at/4077/>.
- Martin, M. (2011). Cutadapt removes adapter sequences from high-throughput sequencing reads. *EMBnet. J. 17*, 10.
- Maslove, D.M., Shapira, T., Tyryshkin, K., Veldhoen, R.A., Marshall, J.C., and Muscedere, J. (2019). Validation of diagnostic gene sets to identify critically ill patients with sepsis. *J. Crit. Care 49*, 92–98.
- Mathew, D., Giles, J.R., Baxter, A.E., Greenplate, A.R., Wu, J.E., Alanio, C., Oldridge, D.A., Kuri-Cervantes, L., Pampena, M.B., D'Andrea, K., et al. (2020). Deep immune profiling of COVID-19 patients reveals patient heterogeneity and distinct immunotypes with implications for therapeutic interventions. *bioRxiv*. <https://doi.org/10.1101/2020.05.20.106401>.
- McKechnie, J.L., and Blish, C.A. (2020). The Innate Immune System: Fighting on the Front Lines or Fanning the Flames of COVID-19? *Cell Host Microbe 27*, 863–869.
- Meghraoui-Kheddar, A., Chousterman, B.G., Guillou, N., Barone, S.M., Granjeaud, S., Vallet, H., Corneau, A., Guessous, K., Boissonnas, A., Irish, J.M., et al. (2020). Two new immature and dysfunctional neutrophil cell subsets define a predictive signature of sepsis useable in clinical practice. *bioRxiv*. <https://doi.org/10.1101/2020.05.29.123992>.

- Mei, H.E., Leipold, M.D., Schulz, A.R., Chester, C., and Maecker, H.T. (2015). Barcoding of live human peripheral blood mononuclear cells for multiplexed mass cytometry. *J. Immunol.* *194*, 2022–2031.
- Mei, H.E., Leipold, M.D., and Maecker, H.T. (2016). Platinum-conjugated antibodies for application in mass cytometry. *Cytometry A* *89*, 292–300.
- Mengos, A.E., Gastineau, D.A., and Gustafson, M.P. (2019). The CD14(+) HLA-DR(lo/neg) Monocyte: An immunosuppressive phenotype that restrains responses to cancer immunotherapy. *Front. Immunol.* *10*, 1147.
- Merad, M., and Martin, J.C. (2020). Pathological inflammation in patients with COVID-19: a key role for monocytes and macrophages. *Nat. Rev. Immunol.* *20*, 355–362.
- Messner, C.B., Demichev, V., Wendisch, D., Michalick, L., White, M., Freiwald, A., Textoris-Taube, K., Vernardis, S.I., Egger, A.-S., Kreidl, M., et al. (2020). Ultra-high-throughput clinical proteomics reveals classifiers of COVID-19 infection. *Cell Syst.* *11*, 11–24.
- Meyer, C., Cagnon, L., Costa-Nunes, C.M., Baumgaertner, P., Montandon, N., Leyvraz, L., Michielin, O., Romano, E., and Speiser, D.E. (2014). Frequencies of circulating MDSC correlate with clinical outcome of melanoma patients treated with ipilimumab. *Cancer Immunol. Immunother.* *63*, 247–257.
- Middleton, E.A., He, X.-Y., Denorme, F., Campbell, R.A., Ng, D., Salvatore, S.P., Mostyka, M., Baxter-Stoltzfus, A., Borczuk, A.C., Loda, M., et al. (2020). Neutrophil Extracellular Traps (NETs) Contribute to Immunothrombosis in COVID-19 Acute Respiratory Distress Syndrome. *Blood*. Published online June 29, 2020. <https://doi.org/10.1182/blood.2020007008>.
- Monneret, G., Lepape, A., Voirin, N., Bohé, J., Venet, F., Debard, A.L., Thizy, H., Bienvenu, J., Gueyffier, F., and Vanhems, P. (2006). Persisting low monocyte human leukocyte antigen-DR expression predicts mortality in septic shock. *Intensive Care Med.* *32*, 1175–1183.
- Mortaz, E., Alipoor, S.D., Adcock, I.M., Mumby, S., and Koenderman, L. (2018). Update on neutrophil function in severe inflammation. *Front. Immunol.* *9*, 2171.
- Naranjo-Gómez, J.S., Castillo, J.A., Rojas, M., Restrepo, B.N., Diaz, F.J., Velilla, P.A., and Castaño, D. (2019). Different phenotypes of non-classical monocytes associated with systemic inflammation, endothelial alteration and hepatic compromise in patients with dengue. *Immunology* *156*, 147–163.
- Ng, L.G., Ostuni, R., and Hidalgo, A. (2019). Heterogeneity of neutrophils. *Nat. Rev. Immunol.* *19*, 255–265.
- Ni, L., Ye, F., Cheng, M.L., Feng, Y., Deng, Y.Q., Zhao, H., Wei, P., Ge, J., Gou, M., Li, X., et al. (2020). Detection of SARS-CoV-2-Specific Humoral and Cellular Immunity in COVID-19 Convalescent Individuals. *Immunity* *52*, 971–977.
- Nowicka, M., Krieg, C., Crowell, H.L., Weber, L.M., Hartmann, F.J., Guglietta, S., Becher, B., Levesque, M.P., and Robinson, M.D. (2017). CyTOF workflow: differential discovery in high-throughput high-dimensional cytometry datasets. *F1000Res.* *6*, 748.
- Ong, E.Z., Chan, Y.F.Z., Leong, W.Y., Lee, N.M.Y., Kalimuddin, S., Haja Mohideen, S.M., Chan, K.S., Tan, A.T., Bertoletti, A., Ooi, E.E., and Low, J.G.H. (2020). A dynamic immune response shapes COVID-19 progression. *Cell Host Microbe* *27*, 879–882.
- Pellin, D., Loperfido, M., Baricordi, C., Wolock, S.L., Montepeloso, A., Weinberg, O.K., Biffi, A., Klein, A.M., and Biasco, L. (2019). A comprehensive single cell transcriptional landscape of human hematopoietic progenitors. *Nat. Commun.* *10*, 2395.
- Perlman, S., and Dandekar, A.A. (2005). Immunopathogenesis of coronavirus infections: implications for SARS. *Nat. Rev. Immunol.* *5*, 917–927.
- Pfeiler, S., Massberg, S., and Engelmann, B. (2014). Biological basis and pathological relevance of microvascular thrombosis. *Thromb. Res.* *133* (Suppl 1), S35–S37.
- Pillay, J., Kamp, V.M., van Hoffen, E., Visser, T., Tak, T., Lammers, J.W., Ulfman, L.H., Leenen, L.P., Pickkers, P., and Koenderman, L. (2012). A subset of neutrophils in human systemic inflammation inhibits T cell responses through Mac-1. *J. Clin. Invest.* *122*, 327–336.
- Popescu, D.M., Botting, R.A., Stephenson, E., Green, K., Webb, S., Jardine, L., Calderbank, E.F., Polanski, K., Goh, I., Efremova, M., et al. (2019). Decoding human fetal liver haematopoiesis. *Nature* *574*, 365–371.
- Qiu, P., Simonds, E.F., Bendall, S.C., Gibbs, K.D., Jr., Bruggner, R.V., Linderman, M.D., Sachs, K., Nolan, G.P., and Plevritis, S.K. (2011). Extracting a cellular hierarchy from high-dimensional cytometry data with SPADE. *Nat. Biotechnol.* *29*, 886–891.
- Quah, P., Li, A., and Phua, J. (2020). Mortality rates of patients with COVID-19 in the intensive care unit: a systematic review of the emerging literature. *Crit. Care* *24*, 285.
- Remy, K.E., Brakenridge, S.C., Francois, B., Daix, T., Deutschman, C.S., Monneret, G., Jeannot, R., Laterre, P.-F., Hotchkiss, R.S., and Moldawer, L.L. (2020). Immunotherapies for COVID-19: lessons learned from sepsis. *Lancet Respir. Med.* *2*, 2–5.
- Reyes, M., Filbin, M.R., Bhattacharyya, R.P., Billman, K., Eisenhaure, T., Hung, D.T., Levy, B.D., Baron, R.M., Blainey, P.C., Goldberg, M.B., and Hacohen, N. (2020). An immune-cell signature of bacterial sepsis. *Nat. Med.* *26*, 333–340.
- Reymond, N., Imbert, A.M., Devilard, E., Fabre, S., Chabannon, C., Xerri, L., Farmaier, C., Cantoni, C., Bottino, C., Moretta, A., et al. (2004). DNAM-1 and PVR regulate monocyte migration through endothelial junctions. *J. Exp. Med.* *199*, 1331–1341.
- Riegel, A., Maurer, T., Prior, B., Stegmaier, S., Heppert, V., Wagner, C., and Hänsch, G.M. (2012). Human polymorphonuclear neutrophils express RANK and are activated by its ligand, RANKL. *Eur. J. Immunol.* *42*, 975–981.
- Ritchie, A.I., and Singanayagam, A. (2020). Immunosuppression for hyperinflammation in COVID-19: a double-edged sword? *Lancet* *395*, 1111.
- Robbiani, D.F., Gaebler, C., Muecksch, F., Lorenzi, J.C.C., Wang, Z., Cho, A., Agudelo, M., Barnes, C.O., Gazumyan, A., Finkin, S., et al. (2020). Convergent antibody responses to SARS-CoV-2 in convalescent individuals. *Nature*. Published online June 18, 2020. <https://doi.org/10.1038/s41586-020-2456-9>.
- Sanchez-Cerrillo, I., Landete, P., Aldave, B., Sanchez-Alonso, S., Sanchez-Azofra, A., Marcos-Jimenez, A., Avalos, E., Alcaraz-Serna, A., de los Santos, I., Mateu-Alberro, T., et al. (2020). Differential Redistribution of Activated Monocyte and Dendritic Cell Subsets to the Lung Associates with Severity of COVID-19. *medRxiv*. <https://doi.org/10.1101/2020.05.13.20100925>.
- Sander, L.E., Sackett, S.D., Dierssen, U., Beraza, N., Linke, R.P., Müller, M., Blander, J.M., Tacke, F., and Trautwein, C. (2010). Hepatic acute-phase proteins control innate immune responses during infection by promoting myeloid-derived suppressor cell function. *J. Exp. Med.* *207*, 1453–1464.
- Sawitzki, B., Harden, P.N., Reinke, P., Moreau, A., Hutchinson, J.A., Game, D.S., Tang, Q., Guinan, E.C., Battaglia, M., Burlingham, W.J., et al. (2020). Regulatory cell therapy in kidney transplantation (The ONE Study): a harmonised design and analysis of seven non-randomised, single-arm, phase 1/2A trials. *Lancet* *395*, 1627–1639.
- Scapini, P., Marini, O., Tecchio, C., and Cassatella, M.A. (2016). Human neutrophils in the saga of cellular heterogeneity: insights and open questions. *Immunol. Rev.* *273*, 48–60.
- Schrijver, I.T., Kemperman, H., Roest, M., Kesecioglu, J., and de Lange, D.W. (2017). Myeloperoxidase can differentiate between sepsis and non-infectious SIRS and predicts mortality in intensive care patients with SIRS. *Intensive Care Med.* *Exp.* *5*, 43.
- Schultz, J.L., Mass, E., and Schlitzer, A. (2019). Emerging Principles in Myelopoiesis at Homeostasis and during Infection and Inflammation. *Immunity* *50*, 288–301.
- Schulz, A.R., and Mei, H.E. (2019). Surface barcoding of live PBMC for multiplexed mass cytometry. In *Methods in Molecular Biology* (Humana Press Inc.), pp. 93–108.
- Schuyler, R.P., Jackson, C., Garcia-Perez, J.E., Baxter, R.M., Ogolla, S., Rochford, R., Ghosh, D., Rudra, P., and Hsieh, E.W.Y. (2019). Minimizing Batch Effects in Mass Cytometry Data. *Front. Immunol.* *10*, 2367.
- Segawa, S., Kondo, Y., Nakai, Y., Iizuka, A., Kaneko, S., Yokosawa, M., Furuyama, K., Tsuboi, H., Goto, D., Matsumoto, I., and Sumida, T. (2018).

- Placenta Specific 8 Suppresses IL-18 Production through Regulation of Autophagy and Is Associated with Adult Still Disease. *J. Immunol.* 207, 3534–3545.
- Silvestre-Roig, C., Fridlender, Z.G., Glogauer, M., and Scapini, P. (2019). Neutrophil Diversity in Health and Disease. *Trends Immunol.* 40, 565–583.
- Stiel, L., Delabranche, X., Galoisy, A.C., Severac, F., Toti, F., Mauvieux, L., Meziani, F., and Boisramé-Helms, J. (2016). Neutrophil Fluorescence: A New Indicator of Cell Activation During Septic Shock-Induced Disseminated Intravascular Coagulation. *Crit. Care Med.* 44, e1132–e1136.
- Stiel, L., Meziani, F., and Helms, J. (2018). Neutrophil Activation During Septic Shock. *Shock* 49, 371–384.
- Stuart, T., Butler, A., Hoffman, P., Hafemeister, C., Papalexi, E., Mauck, W.M., 3rd, Hao, Y., Stoeckius, M., Smibert, P., and Satija, R. (2019). Comprehensive Integration of Single-Cell Data. *Cell* 177, 1888–1902.
- Tak, T., Wijten, P., Heeres, M., Pickkers, P., Scholten, A., Heck, A.J.R., Vriskoop, N., Leenen, L.P., Borghans, J.A.M., Tesselaar, K., and Koenderman, L. (2017). Human CD62L^{dim} neutrophils identified as a separate subset by proteome profiling and in vivo pulse-chase labeling. *Blood* 129, 3476–3485.
- Testa, U., Riccioni, R., Diverio, D., Rossini, A., Lo Coco, F., and Peschle, C. (2004). Interleukin-3 receptor in acute leukemia. *Leukemia* 18, 219–226.
- Thomas, M.P., Whangbo, J., McCrossan, G., Deutsch, A.J., Martinod, K., Walch, M., and Lieberman, J. (2014). Leukocyte protease binding to nucleic acids promotes nuclear localization and cleavage of nucleic acid binding proteins. *J. Immunol.* 192, 5390–5397.
- Trouillet-Assant, S., Viel, S., Gaymard, A., Pons, S., Richard, J.C., Perret, M., Villard, M., Brengel-Pesce, K., Lina, B., Mezidi, M., et al.; COVID HCL Study group (2020). Type I IFN immunoprofiling in COVID-19 patients. *J. Allergy Clin. Immunol.* 146, 206–208.
- Uhel, F., Azzaoui, I., Grégoire, M., Pangault, C., Dulong, J., Tadié, J.M., Gacouin, A., Camus, C., Cynober, L., Fest, T., et al. (2017). Early expansion of circulating granulocytic myeloid-derived suppressor cells predicts development of nosocomial infections in patients with sepsis. *Am. J. Respir. Crit. Care Med.* 196, 315–327.
- Veglia, F., Perego, M., and Gabrilovich, D. (2018). Myeloid-derived suppressor cells coming of age. *Nat. Immunol.* 19, 108–119.
- Venet, F., Demaret, J., Gossez, M., and Monneret, G. (2020). Myeloid cells in sepsis-acquired immunodeficiency. *Ann. N Y Acad. Sci.* Published online March 23, 2020. <https://doi.org/10.1111/nyas.14333>.
- Vo, A.V., Takenaka, E., Shibuya, A., and Shibuya, K. (2016). Expression of DNAM-1 (CD226) on inflammatory monocytes. *Mol. Immunol.* 69, 70–76.
- Volkman, J., Schmitz, J., Nordlohne, J., Dong, L., Helmke, A., Sen, P., Immenschuh, S., Bernhardt, W.M., Gwinner, W., Bräsen, J.H., et al. (2020). Kidney injury enhances renal G-CSF expression and modulates granulopoiesis and human neutrophil CD177 in vivo. *Clin. Exp. Immunol.* 199, 97–108.
- Wang, D., Hu, B., Hu, C., Zhu, F., Liu, X., Zhang, J., Wang, B., Xiang, H., Cheng, Z., Xiong, Y., et al. (2020). Clinical Characteristics of 138 Hospitalized Patients With 2019 Novel Coronavirus-Infected Pneumonia in Wuhan, China. *JAMA* 323, 1061–1069.
- Wei, L.L., Wang, W.J., Chen, D.X., and Xu, B. (2020). Dysregulation of the immune response affects the outcome of critical COVID-19 patients. *J. Med. Virol.* <https://doi.org/10.1002/jmv.26181>.
- Wickham, H. (2016). *ggplot2: Elegant Graphics for Data Analysis*. (Springer-Verlag, New York).
- Wilck, A.J., Rustagi, A., Zhao, N.Q., Roque, J., Martínez-Colón, G.J., McKechnie, J.L., Iverson, G.T., Ranganath, T., Vergara, R., Hollis, T., et al. (2020). A single-cell atlas of the peripheral immune response in patients with severe COVID-19. *Nat. Med.* 26, 1070–1076.
- Xia, X., Wen, M., Zhan, S., He, J., and Chen, W. (2020). [An increased neutrophil/lymphocyte ratio is an early warning signal of severe COVID-19]. *Nan Fang Yi Ke Da Xue Xue Bao* 40, 333–336.
- Xu, Z., Shi, L., Wang, Y., Zhang, J., Huang, L., Zhang, C., Liu, S., Zhao, P., Liu, H., Zhu, L., et al. (2020). Pathological findings of COVID-19 associated with acute respiratory distress syndrome. *Lancet Respir. Med.* 8, 420–422.
- You, Q., He, D.M., Shu, G.F., Cao, B., Xia, Y.Q., Xing, Y., Ni, M., Chen, J.F., Shi, S.L., Gu, H.F., et al. (2019). Increased formation of neutrophil extracellular traps is associated with gut leakage in patients with type 1 but not type 2 diabetes. *J. Diabetes* 11, 665–673.
- Younos, I.H., Abe, F., and Talmadge, J.E. (2015). Myeloid-derived suppressor cells: their role in the pathophysiology of hematologic malignancies and potential as therapeutic targets. *Leuk. Lymphoma* 56, 2251–2263.
- Yu, G., Wang, L.G., Han, Y., and He, Q.Y. (2012). clusterProfiler: an R package for comparing biological themes among gene clusters. *OMICS* 16, 284–287.
- Zhou, F., Yu, T., Du, R., Fan, G., Liu, Y., Liu, Z., Xiang, J., Wang, Y., Song, B., Gu, X., et al. (2020a). Clinical course and risk factors for mortality of adult inpatients with COVID-19 in Wuhan, China: a retrospective cohort study. *Lancet* 395, 1054–1062.
- Zhou, Z., Ren, L., Zhang, L., Zhong, J., Xiao, Y., Jia, Z., Guo, L., Yang, J., Wang, C., Jiang, S., et al. (2020b). Overly Exuberant Innate Immune Response to SARS-CoV-2 Infection. *SSRN Electron. J.* <https://doi.org/10.2139/ssrn.3551623>.
- Zuo, Y., Yalavarthi, S., Shi, H., Gockman, K., Zuo, M., Madison, J.A., Blair, C., Weber, A., Barnes, B.J., Egeblad, M., et al. (2020). Neutrophil extracellular traps in COVID-19. *JCI Insight* 5, e138999.

STAR★METHODS

KEY RESOURCES TABLE

REAGENT or RESOURCE	SOURCE	IDENTIFIER
Antibodies		
HLA-DR BV421 (L243)	Biolegend	Cat# 307635; RRID:AB_10897449
CD4 BV510 (OKT4)	Biolegend	Cat# 317444; RRID:AB_2561866
CD16 BV605 (3G8)	Biolegend	Cat# 302039; RRID:AB_2561354
CD45 BV711 (HI30)	Biolegend	Cat# 304050; RRID:AB_2563466
CD8 BV785 (SK1)	Biolegend	Cat# 344740; RRID:AB_2566202
CD66b FITC (G10F5)	Biolegend	Cat# 305104; RRID:AB_314496
CD14 PerCp-Cy5.5 (MφP9)	Becton Dickinson	Cat# 562692; RRID:AB_2737726
CD56 PE (MY31)	Becton Dickinson	Cat# 345810; RRID:AB_396511
CD3 PE/Dazzle (UCHT1)	Biolegend	Cat# 300450; RRID:AB_2563618
CD11c PE/Cy5 (B-ly6)	Becton Dickinson	Cat# 551077; RRID:AB_394034
Siglec8 PE/Cy7 (7C9)	Biolegend	Cat# 347112; RRID:AB_2629720
CD203c APC (NP4D6)	Biolegend	Cat# 324609; RRID:AB_2099774
CD1c AlexaFluor700 (L161)	Biolegend	Cat# 331530; RRID:AB_2563657
CD19 APC/Fire 750 (HIB19)	Biolegend	Cat# 302258; RRID:AB_2629691
CD45 89Y (HI30)	Fluidigm	Cat# 3089003; RRID:AB_2661851
HLA-DR purified (L243)	Biolegend	Cat# 307602; RRID:AB_314680
CD3 purified (UCHT1)	Biolegend	Cat# 300443; RRID:AB_2562808
CD196 141Pr (G034E3)	Fluidigm	Cat# 3141003A; RRID:AB_2687639
CD19 142Nd (HIB-19)	Fluidigm	Cat# 3142001; RRID:AB_2651155
CD123 143Nd (6H6)	Fluidigm	Cat# 3143014B; RRID:AB_2811081
CD15 144Nd (W6D3)	Fluidigm	Cat# 3144019B
CD138 145Nd (DL101)	Fluidigm	Cat# 3145003B
CD64 146Nd (10.1)	Fluidigm	Cat# 3146006; RRID:AB_2661790
CD21 purified (Bu32)	Biolegend	Cat# 354902; RRID:AB_11219188
CD226 purified (REA1040)	Miltenyi Biotec	Produced at request
IgD purified (IgD26)	Biolegend	Cat# 348235; RRID:AB_2563775
ICOS 148Nd (C398.4A)	Fluidigm	Cat# 3148019B; RRID:AB_2756435
CD206 purified (152)	Biolegend	Cat# 321127; RRID:AB_2563729
CD96 purified (REA195)	Miltenyi Biotec	Produced at request
KLRG1 purified (REA261)	Miltenyi Biotec	Produced at request
TCRgd purified (11F2)	Miltenyi Biotec	Produced at request
FceRI 150Nd (AER-37)	Fluidigm	Cat# 3150027B
CD155 purified (REA1081)	Miltenyi Biotec	Produced at request
CD95 purified (DX2)	Biolegend	Cat# 305631; RRID:AB_2563766
TIGIT 153Eu (MBSA43)	Fluidigm	Cat# 3153019B; RRID:AB_2756419
CD62L 153Eu (DREG56)	Fluidigm	Cat# 3153004B; RRID:AB_2810245
CD62L purified (DREG56)	Biolegend	Cat# 304835; RRID:AB_2563758
CD1c purified (L161)	Biolegend	Cat# 331502; RRID:AB_1088995
CD27 155Gd (L128)	Fluidigm	Cat# 3155001B; RRID:AB_2687645
CXCR3 156Gd (G025H7)	Fluidigm	Cat# 3156004B; RRID:AB_2687646
KLRF1 purified (REA845)	Miltenyi Biotec	Produced at request
CD10 158Gd (HI10a)	Fluidigm	Cat# 3158011B
CD33 158Gd (WM53)	Fluidigm	Cat# 3158001; RRID:AB_2661799

(Continued on next page)

Continued

REAGENT or RESOURCE	SOURCE	IDENTIFIER
CD14 160Gd (RMO52)	Fluidigm	Cat# 3160006; RRID:AB_2661801
CD28 purified (L293)	BD Bioscience	Cat# 348040; RRID:AB_400367
CD69 162Dy (FN50)	Fluidigm	Cat# 3162001B
CD294 163Dy (BM16)	Fluidigm	Cat# 3163003B; RRID:AB_2810253
RANKL APC	Miltenyi Biotec	Cat# 130-098-511; RRID:AB_2656691
Anti-APC 163Dy	Fluidigm	Cat# 3163001B; RRID:AB_2687636
CXCR5 164Dy (51505)	Fluidigm	Cat# 3164016B; RRID:AB_2687858
Siglec 8 164Dy (7C9)	Fluidigm	Cat# 3164017B
CD34 166Er (581)	Fluidigm	Cat# 3166012B; RRID:AB_2756424
CD38 167Er (HIT2)	Fluidigm	Cat# 3167001B; RRID:AB_2802110
Ki67 168Er (Ki-67)	Fluidigm	Cat# 3168007B; RRID:AB_2800467
CD25 169Tm (2A3)	Fluidigm	Cat# 3169003; RRID:AB_2661806
CD24 169Tm (ML5)	Fluidigm	Cat# 3169004B; RRID:AB_2688021
Lag3 purified (11C3C65)	Biolegend	Cat# 369302; RRID:AB_2616876
RANK purified (80704)	R&D Systems	Cat# MAB683; RRID:AB_2205330
CD161 purified (HP-3G10)	Biolegend	Cat# 339919; RRID:AB_2562836
CD11b purified (ICRF44)	Biolegend	Cat# 301337; RRID:AB_2562811
CD45RO purified (4G11)	DRFZ Berlin	N/A
CD44 purified (BJ18)	Biolegend	Cat# 338811; RRID:AB_2562835
CD137 173Yb (4B4-1)	Fluidigm	Cat# 3173015B
PD-1 175Lu (EH12.2H7)	Fluidigm	Cat# 3175008; RRID:AB_2687629
PD-L1 175Lu (29.E2A3)	Fluidigm	Cat# 3175017B; RRID:AB_2687638
CD56 176Yb (NCAM16.2)	Fluidigm	Cat# 3176008; RRID:AB_2661813
CD8A purified (GN11)	DRFZ Berlin	N/A
IgM purified (MHM-88)	Biolegend	Cat# 314502; RRID:AB_493003
CD11c purified (Bu15)	Biolegend	Cat# 337221; RRID:AB_2562834
B2M purified (2M2)	Biolegend	Cat# 316302; RRID:AB_492835
CD16 209Bi (3G8)	Fluidigm	Cat# 3209002B; RRID:AB_2756431
A0251 anti-human Hashtag 1	Biolegend	Cat# 394601; RRID:AB_2750015
A0252 anti-human Hashtag 2	Biolegend	Cat# 394603; RRID:AB_2750016
A0253 anti-human Hashtag 3	Biolegend	Cat# 394605; RRID:AB_2750017
A0254 anti-human Hashtag 4	Biolegend	Cat# 394607; RRID:AB_2750018
A0255 anti-human Hashtag 5	Biolegend	Cat# 394609; RRID:AB_2750019
A0256 anti-human Hashtag 6	Biolegend	Cat# 394611; RRID:AB_2750020
A0257 anti-human Hashtag 7	Biolegend	Cat# 394613; RRID:AB_2750021
CD235ab Biotin (HIR2)	Biolegend	Cat# 306618; RRID:AB_2565773
Chemicals, Peptides, and Recombinant Proteins		
BD Horizon Brilliant Stain Buffer	Becton Dickinson	Cat# 563794
RBC lysis buffer 10X	Biolegend	Cat# 420301
Pierce 16% Formaldehyde (w/v), Methanol-free	Thermo Fisher	Cat# 28908
RPMI 1640 Medium	GIBCO	Cat# 11875093
Fetal Bovine Serum	PAN Biotec	Cat# 3302
Stain Buffer (FBS)	Becton Dickinson	Cat# 554656
Pancoll human, Density: 1.077 g/ml	Pan Biotec	Cat# P04-601000
Dulbecco'S Phosphate Buffered Saline, MO	Sigma-Aldrich	Cat# D8537

(Continued on next page)

Continued

REAGENT or RESOURCE	SOURCE	IDENTIFIER
FcR Blocking Reagent, human	Miltenyi	Cat# 130-059-901
Cell-ID Intercalator-Ir	Fluidigm	Cat# 201192A
Permeabilization buffer 10X	eBioscience	Cat# 00-8333-56
Maxpar PBS	Fluidigm	Cat# 201058
Maxpar Cell Staining buffer	Fluidigm	Cat# 201068
Maxpar X8 Multimetal Labeling Kit	Fluidigm	Cat# 201300
Proteomic stabilizer	Smart Tube Inc.	Cat# PROT1
Nuclease-Free Water	Invitrogen	Cat# AM9937
KAPA HiFi HotStart Ready Mix	Roche	Cat# KK2601
Human Tru Stain FcX	Biolegend	Cat# 422301
TE Buffer, pH8.0, 1mM disodium EDTA	Thermo Fisher	Cat# 12090015
SPRIselect	Beckmann Coulter	Cat# B23318
10% Tween 20	BIO-RAD	Cat# 1662404
Buffer EB	QIAGEN	Cat# 19086
Ethanol, Absolute	Fisher Bioreagents	Cat# BP2818-500
Glycerol, 85%	Merck	Cat# 1040941000
Bovine Serum Albumin (IgG-Free, Protease-Free)	Jackson Immuno Research	Cat# 001-000-161
LPS, TLRpure	Innaxon	Cat# IAX-100-010
Tween20	Sigma-Aldrich	Cat# P1379-500M
MagniSort™ Negative Selection Beads	Thermo Fisher	Cat# MSNB-6002-74
Lysercell WDF	Sysmex	Cat# AL-337-564
Fluorocell™ WDF	Sysmex	Cat# CV-377-552
Critical Commercial Assays		
LIVE/DEAD Fixable Yellow Dead Cell Stain Kit	Thermo Fisher	Cat# L34967
LEGENDplex™ Human Inflammation Panel 1 (Mix&Match)	Biolegend	Cat# 740809
Human Single-Cell Multiplexing Kit	Becton Dickinson	Cat# 633781
BD Rhapsody WTA Amplification Kit	Becton Dickinson	Cat# 633801
BD Rhapsody Cartridge Kit	Becton Dickinson	Cat# 633733
BD Rhapsody cDNA Kit	Becton Dickinson	Cat# 633773
High Sensitivity D5000 ScreenTape	Agilent	Cat# 5067-5592
Qubit dsDNA HS Assay Kit	ThermoFisher	Cat# Q32854
Chromium Next GEM Single Cell 3' GEM, Library & Gel Bead Kit v3.1	10x genomics	Cat# 1000121
Chromium Next GEM Chip G Single Cell Kit	10x genomics	Cat# 1000120
Single Index Kit T Set A	10x genomics	Cat# 1000213
High Sensitivity DNA Kit	Agilent	Cat# 5067-4626
NovaSeq 6000 S1 Reagent Kit (100 cycle)	Illumina	Cat# 200012865
NovaSeq 6000 S2 Reagent Kit (100 cycle)	Illumina	Cat# 20012862
NovaSeq 6000 S2 Reagent Kit (200 cycles)	Illumina	Cat# 20040326
NovaSeq 6000 S2 Reagent Kit (200 cycles)	Illumina	Cat# 20040326
NextSeq 500/550 High Output Kit v2.5 (150 Cycles)	Illumina	Cat# 20024907
Pan Monocyte Isolation Kit, human	Miltenyi	Cat# 130-096-537
CE/IVD Phagoburst	BD Biosciences	Cat# 341058
CD/IVD PHAGOTEST	BD Biosciences	Cat# 341060

(Continued on next page)

Continued

REAGENT or RESOURCE	SOURCE	IDENTIFIER
Deposited Data		
scRNA-seq raw data	This paper	EGAS00001004571
Processed scRNA-seq count data and code	This paper	http://fastgenomics.org
Supplemental Tables S1–S4	This paper	https://data.mendeley.com/datasets/hwxhw2sxys/1
Oligonucleotides		
SI-PCR primer	IDT	AATGATACGGCGACCACCGAGATCTA CACTCTTTCCCTACACGACGC*T*C
HTO additive primer	IDT	GTGACTGGAGTTCAGACGTGTGC*T*C
D701_S	IDT	CAAGCAGAAGACGGCATACGAGA TCGAGTAATGTGACTGGAGTTCAGACGTGT*G*C
D702_S	IDT	CAAGCAGAAGACGGCATACGAGA TTCTCCGGAGTGGAGTTCAGACGTGT*G*C
D703_S	IDT	CAAGCAGAAGACGGCATACGAGATA ATGAGCGGTGACTGGAGTTCAGACGTGT*G*C
D705_S	IDT	CAAGCAGAAGACGGCATACGAGATTC TGAATGTGACTGGAGTTCAGACGTGT*G*C
Software and Algorithms		
CellRanger	10x genomics	v3.1.0
Bcl2fastq2	Illumina	v2.20
STAR	Dobin et al., 2013	v2.6.1b
Cutadapt	Martin, 2011	v1.16
Dropseq-tools	https://github.com/broadinstitute/Drop-seq/	v2.0.0
R	https://www.cran.r-project.org	v3.6.2
Seurat (R package)	Butler et al., 2018 ; Hafemeister and Satija, 2019 ; Stuart et al., 2019	v3.1.4, v3.1.2 (CRAN)
Harmony (R package)	Korsunsky et al., 2019 (https://github.com/immunogenomics/harmony)	v1.0
Destiny (R package)	Angerer et al., 2016	v 3.0.1
ClusterProfiler (R package)	Yu et al., 2012	v3.10.1 (CRAN)
SingleR (R package)	Aran et al., 2019	v1.0.5 (Bioconductor)
DirichletReg (R package)	Maier, 2014	v0.6.3.1 (CRAN)
AUCell (R package)	Aibar et al., 2017	v1.6.1 (CRAN)
Cytobank	Kotecha et al., 2010 https://www.cytobank.org	https://doi.org/10.1002/0471142956.cy1017s53
SPADE (Cytobank)	Qiu et al., 2011	Cytobank is running a version of SPADE derived from v1.10.2
flowCore (R package)	https://www.bioconductor.org/packages/release/bioc/html/flowCore.html	v1.48.1 (Bioconductor), 10.18129/B9.bioc.flowCore
CytoML (R package)	https://github.com/RGLab/CytoML	v1.8.1 (Bioconductor), 10.18129/B9.bioc.CytoML
CytofBatchAdjust (R package)	https://github.com/CUHIMSR/CytofBatchAdjust	https://doi.org/10.3389/fimmu.2019.02367
uwot (R package)	https://cran.r-project.org/web/packages/uwot/index.html	v0.1.8 (CRAN)
ComplexHeatmap (R package)	Gu et al., 2016	v1.20.0 (Bioconductor)

(Continued on next page)

Continued

REAGENT or RESOURCE	SOURCE	IDENTIFIER
lme4 (R package)	Nowicka et al., 2017	v1.1-21 (CRAN)
multcomp (R package)	Hothorn et al., 2008	v1.4-13 (CRAN)
lsmmeans (R package)	Lenth, 2016	v2.30-0 (CRAN)
Prism (software)	https://www.graphpad.com	v8
FlowJo	https://www.flowjo.com	v10.6.1
Cytoscape	https://www.cytoscape.org	v3.7.1 (https://doi.org/10.1101/gr.1239303)
iRegulon	Janky et al., 2014	v1.3

RESOURCE AVAILABILITY**Lead Contact**

Further information and requests for resources and reagents should be directed to and will be fulfilled by the Lead Contact, Joachim L. Schultze (j.schultze@uni-bonn.de).

Materials Availability

This study did not generate new unique reagents.

Data and Code Availability

ScRNA-seq data generated during this study are deposited at the European Genome-phenome Archive (EGA) under access number EGAS00001004571, which is hosted by the EBI and the CRG.

EXPERIMENTAL MODEL AND SUBJECT DETAILS

Samples from patients with COVID-19 were collected within two cohort studies ([Kurth et al., 2020](#)) designed to allow deep molecular and immunological transcriptomic and proteomic profiling of COVID-19 in blood. Patients for which sufficient material was available for scRNA-seq, CyTOF or flow cytometry analysis, were included in this study. This study was designed to describe immunological deviations in COVID-19 patients without intention of the development of new treatments or new diagnostics, and therefore sample size estimation was not included in the original study design.

Cohort 1 / Berlin cohort

This study includes a subset of patients enrolled between March 2 and July 02 2020 in the Pa-COVID-19 study, a prospective observational cohort study assessing pathophysiology and clinical characteristics of patients with COVID-19 at Charité Universitätsmedizin Berlin ([Kurth et al., 2020](#)). The study is approved by the Institutional Review board of Charité (EA2/066/20). Written informed consent was provided by all patients or legal representatives for participation in the study. The patient population included in all analyses of cohort 1 consists of 10 control donors (samples collected in 2019 before SARS-CoV2 outbreak), 8 patients presenting with flu-like illness but tested SARS-CoV-2-negative, 25 mild and 29 severe COVID-19 patients ([Figures 1A and 1B](#); [Table S1](#)). Information on age, sex, medication, and co-morbidities is listed in [Table S1](#). All COVID-19 patients were tested positive for SARS-CoV-2 RNA in nasopharyngeal swabs and allocated to mild (WHO 2-4) or severe (5-7) disease according to the WHO clinical ordinal scale. We also included publicly available single-cell transcriptome data derived from 22 control samples into the analysis; 3 samples were derived from 10x Genomics, San Francisco, CA 94111, USA (5k_pbmc_v3: https://support.10xgenomics.com/single-cell-gene-expression/datasets/3.0.2/5k_pbmc_v3, pbmc_10k_v3: https://support.10xgenomics.com/single-cell-gene-expression/datasets/3.0.0/pbmc_10k_v3, pbmc_1k_v3: https://support.10xgenomics.com/single-cell-gene-expression/datasets/3.0.0/pbmc_1k_v3), 19 samples derived from [Reyes et al. \(2020\)](#).

Cohort 2 / Bonn cohort

This study was approved by the Institutional Review board of the University Hospital Bonn (073/19 and 134/20). After providing written informed consent, 19 control donors and 22 COVID-19 patients ([Figures 1A and 1B](#); [Table S1](#)) were included in the study. In patients who were not able to consent at the time of study enrollment, consent was obtained after recovery. Information on age, sex, medication, and co-morbidities are listed in [Table S1](#). COVID-19 patients who tested positive for SARS-CoV-2 RNA in nasopharyngeal swabs were recruited at the Medical Clinic I of the University Hospital Bonn between March 30 and June 17, 2020 and allocated to mild (WHO 2-4) or severe (5-7) disease according to the WHO clinical ordinal scale. Controls in cohort 2 were collected from healthy

people or from otherwise hospitalized patients with a wide range of diseases and comorbidities including chronic inflammatory immune responses. These individuals were either tested negative for SARS-CoV-2, serologically negative or had no indication for acute COVID-19 disease based on clinical or laboratory parameters.

METHOD DETAILS

Isolation of blood cells for scRNA-seq

Cohort 1 / Berlin cohort

PBMC were isolated from heparinized whole blood by density centrifugation over Pancoll (density: 1.077 g/ml; PAN-Biotech). If the pellet was still slightly red, remaining CD235ab⁺ cells (Erythrocytes) were depleted by Negative Selection (*MagniSort* Thermo Fisher). Subsequently the PBMC were prepared for 3' scRNA-seq (10xGenomics) or cryopreserved and analyzed later.

Cohort 2 / Bonn cohort

In the Bonn cohort, scRNA-seq was performed on fresh whole blood, fresh PBMC and frozen PBMC. Briefly, PBMC were isolated from EDTA-treated or heparinized peripheral blood by density centrifugation over Pancoll or Ficoll-Paque density centrifugation (density: 1.077 g/ml). Cells were then washed with DPBS, directly prepared for scRNA-seq (BD Rhapsody) or cryopreserved in RPMI1640 with 40% FBS and 10% DMSO. Whole blood was prepared by treatment of 1ml peripheral blood with 10ml of RBC lysis buffer (Biolegend). After one wash in DPBS cells were directly processed for scRNA-seq (BD Rhapsody) or multi-color flow cytometry (MCFC). Frozen PBMC were recovered by rapidly thawing frozen cell suspensions in a 37°C water bath followed by immediate dilution in pre-warmed RPMI-1640+10% FBS (GIBCO) and centrifugation at 300 g for 5min. After centrifugation, the cells were resuspended in RPMI-1640+10% FBS and processed for scRNA-seq. Antibody cocktails were cryopreserved as described before (Schulz and Mei, 2019).

Antibodies used for mass cytometry

All anti-human antibodies pre-conjugated to metal isotopes were obtained from Fluidigm Corporation (San Francisco, US). All remaining antibodies were obtained from the indicated companies as purified antibodies and in-house conjugation was done using the MaxPar X8 labeling kit (Fluidigm). Table S2 shows a detailed list of all antibodies used for panel 1 and panel 2.

Sample processing, antigen staining and data analysis of mass cytometry-based immune cell profiling

500µl of whole blood (heparin) was fixed in 700µl of proteomic stabilizer (Smart Tube Inc., San Carlos, US) as described in the user manual and stored at -80°C until further processing. Whole blood samples were thawed in Thaw/Lyse buffer (Smart Tube Inc.). For barcoding antibodies recognizing human beta-2 microglobulin (B2M) were conjugated in house to ¹⁰⁴Pd, ¹⁰⁶Pd, ¹⁰⁸Pd, ¹¹⁰Pd, ¹⁹⁸Pt (Mei et al., 2015, 2016; Schulz and Mei, 2019). Up to 10 individual samples were stained using a staining buffer from Fluidigm with a combination of two different B2M antibodies for 30min at 4°C. Cells were washed and pooled for surface and intracellular staining.

For surface staining the barcoded and pooled samples were equally divided into two samples. Cells were resuspended in antibody staining cocktails for panel 1 or panel 2 respectively (Table S2) and stained for 30min at 4°C. For secondary antibody staining of panel 2, cells were washed and stained with anti-APC ¹⁶³Dy for 30min at 4°C. After surface staining cells were washed with PBS and fixed overnight in PFA solution diluted in PBS to 2%.

For intracellular staining cells were washed twice with a permeabilization buffer (eBioscience, San Diego, US) and stained with the respective antibodies diluted in a permeabilization buffer for 30min at room temperature. After washing, cells were stained with iridium intercalator (Fluidigm) diluted in 2% PFA for 20min at room temperature. Cells were washed once with PBS and then twice with ddH₂O and kept at 4°C until mass cytometry measurement.

A minimum of 100,000 cells per sample and panel were acquired on a CyTOF2/Helios mass cytometer (Fluidigm). For normalization of the fcs files 1:10 EQ Four Element Calibration Beads (Fluidigm) were added. Cells were analyzed using a CyTOF2 upgraded to Helios specifications, with software version 6.7.1014, using a narrow bore injector. The instrument was tuned according to the manufacturer's instructions with tuning solution (Fluidigm) and measurement of EQ four element calibration beads (Fluidigm) containing ^{140/142}Ce, ^{151/153}Eu, ¹⁶⁵Ho and ^{175/176}Lu served as a quality control for sensitivity and recovery. Directly prior to analysis, cells were resuspended in ddH₂O, filtered through a 20-µm cell strainer (Celltrics, Sysmex), counted and adjusted to 5-8 x 10⁵ cells/ml. EQ four element calibration beads were added at a final concentration of 1:10 v/v of the sample volume to be able to normalize the data to compensate for signal drift and day-to-day changes in instrument sensitivity. Samples were acquired with a flow rate of 300-400 events/s. The lower convolution threshold was set to 400, with noise reduction mode turned on and cell definition parameters set at event duration of 10-150 pushes (push = 13µs). The resulting flow cytometry standard (FCS) files were normalized and randomized using the CyTOF software's internal FCS-Processing module on the non-randomized ('original') data. The default settings in the software were used with time interval normalization (100 s/minimum of 50 beads) and passport version 2. Intervals with less than 50 beads per 100 s were excluded from the resulting FCS file.

Blood processing for multi-color flow cytometry

1ml of fresh blood from control or COVID-19 donors was treated with 10ml of RBC lysis buffer (Biolegend). After RBC lysis, cells were washed with DPBS and 1-2 million cells were used for flow cytometry analysis. Cells were then stained for surface markers (Table S3) in DPBS with BD Horizon Brilliant Stain Buffer (Becton Dickinson) for 30min at 4°C. To distinguish live from dead cells, the cells were incubated with LIVE/DEAD Fixable Yellow Dead Cell Stain Kit (1:1000 – Thermo Scientific). Following staining and washing, the cell suspension was fixed with 4% PFA for 5min at room temperature to prevent any possible risk of contamination during acquisition of the samples. Flow cytometry analysis was performed on a BD Symphony instrument (Becton Dickinson) configured with 5 lasers (UV, violet, blue, yellow-green, red).

Ex vivo functional analysis of neutrophils

Determination of neutrophil oxidative burst and phagocytosis was performed by flow cytometry using the CE/IVD PHAGOBURST and PHAGOTEST assay (BD Biosciences, Heidelberg, Germany) according to the manufacturer's instructions.

Briefly, heparinized whole blood was incubated with PMA, unlabeled opsonized *E. coli* bacteria or washing solution (negative control) at 37°C for 10min. Dihydrorhodamine (DHR 123) was then added for 10min, erythrocytes were lysed and DNA staining solution was added. The freely cell permeable nonfluorescent Dihydrorhodamine 123 becomes fluorescent when oxidized by reactive oxygen species. Stained samples were analyzed on a Navios flow cytometer (Beckman Coulter, Krefeld, Germany) within less than 30min. The respiratory burst intensity in neutrophils was determined by analysis of increase in the mean fluorescence intensity (MFI) in the FL1 Channel in the stimulated samples compared to the unstimulated control.

For analysis of neutrophil phagocytic activity, heparinized whole blood was incubated with FITC-labeled opsonized *E. coli* bacteria for 10min at 37°C or 0°C (negative control). After incubation, the reaction was stopped, erythrocytes were lysed and the DNA staining solution was added. Stained samples were analyzed on a Navios flow cytometer (Beckman Coulter, Krefeld, Germany) within less than 30min. The phagocytic activity of neutrophils was determined by the increase in MFI in the FL1 Channel in the stimulated sample compared to the unstimulated control. Data were analyzed using prism version 8. Mixed-effect-analysis and Sidak's multiple comparison test was applied to report statistical differences of *E. coli*- and PMA-induced ROS production as well as phagocytosis between mild and severe COVID-19 patients.

Ex vivo functional analysis of monocytes

Monocytes were isolated from frozen PBMCs by negative selection using the Pan Monocyte Isolation Kit (Miltenyi, Bergisch Gladbach, Germany). The purity of isolated cells was assessed by BD Canto 2 flow cytometer, and preparations with > 85% purity were used for experiments. Monocytes were resuspended in complete RPMI1640 medium (GIBCO) supplemented with 10% heat-inactivated fetal bovine serum (Pan Biotech), 10 U/ml penicillin and 10 µg/ml streptomycin (Sigma-Aldrich, USA), and stimulated for 8h with LPS (1 ng/ml; TLRpure; Innaxon, UK). After stimulation, cell-free supernatants were collected and tested for IL-1β, IFNγ, and TNFα, respectively, using the cytokine bead assay *Legend-Plex Mix&Match inflammation panel 1 kit* (Biolegend, USA). Cytokine-bound beads were measured with a BD Canto 2 flow cytometer and analyzed using Legend-Plex Software 8.0 (Biolegend, USA).

Hematological analyses of the granulocyte compartment

Blood samples were collected into K₃EDTA evacuated plastic tubes (Greiner Bio-One GmbH, Frickenhausen, Germany) and were subsequently analyzed using Sysmex XN-10 hematology analyzers within a XN-2000 or XN-9100 configuration (Sysmex Corporation, Kobe, Japan) as previously described (Stiel et al., 2016). Immature granulocytes (IG) were quantified by automated flow cytometry using the Sysmex WBC differential channel in XN-10 hematology analyzers within a XN-2000 or XN-9100 configuration (Sysmex Corporation, Kobe, Japan). Whole blood was treated with LysercellWDF for cell permeabilization and stained with the nucleic acid polymethine fluorescent dye FluorocellWDF according to Sysmex-proprietary protocols without modifications. Subsequent differentiation of white blood cells into lymphocytes, monocytes, neutrophils, eosinophils, and immature granulocytes was achieved by flow cytometry using a 663 nm laser. The cell populations' distinct forward-scattered light (FSC = NE-WZ, i.e., cell volume), side-scattered light (SSC = NE-WX, i.e., granularity), and side-fluorescent light (SFL = NE-WY, i.e., nucleic acid content) properties allowed determining the width of neutrophil cytometric dispersions applying Sysmex-proprietary algorithms. Data were analyzed using prism version 8. Mann Whitney test was used to report differences in IG count, whereas mixed-effect-analysis and Sidak's multiple comparison test was applied to report statistical differences of NE-WX, NE-WY and NE-WZ between mild and severe COVID-19 patients.

10x Genomics Chromium single-cell RNA-seq

PBMC were isolated and prepared as described above. Afterward, patient samples were hashtagged with TotalSeq-A antibodies (Biolegend) according to the manufacturer's protocol for TotalSeq™-A antibodies and cell hashing with 10x Single Cell 3' Reagent Kit v3.1. 50µL cell suspension with 1x10⁶ cells were resuspended in staining buffer (2% BSA, Jackson Immuno Research; 0.01% Tween-20, Sigma-Aldrich; 1x DPBS, GIBCO) and 5 µL Human TruStain FcX™ FcBlocking (Biolegend) reagent were added. The blocking was performed for 10min at 4°C. In the next step 1µg unique TotalSeq-A antibody was added to each sample and incubated for 30min at 4°C. After the incubation time 1.5mL staining buffer were added and centrifuged for 5min at 350g and 4°C. Washing was repeated for a total of 3 washes. Subsequently, the cells were resuspended in an appropriate volume of 1x DPBS (GIBCO), passed through a 40µm mesh (Flowmi™ Cell Strainer, Merck) and counted, using a Neubauer Hemocytometer (Marienfeld). Cell counts were

adjusted and hashtagged cells were pooled equally. The cell suspension was super-loaded, with 50,000 cells, in the Chromium™ Controller for partitioning single cells into nanoliter-scale Gel Bead-In-Emulsions (GEMs). Single Cell 3' reagent kit v3.1 was used for reverse transcription, cDNA amplification and library construction of the gene expression libraries (10x Genomics) following the detailed protocol provided by 10x Genomics. Hashtag libraries were prepared according to the cell hashing protocol for 10x Single Cell 3' Reagent Kit v3.1 provided by Biolegend, including primer sequences and reagent specifications. Biometra Trio Thermal Cycler was used for amplification and incubation steps (Analytik Jena). Libraries were quantified by Qubit™ 2.0 Fluorometer (ThermoFisher) and quality was checked using 2100 Bioanalyzer with High Sensitivity DNA kit (Agilent). Sequencing was performed in paired-end mode with a S1 and S2 flow cell (2 × 50 cycles) using NovaSeq 6000 sequencer (Illumina).

BD Rhapsody single-cell RNA-seq

Whole transcriptome analyses, using the BD Rhapsody Single-Cell Analysis System (BD, Biosciences) were performed on PBMC and whole blood samples prepared as described above. Cells from each sample were labeled with sample tags (BD Human Single-Cell Multiplexing Kit) following the manufacturer's protocol. Briefly, a total number of 1×10^6 cells were resuspended in 180 μ l of Stain Buffer (FBS) (BD PharMingen). The sample tags were added to the respective samples and incubated for 20min at room temperature. After incubation, 200 μ l stain buffer was added to each sample and centrifuged for 5min at 300 g and 4°C. Samples were washed one more time. Subsequently cells were resuspended in 300 μ l of cold BD Sample Buffer and counted using Improved Neubauer Hemocytometer (INCYTO). Labeled samples were pooled equally in 650 μ l cold BD Sample Buffer. For each pooled sample two BD Rhapsody cartridges were super-loaded with approximately 60,000 cells each. Single cells were isolated using Single-Cell Capture and cDNA Synthesis with the BD Rhapsody Express Single-Cell Analysis System according to the manufacturer's recommendations (BD Biosciences). cDNA libraries were prepared using the BD Rhapsody Whole Transcriptome Analysis Amplification Kit following the BD Rhapsody System mRNA Whole Transcriptome Analysis (WTA) and Sample Tag Library Preparation Protocol (BD Biosciences). The final libraries were quantified using a Qubit Fluorometer with the Qubit dsDNA HS Kit (ThermoFisher) and the size-distribution was measured using the Agilent high sensitivity D5000 assay on a TapeStation 4200 system (Agilent technologies). Sequencing was performed in paired-end mode (2*75 cycles) on a NovaSeq 6000 and NextSeq 500 System (Illumina) with NovaSeq 6000 S2 Reagent Kit (200 cycles) and NextSeq 500/550 High Output Kit v2.5 (150 Cycles) chemistry, respectively.

QUANTIFICATION AND STATISTICAL ANALYSIS

Data pre-processing of 10x Genomics Chromium scRNA-seq data

Cell Ranger v3.1.0 (10x Genomics) was used to process scRNA-seq. To generate a digital gene expression (DGE) matrix for each sample, we mapped their reads to a combined reference of GRCh38 genome and SARS-CoV-2 genome and recorded the number of UMIs for each gene in each cell.

Data pre-processing of BD Rhapsody scRNA-seq data

After demultiplexing of bcl files using Bcl2fastq2 V2.20 from Illumina and quality control, paired-end scRNA-seq reads were filtered for valid cell barcodes using the barcode whitelist provided by BD. Cutadapt 1.16 was then used to trim NexteraPE-PE adaptor sequences where needed and to filter reads for a PHRED score of 20 or above (Martin, 2011). Then, STAR 2.6.1b was used for alignment against the Gencode v27 reference genome (Dobin et al., 2013). Dropseq-tools 2.0.0 were used to quantify gene expression and collapse to UMI count data (<https://github.com/broadinstitute/Drop-seq/>). For hashtag-oligo based demultiplexing of single-cell transcriptomes and subsequent assignment of cell barcodes to their sample of origin the respective multiplexing tag sequences were added to the reference genome and quantified as well.

ScRNA-seq data analysis of 10x Chromium data of cohort 1

ScRNA-seq UMI count matrices were imported to R 3.6.2 and gene expression data analysis was performed using the R/Seurat package 3.1.4 (Butler et al., 2018; Hafemeister and Satija, 2019). Demultiplexing of cells was performed using the *HTODemux* function implemented in Seurat.

Data quality control

We excluded cells based on the following quality criteria: more than 25% mitochondrial reads, more than 25% *HBA/HBB* gene reads, less than 250 expressed genes or more than 5,000 expressed genes and less than 500 detected transcripts. We further excluded genes that were expressed in less than five cells. In addition, mitochondrial genes have been excluded from further analysis.

Normalization

LogNormalization (Seurat function) was applied before downstream analysis. The original gene counts for each cell were normalized by total UMI counts, multiplied by 10,000 (TP10K) and then log transformed by $\log_{10}(TP10k+1)$.

Data integration

After normalization, the count data was scaled regressing for total UMI counts and principal component analysis (PCA) was performed based on the 2,000 most variable features identified using the *vst* method implemented in Seurat. Subsequently, the scRNA-seq data from cohort 1 was integrated with publicly available 10x scRNaseq data of healthy controls using the ‘harmony’ algorithm (Korsunsky et al., 2019) based on the first 20 principal components to correct for technical differences in the gene expression counts of the different data sources (Control samples from Reyes et al. (2020), 10x v3.1 PBMC benchmarking data from healthy controls and 10x v3.1 scRNA-seq data from cohort 1). We downloaded the count matrices for the publicly available scRNA-seq data and filtered the cells using the above-mentioned quality criteria prior to data integration. For two-dimensional data visualization we performed UMAP based on the first 20 dimensions of the ‘harmony’ data reduction. The cells were clustered using the Louvain algorithm based on the first 20 ‘harmony’ dimensions with a resolution of 0.4.

Differential expression tests and cluster marker genes

Differential expression (DE) tests were performed using FindMarkers/FindAllMarkers functions in Seurat with Wilcoxon Rank Sum test. Genes with > 0.25 log-fold changes, at least 25% expressed in tested groups, and Bonferroni-corrected p values < 0.05 were regarded as significantly differentially expressed genes (DEGs). Cluster marker genes were identified by applying the DE tests for upregulated genes between cells in one cluster to all other clusters in the dataset. Top ranked genes (by log-fold changes) from each cluster of interest were extracted for further illustration. The exact number and definition of samples used in the analysis are specified in the legend of Figure 2A and summarized in Table S1.

Cluster annotation

Clusters were annotated based on a double-checking strategy: 1) by comparing cluster marker genes with public sources, and 2) by directly visualizing the expression pattern of CyTOF marker genes.

GO enrichment analysis

Significant DEGs between each monocyte cluster and the rest of monocyte subpopulations were identified by FindMarkers function from the Seurat package using Wilcoxon Rank Sum test statistics for genes expressed in at least 25% of all monocyte clusters. P values were corrected for multiple testing using Bonferroni correction and genes with corrected p values lower or equal 0.05 have been taken as significant DEGs for GO enrichment test by R package/ClusterProfiler v.3.10.1 (Yu et al., 2012).

Correlation analysis of marker genes for monocyte and neutrophils between cohort 1 and 2

To systematically compare the similarity of marker gene expression in the identified monocyte/neutrophils subpopulations between the two cohorts, the Spearman correlation coefficients were calculated based on the union of the top 50 marker genes of each cluster sorted by fold change in the two cohorts, based on their average expression of all cells in the specific subpopulation. The pairwise comparisons were performed, and the correlation coefficients were displayed using a heatmap.

Subset analysis of the neutrophils within the PBMC dataset of cohort 1

The neutrophil space was investigated by subsetting the PBMC dataset to those clusters identified as neutrophils and immature neutrophils (cluster 5 and 6). Within those subsets, we selected top 2,000 variable genes and repeated the clustering using the SNN-graph based Louvain algorithm mentioned above with a resolution of 0.6. The dimensionality of the data was then reduced to 10 PCs, which served as input for the UMAP calculation. To categorize the observed neutrophil clusters into the respective cell cycle states, we applied the CellCycleScoring function of Seurat and visualized the results as pie charts.

A gene signature enrichment analysis using the ‘AUCell’ method (Aibar et al., 2017) was applied to link observed neutrophil clusters to existing studies and neutrophils of cohort 2. We set the threshold for the calculation of the area under the curve (AUC) to marker genes from collected publications and top 30 of the ranked marker genes from each of neutrophil clusters from cohort 2. The resulting AUC values were normalized the maximum possible AUC to 1 and subsequently visualized in violin plots or UMAP plots.

ScRNA-seq data analysis of Rhapsody data of cohort 2

General steps for Rhapsody data downstream analysis

ScRNA-seq UMI count matrices were imported to R 3.6.2 and gene expression data analysis was performed using the R/Seurat package 3.1.2 (Butler et al., 2018). Demultiplexing of cells was performed using the *HTODemux* function implemented in Seurat. After identification of singlets, cells with more than 25% mitochondrial reads, less than 250 expressed genes or more than 5,000 expressed genes and less than 500 detected transcripts were excluded from the analysis and only those genes present in more than 5 cells were considered for downstream analysis. The following normalization, scaling and dimensionality reduction steps were performed independently for each of the data subsets used for the different analyses as indicated respectively. In general, gene expression values were normalized by total UMI counts per cell, multiplied by 10,000 (TP10K) and then log transformed by $\log_{10}(TP10k+1)$. Subsequently, the data was scaled, centered and regressed against the number of detected transcripts per cell to correct for heterogeneity associated with differences in sequencing depth. For dimensionality reduction, PCA was performed on the top 2,000 variable genes identified using the *vst* method implemented in Seurat. Subsequently, UMAP was used for two-dimensional representation of the

data structure. Cell type annotation was based on the respective clustering results combined with data-driven cell type classification algorithms based on reference transcriptome data (Aran et al., 2019) and expression of known marker genes.

scRNA-seq analysis of the complete BD Rhapsody dataset of cohort 2 including data from frozen and fresh PBMC and whole blood

ScRNA-seq count data of 229,731 cells derived from fresh and frozen PBMC samples purified by density gradient centrifugation and whole blood after erythrocyte lysis of cohort 2 (Bonn, BD Rhapsody) were combined, normalized and scaled as described above (see Figure S6A). After variable gene selection and PCA, UMAP was performed based on the first 20 principal components (PCs). No batch correction or data integration strategies were applied to the data. Visualization of the cells (Figure S6A) showed overlay of cells of the same type (e.g., T cells clustered within the same cluster, irrespective of cell isolation procedure). In other words, cell type distribution was unaffected by the technical differences in sample handling. Data quality and information content was visualized as violin plots showing the number of detected genes, transcripts (UMIs) and genic reads per sample handling strategy split by PBMC and granulocyte fraction.

scRNA-seq analysis of fresh and frozen PBMC samples

ScRNA-seq count data of 139,848 cells derived from fresh and frozen PBMC samples of cohort 2 (Bonn, BD Rhapsody) purified by density gradient centrifugation were normalized and scaled as described above. After variable gene selection and PCA, UMAP was performed and the cells were clustered using the Louvain algorithm based on the first 20 PCs and a resolution of 0.4. Cluster identities were determined by reference-based cell classification and inference of cluster-specific marker genes using the Wilcoxon rank sum test using the following cutoffs: genes have to be expressed in more than 20% of the cells of the respective cluster, exceed a logarithmic fold change cutoff to at least 0.2, and exhibited a difference of > 10% in the detection between two clusters. The exact number and definition of samples used in the analysis are specified in the legend of Figure 2D and summarized in Table S1.

Quantification of the percentages of cell clusters in the PBMC scRNA-seq data of both cohorts separated by disease group

To compare shifts in the monocyte and neutrophil populations in the PBMC compartment of COVID-19 patients, the percentages of the cellular subsets - as identified by clustering and cluster annotation explained above for the two independent scRNA-seq datasets (cohort 1 and cohort 2) - of the total number of PBMC in each dataset were quantified per sample and visualized together in boxplots. To determine the statistical significance of differences in cell proportions between the different conditions, a Dirichlet regression model was used, due to the fact that the proportions are not independent of one another. The R/*DirichletReg* (Maier, 2014) package was used. The p values were corrected for multiple testing using the Benjamini-Hochberg procedure.

Subset analysis of the monocytes within the PBMC dataset of cohort 2

The monocyte space was investigated by subsetting the PBMC dataset to those clusters identified as monocytes (cluster 0-4), removing cells with strong multi-lineage marker expressions, and repeating the variable gene selection (top 2,000 variable genes), regression for the number of UMIs and scaling as described above. The dimensionality of the data was then reduced to 8 PCs, which served as input for the UMAP calculation. The SNN-graph based Louvain clustering of the monocytes was performed using a resolution of 0.2. Marker genes per cluster were calculated using the Wilcoxon rank sum test using the following cutoffs: genes have to be expressed in > 20% of the cells, exceed a logarithmic fold change cutoff to at least 0.25, and exhibited a difference of > 10% in the detection between two clusters. The exact number and definition of samples used in the analysis are specified in the legend of Figure 4A and summarized in Table S1.

Time kinetics analysis of identified monocyte clusters

For each patient and time point of sample collection, the proportional occupancy of the monocyte clusters was calculated, and the relative proportions were subsequently visualized as a function of time.

Analysis of scRNA-seq data from fresh PBMC and whole blood samples of cohort 2

ScRNA-seq count data derived from fresh PBMC samples purified by density gradient centrifugation and whole blood after erythrocyte lysis of cohort 2 (BD Rhapsody) were normalized, scaled, and regressed for the number of UMI per cell as described above. After PCA based on the top 2,000 variable genes, UMAP was performed using the first 30 PCs. Cell clusters were determined using Louvain clustering implemented in Seurat based on the first 30 principle components and a resolution of 0.8. Cluster identities were assigned as detailed above using reference-based classification and marker gene expression. Subsequently, the dataset was sub-setted for whole blood samples after erythrocyte lysis and clusters identified as neutrophils and immature neutrophils, and re-scaled and regressed. After PCA on the top 2,000 variable genes, the neutrophil subset data was further processed using the data integration approach implemented in Seurat (Stuart et al., 2019) based on the first 30 PCs removing potential technical biases of separate experimental runs. UMAP and clustering were performed as described above on the top 12 PCs using a resolution of 0.3. Differentially expressed genes between clusters were defined using a Wilcoxon rank sum test for differential gene expression implemented in

Seurat. Genes had to be expressed in > 10% of the cells of a cluster, exceed a logarithmic threshold > 0.1. The exact number and definition of samples used in the analysis are specified in the legend of [Figure 7A](#) and summarized in [Table S1](#).

Quantification of percentages of cell subsets in whole blood scRNA-seq data of cohort 2

After cell type classification of the combined scRNA-seq dataset of fresh PBMC and whole blood samples of cohort 2 described above, 89,883 cells derived from whole blood samples after erythrocyte lysis were subsetted. Percentages of cell subsets in those whole blood samples of the total number of cells were quantified per sample and visualized in boxplots separated by disease stage and group.

Confusion matrix

For each cluster of neutrophils, the relative proportion across disease severity and time point was visualized as a fraction of samples from the respective condition contributing to the cluster.

GO enrichment

Gene set enrichment was performed on gene sets from the Kyoto Encyclopedia of Genes and Genomes (KEGG) database ([Kanehisa, 2019](#)), Hallmark gene sets ([Liberzon et al., 2015](#)) and Gene Ontology (GO) ([Ashburner et al., 2000](#); [Carbon et al., 2019](#)) using the R package/ClusterProfiler v.3.10.1 ([Yu et al., 2012](#)).

Cell cycle state analysis of scRNA-seq data

To categorize the cells within the neutrophil clusters into the respective cell cycle states, we applied the *CellCycleScoring* function of Seurat and visualized the results as pie charts.

Trajectory analysis

Trajectory analysis was performed using the *destiny* algorithm v3.0.1 ([Angerer et al., 2016](#)). In brief, the neutrophil space was subsetted to only severe patients (early and late) and only the most prominent clusters of the latter (clusters 1,2,6,8). The normalized data were scaled and regressed for UMIs and a diffusion map was calculated based on the top 2,000 variable genes with a sum of at least 10 counts over all cells. Based on the diffusion map, a diffusion pseudo time was calculated to infer a transition probability between the different cell states of the neutrophils. Subsequently, the density of the clusters along the pseudotime and marker gene expression for each cluster were visualized.

Enrichment of gene sets was performed using the 'AUCell' method ([Aibar et al., 2017](#)) implemented in the package (version 1.4.1) in R. We set the threshold for the calculation of the AUC to the top 3% of the ranked genes and normalized the maximum possible AUC to 1. The resulting AUC values were subsequently visualized in violin plots or UMAP plots.

Transcription factor prediction analysis

The Cytoscape (version v3.7.1, <https://doi.org/10.1101/gr.1239303>) plug-in iRegulon ([Janky et al., 2014](#)) (version 1.3) was used to predict the transcription factors potentially regulating cluster-specifically expressed gene sets in the neutrophil and monocyte subset analysis in cohort 2. The genomic regions for TF-motif search were limited to 10kb around the respective transcriptional start sites and filtered for predicted TFs with a normalized enrichment score > 4.0. Next, we filtered for TFs, which exceeded a cumulative normalized expression cutoff of 50 in the respective cluster. Subsequently, we selected transcription factors of known relevance in the context of neutrophil and monocyte biology and constructed a network linking target genes among the cluster-specifically expressed marker genes and their predicted and expressed regulators for visualization in Cytoscape.

Mass cytometry data analysis

Cytobank.org was used for de-barcoding of individual samples and manually gating of cell events to remove doublets, normalization beads and dead cells ([Kotecha et al., 2010](#)). Per channel intensity ranges were aligned between batches of measurements using a reference sample acquired across all batches and the *BatchAdjust* function to compute scaling factors at the 95th event percentiles ([Schuyler et al., 2019](#)). For semi-automated gating of populations of interest, high-resolution SPADE clustering was conducted on all indicated asinh-transformed markers ([Table S2](#)) with 400 target nodes ([Qiu et al., 2011](#)). Individual SPADE nodes were then aggregated and annotated to cell subsets (bubbles) according to the expression of lineage-specific differentiation markers. Clustering results and FCS files were subsequently loaded into the R CytoML/flowCore environment (10.18129/B9.bioc.CytoML, 10.18129/B9.bioc.flowCore) for further downstream analyses. To generate UMAP representations all events of a given population of interest were down-sampled to 70,000 cells and then embedded using the *tumap* function (R uwot package, <https://cran.r-project.org/web/packages/uwot/index.html>) parameterized by local neighborhood 50, learning rate 0.5, and using the indicated markers ([Table S2](#)) as input dimensions. For statistical analysis of cell population abundances, we fitted a generalized linear mixed-effects model (GLMM) for each population using the *lme4* package ([Nowicka et al., 2017](#)). P values resulting from differential abundance testing (via R *multcomp* and *lsmmeans* packages) were adjusted using the Benjamini-Hochberg procedure and an FDR-cutoff of 5% across all clusters/subsets and between-group comparisons ([Hothorn et al., 2008](#); [Lenth, 2016](#)). Additionally, indicated surface marker positive populations were exported from Cytobank and analyzed using prism 8. Kruskal-Wallis and Dunn's multiple comparison test was used to

compare differences in proportions between patient groups, whereas mixed-effect-analysis and Sidak's multiple comparison test was applied to report time-dependent differences. The exact numbers and definitions of samples used in the analyses are specified in the respective figure legends and summarized in [Table S1](#).

Data Analysis of Flow Cytometry Data

Flow cytometry data analysis was performed with FlowJo V10.6.1. Cell type was defined as granulocytes (CD45⁺, CD66b⁺), non-classical monocytes (CD45⁺, CD66b⁻, CD19⁻, CD3⁻, CD56⁻, CD14^{lo}, CD16⁺). Relative cell percentage or mean fluorescence intensity (MFI) was used for visualization and statistical analysis was done using unpaired t test.

Data visualization

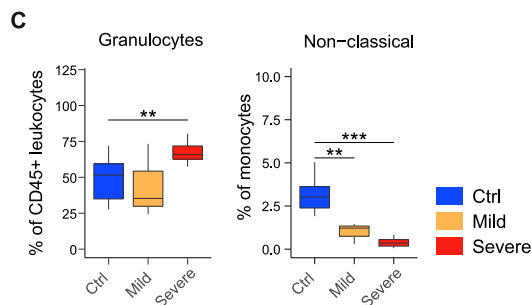
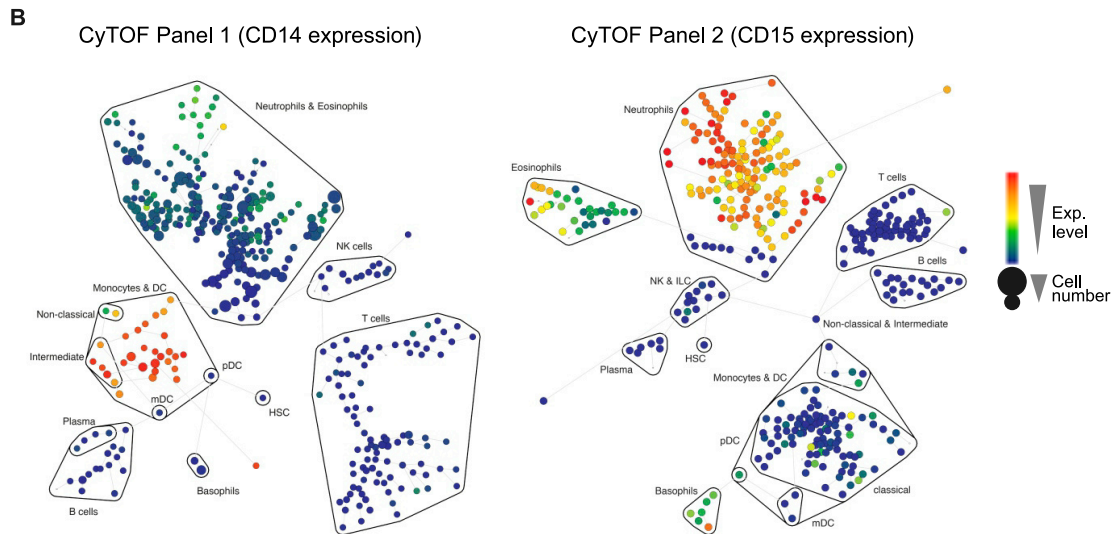
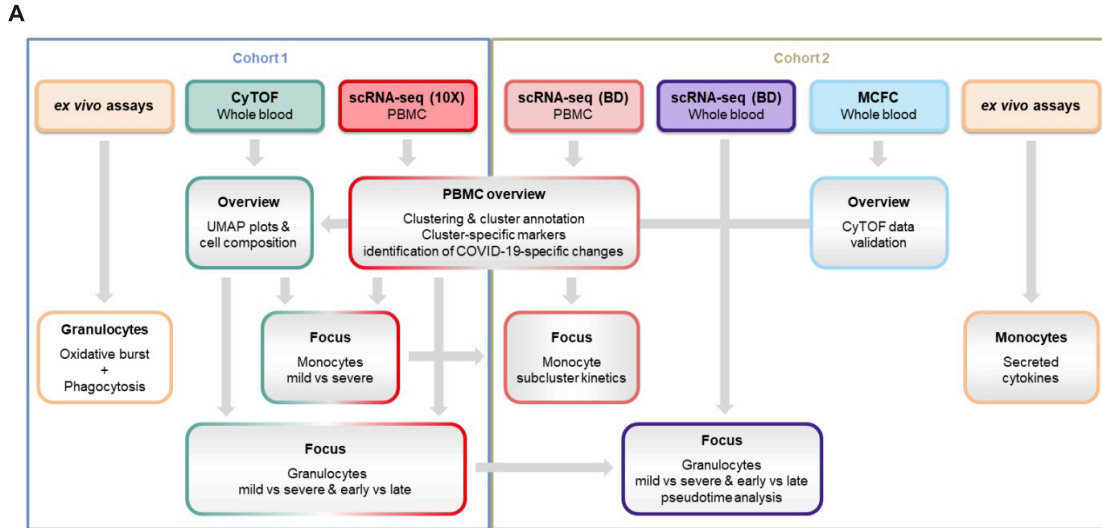
In general, the R packages Seurat and the ggplot2 package (version 3.1.0) ([Wickham, 2016](#)) were used to generate figures. For visualization of mass cytometry data, cluster minimum-spanning trees were rendered using Cytobank, the ComplexHeatmap package ([Gu et al., 2016](#)) was used to display subset phenotypes and GraphPad Prism to generate boxplots of quantitative data.

ADDITIONAL RESOURCES

Part of the patients included in this study have been recruited within the clinical trial DRKS00021688, registered at the German registry for clinical studies ([Kurth et al., 2020](#)).

In addition to the deposition of the raw sequencing data on EGA, we provide an interactive platform for data inspection and analysis via FASTGenomics. The FASTGenomics platform (fastgenomics.org) provides processed count tables of the datasets generated in this study as well as key analytical results, such as UMAP coordinates and cluster identities, and the code written to analyze the respective data.

Supplemental Figures



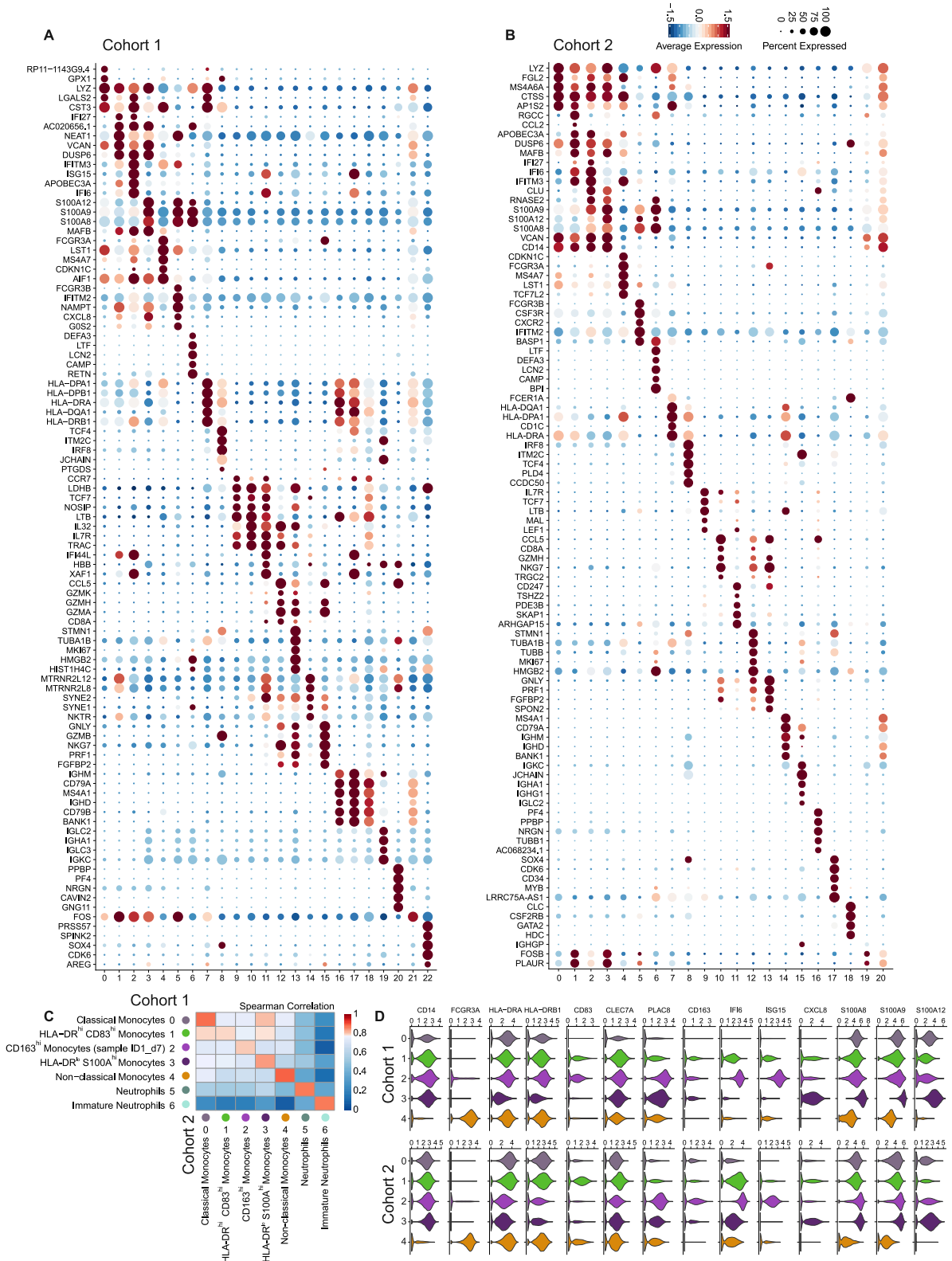
(legend on next page)

Figure S1. Overview of Sample Analysis Pipeline, Major Leukocyte Lineages Definition, and Quantification by CyTOF and MCFC, Related to Figure 1

A, Overview of the analysis pipeline for scRNA-seq and proteomics of COVID-19 samples.

B, High resolution SPADE analysis with 400 target nodes and individual nodes aggregated to the indicated major immune cell lineages according to the expression of lineage specific cell marker such as CD14 for monocytes and CD15 for neutrophils of whole blood samples collected from FLI patients, COVID-19 patients and controls and stained with CyTOF panel 1 and 2, respectively.

C, Boxplots of the composition of total granulocytes and non-classical monocytes within whole blood samples from the second cohort of COVID-19 patients showing either mild ($n = 3$) or severe disease ($n = 7$) as well as controls ($n = 11$) measured by flow cytometry. Statistical analysis was performed using unpaired t test. ** $p < 0.01$, *** $p < 0.001$.



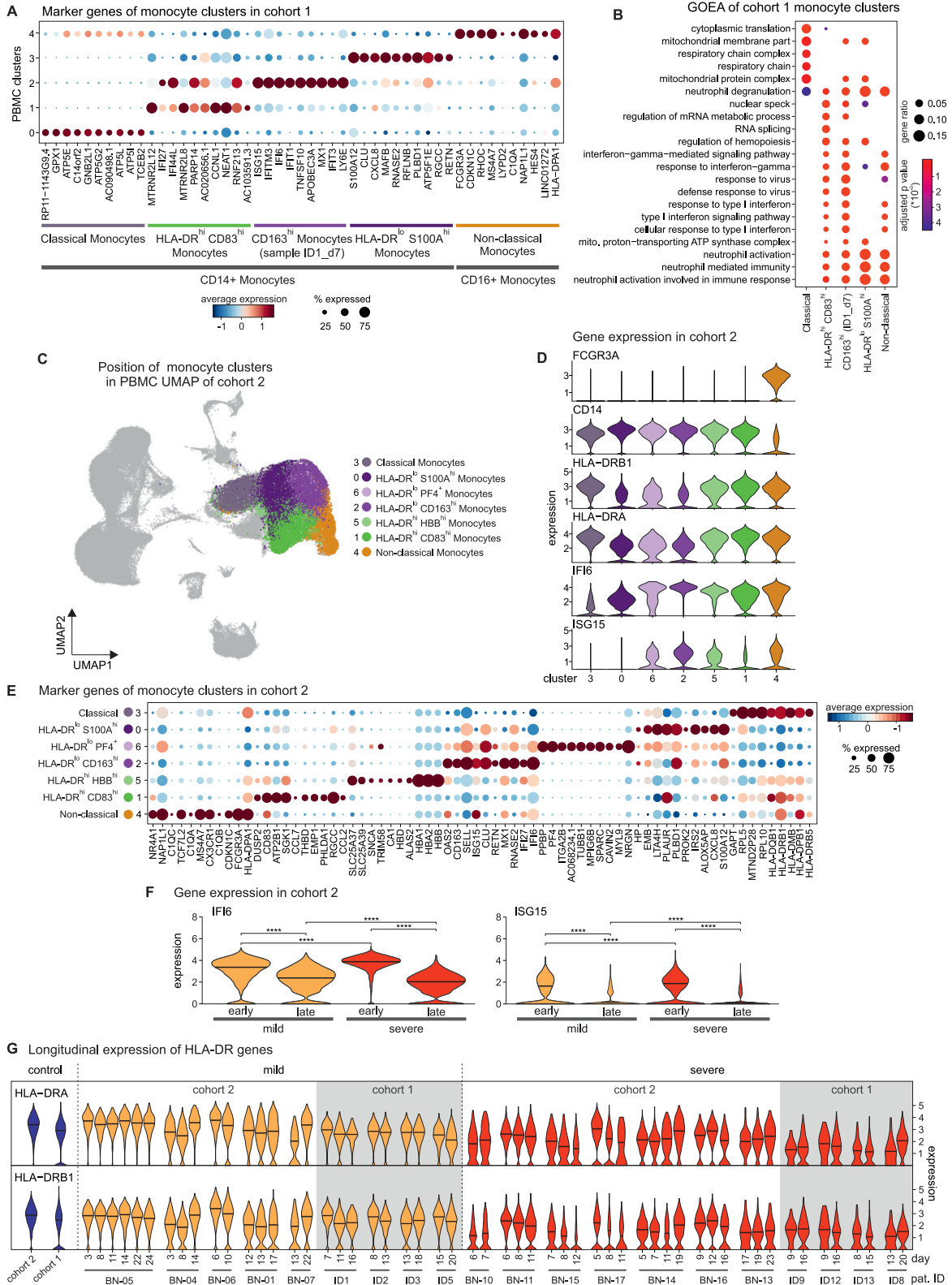
(legend on next page)

Figure S2. Cluster-Specific Marker Gene Expression Shows Inflammatory Activation Signatures of Monocyte Subsets and the Appearance of Neutrophil Subsets in the PBMC Fraction, Related to [Figure 2](#)

(A), Dot plots of the top 5 marker genes sorted by average log fold change determined for the clusters depicted in [Figure 2A](#).

(B), Dot plot representation of the top 5 marker genes sorted by average log fold change determined for the clusters depicted in [Figure 2D](#).

C: Heatmap of the Spearman correlation coefficients between myeloid cell subsets in two cohorts, based on the union of top 50 marker genes per cluster.



(legend on next page)

Figure S3. Transcriptional Differences of Monocytes from Mild and Severe COVID-19, Related to Figure 4

A, Dot plot of the top 10 marker genes sorted by average log fold change of the clusters within the monocyte space of cohort 1 (related to [Figure 2](#), [Table S4](#)).

B, Gene ontology enrichment analysis based on the complete marker genes obtained for each monocyte cluster of cohort 1, showing the top 10 significant terms enriched in each cluster ranked by adjusted p values.

C, Back-mapping of monocyte clusters of cohort 2 ([Figure 4C](#)) onto the PBMC UMAP of cohort 2 ([Figure 2D](#)). The legend shows the association of the colors to the clusters together with the labeling of the clusters based on expressed marker genes (according to [Figures 2](#) and [S3D–S3F](#)).

D, Violin plots of marker gene expression in the monocyte clusters identified in the complete PBMC space of cohort 2 ([Figures 2C](#) and [2D](#)).

E, Dot plot of the top 10 marker genes sorted by average log fold change calculated for the monocyte clusters ([Figure 4C](#)).

F, Violin plots of the *IFI6* and *ISG15* expression in cells of mild and severe patients, additionally divided into early (1–10 days after disease onset) and late (> 10 days after disease onset). Statistical analysis was performed using Wilcoxon Rank Sum test adjusted with the Bonferroni method, ****p < 0.0001.

G, Violin plots showing the time-dependent change of *HLA-DRA* and *HLA-DRB1* expression in the monocyte population of cohort 1 (mild: n = 4; severe: n = 4) and cohort 2 (mild: n = 5; severe: n = 7). Mild samples are colored in yellow, severe samples in red and controls in blue, with the latter shown as reference violin plots representing the expression of all control monocytes in the respective cohort (cohort 1: n = 22, cohort 2: n = 6).

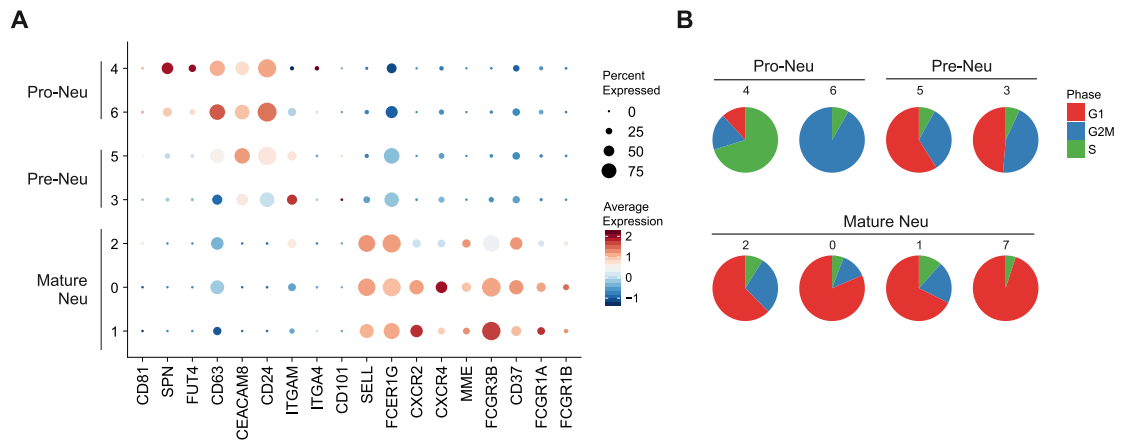


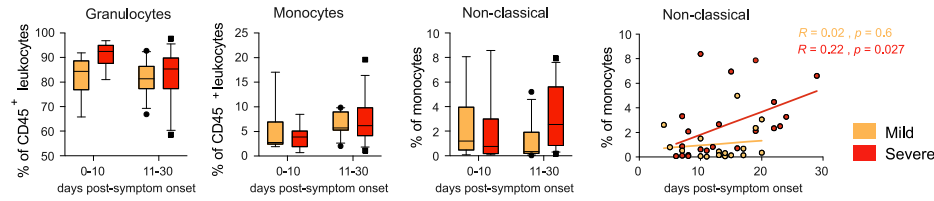
Figure S4. Additional Analysis of Dysfunctional Neutrophils in PBMC Fraction, Related to Figure 5

A, Dot plot of marker genes associated with immature neutrophils (pro- and pre-neutrophils), and mature neutrophils.

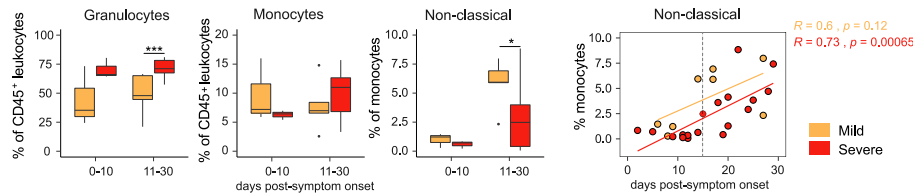
B, Pie charts showing the proportion of cells predicted to be in a given cell cycle stage. The numbers refer to the cell clusters presented in panel A.

A

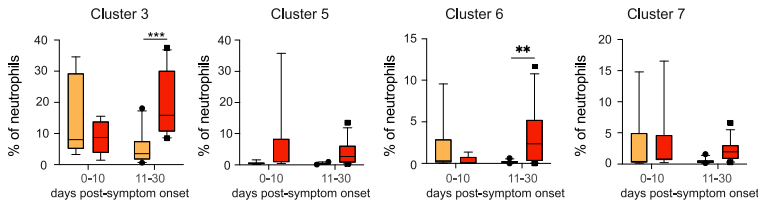
Cohort 1



Cohort 2

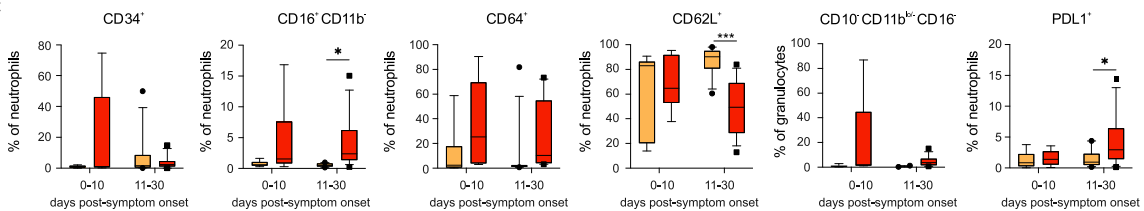


B

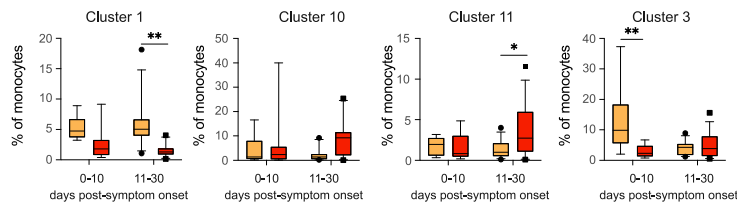


Cluster	Marker	Function
3	CD11b ⁺ CD16 ⁺ CD62L ⁺ CD64 ^{int}	Mature, partially activated & aged
5	CD24 ⁺ CD11b ^{int} CD16 ⁺ CD62L ⁺ CD64 ^{int}	Immature, pro-Neutrophil 2-like activated
6	CD34 ⁺ CD38 ⁺ CD11b ⁺ CD16 ^{int} PDL1 ⁺	Immature, pro-Neutrophil 14-like, PDL1 ⁺
7	CD11b ⁺ CD16 ^{int} CD33 ^h	Immature, pro-Neutrophil-like, CD33 ^h

C

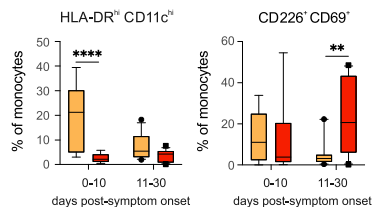


D



Cluster	Marker	Function
1	HLA-DR ^{hi} CD11c ⁺ CD16 ⁺ CD14 ⁺	Classical, activated
3	HLA-DR ^{int} CD11c ⁺ CD16 ⁺ CD14 ⁺	Intermediate, activated, "Mild & FLI"
10	HLA-DR ^{int} CD11c ⁺ CD10 ⁺ CD226 ⁺ CD69 ⁺ CD16 ⁺ CD14 ⁺	Classical, alternatively activated, macrophage-like, "Severe"
11	HLA-DR ^{int} CD11c ⁺ CD16 ⁺ CD14 ⁺	Intermediate, inflammatory "FLI"

E



F

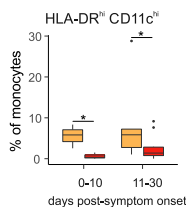


Figure S5. Longitudinal Analysis of Neutrophil and Monocyte Cell Populations, Related to Figure 6

A, Box and whisker (10-90 percentile) plots of time-dependent differences in total granulocytes and monocytes, non-classical monocytes and correlation analysis between days post-symptom onset and proportion of non-classical monocytes.

B, Box and whisker (10-90 percentile) plots of time-dependent differences in main neutrophil cell cluster 3, 5, 6 and 7 in cohort 1.

(legend continued on next page)

C, Box and whisker (10-90 percentile) plots of time-dependent differences in proportions of CD34⁺, CD11b^{lo/-}CD16⁻, CD64⁺, CD62L⁺, CD10⁻CD11b^{lo/-}CD16⁻ (reported from panel 1) and PD-L1⁺ neutrophils in cohort 1.

D, Box and whisker (10-90 percentile) plots of time-dependent differences in main monocyte cluster 1, 10 (belonging to CD14^{hi}CD16⁻ classical monocytes), cluster 11 and 3 (belonging to CD14^{hi}CD16⁺ intermediate monocytes) in cohort 1.

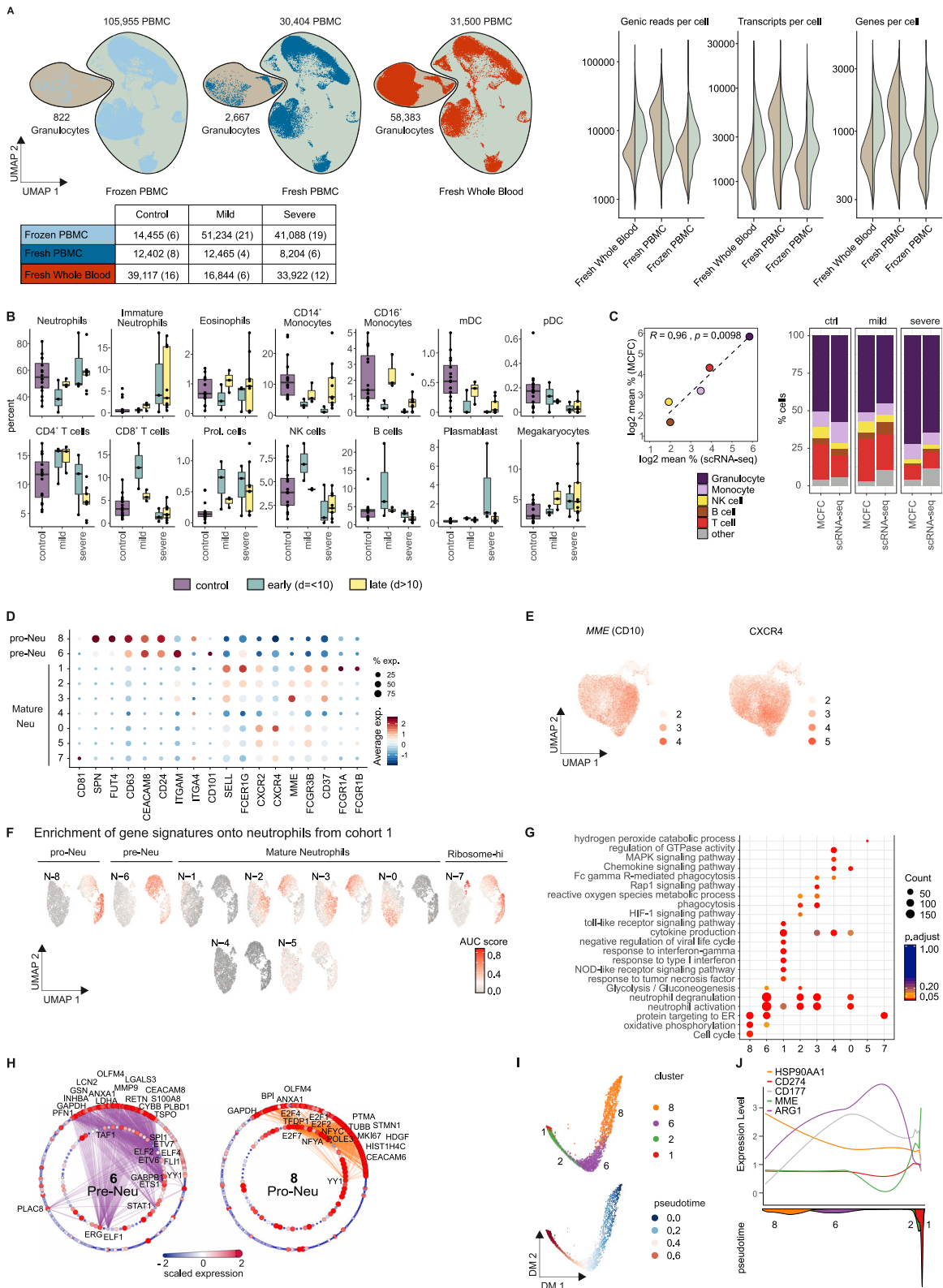
E, Box and whisker (10-90 percentile) plots of time-dependent differences in CXCR3⁺, HLA-DR^{hi}CD11c^{hi} and CD226⁺CD69⁺ monocytes.

(F), Box and whisker (10-90 percentile) plot showing time-dependent differences in HLA-DR^{hi}CD11c^{hi} monocytes in cohort 2.

Measurements in cohort 1 were done applying mass cytometry on whole blood samples distinguishing between COVID-19 patients with mild (days 0-10: n = 6, days 11-30: n = 12) or severe disease (days 0-10: n = 9, days 11-30: n = 13) course. Mixed-effect-analysis and Sidak's multiple comparison test was used to calculate significant differences

Measurements in cohort 2 were done with flow cytometry on 26 whole blood samples from COVID-19 patients showing either mild (n = 8) or severe disease (n = 18) course as well as 11 samples from age-matched controls (n = 10).

*p < 0.05, **p < 0.01, ***p < 0.001, ****p < 0.0001



(legend on next page)

Figure S6. Overview of scRNA-Seq Dataset from Cohort 2 and Additional Characterization of Neutrophils, Related to Figure 7

(A), UMAP (on the left) of the complete scRNA-seq dataset from cohort 2 (frozen PBMC, fresh PBMC, fresh whole blood), encompassing 98 samples from 16 controls, 8 mild, and 10 severe COVID-19 patients. Right panel: violin plots of the number of genic reads, transcripts and genes expressed in the PBMC (right) versus the granulocyte fraction (left) across the different datasets of cohort 2. The UMAP is split by experimental condition and the classified granulocyte and PBMC fractions are marked separately. The table below indicates the number of cells per experimental condition separated by control, COVID-19 mild and COVID-19 severe. The numbers of samples are indicated in brackets.

(B), Box and whisker plots (25–75 percentile) of cell type frequencies identified by scRNA-seq in fresh whole blood samples after erythrocyte lysis comparing 16 samples from 15 controls, 6 from 5 mild COVID-19 and 12 from 4 severe COVID-19 patients.

(C), Comparison between cell frequencies identified by scRNA-seq and MCFC. Pearson's correlation between the mean of each cell population measured in MCFC (y axis) and by scRNA-seq of $R^2 = 0.96$ with $p = 0.0098$ (left). The stacked bar chart sorted by disease severity shows the cell type frequency for controls ($n = 16$), mild ($n = 5$) and severe COVID-19 samples ($n = 18$) split by scRNA-seq and MCFC.

(D), Dot plot of literature-based marker genes classifying different neutrophil subsets.

(E), UMAP of neutrophils showing the scaled expression of *MME*(CD10) and *CXCR4* with enrichment in the control-specific clusters 0.

(F), UMAP of AUCell-based enrichment of gene signatures derived from the neutrophil clusters from cohort 2 on the UMAP visualization of cohort 1. The UMAP is colored by the 'Area Under the Curve' (AUC) scores of each cell.

(G), Dot plot visualization of selected significantly enriched Gene Ontology terms and KEGG pathways for each cluster from the neutrophil space. The dots are colored by their adjusted p value and the size of the dots is defined by the number of genes found in the Gene Ontology term.

(H), Network representation of marker genes and their predicted upstream transcriptional regulators for neutrophil clusters 6 (pre-Neutrophils) and 8 (pro-Neutrophils). Edges represent predicted transcriptional regulation. Transcription factors in the inner circle and their predicted target genes in the outer circle are represented as nodes sized and colored according to the scaled expression level across all clusters. Selected genes and transcription factors were labeled based on connectivity and literature mining.

(I), Diffusion map dimensionality reduction of the main neutrophil clusters 8, 6, 2, and 1 from the severe COVID-19 patients (top) and diffusion pseudotime visualized on the diffusion map indicating the transition probability of the different clusters in the following order: 8 - 6 - 2 - 1 (bottom).

(J), Genes specific for each cluster (*HSP90AA1*, *CD274*(PD-L1), *CD177*, *MME*(CD10), *ARG1*) visualized along the diffusion pseudotime (top) with the density of each cluster along the pseudotime (bottom) highlighting the proposed order of differentiation of the different neutrophil subsets.






CD4⁺ T cell calibration of antigen-presenting cells optimizes antiviral CD8⁺ T cell immunity

Received: 8 November 2021

Accepted: 13 April 2023

Published online: 15 May 2023

 Check for updates

Elise Gressier ^{1,16}✉, Jonas Schulte-Schrepping ^{2,3,16}, Lev Petrov⁴, Sophia Brumhard⁵, Paula Stubbemann⁵, Anna Hiller⁵, Benedikt Obermayer ⁶, Jasper Spitzer ⁷, Tomislav Kostevc⁴, Paul G. Whitney¹, Annabell Bachem¹, Alexandru Odainic ^{1,7}, Carolien van de Sandt ¹, Thi H. O. Nguyen ¹, Thomas Ashhurst ⁸, Kayla Wilson ¹, Clare V. L. Oates¹, Linden. J. Gearing ^{9,10}, Tina Meischel ¹, Katharina Hochheiser¹, Marie Greyer¹, Michele Clarke¹, Maike Kreutzenbeck⁷, Sarah S. Gabriel ¹, Wolfgang Kastenmüller ¹¹, Christian Kurts¹², Sarah L. Londrigan ¹, Axel Kallies ¹, Katherine Kedzierska ¹, Paul J. Hertzog^{9,10}, Eicke Latz ⁷, Yu-Chen E. Chen¹³, Kristen J. Radford ¹³, Michael Chopin¹⁴, Jan Schroeder¹, Florian Kurth ⁵, Thomas Gebhardt ¹, Leif E. Sander ⁵, Birgit Sawitzki⁴, Joachim L. Schultze^{2,3,15}, Susanne V. Schmidt^{7,17} & Sammy Bedoui ^{1,12,17}✉

Antiviral CD8⁺ T cell immunity depends on the integration of various contextual cues, but how antigen-presenting cells (APCs) consolidate these signals for decoding by T cells remains unclear. Here, we describe gradual interferon- α /interferon- β (IFN α/β)-induced transcriptional adaptations that endow APCs with the capacity to rapidly activate the transcriptional regulators p65, IRF1 and FOS after CD4⁺ T cell-mediated CD40 stimulation. While these responses operate through broadly used signaling components, they induce a unique set of co-stimulatory molecules and soluble mediators that cannot be elicited by IFN α/β or CD40 alone. These responses are critical for the acquisition of antiviral CD8⁺ T cell effector function, and their activity in APCs from individuals infected with severe acute respiratory syndrome coronavirus 2 correlates with milder disease. These observations uncover a sequential integration process whereby APCs rely on CD4⁺ T cells to select the innate circuits that guide antiviral CD8⁺ T cell responses.

Antigen-presenting cells (APCs) depend on capturing and presenting viral antigens through major histocompatibility complex (MHC) molecules to prime naive T cells and restimulate antigen-experienced T cells during virus infections^{1–3}. Effective T cell responses also hinge on a variety of non-antigenic signals that are relayed from APCs to T cells by co-stimulatory molecules and soluble mediators. It is well established that such contextual cues broadly reflect the exposure of APCs to inflammatory cytokines, such as interferon- α /interferon- β (IFN α/β) and danger signals that stimulate the NF- κ B pathway^{3,4}. Yet, the number of co-stimulatory molecules and soluble mediators that APCs use to convey these cues to T cells is discrete, and the expression of many of these factors continues

to change as the APCs interact with T cells. For example, CD4⁺ T cells responding to antigen rapidly increase the expression of CD40L and provide stimulation back to the APC via CD40 and the NF- κ B pathway⁵. Such ‘T cell help’ involves cooperation with innate stimuli^{6,7}, but how APCs integrate these different signals at the cellular level and whether such cooperation requires prolonged interactions with CD4⁺ T cells or follows more dynamic patterns is currently unclear. Resolving how APCs integrate and relay these different signals to CD8⁺ T cells is important for our general understanding of how the innate–adaptive cross-talk regulates T cell responses and will provide key insights required to improve CD8⁺ T cell responses during infection and vaccination.

A full list of affiliations appears at the end of the paper. ✉ e-mail: elise.gressier07@gmail.com; sbedoui@unimelb.edu.au

Here, we systematically dissected how APCs integrate stimulation through IFN α/β and CD40 from CD4⁺ T cells. We identified an iterative process whereby APCs require IFN α/β -dependent rewiring of the signaling cascade downstream of CD40 that enables the subsequent partition of NF- κ B-, IRF1- and FOS-dependent genes into distinct patterns of co-stimulatory molecule expression and mediator provision. This carefully sequenced integration process is critical for antiviral CD8⁺ T cell responses in a mouse virus infection model, and its activity in APCs from individuals infected with severe acute respiratory syndrome coronavirus 2 (SARS-CoV-2) correlates with CD8⁺ T cell responses and milder forms of coronavirus disease 2019 (COVID-19).

Results

IFN α/β and CD40 induce distinct responses by dendritic cells

To dissect how APCs integrate signals from IFN α/β and CD40 stimulation, we initially focused on type I conventional dendritic cells (cDC1s), known platforms for T cell help^{8,9}. We exposed bone marrow-derived CD24^{hi}CD11b^{lo} cDC1s (hereafter, BMDC1s) to IFN α and an antibody that mimics T cell help by cross-linking CD40⁶. RNA sequencing (RNA-seq) revealed that CD40 induced some changes in BMDC1s, but this response was limited compared to >1,000 differentially expressed (false discovery rate (FDR) > 0.05, 1.5-fold change) genes induced by IFN α (Fig. 1a and Supplementary Table 1). Most IFN-stimulated genes (ISGs)¹⁰ remained unaffected by additional CD40 stimulation (Fig. 1a, 'CD40-unresponsive genes'). However, a subgroup of genes, which included *Ccl4* and *Il15*, was further increased when IFN α and CD40 antibody were applied together (Fig. 1a, 'amplified genes'). We also observed genes that could not be induced by either stimulus alone but were strongly increased in BMDC1s exposed to both IFN α and CD40 antibody (Fig. 1a, 'combinatorial genes'). This response included *Ccl5* and *Tnf* and other genes with known roles in the interplay between APCs and T cells, such as *Cd83* and *Cxcl16* (Fig. 1a). We validated these distinct response patterns in separate experiments, focusing on interleukin-15 (IL-15) and CCL4 as examples for the amplified response and tumor necrosis factor- α (TNF- α) and CCL5 for the combinatorial synergy between IFN α and CD40 stimulation (Fig. 1b,c and Extended Data Fig. 1a). Comparable responses could also be elicited when CD40 synergized with IFN β (Extended Data Fig. 1b) or other innate stimuli, such as polyinosinic–polycytidylic acid (poly(I:C)), lipopolysaccharide (LPS) or cytosine–phosphate–guanine (CpG), which triggered Toll-like receptor 3 (TLR3), TLR4 and TLR9, respectively (Extended Data Fig. 1c). These findings indicate that CD40 synergizes with various innate stimuli in inducing 'amplified' and 'combinatorial' responses in BMDC1s.

cDC1s require *in vivo* stimulation from both IFN α/β and CD4⁺ T cells through CD40 to 'amplify' their capacity to provide IL-15 to herpes simplex virus (HSV)-specific CD8⁺ T cells⁶. To investigate whether priming of HSV-specific CD8⁺ T cells requires mediators that can only be induced by the synergy between IFN α/β and CD40 (such as CXCL16 and CCL5), we transferred *Cxcr6*^{+/+} and *Cxcr6*^{-/-} bone marrow cells into irradiated hosts and infected them 6–8 weeks later with HSV-1 on the skin. Seven days later, splenic HSV-specific *Cxcr6*^{-/-} CD8⁺ T cells produced less IFN γ in response to *ex vivo* antigen restimulation than their *Cxcr6*^{+/+} counterparts (Fig. 1d). CCL5-competent transgenic HSV-specific CD8⁺ T cells transferred into *Ccl5*^{-/-} mice also had a significant, albeit more subtle, defect in IFN γ production in response to *ex vivo* antigen restimulation compared to wild-type recipients of HSV-specific transgenic CD8⁺ T cells (Fig. 1e), indicating that multiple genes required stimulation through both IFN α/β and CD40 for optimal helper-dependent DC–CD8⁺ T cell interactions *in vivo*.

IFN α/β change transcription downstream of CD40

Next, we tested whether IFN α/β and CD40 antibody acted concurrently or in sequence. To first investigate whether CD40 stimulation conditioned a more efficient response of BMDC1s to IFN α/β , we stimulated BMDC1s with CD40 antibody for 4 h and added IFN α for the last 15,

30, 60, 120 or 180 min of the stimulation. *Il15* expression increased after 1–2 h of IFN α stimulation, and this expression increased more than twofold in the presence of CD40 antibody (Fig. 2a). *Tnf*, *Cxcl16* and *Cd83* were also induced in BMDC1s after 2–3 h of IFN α stimulation (Fig. 2a), indicating that BMDC1s required ~2 h of IFN α/β exposure before they responded to CD40 triggering. We then determined whether IFN α/β conditioned the BMDC1s for CD40 responses by exposing BMDC1s to IFN α/β over 4 h and adding CD40 antibody for the last 15, 30, 60, 120 or 180 min. *Tnf*, *Cxcl16* and *Cd83* increased after 30–60 min (Fig. 2a), which showed that BMDC1s responded rapidly to CD40 stimulation if exposed to IFN α/β for ~2 h and suggested that BMDC1 need to be exposed to IFN α/β prior to CD40 stimulation IFN α/β conditions the dendritic cells (DCs) to become receptive to T cell help. We also tested this requirement *in vivo* using HSV-1 skin infection⁶. CD8⁺ cDC1s residing in the brachial lymph nodes of wild-type mice increased MHC class II expression 2 days after infection, but this increase was absent in *Ifnar2*^{-/-} mice (Extended Data Fig. 1d). Because lack of CD4⁺ T cells does not impact MHC class II expression by CD8⁺ cDC1s in the brachial lymph nodes of wild-type mice infected 2 days earlier with HSV-1 on the skin⁶, these findings indicate that IFN α/β signals also need to precede CD40-mediated T cell help *in vivo*.

Next, we tested whether IFN α/β prepared DCs for T cell help by increasing CD40 expression⁷. IFN α -stimulated and unstimulated BMDC1s increased the expression of CD40 over time similarly (Extended Data Fig. 1e), indicating that surface CD40 expression was not rate limiting in these responses. To investigate whether the 'amplified' and 'combinatorial' responses resulted from the effect of IFN α/β on the pathways downstream of CD40, we performed RNA-seq of BMDC1s stimulated with IFN α for 4 h (BMDC1-IFN- α) and compared gene expression to BMDC1s additionally stimulated with CD40 antibody for the last 15 min (BMDC1-IFN α + CD40-15min) or 30 min (BMDC1-IFN α + CD40-30min) or over the entire 4-h period (BMDC1-IFN α + CD40-4h). Overall, BMDC1s changed expression of 341 genes over the 15-min, 30-min and 4-h time points compared to BMDC1-IFN α , BMDC1-CD40 or unstimulated BMDC1s (Fig. 2b). Unsupervised self-organizing maps (SOMs) of these 341 genes identified smaller groups of genes appearing transiently at 15 min and 30 min (that is, *Ifi44*, *Ifit3* and *Fos*), while different and larger sets of genes clustered at 4 h (that is, *Cd83*, *Il15*, *Cxcl16*, *Il27* and *Cd80*) (Fig. 2c and Supplementary Table 2). General cellular processes, such as 'enhanced survival' and 'increased mRNA stability', were enriched in BMDC1-IFN α + CD40-30min, while more specific responses, including 'regulation of cytokine production', characterized BMDC1-IFN α + CD40-4h (Fig. 2d). We also performed coexpression analysis¹¹ to identify similarly expressed groups of genes ('modules') independently of fold change cutoffs used to define differentially expressed genes across all time points (Fig. 2e and Supplementary Table 3). Genes in modules 1 and 3, such as *Cxcl16* and *Tnf*, responded to the combination of IFN α and CD40 antibody at 30 min and 4 h (Extended Data Fig. 2a). Modules 2 and 4 grouped genes that were induced by IFN α (that is, *Oas1l*, *Isg20* and *Il2rg*) or CD40 antibody (that is, *Cxcr4*, *Apol7c* and *Il12b*), respectively, while modules 5 and 6 contained genes with little responsiveness to either stimulation (that is, *Itga3*, *Sox4* and *Irak1*) (Fig. 2e). These modules also differed in GO term enrichments (Fig. 2d). Together, these analyses indicate that IFN α/β changed how BMDC1s responded at the transcriptional level to CD40 stimulation.

IFN α enable CD40 to activate p65, FOS and IRF1

Next, transcription factor binding motif prediction analysis of the 'amplified' genes suggested the involvement of overlapping transcriptional regulators, including members of the IRF and STAT families (Fig. 3a). More specifically, BMDC1-IFN α + CD40-30min and BMDC1-IFN α + CD40-4h were enriched for binding sites for NF- κ B, including NFKB1, REL, RELA (p65 subunit) and RELB (Fig. 3a). To test these predictions, we examined canonical and non-canonical NF- κ B

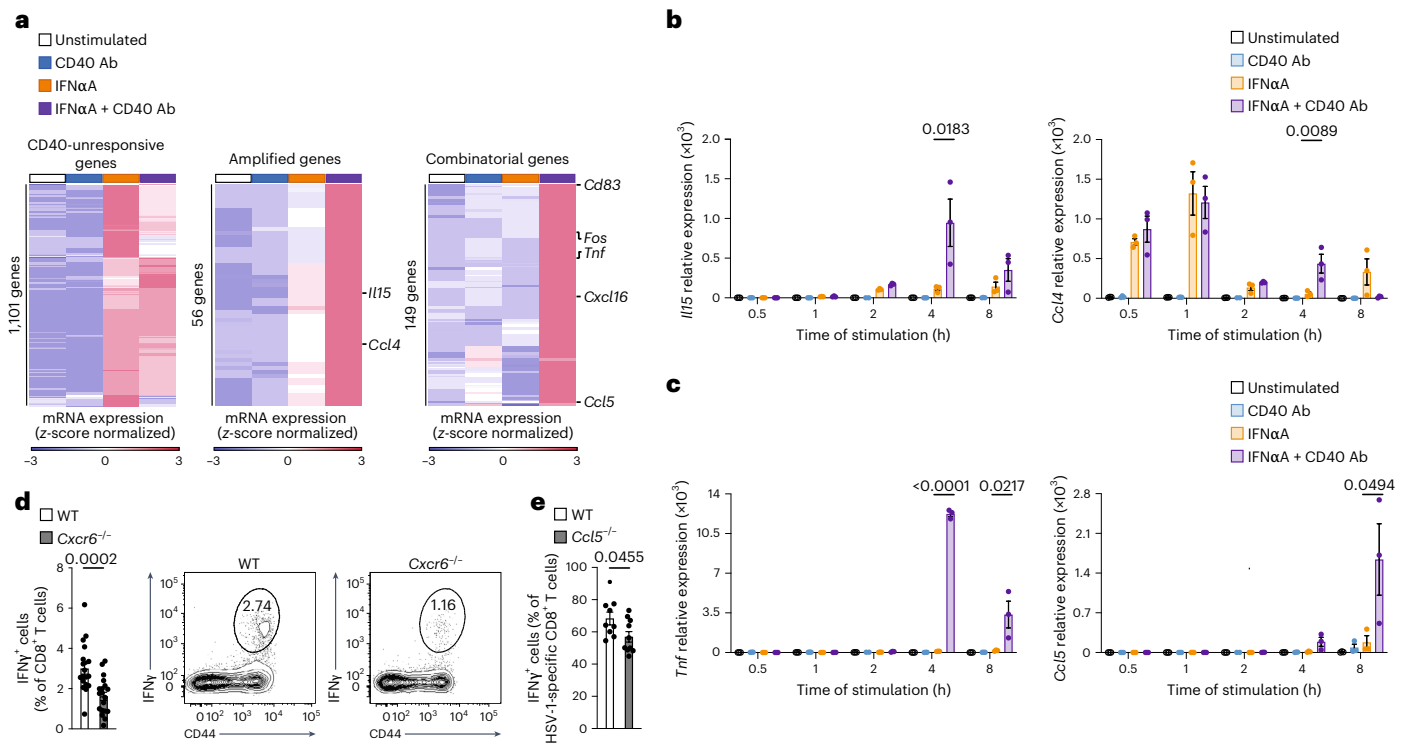


Fig. 1 | IFN α/β and CD40 induce distinct and combinatorial responses in cDC1s. **a**, Changes in gene expression of BMDC1s stimulated for 4 h with IFN α A ($n = 6$ independent experiments), CD40 antibody (Ab) ($n = 3$ independent experiments) or IFN α A + CD40 antibody ($n = 3$ independent experiments) compared to unstimulated BMDC1s ($n = 6$ independent experiments). Differentially expressed genes are displayed as heat maps after z-score transformation of counts per million (CPM). Statistical differences were assessed by one-way analysis of variance (ANOVA); FDR-adjusted $P \leq 0.05$ and fold change greater than 1.5. **b, c**, Relative expression of *Il15* and *Ccl4* (**b**) and *Tnf* and *Ccl5* (**c**) over time in BMDC1s stimulated with IFN α A and/or CD40 antibody. Data are mean \pm s.e.m. from two to three independent experiments. Statistically significant differences between conditions were assessed by one-way ANOVA;

adjusted P values are indicated. **d**, IFN γ production after ex vivo antigen restimulation for 5 h by splenic wild-type (WT) and *Cxcr6*^{-/-} HSV-1-specific CD8⁺ T cells 10 days after HSV-1 skin infection of wild-type mice that were irradiated and reconstituted with an equal mix of *Cxcr6*^{-/-} and wild-type bone marrow cells 6–8 weeks earlier. Data are mean \pm s.e.m. from three independent experiments ($n \geq 5$ per experiment). **e**, IFN γ production after ex vivo antigen restimulation for 5 h by transgenic HSV-1-specific CD8⁺ T cells (gBT-1 cells) transferred as naive gBT-1 cells into wild-type or *Ccl5*^{-/-} mice 1 day before HSV-1 infection and isolated from the spleen 7 days after infection. Data are mean \pm s.e.m. from three independent experiments ($n \geq 1$ per experiment). Statistical significance between conditions in **d** and **e** was assessed by two-tailed Wilcoxon rank-sum test, and respective P values are indicated.

signaling cascades in the interplay between IFN α A and CD40 antibody. The induction of amplified genes (*Il15* and *Ccl4*) and combinatorial genes (*Tnf* and *Cxcl16*) in BMDC1-IFN α A + CD40-4h was similar between *Nfkb2*^{-/-} and wild-type BMDC1s (data not shown), indicating that the non-canonical NF- κ B pathway was not required. BMDC1-IFN α A + CD40-15min resulted in I κ B α degradation and p65 phosphorylation (Fig. 3b and Extended Data Fig. 2c), and the NF- κ B inhibitor ammonium pyrrolidinedithiocarbamate (PDTC)¹² impaired the increased expression of *Tnf* and *Ccl4* in BMDC1-IFN α A + CD40-4h (Fig. 3c). These findings highlight that IFN α/β conditioning enabled CD40 to trigger the canonical NF- κ B pathway in BMDC1s.

The transcriptional regulator FOS was induced in BMDC1-IFN α A + CD40-15min compared to in BMDC1-IFN α A, BMDC1-CD40 and BMDC1-IFN α A + CD40-4h (Fig. 3d and Supplementary Table 2). We therefore deleted FOS from FLT3L-propagated BMDCs using CRISPR–Cas9 and stimulated these cells for 4 h with IFN α A and CD40 antibody. Compared to non-targeting guide control (NTC) BMDCs, *Il15ra* and *Il27*, but not *Cxcl16* or *Nfkb2*, were reduced in the absence of FOS (Fig. 3e). ERK¹³ and CD40 signaling¹⁴ can activate FOS, and we found phosphorylated p38 and ERK in BMDC1-IFN α A + CD40-15min (Fig. 3f). Inhibition of ERK by nimbolide prevented the increase in *Ccl4* expression and partially reduced *Tnf* expression in BMDC1-IFN α A + CD40-4h compared to in BMDC1-IFN α A (Fig. 3c). Together, these findings indicate that

IFN α/β conditioning enables CD40 to activate FOS, likely through activation of ERK and p38.

The ‘combinatorial’ genes induced by IFN α/β and CD40 antibody were enriched in IRF1 binding sites (Fig. 3g), and expression of *Irf1* was increased in BMDC1-IFN α A + CD40-30min and BMDC1-IFN α A + CD40-4h compared to in BMDC1-IFN α A (Fig. 3h). IRF1 binding signals were enriched in combinatorial genes in BMDC1-IFN α A + CD40-4h compared to in BMDC1-NS, BMDC1-IFN α A and BMDC1-CD40, as revealed by cleavage under targets and tagmentation (CUT&TAG) analysis (Fig. 3i). Endogenous IRF1 was bound to the promoter region of *Cxcl16* in BMDC1-IFN α A + CD40-4h but not in BMDC1-IFN α A, BMDC1-CD40 or BMDC1-NS (Fig. 3j). Moreover, *Irf1*^{-/-} BMDC1s did not induce the expression of *Cxcl16* in response to 4 h of combined IFN α/β and CD40 antibody stimulation (Fig. 3k), and transcription factor binding motifs in the vicinity of IRF1 binding sites were enriched for motifs recognized by p65 (Fig. 3l). Together, these findings show that IFN α/β conditioning enhances the capacity of cDC1s to degrade I κ B α and phosphorylate p65, p38 and ERK downstream of CD40, thus enabling CD4⁺ T cells to induce p65-, IRF1- and FOS-dependent transcriptional programs.

Mild COVID-19 is associated with IFN α/β and CD40 synergy Imbalances in IFN α/β provision¹⁵ and low-avidity CD4⁺ T cell responses¹⁶ are associated with severe COVID-19 (refs. 17,18), while milder outcomes correlate with virus-specific CD8⁺ T cells¹⁸ and the ability of individuals

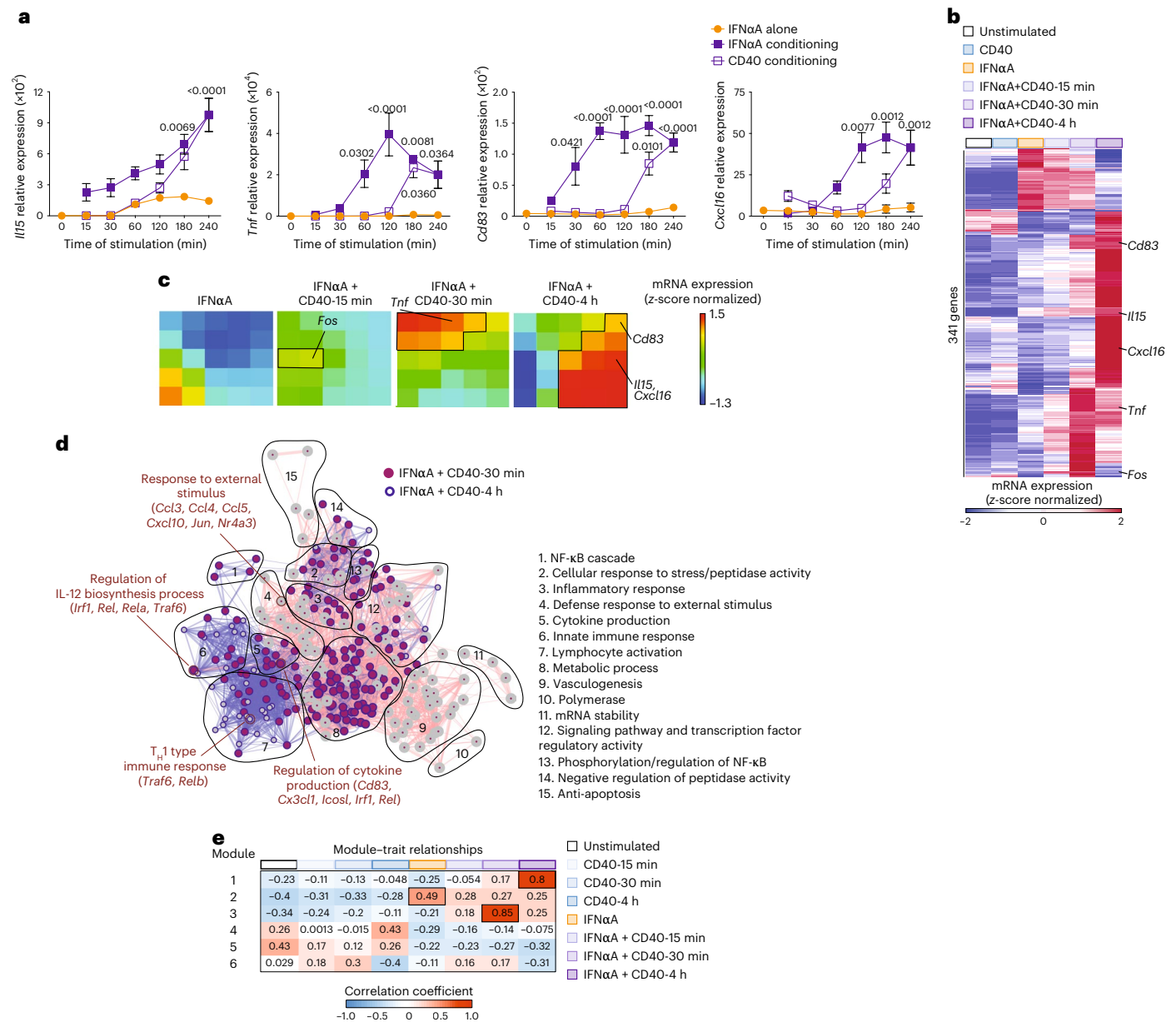


Fig. 2 | IFNα/β conditions cDC1s to enhance transcription in response to CD40 stimulation. **a**, Changes in the expression of *Il15*, *Tnf*, *Cd83* and *Cxcl16* in BMDCs stimulated with IFNα for 4 h and stimulated additionally with CD40 antibody for the last 15, 30, 60, 120, 180 and 240 min (‘IFNα conditioning’) or with CD40 antibody for 4 h and stimulated additionally with IFNα for the last 15, 30, 60, 120, 180 and 240 min (‘CD40 conditioning’) compared to BMDCs exposed to IFNα alone (at least three independent experiments for each time point). Error bars represent mean ± s.e.m. Statistically significant differences between the corresponding conditions and IFNα at 4 h alone were assessed by one-way ANOVA. **b, c**, Heat map (**b**) and SOM (**c**) of differentially expressed genes between BMDCs left unstimulated or stimulated with IFNα alone (IFNα; *n* = 6 independent experiments) or with IFNα for 4 h + CD40 for 15 min (IFNα + CD40-15min; *n* = 3 independent experiments), 30 min (IFNα + CD40-30min; *n* = 3 independent experiments) or 4 h (IFNα + CD40-4h; *n* = 3 independent experiments). The 341 genes were clustered into 25 SOM clusters that follow similar patterns of expression with the identification of

select genes in their respective clusters. **d**, Gene Ontology (GO) terms enriched in IFNα + CD40-30min SOM clusters (clusters 1–4 and 6–8, as in panel c) and IFNα + CD40-4h SOM clusters (clusters 5, 9, 10, 13–15, 18–20 and 23–25, as in panel c). Nodes represent the GO term, edges represent a score inversely proportional to the genes shared between the two GO terms, and the size of the nodes is proportional to the enrichment score. GO terms with a *P* value of ≤0.005 that relate to three or more GO terms are displayed; T_H1, type 1 helper T cell. **e**, Correlation coefficients of weighted gene correlation network analysis (WGCNA) eigengenes combining transcriptional results from RNA-seq of BMDCs that were unstimulated (*n* = 6 independent experiments) or stimulated with CD40 for 15 min (CD40-15min; *n* = 3 independent experiments), CD40 for 30 min (CD40-30min; *n* = 3 independent experiments), CD40 for 4 h (CD40-4h; *n* = 3 independent experiments), IFNα alone for 4 h (IFNα; *n* = 6 independent experiments), IFNα for 4 h + CD40 for 15 min (IFNα + CD40-15min), IFNα for 4 h + CD40 for 30 min (IFNα + CD40-30min) or IFNα for 4 h + CD40 for 4 h (IFNα + CD40-4h; *n* = 3 independent experiments).

to respond to CCL5 (ref. 19) and CXCL16 (ref. 20). To investigate the synergy between IFNα/β and CD40 during SARS-CoV-2 infection, we isolated CD14⁺HLA-DR⁺ DCs from the blood of individuals with COVID-19 4 to 35 days after symptom onset²¹. This included mild to moderate

disease (WHO (World Health Organization) score of 2–5) and severe disease (WHO score of 6–8) (Supplementary Table 7). CD14⁺HLA-DR⁺ DCs from individuals with severe disease had significantly reduced expression of MHC class II (HLA-DR) compared to CD14⁺HLA-DR⁺ DCs from

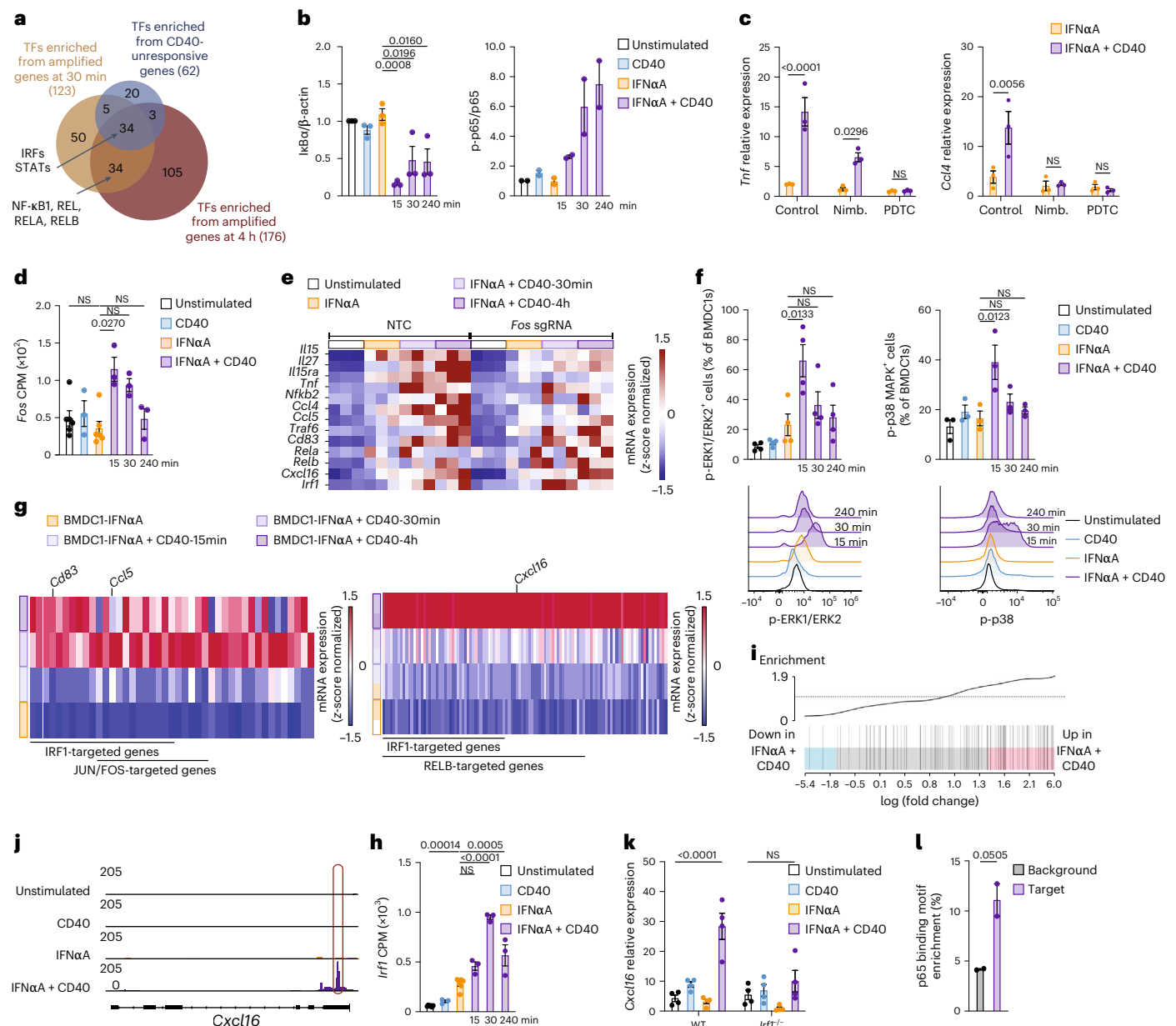


Fig. 3 | IFN α conditioning enables CD40 to activate a network of transcription factors that includes p65, IRF1 and FOS. **a**, Transcription factor (TF) motifs enriched for 'CD40-unresponsive genes' and 'amplified genes' at 30 min and 4 h (as in Fig. 2b) and displayed as Venn diagrams. **b**, IkB α degradation ($n = 3$ independent experiments) and p65 phosphorylation ($n = 2$ independent experiments) in BMDCs, as in Fig. 2b. **c**, *Tnf* and *Ccl4* expression in BMDCs stimulated as in Fig. 2b in the absence or presence of inhibitors for ERK (nimbolide) and the NF- κ B pathway (PDTC). Data are displayed relative to treatment alone and are pooled from three independent experiments. Error bars represent mean \pm s.e.m. Adjusted *P* values of the statistically significant differences as assessed by two-way ANOVA are indicated; Nimb, nimbolide; NS, not significant. **d**, *Fos* expression based on RNA-seq of BMDCs, stimulated as Fig. 2b, expressed as CPM. **e**, Relative expression of select genes (*Il15*, *Il27*, *Il15ra*, *Tnf*, *Nfkb2*, *Ccl4*, *Ccl5*, *Traf6*, *Cd83*, *Rela*, *Relb*, *Cxcl16* and *Irfl*) in BMDCs transduced with *Fos* single guide RNA (sgRNA) or NTC and stimulated as in Fig. 2b ($n = 3$ independent experiments). **f**, Phosphorylation of ERK1/ERK2

(p-ERK1/ERK2) and p38 MAPK (p-p38 MAPK) ($n = 3-4$ independent experiments) in BMDCs as in Fig. 2b. Pooled data and representative histograms are displayed. **g**, Expression of 'combinatorial genes' in BMDCs as in Fig. 2b. **h**, Expression of *Irfl* in RNA-seq data from BMDCs stimulated as in Fig. 2b, expressed as CPM. **i**, Enrichment of IRF1 binding signals in combinatorial genes in BMDC1-IFN α + CD40-4h ($P < 0.0001$; $n = 2$ replicates). **j**, IRF1 binding signals analyzed using CUT&Tag in BMDCs stimulated as in Fig. 2b ($n = 2$ replicates). **k**, Expression of *Cxcl16* in wild-type or *Irfl*^{-/-} BMDCs stimulated as in Fig. 2b. Data are mean \pm s.e.m. from three independent experiments. Adjusted *P* values were assessed by two-way ANOVA. **l**, p65 binding motif enrichment in DNA bound to IRF1 in BMDCs as in Fig. 2b, expressed as target relative to the entire genomic background data. Statistical testing was performed using the cumulative binomial distribution to compare target binding to background signal. Data are mean \pm s.e.m. from two replicates. Error bars in **b**, **d**, **f** and **h** represent mean \pm s.e.m. Adjusted *P* values of the statistically significant differences between the corresponding conditions as assessed by one-way ANOVA are indicated.

individuals with mild disease (Fig. 4a). A similar pattern was observed in CD14⁺CD11c⁺ monocytes, with a significant reduction in MHC class II expression compared to that observed in mild COVID-19 cases (Fig. 4a).

To test whether IFN α /β signals contribute to MHC class II expression, we collected blood samples 4 to 35 days after symptom onset from individuals with COVID-19 who had developed neutralizing antibodies

against type I IFN (IFN-AAB)²². CD14⁺HLA-DR⁺ DCs and CD14⁺CD11c⁺ monocytes from IFN-AAB⁺ individuals had an even stronger reduction of MHC class II than observed in those from individuals with mild disease (Fig. 4a). The expression of CD40 on CD14⁺HLA-DR⁺ DCs in individuals with severe disease increased irrespective of IFN-AAB but was reduced in CD14⁺CD11c⁺ monocytes in individuals with IFN-AAB (Fig. 4a), suggesting that IFN α/β regulate the ability of DCs and monocytes to receive T cell help through the expression of MHC class II^{5,23,24}.

Next, we used published single-cell RNA-seq (scRNA-seq) data from individuals with COVID-19 (ref. 25) to examine the expression of the 'CD40-unresponsive', 'amplified' and 'combinatorial' gene signatures identified above. This included peripheral blood mononuclear cells (PBMCs) from individuals with COVID-19 (mild, WHO score of 3, $n = 16$; moderate, WHO score of 4–5, $n = 11$; severe, WHO score of 7, $n = 23$) collected within the first 25 days after symptom onset before availability of vaccination. These were compared to samples from healthy or otherwise hospitalized individuals who tested negative for SARS-CoV-2, were serologically negative or had no indication of acute COVID-19 disease based on clinical or laboratory parameters (HC; $n = 13$)²⁵. We analyzed 31,736 classical monocytes and 722 myeloid DCs using reference-based cell-type annotation and clustering (Methods), referred to here as CD14⁺ monocytes and CD1c⁺ DCs, respectively. CD14⁺ monocytes from individuals with mild disease²⁵ were significantly enriched for the 'amplified' and 'combinatorial' responses (that is, *CD83*, *CXCL16*, *NFKB2* and *JUND*) compared to CD14⁺ monocytes from individuals with moderate or severe disease or from healthy control individuals (Fig. 4b,c and Supplementary Table 5). Also, CD1c⁺ DCs from individuals with mild COVID-19 had increased transcription of genes of the 'amplified' and 'combinatorial' responses, such as *CD83*, *EGR1* and *REL*, compared to CD1c⁺ DCs from individuals with severe COVID-19, which in turn had increased expression of CD40-unresponsive genes, such as *IFIT3*, *MXI* and *IRF7* (Fig. 4d and Supplementary Table 6). Similar patterns were observed in scRNA-seq data of a second cohort²⁶, which included three individuals with moderate disease (respiratory symptoms and pneumonia), four individuals with severe disease (supplemental oxygen requirement) collected 2–16 days after symptom onset and five asymptomatic healthy control individuals from whom samples were collected before the widespread circulation of SARS-CoV-2 (Extended Data Fig. 3a).

We also performed scRNA-seq on PBMC samples from the COVID-19 cohort above, which included IFN-AAB⁺ individuals²²

(Supplementary Table 7). CD14⁺ monocytes from IFN-AAB⁺ individuals had lower induction of prototypical ISGs, such as *ISG15* and *IFIT2*, than CD14⁺ monocytes from healthy individuals and individuals with disease without IFN-AAB (Extended Data Fig. 3b). Furthermore, the expression of *HLA-DRA*, *HLA-DRB1*, *TNF*, *CD83* and *CCL4* was reduced in CD14⁺ monocytes from individuals with severe COVID-19 and in IFN-AAB⁺ individuals compared to in healthy individuals and in individuals with COVID-19 without IFN-AAB (Extended Data Fig. 3b). To gain more robust insights into data distribution, we integrated our data with comparable published scRNA-seq data sets^{21,27,28}, including a study examining four IFN-AAB⁺ individuals²⁸. This yielded 179,012 single-cell CD14⁺ monocyte transcriptomes across 263 samples (HC, $n = 39$; WHO score of 1–3, mild, $n = 79$; WHO score of 4–5, moderate, $n = 82$; WHO score of 6–8, severe, $n = 52$; WHO score of 7–8, severe + IFN-AAB, $n = 11$). *HLA-DRB1*, *CD83* and *TNF* were significantly reduced in individuals with COVID-19 with increasing disease severity, reaching a minimum in individuals with IFN-AAB (Extended Data Fig. 3b). Furthermore, the 'amplified' and 'combinatorial' signatures were reduced in CD14⁺ monocytes from individuals with severe COVID-19, with and without IFN-AAB, compared to in CD14⁺ monocytes from individuals with mild disease (Extended Data Fig. 3c). Together, these findings indicate that IFN α/β signals are critical drivers of 'amplified' and 'combinatorial' responses during SARS-CoV-2 infection.

Reanalysis of published single-cell assay for transposase-accessible chromatin with sequencing (scATAC-seq) data sets²⁹ from PBMCs of individuals with COVID-19 indicated that CD14⁺ monocytes from individuals with mild disease had significantly increased accessibility of more than 300 genes, including *IL15*, *CD83*, *TNF* and *CXCL16*, compared to CD14⁺ monocytes from individuals with moderate and severe COVID-19 (Fig. 4e,f). Furthermore, Hallmark enrichment analysis of more accessible genes in CD14⁺ monocytes from individuals with mild COVID-19 compared to CD14⁺ monocytes from healthy control individuals identified 'IFN γ response' and 'TNF signaling via NF- κ B' as major pathways differentially regulated in mild COVID-19 (Fig. 4g). To investigate whether these responses can be elicited in vitro in human cDC1s, we differentiated human CD141⁺CADMI⁺CLEC9A⁺ cDC1s (hDC1s) from blood-derived CD34⁺ stem cells using FLT3L, stem cell factor and IL-4 (ref. 30) and stimulated them with human recombinant IFN α and human CD40 Ab separately or in combination for 18 h. hDC1s

Fig. 4 | Combinatorial responses to IFN α/β and CD40 antibody by DCs and monocytes correlate with milder outcomes of COVID-19. a, HLA-DR expression of CD14⁺CD11c⁺ monocytes and CD14⁺HLA-DR⁺ DCs from individuals with COVID-19 with mild or moderate symptoms (WHO score of 2–5; $n = 11$) or severe disease with (WHO score of 6–8; $n = 3–6$) and without ($n = 10$) IFN-AAB.

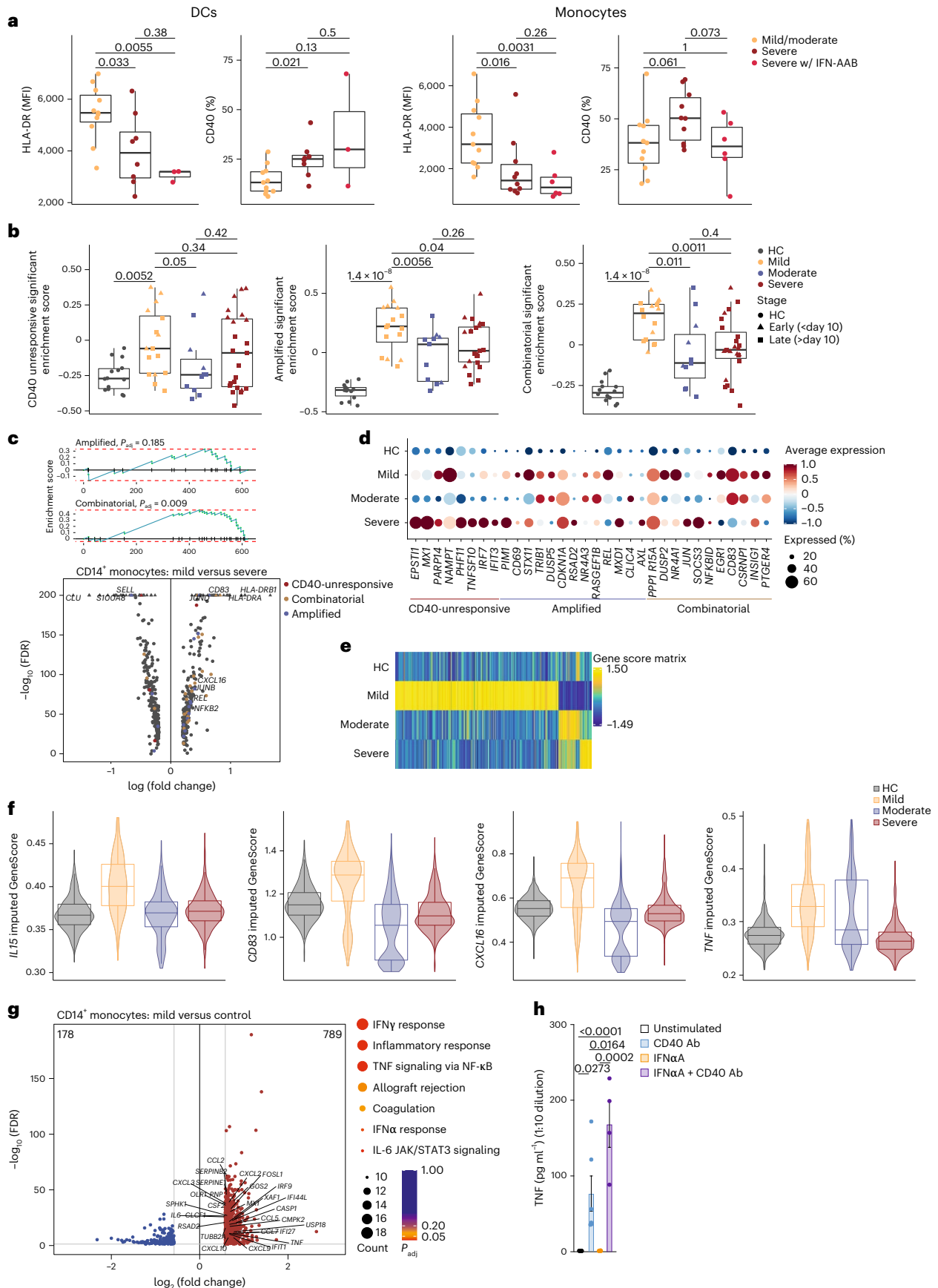
Data are displayed as box and whisker plots showing the median and the 25th and 75th percentiles and two whiskers at 1.5 \times the interquartile range (IQR) of the mean fluorescence intensity (MFI) and percentage of CD40⁺ cells.

b, Single-sample gene set variation analysis (GSVA) of the 'CD40-unresponsive', 'amplified' and 'combinatorial' gene signatures in scRNA-seq data from CD14⁺ monocytes and CD1c⁺ DCs from PBMCs of individuals with mild (WHO score of 3; $n = 16$), moderate (WHO score of 4–5; $n = 11$) or severe (WHO score of 7; $n = 23$) COVID-19 and healthy control (HC) individuals ($n = 13$; reanalyzed from ref. 25). Box plots as in panel **a**. Data points are colored and shaped according to disease severity and stage based on days after onset of symptoms, respectively. Wilcoxon rank-sum test P values are shown. **c**, Gene set enrichment analysis plots (top) showing enrichment curves of the 'amplified' and 'combinatorial' signatures in the differentially expressed genes (two-sided Wilcoxon rank-sum test, minimum percentage = 0.1, $\log_2(\text{fold change}) > 0.2$) in CD14⁺ monocytes from mild compared to severe COVID-19 cases as in **b**. The $\log_{10}(\text{FDR } P \text{ values})$ and the $\log_2(\text{fold change})$ values of the differentially expressed genes are shown as a volcano plot (bottom). Genes are colored according to the 'CD40-unresponsive', 'amplified' or 'combinatorial' signature; P_{adj} , adjusted P value.

d, Differential expression of 'CD40-unresponsive', 'amplified' and 'combinatorial' signature genes in CD1c⁺ DCs from healthy control individuals and individuals with mild, moderate and severe cases of COVID-19, as in **a**, determined using a two-sided Wilcoxon rank-sum test. **e**, Heat map showing GeneScores for disease-specific, significantly differentially accessible genes in scATAC-seq data of CD14⁺ monocytes from PBMC samples derived from individuals with mild (WHO score of 1–3; $n = 7$ samples), moderate (WHO score of 4–5; $n = 4$) or severe (WHO score of 6–7; $n = 6$) COVID-19 and healthy control individuals ($n = 6$; reanalyzed from ref. 29) determined using a two-sided Wilcoxon rank-sum test (FDR ≤ 0.01 and $\log_2(\text{fold change}) \geq 0.58$). **f**, Imputed GeneScores of *IL15*, *CD83*, *CXCL16* and *TNF* in CD14⁺ monocytes grouped according to COVID-19 severity as in **e**. Data are displayed as violin plots with overlaying box and whisker plots showing the median and 25th and 75th percentiles and two whiskers at 1.5 \times IQR. **g**, Differentially accessible genes (FDR ≤ 0.01 and $\log_2(\text{fold change}) \geq 0.58$) in CD14⁺ monocytes from individuals with mild COVID-19 compared to healthy control individuals, as in **e**, visualized as a volcano plot showing $-\log_{10}(\text{FDR})$ and $\log_2(\text{fold change})$ values (left) and the corresponding enriched Hallmark terms for the 789 genes with increased accessibility in mild COVID-19 CD14⁺ monocytes compared to healthy control monocytes displayed as dot plots showing gene counts and adjusted P values per term (right). **h**, Secretion of TNF in hDC1s stimulated with IFN α and/or CD40 antibody for 18 h. Data are mean \pm s.e.m. from six donors. Statistical significance for differences between conditions was assessed by one-way ANOVA, and adjusted P values are indicated.

secreted TNF in response to IFN α when aided by CD40 triggering, but not after treatment with IFN α alone (Fig. 4h). These observations indicated that APCs from individuals with mild, but not severe,

COVID-19 had increased chromatin accessibility and transcription of genes requiring the synergy between IFN α/β and CD40 described in the mouse experiments.



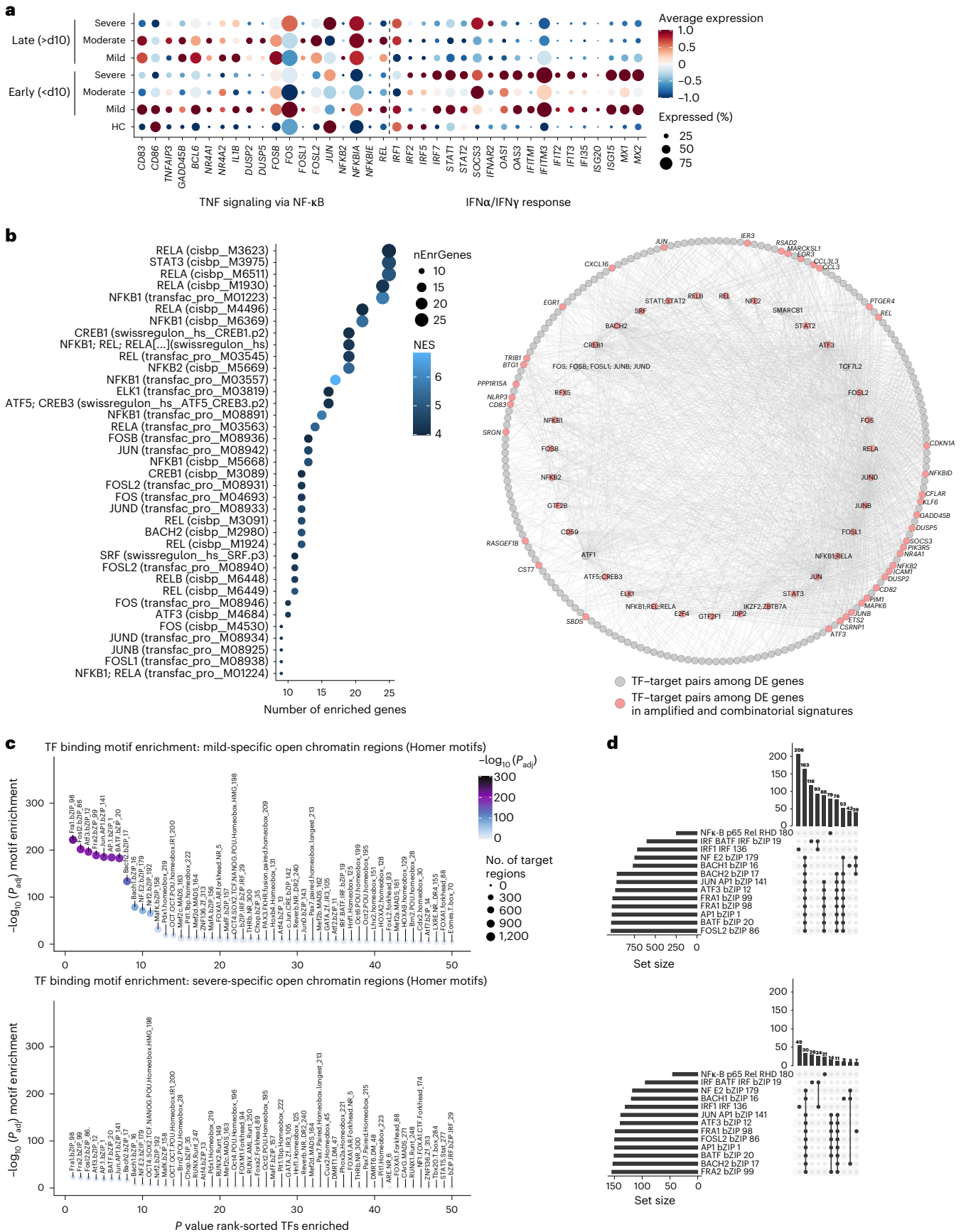


Fig. 5 | Enrichment of NF- κ B- and FOS-dependent transcriptional responses in APCs from individuals with mild, but not severe, COVID-19. **a**, Differentially expressed genes between disease severities and stages in CD14⁺ monocytes representing the significantly enriched Hallmark terms ‘IFN γ response’, ‘IFN α response’ and ‘TNF signaling via NF- κ B’, displayed as dot plots. **b**, RcisTarget transcription factor binding motif enrichment based on differentially expressed genes (two-tailed Wilcoxon rank-sum test, minimum percentage = 0.1, \log_2 (fold change) > 0.2) in CD14⁺ monocytes from individuals with mild compared to severe COVID-19, as in Fig. 4a. Data are visualized as a dot plot (left) showing the number of enriched genes and the normalized enrichment score per motif. The inner circle (right) shows the enriched transcription factors for all differentially expressed (DE) genes, and the outer circle shows the respective target genes responsible

for their enrichments. Transcription factors enriched for the genes overlapping with the ‘amplified’ and ‘combinatorial’ gene signatures and the target genes are colored in red. NES, normalized enrichment score. **c**, Transcription factor binding motif enrichment based on significantly differentially accessible peaks in CD14⁺ monocytes from individuals with mild or severe COVID-19 compared to CD14⁺ monocytes from healthy control individuals. Data are based on scATAC-seq data²⁹ and are displayed as dot plots showing FDR-adjusted *P* values of the enrichments and the number of target regions per transcription factor binding motif. **d**, Target regions of the top 10 highest enriched transcription factor binding motifs and motifs corresponding to IRF1 and p65 (RELA), shown as UpSet plots comparing the number of target regions.

CD40 triggers NF- κ B and FOS-dependent transcription in mild COVID-19

To explore whether IFN α / β also affected the signaling cascade downstream of CD40 in human APCs, we subjected the differentially expressed genes that were significantly higher in CD14⁺ monocytes from individuals with mild COVID-19 than in CD14⁺ monocytes from individuals with severe COVID-19 to enrichment analyses using the Hallmark database³¹ and transcription factor binding motifs³². There was a significant enrichment of genes associated with the NF- κ B pathway, including *CD83*, *CD86*, *TNFAIP3*, *IL1B*, *DUSP2*, *NFKB2* and *REL* (Fig. 5a and Supplementary Table 5). We also observed preferential involvement of the NF- κ B family (NFKB1, RELA and RELB) and the FOS and JUN families (AP-1; Fig. 5b). Visualization of the links between predicted transcription factors and their target genes within the differentially expressed genes between mild and severe COVID-19 indicated a dense regulatory network controlled by NF- κ B, FOS and JUN transcription factors (Fig. 5b).

Similarly, transcription factor binding motif enrichment analyses in differentially accessible chromatin regions of CD14⁺ monocytes from individuals with mild or severe COVID-19 compared to those from healthy control individuals²⁹ predicted members of the FOS family as key regulators (Fig. 5c). The enrichment score and number of accessible target regions of the predicted transcription factors, including FRA1/FRA2, FOSL2 and JUN, were higher in CD14⁺ monocytes from individuals with mild COVID-19 than in CD14⁺ monocytes from individuals with severe COVID-19 (Fig. 5c,d). Furthermore, the top 10 predicted transcription factor binding motifs and motifs corresponding to IRF1 and p65 (RELA) revealed large and distinct sets of target regions for the identified key regulator families among more accessible chromatin regions in CD14⁺ monocytes from mild COVID-19 cases than those from healthy control individuals. There were also substantially lower numbers of target regions with increased accessibility in CD14⁺ monocytes from individuals with severe COVID-19 than in CD14⁺ monocytes from healthy control individuals (Fig. 5d). These findings suggest that the

amplified and combinatorial responses enriched in CD14⁺ monocytes in individuals with mild COVID-19 are regulated by signal integration through transcription factors of the NF- κ B, FOS and JUN families.

Mild COVID-19 is associated with ‘helped’ CD8⁺ T cells

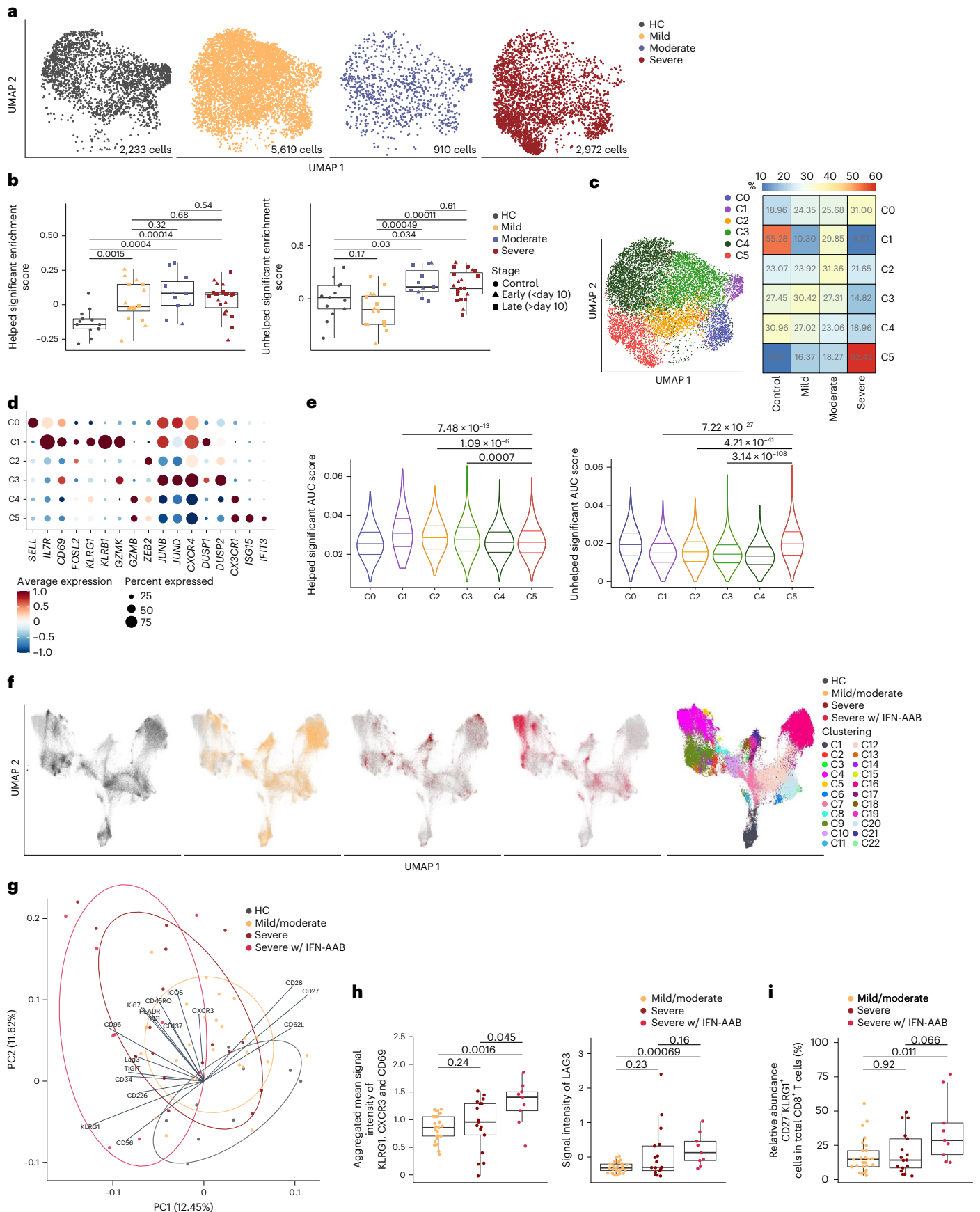
To test whether IFN α / β -dependent provision of T cell help to DCs and monocytes affects the CD8⁺ T cell response, we used the PBMC scRNA-seq data set from the cohort of individuals with COVID-19 and healthy control individuals defined above (Fig. 4b). We analyzed 11,734 CD8⁺ T cells using reference-based cell-type annotation and clustering (Methods) and compared their transcriptional profiles to published gene signatures that reflected CD8⁺ T cell priming in the presence (‘helped’) or absence (‘unhelped’) of CD4⁺ T cell help for DCs³³. CD8⁺ T cells from individuals with moderate and severe COVID-19 were enriched for ‘unhelped’ profiles (including *CD200*, *CD200R1*, *BTLA*, *ID3* and *PDCDI*) compared to CD8⁺ T cells from individuals with mild COVID-19 (Fig. 6a,b). Clustering analysis further indicated that individuals with mild and moderate COVID-19 were enriched in CD8⁺ T cell subsets with transcriptional profiles (*IL7R*, *TCF7*, *JUNB* and *JUND*) indicative of early effector or activated memory T cells^{34,35} (Fig. 6c,d and Supplementary Table 8, cluster 3). CD8⁺ T cells with characteristics of terminal differentiation (*CX3CR1* and *ISG15*, cluster 5) also dominated in individuals with severe COVID-19 (Fig. 6c,d) and had a reduction in ‘helped’ signatures (that is, *CD69*, *IL2RA* and *TNF*) and a corresponding gain in the ‘unhelped’ signature (that is, *IL6R*, *CD9*, *ISG15* and *PDCDI*) (Fig. 6e). We found comparable patterns in published scRNA-seq data from two other cohorts of individuals with COVID-19 (Extended Data Fig. 4a–c)^{36,37}. We used cytometry by time of flight (CyTOF) to examine protein expression in CD8⁺ T cells from blood samples of 9 healthy control individuals and individuals with COVID-19 with mild (WHO score of 2–3; *n* = 25) or severe (WHO score of 7–8; *n* = 18) disease and IFN-AAB⁺ individuals with severe disease (WHO score of 7–8; *n* = 9)²¹ collected 4 to 30 days after symptom onset (Supplementary Table 7). Dimensionality reduction using uniform manifold approximation and

Fig. 6 | Severe outcomes of COVID-19 are associated with ‘unhelped’ CD8⁺ T cells. **a**, UMAP visualization of scRNA-seq profiles of 11,734 CD8⁺ T cells from individuals with mild (WHO score of 3; *n* = 16), moderate (WHO score of 4–5; *n* = 11) or severe (WHO score of 7; *n* = 23) COVID-19 and healthy control individuals (*n* = 13; reanalyzed from ref. 25). Cells are split and colored according to disease severity. **b**, GSEA of ‘helped’ and ‘unhelped’ T cell signatures derived from published gene expression³³ profiles of mouse CD8⁺ T cells primed in the presence or absence of CD4⁺ T cells. Data are displayed as box and whisker plots showing the median and 25th and 75th percentiles and two whiskers at 1.5 \times IQR. Two-sided Wilcoxon rank-sum test *P* values are shown. **c**, UMAP of CD8⁺ T cells segregated into clusters 0–5 (left) and heat map of the respective proportionate cluster occupancy per disease severity (right) as in **a**. **d**, Expression of key genes associated with clusters 0–5 as in **c**. **e**, AUCell enrichment of genes derived from published gene expression³³ profiles of mouse CD8⁺ T cells primed in the presence or absence of CD4⁺ T cells as in **b**, grouped according to the clustering as in **c** and displayed as violin plots of area under the curve (AUC) scores. FDR-

corrected Dunn’s multiple comparison test *P* values are indicated. **f**, UMAP visualization of CD8⁺ T cells from whole-blood samples from healthy control individuals (*n* = 10) and individuals with COVID-19 (mild, *n* = 22; severe, *n* = 21; severe with IFN-AAB, *n* = 9) analyzed by CyTOF. The rightmost plot shows the UMAP colored according to FlowSOM clustering, while the four plots on the left show the distribution of events across the groups. **g**, PCA analysis plot showing average PC1 and PC2 values for all the events per individual as in **f**, colored according to the sample group. Ellipses show an estimated region of group accumulation, arrows represent correlation of the respective marker with either of the PC axes, and arrow length represents correlation strength. **h**, Mean scaled signal intensities for KLRG1, CXCR3 and CD69 (left) and LAG3 (right) displayed as box and whisker plots showing the median and 25th and 75th percentiles and two whiskers at 1.5 \times IQR. **i**, Relative abundance of CD27⁺ KLRG1⁺ cells in the total CD8⁺ T cell fraction displayed as box and whisker plots showing the median and the 25th and 75th percentiles and two whiskers at 1.5 \times IQR. Statistics in **h** and **i** show two-sided Benjamini–Hochberg-corrected pairwise Wilcoxon *P* values.

projection (UMAP) and clustering with the FlowSOM algorithm indicated differences in the composition of CD8⁺ T cells between individuals with COVID-19 with different disease severity (Fig. 6f). Individuals with

mild COVID-19 had increased proportions of CD27⁺CD8⁺ T cells with memory potential⁶ (Fig. 6f and Extended Data Fig. 4d,e, clusters 17, 19 and 21), while individuals with severe COVID-19 had greater proportions



of CD27⁺ KLRG1⁺ CD8⁺ T cells (clusters 3 and 8) than healthy individuals or individuals with mild disease (Fig. 6f and Extended Data Fig. 4d,e). Principal component analysis (PCA) of CD8⁺ T cells from individuals with mild and severe COVID-19 identified the expression of CD27 and KLRG1 as distinct features of CD8⁺ T cells from individuals with mild and severe disease, respectively (Fig. 6g,i), and CD8⁺ T cells from individuals with severe disease were enriched for LAG3 (Fig. 6h), a molecule induced by priming with unhelped DCs³³. These findings indicate that severe outcomes of COVID-19 are associated with unhelped phenotypes of CD8⁺ T cells.

Discussion

Our findings uncovered an iterative consolidation process, in which innate stimuli, such as IFN α / β or TLR agonists, determined broad response options in APCs, and CD4⁺ T cells subsequently partitioned these into distinct sets of co-stimulatory molecules, cytokines and chemokines through CD40L. Together, these consecutive signals endowed APCs with optimal capacities to orchestrate effective antiviral CD8⁺ T cell responses in mouse HSV-1 infections and during community-acquired SARS-CoV-2 infections, where effective consolidation of IFN α / β and CD40 signals in APCs correlated with milder outcomes of COVID-19.

The conditioning of APCs by IFN α / β to become receptive to T cell help involved increased expression of MHC class II and distinct changes in how the APCs responded to CD40 stimulation. The changes in CD40 responsiveness were not just a function of increased expression of CD40 alone⁸, as spontaneously matured CD40^{hi} DCs in mice and CD40^{hi} APCs in individuals with severe COVID-19 were unable to engage ‘helper’-dependent programs. Instead, the capacity to receive help depended on additional changes in the signaling cascade downstream of CD40. These endowed APCs with the capacity to rapidly engage a network of transcription factors, including p65, IRF1 and FOS, and likely others, such as JUN, to select a distinct group of genes that provide the DCs with optimal capacities to prime CD8⁺ T cells responding to antigen. Some of the transcription factors were directly regulated by IFN α / β and CD40 stimulation, suggesting that conditioning also enhanced the availability of relevant transcription factors. These responses were not exclusive to the cooperation between IFN α / β and CD40, as similar patterns of CD40-dependent calibration also occurred in DCs stimulated through different TLRs. Together with increased chromatin accessibility at binding sites for the above-mentioned transcription factors in promoter regions of key genes regulated through IFN α / β and CD40, our study revealed a multitude of transcriptional and post-translational changes as a functional basis for how innate cues condition APCs to become receptive to T cell help, thus enabling CD4⁺ T cells to calibrate APCs for optimal stimulation of CD8⁺ T cell responses.

We have investigated the relevance of these findings for antiviral CD8⁺ T cell immunity in a mouse model of HSV-1 skin infection and showed that optimal HSV-specific CD8⁺ T cell responses depended on contextual cues that require IFN α / β and NF- κ B signal integration by DCs. Notably, we translated these experimental insights to individuals with SARS-CoV-2 infection and demonstrated that the consecutive activation of APCs by IFN α / β and CD4⁺ T cells played an important role in regulating how APCs orchestrate CD8⁺ T cell responses during COVID-19. This interpretation not only helps align a number of currently unlinked findings in COVID-19, such as an association of milder disease with effective provision of CXCL16 (ref. 20) and CCL5 (ref. 19), high-avidity CD4⁺ T cells¹⁶ and effective CD8⁺ T cell responses¹⁸, but also raises the prospect of ‘unhelped’ APCs launching too many terminally differentiated CD8⁺ T cells that contribute to immunopathology in individuals with severe COVID-19. It is important to acknowledge limitations around our findings in individuals with COVID-19. Our study cannot discern if the observed failures in signal integration by APCs and preponderance of terminally differentiated CD8⁺ T cells are

a ‘cause’ or ‘effect’ of severe COVID-19 or are more likely a complex combination of both. Moreover, it is possible that interindividual differences in T cell antigen receptor epitopes, precursor frequencies of antigen-specific CD8⁺ T cells and a great number of many other covariates (that is, age, gender and comorbidities) influence the interaction between APCs and CD8⁺ T cells in individuals with COVID-19. However, having validated our findings across multiple unrelated clinical data sets, it is unlikely that our findings simply represent the confounding effects of any one of these covariates. We likely also missed some of the more nuanced aspects of the interaction between APCs and naive CD8⁺ T cells that take place in lymph nodes before symptom onset, which are difficult to capture as the precise time point of infection is unknown in community-acquired infections, and lymph nodes are not as amenable as blood for routine sampling, especially in individuals with mild disease.

Collectively, our findings demonstrate the reliance of antiviral immunity on a step-wise, carefully orchestrated consolidation process, whereby APCs combine and integrate innate signals and, after selection by CD4⁺ T cells, produce a discrete set of co-stimulatory molecules and soluble mediators that adapt responding CD8⁺ T cells to the specific challenge. In showing how innate and adaptive signals cooperate to partition tailored responses from multiple broad and overlapping innate pathways and demonstrating functional relevance of these processes in mouse and human virus infections, our study provides critical new insights into how the host mounts effective antiviral immunity.

Online content

Any methods, additional references, Nature Portfolio reporting summaries, source data, extended data, supplementary information, acknowledgements, peer review information; details of author contributions and competing interests; and statements of data and code availability are available at <https://doi.org/10.1038/s41590-023-01517-x>.

References

1. Chow, A., Brown, B. D. & Merad, M. Studying the mononuclear phagocyte system in the molecular age. *Nat. Rev. Immunol.* **11**, 788–798 (2011).
2. Joffre, O. P., Segura, E., Savina, A. & Amigorena, S. Cross-presentation by dendritic cells. *Nat. Rev. Immunol.* **12**, 557–569 (2012).
3. Cabeza-Cabrero, M., Cardoso, A., Minutti, C. M., Pereira da Costa, M. & Reis e Sousa, C. Dendritic cells revisited. *Annu. Rev. Immunol.* **39**, 131–166 (2021).
4. Ardouin, L. et al. Broad and largely concordant molecular changes characterize tolerogenic and immunogenic dendritic cell maturation in thymus and periphery. *Immunity* **45**, 305–318 (2016).
5. Borst, J., Ahrends, T., Babala, N., Melief, C. J. M. & Kastenmuller, W. CD4⁺ T cell help in cancer immunology and immunotherapy. *Nat. Rev. Immunol.* **18**, 635–647 (2018).
6. Greyer, M. et al. T cell help amplifies innate signals in CD8⁺ DCs for optimal CD8⁺ T cell priming. *Cell Rep.* **14**, 586–597 (2016).
7. Schulz, O. et al. CD40 triggering of heterodimeric IL-12 p70 production by dendritic cells in vivo requires a microbial priming signal. *Immunity* **13**, 453–462 (2000).
8. Eickhoff, S. et al. Robust anti-viral immunity requires multiple distinct T cell-dendritic cell interactions. *Cell* **162**, 1322–1337 (2015).
9. Hor, J. L. et al. Spatiotemporally distinct interactions with dendritic cell subsets facilitates CD4⁺ and CD8⁺ T cell activation to localized viral infection. *Immunity* **43**, 554–565 (2015).
10. Rusinova, I. et al. Interferome v2.0: an updated database of annotated interferon-regulated genes. *Nucleic Acids Res.* **41**, D1040–D1046 (2013).

11. Yu, X. et al. Isotype switching converts anti-CD40 antagonism to agonism to elicit potent antitumor activity. *Cancer Cell* **37**, 850–866 (2020).
12. Schreck, R., Meier, B., Mannel, D. N., Droge, W. & Baeuerle, P. A. Dithiocarbamates as potent inhibitors of nuclear factor κ B activation in intact cells. *J. Exp. Med.* **175**, 1181–1194 (1992).
13. Lavoie, H., Gagnon, J. & Therrien, M. ERK signalling: a master regulator of cell behaviour, life and fate. *Nat. Rev. Mol. Cell Biol.* **21**, 607–632 (2020).
14. Kashiwada, M. et al. Tumor necrosis factor receptor-associated factor 6 (TRAF6) stimulates extracellular signal-regulated kinase (ERK) activity in CD40 signaling along a Ras-independent pathway. *J. Exp. Med.* **187**, 237–244 (1998).
15. Hadjadj, J. et al. Impaired type I interferon activity and inflammatory responses in severe COVID-19 patients. *Science* **369**, 718–724 (2020).
16. Bacher, P. et al. Low-avidity CD4⁺ T cell responses to SARS-CoV-2 in unexposed individuals and humans with severe COVID-19. *Immunity* **53**, 1258–1271 (2020).
17. Schultze, J. L. & Aschenbrenner, A. C. COVID-19 and the human innate immune system. *Cell* **184**, 1671–1692 (2021).
18. Sette, A. & Crotty, S. Adaptive immunity to SARS-CoV-2 and COVID-19. *Cell* **184**, 861–880 (2021).
19. Galani, I. E. et al. Untuned antiviral immunity in COVID-19 revealed by temporal type I/III interferon patterns and flu comparison. *Nat. Immunol.* **22**, 32–40 (2021).
20. Pairo-Castineira, E. et al. Genetic mechanisms of critical illness in COVID-19. *Nature* **591**, 92–98 (2021).
21. Georg, P. et al. Complement activation induces excessive T cell cytotoxicity in severe COVID-19. *Cell* **185**, 493–512 (2022).
22. Akbil, B. et al. Early and rapid identification of COVID-19 patients with neutralizing type I interferon auto-antibodies. *J. Clin. Immunol.* **42**, 1111–1129 (2022).
23. Bedoui, S., Heath, W. R. & Mueller, S. N. CD4⁺ T-cell help amplifies innate signals for primary CD8⁺ T-cell immunity. *Immunol. Rev.* **272**, 52–64 (2016).
24. Wu, R. & Murphy, K. M. DCs at the center of help: origins and evolution of the three-cell-type hypothesis. *J. Exp. Med.* **219**, e20211519 (2022).
25. Schulte-Schrepping, J. et al. Severe COVID-19 is marked by a dysregulated myeloid cell compartment. *Cell* **182**, 1419–1440 (2020).
26. Arunachalam, P. S. et al. Systems biological assessment of immunity to mild versus severe COVID-19 infection in humans. *Science* **369**, 1210–1220 (2020).
27. Su, Y. et al. Multi-omics resolves a sharp disease-state shift between mild and moderate COVID-19. *Cell* **183**, 1479–1495 (2020).
28. van der Wijst, M. G. P. et al. Type I interferon autoantibodies are associated with systemic immune alterations in patients with COVID-19. *Sci. Transl. Med.* **13**, eabh2624 (2021).
29. Wilk, A. J. et al. Multi-omic profiling reveals widespread dysregulation of innate immunity and hematopoiesis in COVID-19. *J. Exp. Med.* **218**, e20210582 (2021).
30. Pearson, F. E. et al. Human CLEC9A antibodies deliver Wilms' tumor 1 (WT1) antigen to CD141⁺ dendritic cells to activate naive and memory WT1-specific CD8⁺ T cells. *Clin. Transl. Immunol.* **9**, e1141 (2020).
31. Liberzon, A. et al. The Molecular Signatures Database (MSigDB) Hallmark gene set collection. *Cell Syst.* **1**, 417–425 (2015).
32. Aibar, S. et al. SCENIC: single-cell regulatory network inference and clustering. *Nat. Methods* **14**, 1083–1086 (2017).
33. Ahrends, T. et al. CD4⁺ T cell help confers a cytotoxic T cell effector program including coinhibitory receptor downregulation and increased tissue invasiveness. *Immunity* **47**, 848–861 (2017).
34. Kaech, S. M. & Wherry, E. J. Heterogeneity and cell-fate decisions in effector and memory CD8⁺ T cell differentiation during viral infection. *Immunity* **27**, 393–405 (2007).
35. Pipkin, M. E. Runx proteins and transcriptional mechanisms that govern memory CD8 T cell development. *Immunol. Rev.* **300**, 100–124 (2021).
36. Bernardes, J. P. et al. Longitudinal multi-omics analyses identify responses of megakaryocytes, erythroid cells, and plasmablasts as hallmarks of severe COVID-19. *Immunity* **53**, 1296–1314 (2020).
37. Chua, R. L. et al. COVID-19 severity correlates with airway epithelium-immune cell interactions identified by single-cell analysis. *Nat. Biotechnol.* **38**, 970–979 (2020).

Publisher's note Springer Nature remains neutral with regard to jurisdictional claims in published maps and institutional affiliations.

Springer Nature or its licensor (e.g. a society or other partner) holds exclusive rights to this article under a publishing agreement with the author(s) or other rightsholder(s); author self-archiving of the accepted manuscript version of this article is solely governed by the terms of such publishing agreement and applicable law.

© The Author(s), under exclusive licence to Springer Nature America, Inc. 2023

¹Department of Microbiology and Immunology at the Doherty Institute for Infection and Immunity, The University of Melbourne, Melbourne, Victoria, Australia. ²Life and Medical Sciences (LIMES) Institute, University of Bonn, Bonn, Germany. ³Systems Medicine, Deutsches Zentrum für Neurodegenerative Erkrankungen (DZNE), Bonn, Germany. ⁴Translational Immunology, Berlin Institute of Health (BIH) & Charité University Medicine, Berlin, Germany. ⁵Infectious Diseases and Respiratory Medicine, Charité, Universitätsmedizin Berlin, Berlin, Germany. ⁶Berlin Institute of Health at Charité, Universitätsmedizin Berlin, Core Unit Bioinformatics, Berlin, Germany. ⁷Institute of Innate Immunity, University of Bonn, Bonn, Germany. ⁸Sydney Cytometry Core Research Facility, Charles Perkins Centre, Centenary Institute and University of Sydney, Sydney, New South Wales, Australia. ⁹Centre for Innate Immunity and Infectious Diseases, Hudson Institute of Medical Research, Clayton, Victoria, Australia. ¹⁰Department of Molecular and Translational Science, Monash University, Clayton, Victoria, Australia. ¹¹Würzburg Institute of Systems Immunology, Max Planck Research Group, Julius-Maximilians-Universität Würzburg, Würzburg, Germany. ¹²Institute of Experimental Immunology, University of Bonn, Bonn, Germany. ¹³Mater Research Institute, The University of Queensland, Brisbane, Queensland, Australia. ¹⁴Department of Biochemistry, Biomedicine Discovery Institute, Monash University, Clayton, Victoria, Australia. ¹⁵PRECISE Platform for Single Cell Genomics and Epigenomics, DZNE and University of Bonn, Bonn, Germany. ¹⁶These authors contributed equally: Elise Gressier, Jonas Schulte-Schrepping. ¹⁷These authors jointly supervised this work: Susanne V. Schmidt, Sammy Bedoui.

✉ e-mail: elise.gressier07@gmail.com; sbedoui@unimelb.edu.au

Methods

Mice

C57BL/6, *Ccl5*^{-/-}, *Cxcr6*^{-/-}, *Ifnar2*^{-/-}, *Irf1*^{-/-} and CD45.1⁺ gBT-I mice were bred and maintained at the animal facility of the Department of Microbiology and Immunology, The University of Melbourne. All animal experiments were approved by The University of Melbourne Animal Ethics Committee.

Human samples

This study includes a subset of individuals enrolled between March 2020 and April 2021 in the Pa-COVID-19 study, a prospective observational cohort study assessing pathophysiology and clinical characteristics of individuals with COVID-19 at Charité Universitätsmedizin, Berlin³⁸. The study was approved by the Institutional Review board of Charité (EA2/066/20). Written informed consent was provided by all individuals or legal representatives for participation in the study. Specifics about the participants per application (flow cytometry, CyTOF and scRNA-seq), including COVID-19 status, time point of sampling after onset of symptoms, sex, age and outcome, are listed in Supplementary Table 7 and are described elsewhere^{21,22}. Human umbilical cord blood was obtained with written informed consent from the Queensland Cord Blood Bank and approval from the Mater Human Research Ethics Committee (HREC13/MHS/86).

In vitro generation of BMDCs

Single-cell suspensions from mouse bone marrow were cultured with FLT3L to generate BMDCs⁶. Red blood cells were removed using 1 ml of red blood cell lysis buffer (Sigma-Aldrich) per mouse for 90 s. Cells were cultured at 1.5×10^6 cells per ml in complete medium supplemented with 1.32 mM L-glutamine, 10% fetal calf serum, 90 μ M β -mercaptoethanol, 100 U ml⁻¹ penicillin, 0.2 g liter⁻¹ streptomycin and 150 ng ml⁻¹ FLT3L (BioXCell). Following 8 days of culture at 37 °C, cells were stained for 30 min on ice with CD45R/B220 (RA3-6B2), SIRP α (P84), CD11c (N418), CD11b (M1/70), I-A/E (M5114) and CD24 (M1/69) antibodies. cDC1 or CD8⁺ DC equivalents were identified by CD24^{high}SIRP α ^{low}CD11b^{low}CD45R/B220⁻ and were sorted using a FACS Aria III (BD Biosciences). Following sorting, BMDCs were washed and resuspended before stimulation. Stimulation was performed on bulk BMDCs or sorted BMDCs with IFN α (PBL; 1,000 U ml⁻¹), IFN β (R&D Systems; 1 μ g ml⁻¹), LPS (Sigma-Aldrich; 10 μ g ml⁻¹), CpG (1668, GeneWorks; 1.6 nmol ml⁻¹) or poly(I:C) (InvivoGen; 10 μ g ml⁻¹) in the presence or absence of monoclonal antibody to CD40 (CD40 Ab; FGK45.5, Miltenyi Biotec; 10 μ g ml⁻¹). Cells and supernatants were collected at different time points thereafter. Pharmacological inhibition of NF- κ B and ERK pathways was achieved with 1 h pretreatment using PDTC (ab141406, 10 μ M) and nimbolide (ab142138, 10 μ M), respectively.

Cytokine and chemokine determination

Supernatants were subjected to BD Cytometric Bead Array measurement of CCL4 (limit of detection of 4.88 pg ml⁻¹), CCL5 (limit of detection of 1.22 or 4.88 pg ml⁻¹) and TNF- α (limit of detection of 39.07 or 9.7 pg ml⁻¹), according to the manufacturer's instructions. Samples were assessed using an LSRFortessa and FACS Diva software 6.1.3, and all concentrations were determined relative to a standard curve.

Real-time PCR

Cells were resuspended in TRIzol (Life Technologies), and mRNA was extracted using a Direct-zol RNA MicroPrep kit (Zymo Research) following the manufacturer's instructions. cDNA was synthesized with an Omniscript RT kit for reverse transcription (Qiagen) using oligo(dT) primers (Promega) and RNaseOUT recombinant ribonuclease inhibitor (Thermo Fisher Scientific). Real-time PCR was performed with Taqman Universal PCR master mix (Life Technologies) with primers/probes for 18S (Mm03928990_g1), *B2m* (Mm00437762_m1), *Ccl4* (Mm00443111_m1), *Ccl5* (Mm01302427_m1), *Cd83* (Mm00486868_m1), *Cxcl16*

(Mm00469712_m1), *Gapdh* (Mm99999915_g1), *Hprt* (Mm00446968_m1), *Il15* (Mm00434210_m1), *Il15ra* (Mm04336046_m1), *Il27* (Mm00461162_m1), *Irf1* (Mm01288580_m1), *Nfkb2* (Mm00479807_m1), *Rela* (Mm00501346_m1), *Relb* (Mm00485664_m1), *Tnf* (Mm00443258_m1) and *Traf6* (Mm00493836_m1).

RNA-seq and data analysis

Gene expression changes were investigated using RNA-seq. Up to 100 ng of total RNA was used for library preparation, according to the manufacturer's protocol, and was either sequenced in a 125-base pair (bp) paired-end run on a HiSeq HT sequencer (Illumina) or in a 50-bp single-read QuantSeq 3'-mRNA (Lexogen) run. Reads were aligned against the mouse genome mm10 by STAR v2.5.3a. Gene quantification was performed via the E/M algorithm in PartekFlow (v8.0.19.0707) and normalized as CPM. Genes with a mean expression of ≤ 1 CPM under all conditions were excluded from further analysis, resulting in 10,222 present genes for ANOVA in the Partek Genomics Suite (PGS, v7.18.0402). Genes with a fold change of 1.5 and an FDR-adjusted *P* value of ≤ 0.05 were defined as differentially expressed between two tested conditions. GO enrichment for the modules was performed using DAVID³⁹ with the GOTERM_BP_DIRECT annotation. GO terms were filtered by unadjusted *P* ≤ 0.05 and visualized using ggplot2. Biological interpretation of differentially expressed genes was performed with the following tools. Gene set enrichment analysis was performed using the GSEA application (v4.0.3) and the Hallmark gene set published by the Broad Institute. Enrichments were plotted using ggplot2 (v3.3.3)⁴⁰. Cytoscape was used to visualize enriched GO terms as a network with the two plugins BiNGO (v3.0.3) and EnrichmentMap (v3.2.1). WordCloud plugin (v3.1.3) was used to visualize the most frequent annotation associated within a cluster of GO terms. All present genes were used as input for a WGCNA, performed using the WGCNA R package (v1.70-3), to identify correlations of gene expression within the data set in an unbiased approach. The β -value was set at 23. For the module dissimilarity, a threshold of 0.42 was chosen, and the minimal cluster size was set to 30 genes. The prediction of transcription factor binding motifs was performed using the Cytoscape plugin iRegulon (v1.3) with a minimum normalized enrichment score of 3 and a maximum FDR on motif similarity of 0.001. All potential transcription factors annotated to the enriched binding motifs were used in the Venn diagram to illustrate their overlaps.

CUT&Tag and analysis

The CUT&Tag experiments were performed as previously described⁴¹ with a hyperactive in situ ChIP library prep kit purchased from Epiccypher (CUTANA CUT&Tag Assays) following the manufacturer's recommendations. A minimum of 1×10^5 stimulated BMDCs were bound to activated concanavalin A-coated magnetic beads and were subjected to immunoprecipitation with 0.5 μ g of primary antibody (anti-IRF1, D5E4, Cell Signaling Technology; rabbit anti-mouse IgG control). Immunoprecipitated DNA was amplified with high-fidelity 2 \times PCR mix (Epiccypher) using universal barcodes i5 and uniquely barcoded i7 primers and 21 cycles. PCR products were purified with AMPure XP beads and eluted in water. Libraries were sequenced on an Illumina NextSeq platform, and 150-bp paired-end reads were generated. Fastq reads for each sample were aligned to the mm39 reference genome using bwa (v0.7.17). PCR duplicates were removed using picard tools' MarkDuplicates (v2.25.0), and peaks were called using macs2 (v2.2.7.1) with the '-nomodel' parameter. To establish consensus peaks between all conditions, peak sets were merged using homer's mergePeaks (v4.11.1), and reads in consensus peaks were counted for each replicate using subread's featureCounts (v2.0.0). PCA plots were generated using R (v4.1) and the prcomp function. Differentially occupied peaks were established using the limma package (v3.46.0) and its voom, lmFit and eBayes functions. Motif occupancy at peaks was established with homer and the findMotifsGenome function (v4.11.1).

Immunoblotting

BMDCs were lysed in resuspension with RIPA buffer containing 50 mM Tris-HCl (pH 8), 150 mM sodium chloride, 1% NP-40, 0.5% sodium deoxycholate and 0.1% SDS (Sigma-Aldrich) supplemented with PhosSTOP phosphatase inhibitor cocktail tablets (Roche) and cComplete protease inhibitor cocktail tablets (Roche). Cell lysates were rotated at 4 °C for 30 min and clarified at 4 °C at 13,000g for 10 min. Proteins were denatured for 5 min at 90 °C with sample buffer containing 350 mM Tris-HCl (pH 6.8–5), 5% β -mercaptoethanol, 10% SDS, 36% glycerol and 0.0012% bromophenol blue. Proteins were then separated using NuPAGE 4–12% Bis-Tris gels (Thermo Fisher Scientific). Proteins were transferred onto nitrocellulose membranes (Bio-Rad) and blocked for 30 min with either 5% milk or 5% bovine serum albumin (BSA; for phosphorylated proteins) in PBS or TBS (for phosphorylated proteins) with 0.1% Tween 20. The following primary antibodies were used: rabbit anti-NF- κ B p65 (D14E12), mouse anti-phospho S536 NF- κ B p65 (7F1), rabbit anti-I κ B α (44D4) and rabbit anti- β -actin (13E5), all purchased from Cell Signaling Technology. Membranes were incubated with horseradish peroxidase-conjugated secondary antibodies goat anti-rabbit IgG and horse anti-mouse IgG (Cell Signaling Technology) and subsequently with a Novex ECL chemiluminescent substrate reagent kit before imaging. Quantitative analysis of the signal intensity was performed using ImageJ software.

PhosFlow cytometry

Following in vitro stimulation of BMDCs, 100 μ l of warm PhosFlow Lyse/Fix Buffer (BD Biosciences) was directly added to the samples and incubated for 10 min at 37 °C. Samples were then resuspended in PhosFlow Perm Buffer III (BD Biosciences) and incubated for 30 min on ice. After being washed twice, samples were stained for 1 h at room temperature with the antibodies described above supplemented with antibody to phospho-P44/42 MAPK (ERK1/ERK2; Thr 202/Tyr 204; 197G2; Cell Signaling Technology) and phospho-p38 MAPK (Thr 180/Tyr 182; 4NIT4KK; Thermo Fisher Scientific). A Biosciences Cytek Aurora was used for the measurement of samples, and FlowJo software (TreeStar) was used for analysis.

CRISPR–Cas9 gene editing

Freshly isolated bone marrow precursors were edited via electroporation before culture with FLT3L, as described previously⁴². In brief, per 10×10^6 mouse bone marrow precursors to be electroporated, 61 pmol of Cas9 nuclease (IDT) and 300 pmol of sgRNA (Synthego) were combined and incubated for 10 min at room temperature, generating Cas9–sgRNA ribonucleoprotein complex. Bone marrow precursors (10×10^6) were then washed with $1 \times$ PBS twice and resuspended in 20 μ l of P3 buffer (Lonza) combined with the Cas9–sgRNA complex and electroporated using 4D-Nucleofector (Lonza) using the pulse code CM-137. Prewarmed medium was immediately added in electroporation wells to allow cells to recover for 10 min at 37 °C. Cells were subsequently cultured for 8 days in complete medium supplemented with FLT3L, as described above. sgRNA sequences used were *Fos* (UAGUGCCAAC-UUUAUCCCCA) and *NTC* (GCACUACCAGAGCUAACUCA).

Virus infection and viral titers

HSV-1 KOS was grown using Vero cells (CSL). Mice were epicutaneously infected with 10^6 plaque-forming units of HSV-1, as previously described⁶.

Flow cytometry analysis of in vivo HSV-1 responses

Endogenous HSV-specific CD8⁺ T cells were analyzed using H-2K^b-restricted gB_{498–505}-specific tetramers, as previously described⁶. In some experiments, *Ccl5*^{−/−} and wild-type mice were transferred with 50,000 naive HSV-specific CD8⁺ T cells (gBT-I cells) before infection, and their expansion was measured 10 days later in the spleen, as described previously⁶. IFN γ production in gB_{498–505}-specific CD8⁺

T cells was measured after restimulation for 5 h ex vivo in the presence of brefeldin A. Single-cell suspensions were stained with antibodies to CD16/CD32 (2.4G2, Fc block), CD8 (53-6.7), CD44 (IM7), CD45.2 (104) and CD3 (145-2C11) and, when necessary, with either CD45.1 monoclonal antibody (A20) or tetramer staining. After fixation and permeabilization with BD Cytofix/Cytoperm (BD Biosciences), cells were stained for 20 min at room temperature with antibodies to IFN γ (XMG1.2) in BD Perm/Wash buffer (BD Biosciences) before analysis on a flow cytometer. Dead cells were excluded by using a LIVE/DEAD fixable dead cell stain kit (Thermo Fisher Scientific). A BD LSRFortessa and a FACS Diva or Biosciences Cytek Aurora and SpectroFlo were used for measurement of samples, and FlowJo software (TreeStar) was used for analysis. In some experiments, CD8⁺ DCs from wild-type versus *Irfnar2*^{−/−} mice were analyzed in the brachial lymph node 2 days after HSV-1 skin infection, as previously described⁶. Cells were stained with antibodies to CD11c (N418), CD8 (53-6.7), CD3 (145-2C11, BD Biosciences), CD19 (1D3), NK1.1 (PK136) and IA/E (2G9), and CD8⁺ DCs were then processed on an analytic flow cytometer (LSRFortessa BD Biosciences).

BM chimeras

Mixed chimeras were generated as previously described⁶. C57BL/6 mice were lethally irradiated with 2×550 cGy and were reconstituted with a total of 5×10^6 bone marrow cells, previously depleted for T cells, from *Cxcr6*^{−/−} and wild-type mice in a 1:1 ratio.

scRNA-seq data generation and analysis

scRNA-seq data of PBMCs from individuals with COVID-19 and healthy control individuals collected from April to July 2020 in Bonn, Germany, were used, as previously reported²⁶. Samples were classified by disease severity according to the WHO ordinal scale (WHO score of 3, mild; WHO score of 4–5, moderate; WHO score of 7, severe) and by the time after onset of first symptoms (early: days 0–10, late: >day 11) at the date of sampling. Details about sample procurement and processing, sequencing and data analysis have been previously described²⁵, and an extensive description of the protocol has also been published⁴³. Processed and annotated scRNA-seq data²⁵ were used as published previously and are available at https://beta.fastgenomics.org/p/schulte-schrepping_covid19. The data were imported into R version 4.0.3 and were mainly analyzed using Seurat v3.9.9.

Subset analysis of DCs and monocytes

PBMCs were subjected to Seurat v4 reference mapping following the developer vignette (satijalab.org/seurat/articles/multimodal_reference_mapping.html) using the multimodal PBMC reference data set⁴⁴. Only those cells classified as DC or monocyte subsets were selected to remove any possible cellular contaminations in the data set. Subsequently, the remaining 37,100 cells were reclustered after scaling and regressing for unique molecular identifier (UMI) count per cell, identification of variable genes and PCA in this cellular subspace using the Louvain algorithm with a resolution of 0.2 based on the first 10 PCs. Clusters representing DCs or classical CD14⁺ monocytes were then subsetted, respectively, and the resulting 31,736 monocytes and 722 DCs were analyzed in detail, including rescaling, identification of variable genes, PCA and subsequent UMAP based on the first 10 PCs. Disease severity-specific marker gene analysis was performed using the Wilcoxon rank-sum test with the following cutoffs: genes had to be expressed in more than 10% of the cells of the respective condition and exceed a logarithmic fold change cutoff of at least 0.2. Before dot plot visualization and functional enrichment analyses, sets of differentially expressed genes were filtered for ribosomal protein-coding genes (*RPL/RPS*), mitochondrial genes (MT-) and hemoglobin genes (*HBA1*, *HBA2* and *HBB*). Hallmark enrichment analysis of differentially expressed gene sets was performed using the Hallmark v7.3 database and the enricher function implemented in the R package clusterProfiler v3.18.0 (ref. 45). Gene set enrichment analyses of

'CD40-unresponsive', 'amplified' and 'combinatorial' gene signatures in the differentially expressed genes in monocytes from individuals with mild COVID-19 compared to those from individuals with severe disease were performed using the *fgsea* package v1.16.0. Single-sample GSEA using the 'CD40-unresponsive', 'amplified' and 'combinatorial' signatures derived from the mouse bulk RNA-seq analysis of this study was performed using GSEA v1.38.2 (ref. 46). For this, aggregated expression values of all cells of each sample were calculated using the *AggregateExpression* function in Seurat and were used as input for the sample-specific analysis. Of note, the IFN α A response signature was intersected with the top 100 IFN-response genes derived from an integrated analysis of eight microarray data sets on IFN response of myeloid cells listed in the Interferome database (<http://www.interferome.org/>)⁴⁰ ranked by their combined \log_2 (fold change) values to reduce the signature to a length comparable to the amplified and combinatorial signatures. Transcription factor binding motif enrichment analysis based on the significantly differentially expressed genes in monocytes derived from individuals with mild COVID-19 compared to cells from individuals with severe disease and those differentially expressed genes that intersected with the 'amplified' and 'combinatorial' gene signatures was performed using *RcisTarget*³², the *hg38_refseq-r80_10kb_up_and_down_tss.mc9nr.feather* database and a normalized enrichment score threshold of 4. Enriched transcription factor binding motifs were filtered for the *transfac_pro*, *cisbp* and *swissregulon* databases and those motifs with high-confidence transcription factor annotation (TF_highConf). A network linking enriched target genes and predicted transcriptional regulators based on the *RcisTarget* transcription factor binding motif enrichment results was constructed and visualized in a circular layout using *Cytoscape* v3.7.1.

scRNA-seq analysis of CD14⁺ monocytes from individuals with IFN-AAB and corresponding healthy individuals

PBMC scRNA-seq data were produced from five control samples, five samples from individuals with moderate COVID-19, five samples from individuals with severe COVID-19 and seven samples from individuals with severe COVID-19 with IFN-AAB, which were tested for each individual in virus neutralization assays described in Akbil et al.²². On the day of the experiment, frozen live PBMCs were thawed in prewarmed medium (RPMI 1640 (Gibco), 2% fetal calf serum (Sigma) and 0.01% Pierce Universal Nuclease (Thermo Fisher)). The PBMCs were then labeled with 0.5 μ g of TotalSeq-C hashtag antibodies (Biolegend) in DPBS supplemented with 0.5% BSA and 2 mM EDTA for 30 min at 4 °C and washed at least three times with DPBS + 1% BSA. Subsequently, the PBMCs were counted, and up to seven different samples were pooled in equal proportions. The resulting cell pool was filtered through a 40- μ m mesh (Flowmi Cell Strainer, Merck) and super loaded with 50,000 cells per lane in the Chromium Controller for partitioning single cells into nanoliter-scale Gel Bead-In-Emulsions (GEMs). For reverse transcription, cDNA amplification and library construction of the gene expression libraries, the Chromium Next GEM Single Cell kit 5' v2 (10x Genomics) was used. The Chromium Single Cell 5' Feature Barcode Library kit (10x Genomics) was used for preparing additional hashtag libraries. All libraries were prepared according to the protocols provided by 10x Genomics, quantified by Qubit Flex fluorometer (Thermo Fisher) and quality checked using the 4150 TapeStation system. Sequencing was performed in paired-end mode (R1 26 cycles, R2 90 cycles) on a NovaSeq 6000 (Illumina) with a NovaSeq 6000 S2 reagent kit (100 cycles). After demultiplexing, raw sequencing data were processed with Cell Ranger v5 and aligned against the GRCh38 reference, including TotalSeq-C hashtag barcodes. scRNA-seq UMI count matrices were imported into R 4.0.3, and gene expression data analysis was performed using the R/Seurat package 3.9.9. Cells from pooled samples were demultiplexed using a combination of HTODemux implemented in Seurat and *vireo* (v0.5.6)⁴⁷ after scoring common variants from the 1000Genomes project with *cellsnr-lite* (v1.2.0)⁴⁸.

Events classified as 'negative' and 'doublet' by the HTODemux algorithm were assigned an ID via *vireo* classification. Subsequently, cells were filtered by number of features (over 200 and less than 5,000), percentage of mitochondrial genes (<10% mitochondrial UMIs) and number of counts per cell (<20,000) to exclude debris and doublets. Gene expression values were normalized by total UMI counts per cell, multiplied by 10,000 (TP10K) and log transformed by \log_{10} (TP10k + 1). For cell-type annotation, cells were subjected to Seurat v4 reference mapping following the developer vignette using the multimodal PBMC reference data set⁴⁴. Cells classified as CD14⁺ classical monocytes were selected and reclustered after scaling and identification of variable genes using *vst* and PCA using the Louvain algorithm with a resolution of 0.2 based on the first 10 PCs. A cluster characterized by the expression of T cell marker genes was removed to exclude potential T cell contamination in the CD14⁺ monocyte subset. Averaged gene expression values per sample of selected key genes were visualized as box plots across disease severity groups.

To increase the number of samples per severity group, scRNA-seq data of PBMCs from other COVID-19 cohorts produced using the same scRNA-seq protocol (10x Genomics, 5') by us²¹ and others^{27,28} were included in the analysis and processed as described above. The total number of samples combined in this analysis was 263. All samples were grouped according to their WHO ordinal scale classification into mild (WHO score of 1–3), moderate (WHO score of 4–5) and severe (WHO score of 6–8) COVID-19 disease. In addition, samples known to be derived from individuals with IFN-AAB were subgrouped accordingly. PBMC scRNA-seq data from Van der Wijst et al.²⁸ were downloaded and filtered for the earliest sample available per donor, resulting in 11 control samples and 35 samples from individuals with moderate COVID-19, 26 samples from individuals with severe COVID-19 and 4 samples from individuals with severe COVID-19 with IFN-AAB. PBMC scRNA-seq data from Su et al.²⁷ were downloaded and filtered for the earliest sample available per donor, resulting in 17 control samples and 69 samples from individuals with mild COVID-19, 45 samples from individuals with moderate COVID-19 and 15 samples from individuals with severe COVID-19. PBMC scRNA-seq data from Georg et al.²¹ included six control samples, five samples from individuals with mild COVID-19, two samples from individuals with moderate COVID-19 and six samples from individuals with severe COVID-19. Single-sample GSEA using the 'CD40-unresponsive', 'amplified' and 'combinatorial' signatures derived from the mouse bulk RNA-seq analysis of this study was performed using GSEA v1.38.2.

For validation, we additionally analyzed scRNA-seq data from DCs from PBMC data enriched for DCs as previously published²⁶. After downloading the respective data from the public domain, we selected those cells originally classified as monocytes and DCs and followed the same procedure of filtering the cells using the Seurat v4 reference mapping approach, as outlined above. Differential gene expression analyses and signature enrichment analyses of the 'CD40-unresponsive', 'amplified' and 'combinatorial' signatures were performed as described above.

Subset analysis of CD8⁺ T cells

For detailed analysis of the CD8⁺ T cell compartment, cells classified as T cells according to the original annotation provided were selected from the PBMC data set. These cells were subjected to Seurat v4 reference mapping following the developer vignette (satijalab.org/seurat/articles/multimodal_reference_mapping.html) using the multimodal PBMC reference data set⁴⁴. Only those cells classified as T cells were selected to remove any possible cellular contaminations in the T cell data set. Subsequently, the remaining 45,516 cells were reclustered after scaling, regressing for UMI count per cell, identification of variable genes and PCA in this cellular subspace using the Louvain algorithm with a resolution of 0.2 based on the first 10 PCs. Cluster 1, representing CD8⁺ T cells, was then subsetted, and the resulting 12,386 cells were analyzed in detail, including rescaling, identification of variable

genes, PCA and subsequent UMAP⁴⁹ based on the first 10 PCs. Ribosomal protein-coding genes (*RPL/RPS*), mitochondrial genes (MT-) and hemoglobin genes (*HBA1*, *HBA2* and *HBB*) were excluded from the set of variable features to remove potential sources of technical differences. Single-sample GSVA using the 'helped' and 'unhelped' T cell signatures derived from RNA-seq analysis of CD8⁺ T cells primed in the presence or absence of CD4⁺ T cell responses was performed using GSVA v1.38.2. For this, aggregated expression values of all CD8⁺ T cells of each sample were calculated using the `AggregateExpression` function in Seurat and were used as input for the sample-specific analysis. Clustering of the CD8⁺ T cells was performed using the Louvain algorithm with a resolution of 0.4 based on the first 10 PCs, and cells identified as $\gamma\delta$ T cells were removed. To investigate proportional cluster occupancy per disease severity, cell counts per condition were normalized before calculation of per-cluster percentages. Single-cell gene set enrichment analysis across cells of each CD8⁺ T cell subcluster using the 'helped' and 'unhelped' T cell signatures derived from RNA-seq analysis of CD8⁺ T cells primed in the presence or absence of CD4⁺ T cell responses was performed using AUCell v1.12.0 (ref. 32). For validation, we analyzed CD8⁺ T cells from two other data sets^{36,37}. After downloading the respective data from the public domain, we followed the same procedure of filtering the cells using the Seurat v4 reference mapping approach and performed signature enrichment analysis using the above-mentioned T cell signatures.

Analysis of scATAC-seq data

scATAC-seq data of PBMCs from individuals with COVID-19 and healthy individuals produced using a Chromium Next GEM Single Cell ATAC reagent kit version 1.1 (10x Genomics, PN-1000175) was used, as previously published²⁹. Processed and annotated scATAC-seq data from Wilk et al.²⁹ were downloaded from Gene Expression Omnibus (GEO) under accession number [GSE174072](https://www.ncbi.nlm.nih.gov/geo/query/acc.cgi?acc=GSE174072) and https://github.com/ajwilk/COVID_scMultiome and were imported to R version 4.1.0. After creation of Arrow files and a respective ArchRproject using the R package ArchR version 1.0.1 (ref. 50), the resulting single-cell data were filtered based on the published cell annotation and subsetted to CD14⁺ monocytes. Imputation weights on GeneScores were calculated using MAGIC⁵¹ implemented in ArchR's `addImputeWeights` function. Severity-specific accessible genes were identified using the Wilcoxon rank-sum test comparing gene scores of monocytes from individuals with mild COVID-19 to cells from control donors with the following cutoffs: $FDR \leq 0.05$ and $\log_2(\text{fold change}) \geq 0.58$. Hallmark enrichment analyses were performed using clusterProfiler version 4.0.5 and the Hallmark gene set v6.2. After generation of pseudo-bulk replicates across cells of each COVID-19 severity group, peaks were called using MACS3 (ref. 52) and annotated using ChIPseeker version 1.28.3 (ref. 53). Subsequently, transcription factor binding motifs were identified in the peak regions using the homer motif set. After calculation of severity-specific differentially accessible peak regions ($FDR \leq 0.01$ and $\log_2(\text{fold change}) \geq 2$) comparing chromatin profiles of monocytes from individuals with mild and severe COVID-19 to cells from control donors, motif enrichment analysis was performed using ArchR's `peakAnnoEnrichment` function.

CytoF data and analysis

For mass cytometry data from a publicly available publication²¹, please refer to the Methods part of the work for detailed descriptions of the cohort, data collection and analysis workflows. Here, CD8⁺ T cells were separately reanalyzed and pre-gated using OMIQ cloud-based cytometry analysis software, also in relation to the presence of IFN- γ ²². In addition to the steps described²¹, we performed a PCA using R (4.0.2), where principal components were first calculated for all the events, and averages of principal component values per individual were used in plotting. Figures were rendered with the help of the R package `ggfortify` and `function autoplot`, which allows plotting of eigenvectors of input variables when used on precalculated principal components.

An ellipse was calculated with `ggplot2` to visually estimate the localization of different groups. Marker intensity box plots show average z-score-normalized intensity signals for all the CD8⁺ T cells per individual. Z-score normalization was performed beforehand over all the immune cells acquired in CyTOF.

Flow cytometry analysis of monocytes and DCs in individuals with COVID-19

Fixed whole-blood samples from individuals with COVID-19 were collected, processed and stored, as previously described²⁵. The samples were subsequently thawed to room temperature, and erythrocytes were lysed with Thaw-Lysis buffer (Smart Buffer). After 5 min of treatment with 50 U ml⁻¹ Pierce Universal Nuclease for Cell Lysis (Thermo Scientific) and 20 min of blocking with 1 mg ml⁻¹ beriglobin (CSL Behring), the samples were stained for 30 min at 4 °C with antibodies to CD45 (HI30), CD11c (Bu15), CD14 (M ϕ P9), CD3 (UCHT1), CD19 (SJ25C1), CD40 (5C3), CD83 (HB15e), CD86 (IT2.2), HLA-DR (G46-6), CD16 (3G8), CD141 (1A4) and CD163 (GHI/61). A BD LSRFortessa was used for the measurement of samples, and FlowJo software (TreeStar) was used for analysis. Expression of CD45, CD3, CD19 and HLA-DR was used for granulocyte, T cell, B cell and natural killer cell exclusion, respectively. Monocytes were gated as CD14⁺CD11c⁺ and DCs as CD14⁺HLA-DR⁺ events.

In vitro generation of human CD34⁺ stem cell-derived cDC1s

Human umbilical cord blood was obtained with written informed consent from the Queensland Cord Blood Bank and approval from the Mater Human Research Ethics Committee (HREC13/MHS/86). cDC1s were differentiated in a 9- to 10-d culture of in vitro expanded cord blood CD34⁺ progenitors in 100 ng ml⁻¹ FLT3L (PeproTech), 100 ng ml⁻¹ stem cell factor (PeproTech), 2.5 ng ml⁻¹ IL-4 (Invitrogen) and 2.5 ng ml⁻¹ granulocyte-macrophage colony-stimulating factor (Invitrogen), as previously described³⁰, but with the addition of an irradiated OP9-DL1 stromal cell feeder layer to maximize cDC1 yields⁵⁴. CD141⁺CADM1⁺CLEC9A⁺ cDC1s were enriched to >80% purity by labeling with biotinylated antibodies to human CADM1 (CM004-6) or CD141 (M80) and anti-biotin microbeads, followed by positive selection on an LS column according to manufacturer's instructions (Miltenyi). Purified cDC1s were cultured at a density of 1×10^6 per ml in the presence of 1,000 U ml⁻¹ human IFN α 2a (PBL), 5 μ g ml⁻¹ CD40 agonistic antibody¹¹ (34G12-h2, a gift from M. Cragg at University of Southampton) or a combination. TNF- α was detected in the supernatant after 18 h using a LegendPlex kit (BioLegend) on a CytoFLEX-S (Beckman Coulter) flow cytometer.

Quantification and statistical analysis

Prism v8.4.3 (GraphPad Software) was used to assess statistical significance of non-RNA-seq data; z score = $(x - \text{mean})/s.d.$ The sample size (n), statistical significance and statistical tests are indicated in the legends. Data distribution was assumed to be normal, but this was not formally tested. Data collection and analysis were not performed blind to the conditions of the experiments and no formal randomization was used. No data points were excluded.

Reporting summary

Further information on research design is available in the Nature Portfolio Reporting Summary linked to this article.

Data availability

The RNA-seq data set generated in this study can be accessed via the GEO accession number [GSE171690](https://www.ncbi.nlm.nih.gov/geo/query/acc.cgi?acc=GSE171690).

Code availability

Code used for the analysis of scRNA-seq and scATAC-seq data is available at https://github.com/schultzelab/Gressier_2022. We also provide

the scRNA-seq data sets used in this study and the code to analyze the respective data sets via FASTGenomics (https://beta.fastgenomics.org/p/gressier_2022).

References

38. Kurth, F. et al. Studying the pathophysiology of coronavirus disease 2019: a protocol for the Berlin prospective COVID-19 patient cohort (Pa-COVID-19). *Infection* **48**, 619–626 (2020).
39. Huang da, W., Sherman, B. T. & Lempicki, R. A. Systematic and integrative analysis of large gene lists using DAVID bioinformatics resources. *Nat. Protoc.* **4**, 44–57 (2009).
40. Subramanian, A. et al. Gene set enrichment analysis: a knowledge-based approach for interpreting genome-wide expression profiles. *Proc. Natl Acad. Sci. USA* **102**, 15545–15550 (2005).
41. Kaya-Okur, H. S. et al. CUT&Tag for efficient epigenomic profiling of small samples and single cells. *Nat. Commun.* **10**, 1930 (2019).
42. Freund, E. C. et al. Efficient gene knockout in primary human and murine myeloid cells by non-viral delivery of CRISPR–Cas9. *J. Exp. Med.* **217**, e20191692 (2020).
43. De Domenico, E. et al. Optimized workflow for single-cell transcriptomics on infectious diseases including COVID-19. *STAR Protoc.* **1**, 100233 (2020).
44. Hao, Y. et al. Integrated analysis of multimodal single-cell data. *Cell* <https://doi.org/10.1016/j.cell.2021.04.048> (2021).
45. Wu, T. et al. clusterProfiler 4.0: a universal enrichment tool for interpreting omics data. *Innovation* **2**, 100141 (2021).
46. Hanzelmann, S., Castelo, R. & Guinney, J. GSEA: gene set variation analysis for microarray and RNA-seq data. *BMC Bioinformatics* **14**, 7 (2013).
47. Huang, Y., McCarthy, D. J. & Stegle, O. Vireo: Bayesian demultiplexing of pooled single-cell RNA-seq data without genotype reference. *Genome Biol.* **20**, 273 (2019).
48. Huang, X. & Huang, Y. Cellsnp-lite: an efficient tool for genotyping single cells. *Bioinformatics* **37**, 4569–4571 (2021).
49. McInnes, L., Healy, J. & Melville, J. UMAP: Uniform Manifold Approximation and Projection for dimension reduction. Preprint at <https://doi.org/10.48550/arXiv.1802.03426> (2018).
50. Granja, J. M. et al. ArchR is a scalable software package for integrative single-cell chromatin accessibility analysis. *Nat. Genet.* **53**, 403–411 (2021).
51. van Dijk, D. et al. Recovering gene interactions from single-cell data using data diffusion. *Cell* **174**, 716–729 (2018).
52. Zhang, Y. et al. Model-based analysis of ChIP-seq (MACS). *Genome Biol.* **9**, R137 (2008).
53. Yu, G., Wang, L. G. & He, Q. Y. ChIPseeker: an R/Bioconductor package for ChIP peak annotation, comparison and visualization. *Bioinformatics* **31**, 2382–2383 (2015).
54. Balan, S. et al. Large-scale human dendritic cell differentiation revealing notch-dependent lineage bifurcation and heterogeneity. *Cell Rep.* **24**, 1902–1915 (2018).

Acknowledgements

We thank L. Loyal, A. Thiel, C. Iwert, C. Meisel, R. Rudraraju and K. Subbarao for discussions, F. Koay and D. Godfrey for *Cxcr6*^{-/-} mice and M. Cragg for the human CD40 antibody. The technical expertise in breeding, maintaining and manipulating specific pathogen-free mice by the Doherty Bioresources facility is gratefully acknowledged. We also thank D. Kunkel and J. Keye from the BIH Flow and Mass Cytometry Core Facility for sample acquisition. We are grateful to

the Genomics platform at the Walter & Eliza Hall Institute for Medical Research in Melbourne. Our research is supported by the National Health and Medical Research Council of Australia (APP1124815, APP1071916, APP1103895 and APP1154540), the Sylvia & Charles Viertel Charitable Foundation, a 350th Anniversary Research Grant from Merck KgGA, The Advanced Genomic Collaboration and the International Research Training Group (IRTG2168) funded by the German Research Council and The University of Melbourne. B.S. received support from the European Union's Horizon 2020 research and innovation program (INSTRuCT, 860003) and the German Federal Ministry of Education and Research (BMBF) project RECAST (01K120337). A.H. is supported by the Jürgen Manchot Foundation. E.L. and S.V.S. were supported by the German Federal Ministry of Education and Research through the COVIMMUN project (grant 01K120343). Furthermore, E.L. received support by the Deutsche Forschungsgemeinschaft (DFG, German Research Foundation), grant 397484323, TRR259. We thank the NGS Core Facility of the University Hospital Bonn for library preparation and the generation of the sequencing data. We also would like to thank the German COVID-19 OMICS Initiative (DeCOI) for providing access to scRNA-seq data. J.L.S. was supported by the DFG (IRTG2168, INST 217/1011-1 and INST 217/1017-1, Excellence Cluster ImmunoSensation² (EXC2151/1) under project number 390873048) and SYSCID, receiving funding from the European Union's Horizon 2020 research and innovation program under grant agreement number 733100. We are indebted to the participants, their families and the hospital staff for support, without whom this study would not have been possible.

Author contributions

Conceptualization: S. Bedoui, E.G., J.S.-S. and S.V.S. Methodology: P.G.W., A.B., K.H., M.K., M. Clarke, T.H.O.N., P.S., K.W., C.V.L.O., B.O., C.v.d.S., Y.-C.E.C., K.J.R., T.M., M. Chopin, S. Brumhard, S.S.G., K.K. and S.L.L. Formal analysis: E.G., J.S.-S., A.O., J. Spitzer, L.J.G., P.J.H., L.P., T.K., T.A., F.K., J. Schroeder and B.S. Investigation: E.G., J.S.-S., P.G.W., A.B., M.G. and F.K. Writing, original draft: S. Bedoui and E.G. Writing, review and editing: S. Bedoui, E.G., J.S.-S., S.V.S., J.L.S., W.K., A.K., T.G., E.L., C.K. and L.E.S. Funding acquisition: S. Bedoui, T.G., E.L., J.L.S. and S.V.S.

Competing interests

The authors declare no competing interests.

Additional information

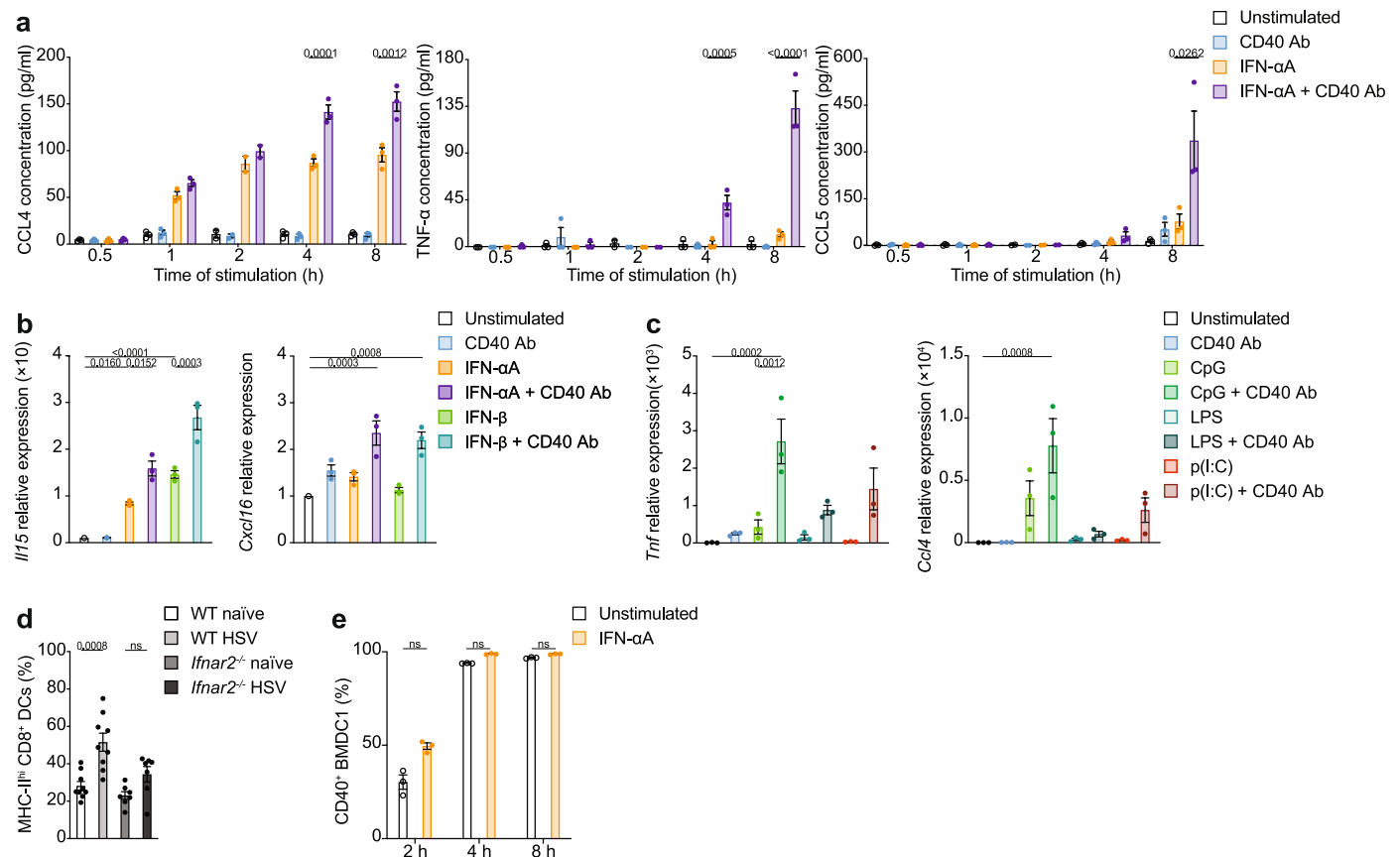
Extended data is available for this paper at <https://doi.org/10.1038/s41590-023-01517-x>.

Supplementary information The online version contains supplementary material available at <https://doi.org/10.1038/s41590-023-01517-x>.

Correspondence and requests for materials should be addressed to Elise Gressier or Sammy Bedoui.

Peer review information *Nature Immunology* thanks Teunis Geijtenbeek, and the other, anonymous, reviewer(s) for their contribution to the peer review of this work. Primary Handling Editor: Ioana Visan, in collaboration with the *Nature Immunology* team. Peer reviewer reports are available.

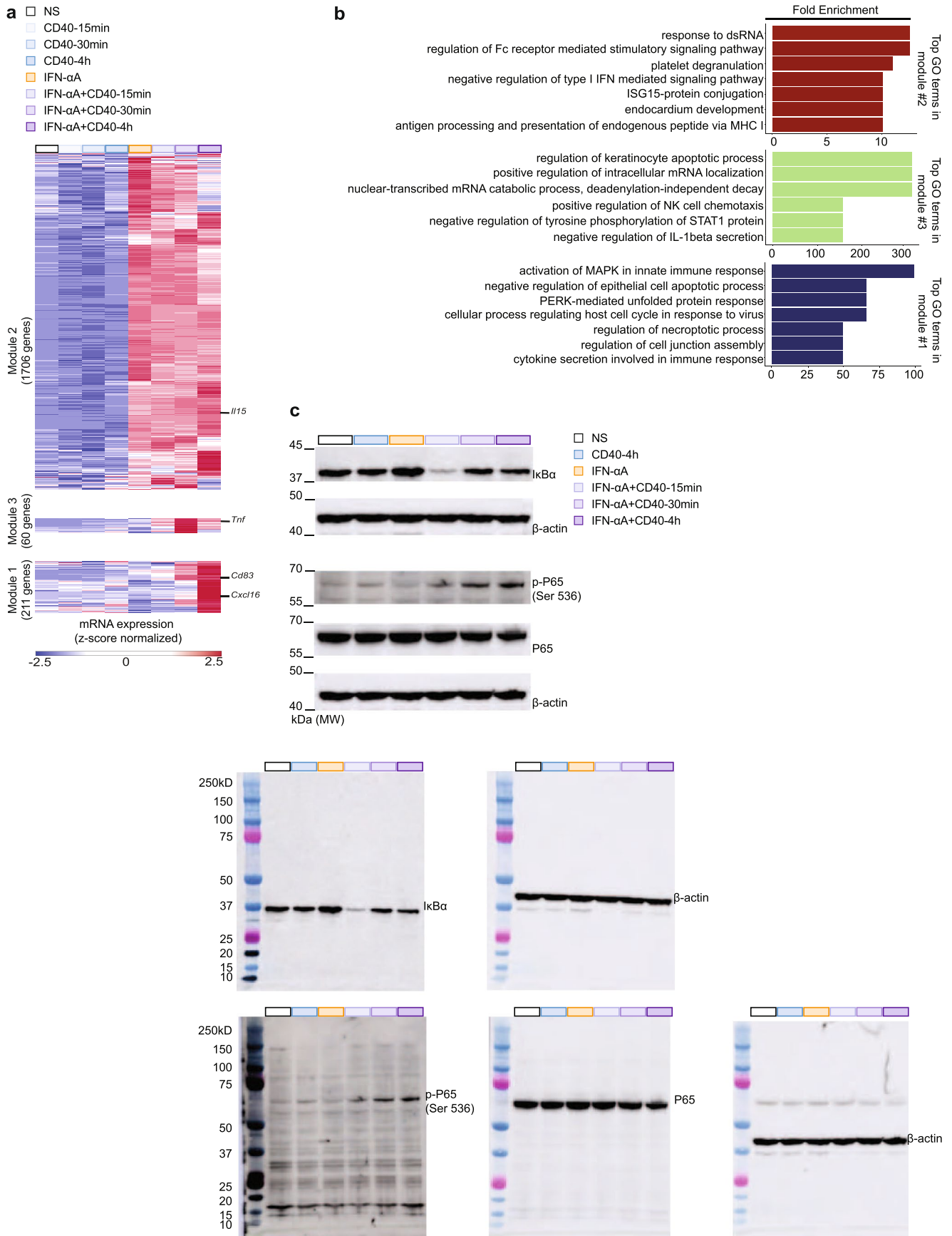
Reprints and permissions information is available at www.nature.com/reprints.

**Extended Data Fig. 1 | CD40 synergizes with varying inflammatory stimuli**

BMDC1. a, 'BMDC1-IFN- α A+CD40' increase secretion of CCL4, TNF- α and CCL5 (from left to right) over time compared to 'BMDC1-IFN- α A', 'BMDC1-CD40' and 'BMDC1-unstimulated'. Data are presented as mean \pm s.e.m pooled from 3 independent experiments. Adjusted p-value of statistically significant differences between conditions as assessed by one-way ANOVA indicated.

b, Changes in *Il15* and *Cxcl16* expression in 'BMDC1-IFN- α A+CD40' and 'BMDC1-IFN- β +CD40' compared to 'BMDC1-IFN- α A' or 'BMDC1-IFN- β ' respectively and to 'BMDC1-CD40' and 'BMDC1-unstimulated'. **c**, *Tnf* and *Ccl4* in expression in BMDC1s stimulated with LPS, CpG or poly(I:C) for 6 h with or without CD40 Ab for the last 30 min. **b-c**, Data are presented as mean \pm s.e.m pooled from

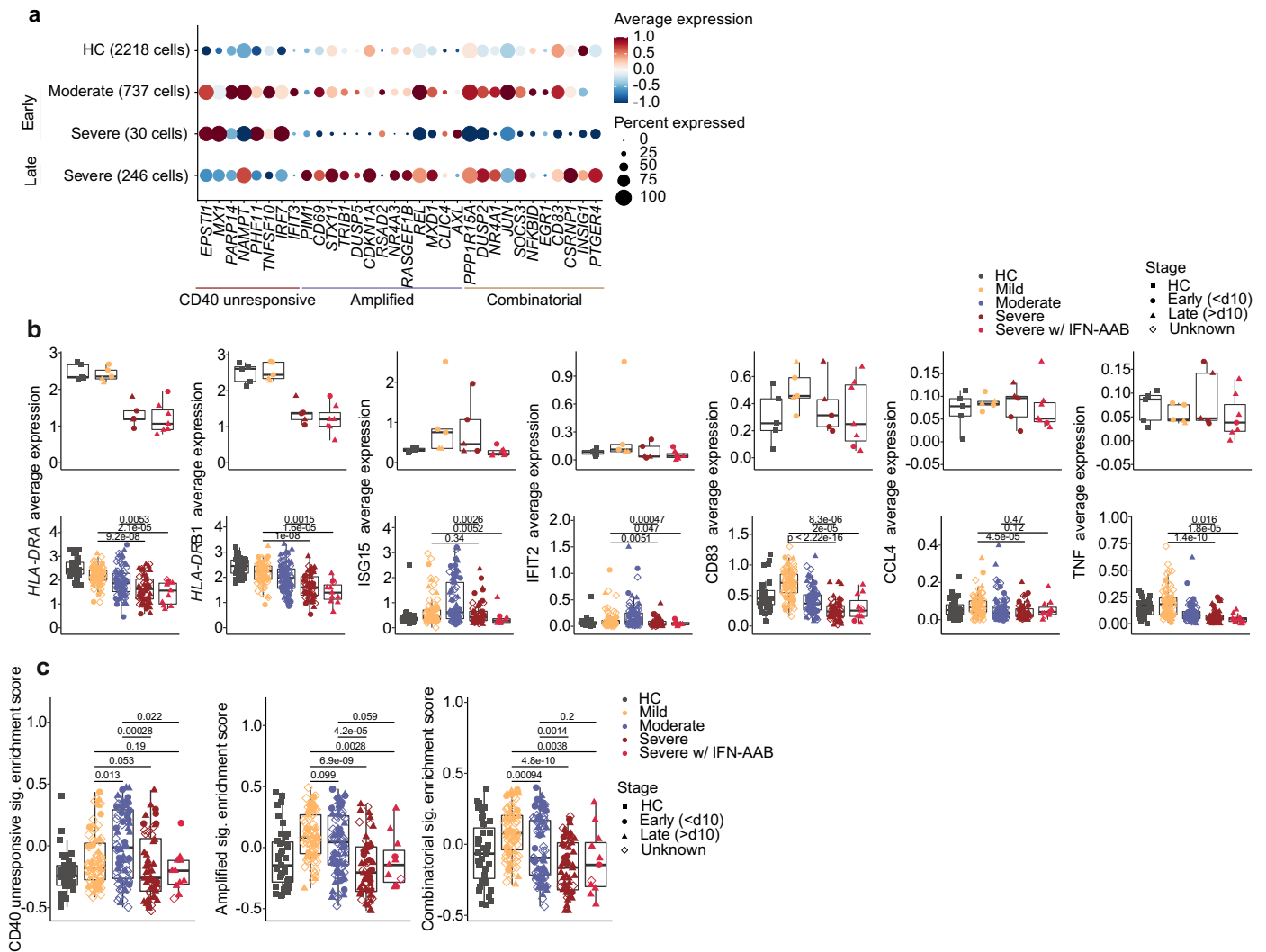
3 independent experiments. Adjusted p-value of statistically significant differences between conditions as assessed by one-way ANOVA indicated; ns = non-significant. **d**, Percent of MHC-II^{hi} CD8⁺ DCs from IFN α R-deficient (*Ifnar2*^{-/-}) and WT mice naïve or 2 days after epicutaneous HSV-1 infection. Data are presented as mean \pm s.e.m pooled from 7 independent experiments ($n \geq 5$ per experiment). Statistically significant differences between conditions as assessed by Mann-Whitney test; two-tailed p-value indicated; ns = non-significant. **e**, 'BMDC1-IFN- α A' and 'BMDC1-unstimulated' increase CD40 expression to comparable levels over time. Data are presented as mean \pm s.e.m pooled from 3 independent experiments. Two-way ANOVA performed between the corresponding conditions ns = non-significant.



Extended Data Fig. 2 | See next page for caption.

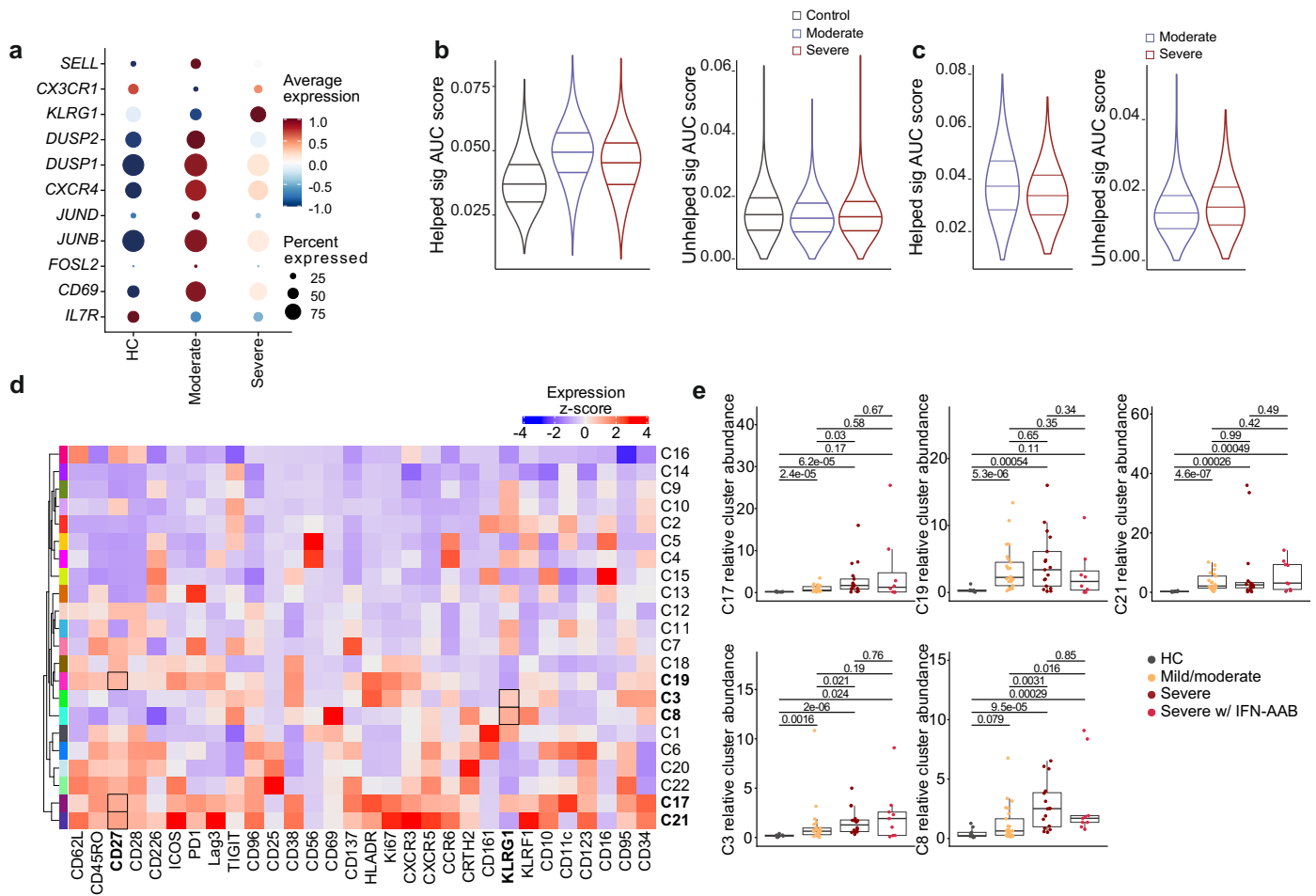
Extended Data Fig. 2 | CD40 stimulation induces successive waves of transcriptional regulation in IFN- α -conditioned BMDC1. **a**, Genes included in modules 1, 2 and 3 from the co-expression analysis (Fig. 2e) displayed as heatmap. **b**, Top GO-terms associated with the genes included in modules 1, 2 and 3 (Fig. 2e). **c**, Representative immunoblotting of I κ B α degradation and

P65 phosphorylation in 'BMDC1-IFN α +CD40-15min', 'BMDC1-IFN α -30min' and 'BMDC1-IFN- α +CD40-4h' compared to 'BMDC1-IFN- α ', 'BMDC1-CD40' and 'BMDC1-unstimulated'. Full gels of the two independent experiments are displayed below. Probing of β -actin and/or total P65 served as loading control.



Extended Data Fig. 3 | Enrichment of APC with ‘help’-dependent transcriptional profiles in patients with moderate COVID-19. **a**, Differentially expressed genes in DCs comparing disease severity and disease stage that correspond to the ‘CD40 unresponsive’, ‘amplified’ and ‘combinatorial’. Data from published DC-enriched scRNAseq data²⁶. **b**, Average gene expression in CD14⁺ monocytes per sample across selected key genes in a cohort of control (n=5), mild (n=5) and severe (n=5) COVID-19 patients and 7 samples derived from patients with IFN-AAB. **c**, Combined data set across 263 samples including controls (n=39), mild COVID-19 (WHO 1-3, n=79), moderate COVID-19 (WHO

4-5, n=82), severe COVID-19 (WHO 6-8, n=52), severe COVID-19 with IFN-AAB (WHO 7-8, n=11). Samples are stratified by disease severity according to the WHO ordinal scale as indicated and segregated by time point of sample collection relative to the onset of symptoms where available. **c**, Single-sample GSEA of the ‘CD40 unresponsive’, ‘amplified’ and ‘combinatorial’ gene signatures in monocytes from COVID-19 and control samples of the combined data set in **b**, stratified by disease severity and plotted as box plots of the enrichment scores. Wilcoxon rank-sum test p-value is shown.



Extended Data Fig. 4 | Enrichment of CD8⁺ T cells with ‘help’-dependent transcriptional profiles in patients with moderate COVID-19. **a**, Differential expression of selected key genes in CD8⁺ T cells derived from PBMCs scRNA-seq data of moderate and severe cases of COVID-19 and healthy HC originally as published³⁶. **b**, AUCell enrichment of CD8⁺ T cells for ‘helped’ and ‘unhelped’ T cell gene signatures derived from RNA-seq analysis of CD8⁺ T cells primed in the presence or absence of CD4⁺ T cell help. Data are stratified by disease severity and plotted as violin plots of the ‘Area Under the Curve’ (AUC) scores. **c**, AUCell enrichment of CD8⁺ T cells for ‘helped’ and ‘unhelped’ T cell gene signatures

derived from RNA-seq analysis of CD8⁺ T cells primed in the presence or absence of CD4⁺ T cell help. Data are derived from scRNA-seq of nasopharyngeal and bronchial samples stratified by disease severity and plotted as violin plots of the ‘Area Under the Curve’ (AUC) scores³⁷. **d**, Heatmap showing z-scaled expression values of indicated proteins across the clusters identified in the CyTOF data of individuals with COVID-19 and HCs. **e**, Box plots showing relative cluster abundances of selected clusters across COVID-19 and control samples stratified according to disease severity and presence of IFN-AAB. Benjamini-Hochberg corrected pairwise Wilcoxon p-values are shown.